4D Printing as a New Paradigm for Advanced Manufacturing

by

Farhang Momeni

A dissertation submitted in partial fulfillment
of the requirements for the degree of
Doctor of Philosophy
(Mechanical Engineering)
in The University of Michigan
2018

Doctoral Committee:

Professor Jun Ni, Chair
Associate Professor Kira Barton
Professor Jinsang Kim
Professor Jyoti Mazumder

Farhang Momeni

farhang@umich.edu

ORCID iD: 0000-0001-9596-3026

ACKNOWLEDGEMENTS

I would like to thank:

- My parents.
- My advisor Prof. Jun Ni for his advice and support during this scientific journey.
- My committee members Prof. Jyoti Mazumder, Prof. Jinsang Kim, and Prof. Kira Barton for their valuable comments and encouragements.
- My co-authors in the article related to chapter 1: Prof. Xun Liu that reviewed the manuscript and provided feedback and Dr. Seyed M. Mehdi Hassani that helped me in drawing some of the figures and checking the figure and citation numbering in the related article.
- My co-authors in the article related to chapter 4: Reza Valizadeh; that I conceived the related study with his input; Seyedali Sabzpoushan for CFD analysis; Seyedali Sabzpoushan, Prof. Mohammad Reza Morad, and Reza Valizadeh for performance analysis and useful discussions on other parts of the article related to this chapter, and Prof. Xun Liu for useful discussions on various elements of the article related to this chapter.
- The Mechanical Engineering Department at the University of Michigan for preparing full funding for the whole duration of my direct Ph.D. program.
- S.M. Wu Manufacturing Research Center in the Mechanical Engineering Department at the University of Michigan.
- Prof. Albert Shih for permission to use the printers in the S.M. Wu Manufacturing Research Center.
- The Mechanical Engineering Department at the University of Michigan for use of the Wind Tunnel facility in Lab I (ME 395), for which I served as a GSI (Graduate

Student Instructor); Mr. Todd Wilber and Mr. John Laidlaw for assistance in setup and usage.

- Mr. Andrea Poli for assistance in DMA tests in the Mechanical Testing Core directed by Prof. Ellen Arruda in the ME Department at the University of Michigan.
- The course "Heat Transfer (ME 335)" taught by Prof. Massoud Kaviany at the University of Michigan, for which I served as a GSI (Graduate Student Instructor).
- The courses "Assembly Modeling for Design and Manufacturing (ME 588)" and "Design for Manufacturability (ME 452)" taught by Prof. Kazuhiro Saitou at the University of Michigan, for which I served as a GSI (Graduate Student Instructor).
- The unlimited meal plan of the University of Michigan that saved my time.
- The Blue buses of the University of Michigan that even work after 11 PM and are free.

TABLE OF CONTENTS

LIST OF TABLES

LIST OF FIGURES

ABSTRACT

4D printing is a new manufacturing paradigm that combines stimuli-responsive materials, mathematics, and multi-material additive manufacturing to yield encoded 3D structures with intelligent behavior over time. This field has received growing interests from various disciplines such as space exploration, renewable energy, bioengineering, textile industry, infrastructures, soft robotics, etc. Here, after a review of 4D printing, three substantial gaps are identified. First, the main difference between 3D and 4D printed structures is one extra dimension that is smart evolution over "time". However, currently, there is no general formula to model and predict this extra dimension. This gap pertains to the design aspect of 4D printing. Second, 3D printing is a well-known manufacturing process with its unique attributes. Now, 4D printing needs to be underpinned as a manufacturing process and its unique attributes should also be proved. This gap pertains to the manufacturing aspect of 4D printing. Third, various shape-morphing 4D printed structures have been illustrated in the literature. However, real applications and products, where 4D printing can provide unique features still need to be demonstrated. This gap pertains to the product development aspect of 4D printing.

To address the first gap (design), we delve into the fourth dimension and reveal three general laws that govern the shape-shifting behaviors of almost all (photochemical-, photothermal-, solvent-, pH-, moisture-, electrochemical-, electrothermal-, ultrasound-, etc.-responsive) multi-material 4D structures. By starting from fundamental concepts, we derive and validate a universal bi-exponential formula that is required to model and predict the fourth dimension of 4D multi-materials. Our results, starting from the most fundamental concepts and ending with governing equations, can serve as general design principles for future research in 4D printing, where the time-dependent behaviors should be understood, modeled, and predicted correctly. Future 4D printing software and hardware developments can also benefit from these results.

To address the second gap (manufacturing), first, we underpin 4D printing as a new manufacturing process and identify its unique attributes. Then, we specifically focus on the energy-saving attribute of 4D printing. We obtain the theoretical limit of energy consumption in 4D printing and prove that 4D printing can be the most energy-efficient manufacturing process.

To address the third gap (product development), we demonstrate two real applications, where 4D printed products can provide unique features. First, we demonstrate a novel wind turbine blade based on 4D printing that provides several advantages in one blade, simultaneously. Scientists reported that leaf veins grow in a manner not only to facilitate their biological and physiological functions but also to sustain the environmental loads. Researchers showed that plant-leaf-mimetic blades could always have better structural properties compared with the conventional structures. However, the plant-leaf-mimetic blade has remained at the level of simulations. We demonstrate the plant-leaf-mimetic blade in practice that simultaneously has the capability of bend-twist-coupling. Second, we introduce the concept of smart solar concentrators inspired by nature and enabled by 4D printing. We found that diurnal flowers mainly have parabolic and nocturnal flowers mainly have hyperbolic petals. Based on this inspiration, we propose a smart solar concentrator that can increase the overall optical efficiency more than 25% compared with its non-smart counterparts.

CHAPTER 1

INTRODUCTION AND A REVIEW OF 4D PRINTING

Research into 4D printing has attracted unprecedented interest since 2013 when the idea was first introduced. It is based on 3D printing technology, but requires additional stimulus and stimulus-responsive materials. Based on certain interaction mechanisms between the stimulus and smart materials, as well as appropriate design of multi-material structures from mathematical modeling, 4D printed structures evolve as a function of time and exhibit intelligent behavior. 4D printing targets a time-dependent and predictable shape/property/functionality evolution. This allows for self-assembly, self-adaptability, and self-repair. This chapter presents a comprehensive review of the 4D printing process and summarizes the practical concepts and related tools that have a prominent role in this field. Unsought aspects of 4D printing are also studied and organized for future research.[1]

1.1 Introduction

3D printing was invented in the 1980s and has been applied in various fields, ranging from biomedical science to space science. 4D printing, a recently developed field originating from 3D printing, shows promising capabilities and broad potential applications. 4D printing was initiated and termed by a research group at MIT (Tibbits, 2013). It relies on the fast growth of smart materials, 3D printers, design (Choi et al., 2015), and mathematical modeling. 4D printing shows advantages over 3D printing in several aspects (Jacobsen, 2016).

In this review, a general guideline is provided by deconstructing the 4D printing into several sections. These sections include definition, motivations, shape-shifting behaviors, material structures, materials, shape-shifting mechanisms and stimuli, mathematics, and applications.

[1] This chapter is based on our journal article published in *Materials & Design 122 (2017)*, entitled "A review of 4D printing", by Farhang Momeni, Seyed M.Mehdi Hassani, Xun Liu, and Jun Ni.

1.1.1 Definition

4D printing was initially defined as 4D printing = 3D printing + time (Figure 1-1), where the shape, property, or functionality of a 3D printed structure can change as a function of time (Tibbits, 2013; 2014; Tibbits et al., 2014; Ge et al., 2013; Pei, 2014; Khoo et al., 2015). As the number of studies conducted on this technology increases, a more comprehensive definition of 4D printing is necessary and presented here. 4D printing is a targeted evolution of the 3D printed structure, in terms of shape, property (other than shape), or functionality. It is capable of achieving self-assembly, self-adaptability, and self-repair. It is time-dependent, printer-independent, and predictable.

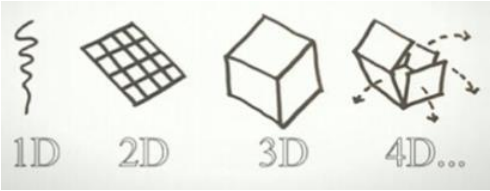

Figure 1-1. A simple illustration of the concept of 4D printing (Young, 2016).

As mentioned above, 4D printing can fabricate dynamic structures with adjustable shapes, properties, or functionality (Tibbits et al., 2014; Pei, 2014; Gladman et al., 2016). This capability mainly relies on an appropriate combination of smart materials in the three-dimensional space (Gladman et al., 2016). Mathematical modeling is required for the design of the distribution of multiple materials in the printed structure. There are at least two stable states in a 4D printed structure, and the structure can shift from one state to another under the corresponding stimulus (Zhou et al., 2015). The differences between 3D printing and 4D printing processes are illustrated in Figure 1-2.

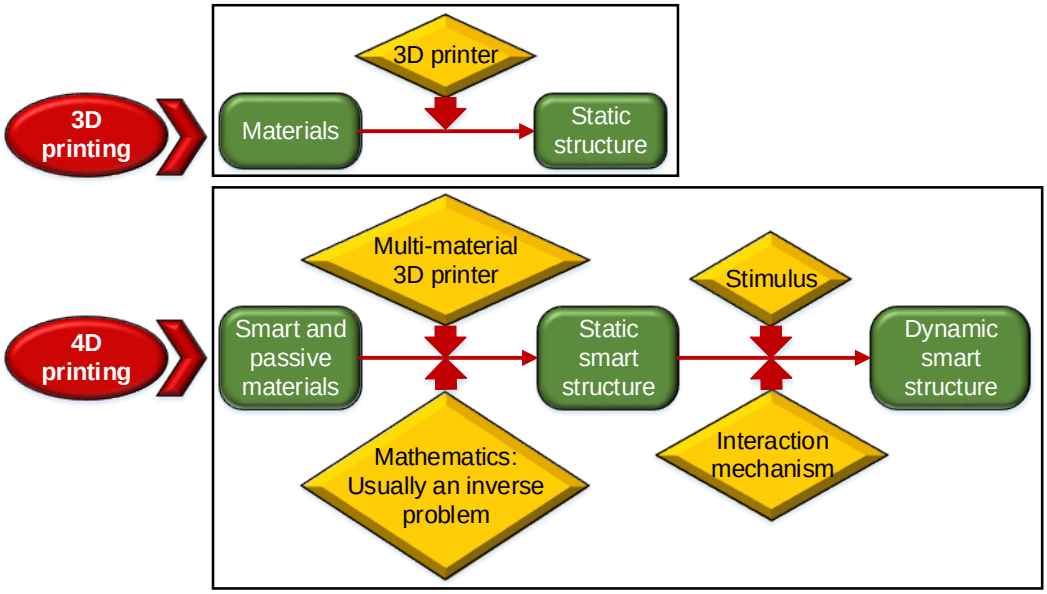

Figure 1-2. The differences between 3D printing and 4D printing processes.

As illustrated in Figure 1-3, the fundamental building blocks of 4D printing are 3D printing facility, stimulus, stimulus-responsive material, interaction mechanism, and mathematical modeling. These elements enable targeted and predictable evolution of 4D printed structures over time and are discussed in further detail below:

- 3D printing facility: Usually, a 4D printed structure is created by combining several materials in the appropriate distribution into a single, one-time printed structure (Raviv et al., 2014). The differences in material properties, such as swelling ratio and thermal expansion coefficient, will lead to the desired shape-shifting behavior. Therefore, 3D printing is necessary for the fabrication of multi-material structures.
- Stimulus: Stimulus is required to trigger the alterations of shape/property/functionality of a 4D printed structure. The selection of the stimuli depends on the requirements of the specific application, which also determines the types of smart materials.
- Smart or stimulus-responsive material: Stimulus-responsive material is one of the most critical components of 4D printing. Stimulus-responsive materials can be classified into several sub-categories, as shown in Figure 1-4. The capability of this group of materials is defined by the following characteristics: self-sensing, decision making, responsiveness, shape memory, self-adaptability, multi-functionality (Khoo et al., 2015), and self-repair. Several review studies on

stimulus-responsive materials have been provided by Roy et al. (2010), Stuart et al. (2010), Sun et al. (2012), and Meng et al. (2013).

- Interaction mechanism: In some cases, the desired shape of a 4D printed structure is not directly achieved by simply exposing the smart materials to the stimulus. The stimulus needs to be applied in a certain sequence under an appropriate amount of time, which is referred to as the interaction mechanism in this review study. For example, one of the main interaction mechanisms is constrained-thermo-mechanics. In this mechanism, the stimulus is heat and the smart material has the shape memory effect. It contains a 4-step cycle. First, the structure is deformed by an external load at a high temperature; second, the temperature is lowered while the external load is maintained; third, the structure is unloaded at the low temperature and the desired shape is achieved; fourth, the original shape can be recovered by reheating.
- Mathematical modeling: Mathematics is necessary for 4D printing in order to design the material distribution and structure needed to achieve the desired change in shape, property, or functionality. Theoretical and numerical models need to be developed to establish the connections between four core elements: material structure, desired shape, material properties, and stimulus properties. These will be discussed in additional details later.

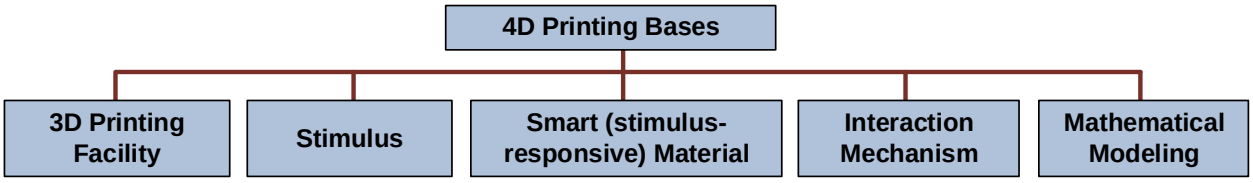

Figure 1-3. 4D printing bases.

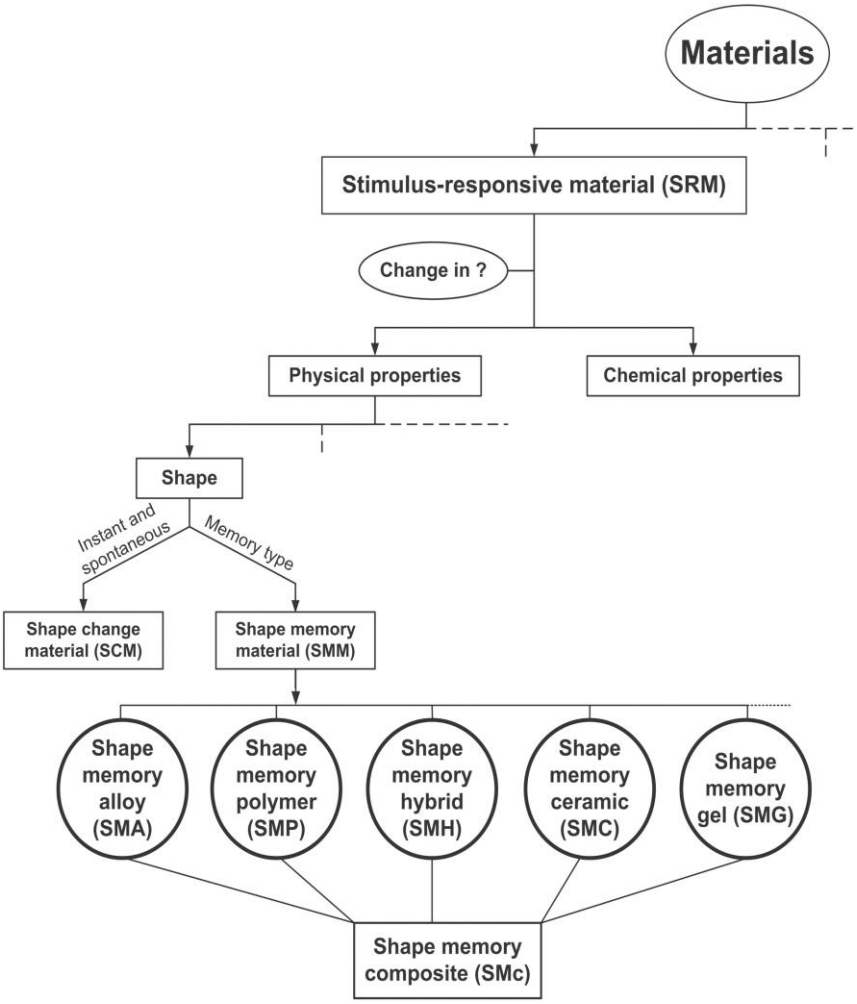

Figure 1-4. Stimulus-responsive materials (Sun et al., 2012).

A 4D printed structure can be regarded as a child born from the marriage between a 3D printer and smart materials. It can walk by being exposed to the external stimulus through an interaction mechanism, and it learns how to walk properly with the assistance of mathematics.

1.1.2 Motivations

4D printing opens new fields for application, in which a structure can be activated for self-assembly, reconfiguration, and replication through environmental free energies (Tibbits, 2014). This brings several advantages, such as significant volume reduction for storage, and transformations that can be achieved with flat-pack 4D printed structures. The latter may include transformations to 3D structures required during actual applications (Tibbits, 2014). Another example is that instead of directly creating a complicated structure using the 3D printing process, simple components from smart materials can be 3D printed first and then self-assembled to reach

that final complex shape (Zhou et al., 2015). In general, the applications of 4D printed structures can be classified into three categories: self-assembly, self-adaptability, and self-repair.

- Self-assembly:

Self-assembly extends from the molecular scale to the planetary scale (Whitesides & Grzybowski, 2002; Campbell et al., 2014). Currently, researchers are interested in macroscale applications (Campbell et al., 2014). One example is the transfer of equipment parts to the inside of a human body through a small hole. The parts can then self-assemble at the desired location for medical purposes (Zhou et al., 2015). Another future application of self-assembly will be on a large scale and in a harsh environment. Individual parts can be printed with small 3D printers and then self-assembled into larger structures, such as space antennae and satellites (Tibbits et al., 2014). This capability paves the way for the creation of transportation systems to the International Space Station (Choi et al., 2015). Further applications include self-assembling buildings, especially in war zones or in outer space where the elements can come together to yield a finished building with minimum human involvement (Campbell et al., 2014). Moreover, some limitations in architectural research and experiments can be removed with the capabilities of 4D printing (Čolić-Damjanovic & Gadjanski, 2016).

- Self-adaptability:

Adaptive infrastructures are another application of 4D printing (Campbell et al., 2014). 4D printing can integrate sensing and actuation directly into a material so that external electromechanical systems are not necessary (Tibbits et al., 2014). This would decrease the number of parts in a structure, assembly time, material and energy costs, as well as the number of failure-prone devices, which is usually utilized in current electromechanical systems (Tibbits et al., 2014). Multi-functional and self-adaptive 4D printed tissues (Khademhosseini & Langer, 2016; Jung et al., 2016) and 4D-printed medical devices, such as tracheal stents (Zarek et al., 2017) and cardiovascular devices (Robinson et al., 2018) are other fascinating applications of 4D printing.

- Self-repair:

The idea of self-assembly can be utilized for self-disassembly. The error-correct and self-repairing capability of 4D manufactured products show tremendous advantages with regard to reusability and recycling (Tibbits, 2014). Self-healing pipes (Campbell et al., 2014) and self-healing hydrogels (Taylor, 2016) are some of the potential applications.

1.1.3 Various shape-shifting types and dimensions

Various shape-shifting types and dimensions that have been studied in 4D printing are categorized in Figure 1-5 along with the related literature (details in Appendix A).

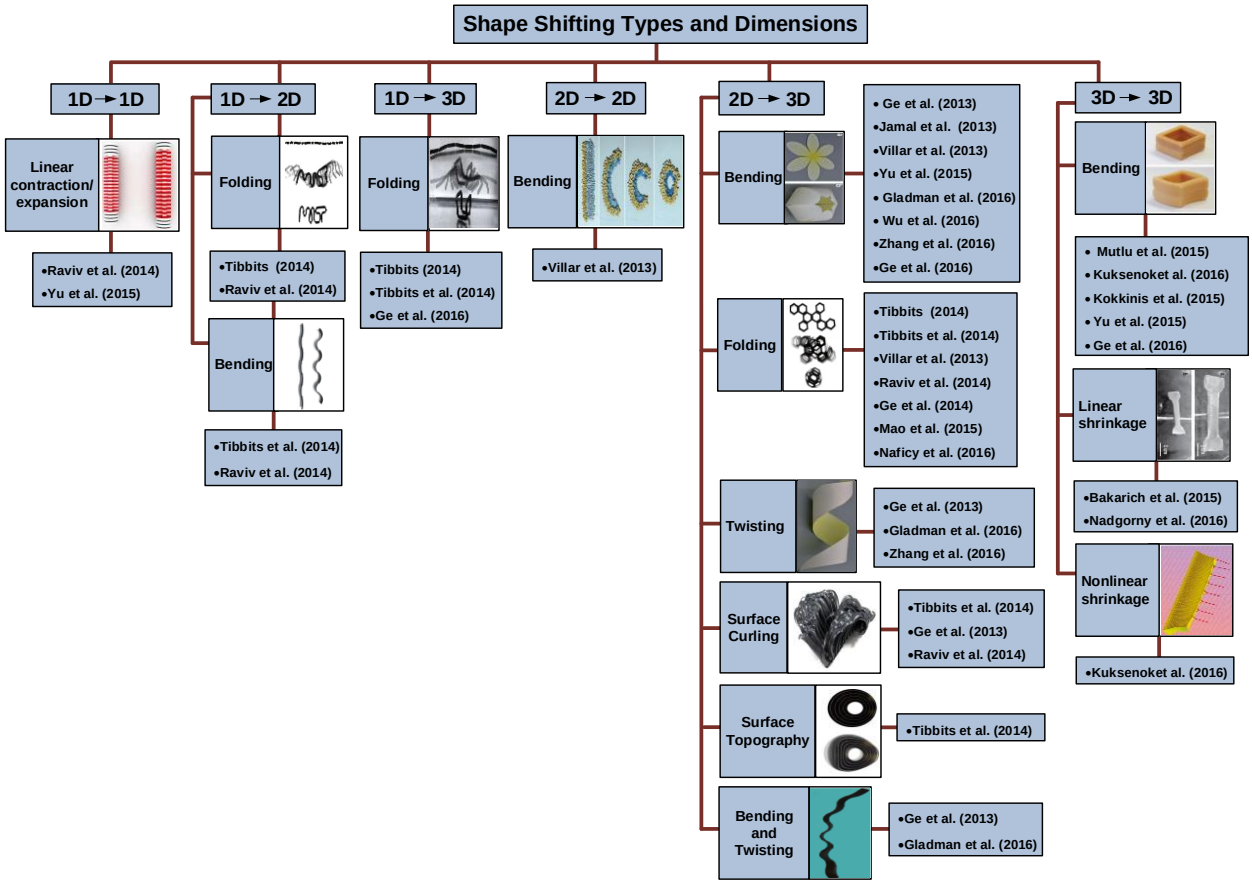

Figure 1-5. Shape-shifting types and dimensions in 4D printing.

In the following, we delve into the elements of 4D printing seen in Figure 1-2. The reader is also invited to have a look at Appendix A for details of various shape-shifting behaviors and applications of 4D printing.

1.2 Material structures

Details of material types are discussed in the next section. In this section, material structures are classified and generally referred to as smart materials and conventional (non-smart) materials. In additive manufacturing, material structures are divided into single-material and multi-material structures. According to Vaezi et al. (2013), multi-material structures can be further classified into

discrete multiple materials, composite materials, and porous materials. For the 4D printing process, a new classification is introduced in this review, and the multi-material structure can be categorized as uniform distribution, gradient distribution, and special patterns. Based on different perspectives, the material structure can also be classified as a structure with or without joints and hinges.

1.2.1 Multi-material structures

In 4D printing, multiple materials usually need to be inserted into a single and one-time printed structure (Raviv et al., 2014). This multi-material structure can be a mixture of different smart materials or a combination of smart materials and conventional materials. The single-material structure in 4D printing should always be fabricated with a smart material. In addition, it needs to be based on the structure with a gradient distribution of materials. The gradient distribution of a single material means that the density of the structure is different at various locations. This anisotropy can generate shape-shifting behaviors such as bending and twisting, which is beyond linear expansion and contraction. Most of the previous studies on 4D printing focused on multi-material structures. In this review, the concept of digital material is described for 4D printing. Based on this concept, all material structures involved in 4D printing can be generalized into three categories.

1.2.2 Digital materials

The digital concept was first introduced in the fields of communication and computation. This digital concept can be similarly expanded into material structures (Hiller et al., 2009). The element that enables us to move from analog materials to digital materials is the physical voxel (Hiller et al., 2009), which is defined as the fundamental and physical bit that occupies 3D physical space. The physical voxel can be of any size and shape (Hiller & Lipson, 2009; 2010; Popescu et al., 2006). In nature, biological structures usually consist of fundamental building blocks that can be considered physical voxels, such as DNA and proteins (Hiller et al. 2009). In 4D printing and associated multi-material structures, the physical voxel can be similarly defined.

Digital material is defined as an assembly of various physical voxels (Hiller & Lipson, 2009; 2010). The spatial arrangement of voxels plays a major role in determining the features of a 4D-printed structure (Raviv et al., 2014). In digital materials, each voxel contains only one material. Adjacent voxels can be composed of different materials. Each voxel has its own properties and the collection of different voxels results in the multi-material structure. According to Hiller et al.

(2010), a negative Poisson's ratio can be achieved with appropriate voxel arrangement in the digital material structure.

The three most important categories of 4D-printed structures for digital materials are uniform distribution (Figure 1-6 (a)), gradient distribution (Figure 1-6 (b)), and special patterns (Figure 1-6 (c)). One main category of special patterns is the fiber and matrix structure. Each structure in Figure 1-6 shows only one single layer, but they can be combined to yield bi-layer or multi-layer structures. In addition, the number of materials can be more than two. One example of a gradient distribution material structure is shown in Figure 1-7 from Tibbits et al. (2014). In this example, the concentration of active and passive materials varies from the center to the perimeter within one layer. The disk can yield various sinusoidal shapes depending on the duration of immersion in water.

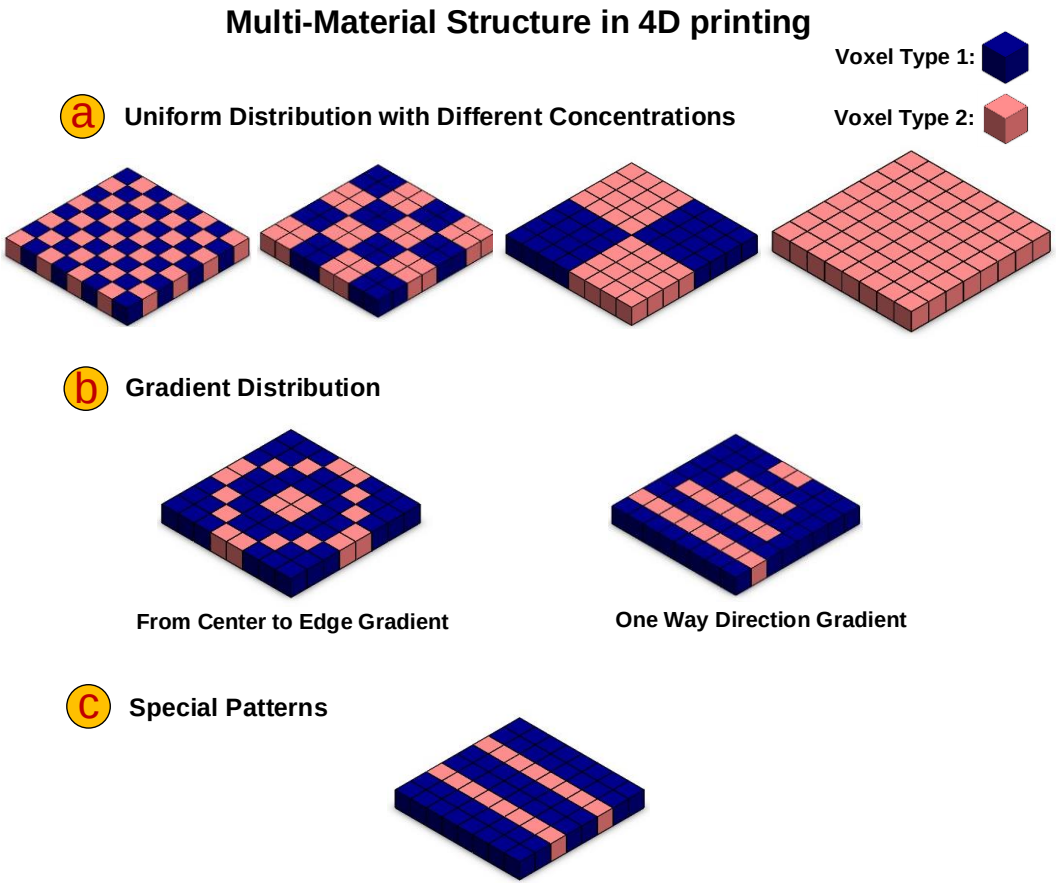

Figure 1-6. 4D-printed material structures (Digital Materials) (a) Uniform distribution with different concentrations, (b) Gradient distribution, and (c) Special patterns.

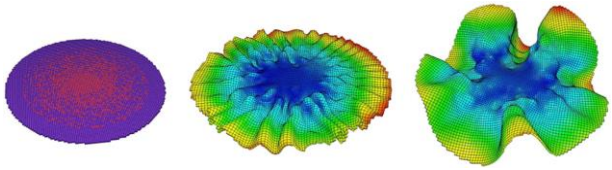

Figure 1-7. The simulation related to gradient distribution of material structure (red indicates the passive material and purple indicates the active material) and the results of its immersion in water over time (left to right) (Tibbits et al., 2014).

In summary, all multi-material structures that have been studied in the 4D printing process are summarized in the following figure, along with the related literature.

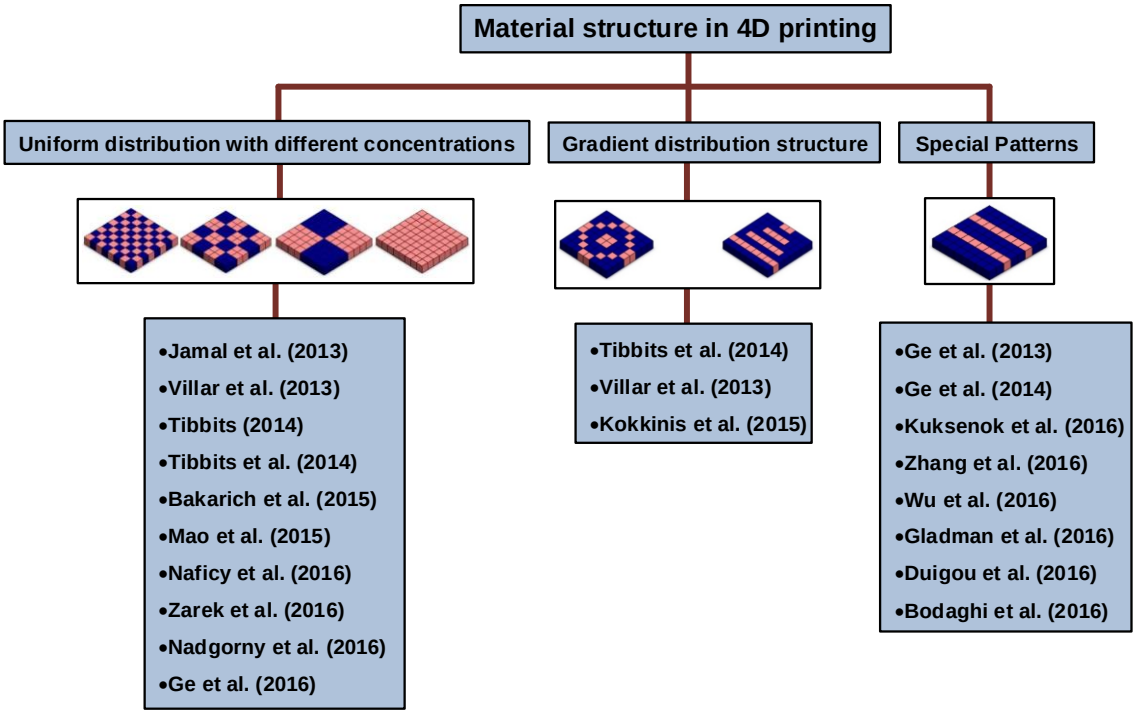

Figure 1-8. Multi-material structures that have been used in 4D printing.

To model the material structure in various length and time scales for digital materials, Myres et al. (1999) developed a software called the Digital Material (Myers et al., 1998). Popescu et al. (2006) proposed a new manufacturing process for digital materials that was reversible for disassembly and could reuse the building blocks of the structure. Huang et al. (2016) demonstrated an approach for ultrafast printing of shape-shifting materials. Zhou et al. (2013) reported that there were several limitations to the current additive manufacturing processes. For example, printers with inkjet nozzles could only print materials with certain viscosities and curing temperatures. The fused deposition modeling (FDM) process was relatively slow and had limited options for its minimum nozzle size. Zhou et al. (2013) investigated several new techniques for digital material

production using mask-image-projection-based stereolithography. Ge et al. (2016) provided an approach for printing multi-material shape memory polymers (SMPs) with a high resolution (up to a few microns). This approach is enabled by a high-resolution projection microstereolithography (PμSL) additive manufacturing system with an automated material exchange mechanism (Figure 1-9). In order to enable 4D printing for biomedical applications, multi-material additive manufacturing systems that can print from aqueous mediums needs to be developed (Loh, 2016). In this regard, the direct-write (DW) printing technique (Lewis, 2006; Gratson & Lewis, 2005; Lebel et al., 2010), which is suitable for printing polymeric solutions (Guo et al., 2013), can be engaged.

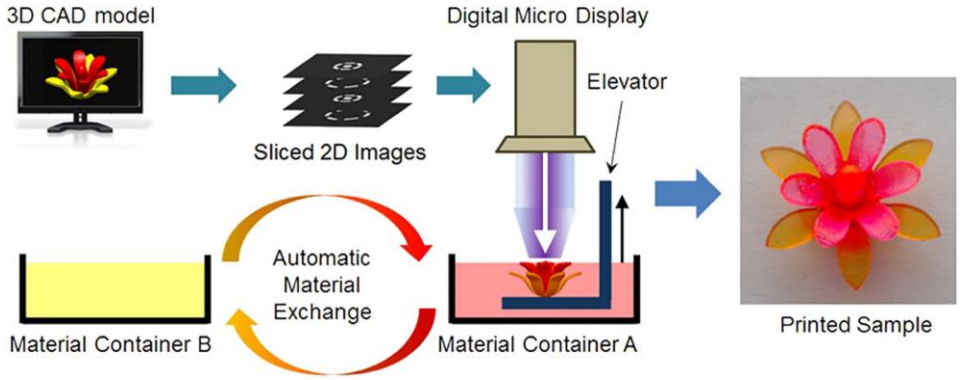

Figure 1-9. Multi-material additive manufacturing system (Ge et al., 2016).

In some studies on 4D printing, shape-shifting behavior is enabled by certain targeted smart hinges embedded inside the structure. In this case, only the hinges are made from smart materials and the other parts are made from conventional materials. A typical example is shown in Figure 1-10. 4D-printed structures with hinges are typically used for folding, wherein the structures can deform through the hinges. In other cases, the structure itself has shape-shifting capability without dependence on the hinges. In these hinge-less structures, the spatial arrangement of passive and active materials is extremely crucial to precisely yield the desired shape-shifting behavior (Tibbits et al. 2014). In general, structures with hinges can achieve local shape-shifting behavior, while the structures without hinges can have both global and local shape-shifting behaviors.

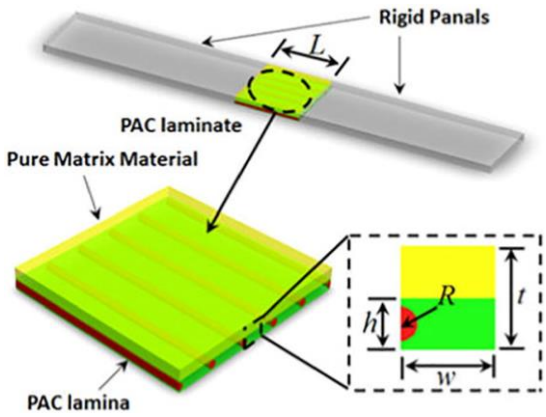

Figure 1-10. Illustration of structures with a smart hinge (Ge et al. 2014).

In summary, structures with hinges vs. structures without hinges in 4D printing are categorized in Figure 1-11, along with the related studies.

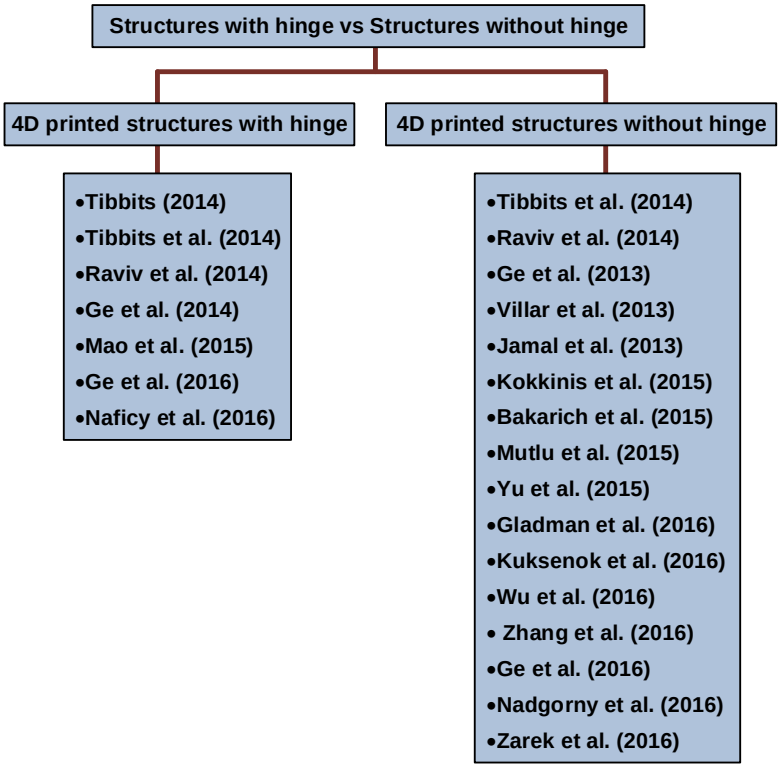

Figure 1-11. Structures with hinges vs. structures without hinges in 4D printing.

1.3 Materials

The development of smart materials should be pursued in parallel with the development of printers. Currently, many 4D printing applications are limited because of unsatisfactory material properties. For example, 4D printing can fabricate artificial muscles; however, the mechanical

properties of current materials are insufficient to yield the desired performance and functions of actual biological muscles (Loh, 2016). Therefore, the development of advanced smart materials with desirable properties that are also compatible with printers is crucial to advance the application of 4D printing. Programmable materials, such as carbon fiber, wood, and textiles, have undeniable influence in many applications, including aerospace, automotive, clothing, construction, healthcare and utility (Loh, 2016).

Tibbits et al. (2014) applied passive plastic and active expandable polymer materials in their experiments. They combined these two materials in various spatial arrangements, as shown in Figures A-7, A-8, and A-9. The expandable material was a hydrophilic UV-curable polymer, which could expand up to 150% of its original volume under water. Raviv et al. (2014) performed a more precise experiment with two base materials similar to those used by Tibbits (2014) and Tibbits et al. (2014). One of the base materials was passive plastic with an elastic modulus of 2 GPa and a Poisson`s ratio of 0.4. The other base material was an expandable material with an elastic modulus of 40 MPa in the dry condition and 5 MPa in water. Its Poisson's ratio is 0.5. This expandable material has a composition of vinyl caprolactam (50 %wt), polyethylene (30 %wt), epoxy diacrylate oligomer (18 %wt), Irgacure 81 (1.9 %wt), and wetting agent (0.1 %w). It could expand up to 200% of its original volume under water. Its material structure contains hydrophilic acrylated monomers that build linear chains during the polymerization process with some difunctional acrylate molecules. This kind of crosslink makes the polymer swell under water rather than being dissolved (Raviv et al. 2014).

Ge et al. (2013) printed glassy shape memory polymer fibers in an elastomeric matrix. The elastomeric matrix has no shape memory effect, i.e., the degree of fixity is 0%. The glass transition temperature, T_g of the matrix is approximately -5 °C. The matrix is in a rubbery state with a modulus of approximately 0.7 MPa at 15 °C. The fiber has a glass transition temperature T_g approximately 35 °C. Its modulus is 3.3 MPa at the lowest temperature of the thermomechanical cycle ($T_L = 15$ °C) and 13.3 MPa at the highest temperature ($T_H = 60$ °C).

Ge et al. (2014) used two base materials: Tangoblack as the elastomeric matrix with $T_g \sim -5$ °C and Verowhite (Gray 60) as the fiber with $T_g \sim 47$ °C. Tangoblack is in a rubbery state at room temperature, which can be polymerized by an ink consisting of urethane acrylate oligomer, Exo-1, 7, 7-trimethylbicyclo (2.2.1) hept-2-yl acrylate, methacrylate oligomer, polyurethane resin, and photo initiator. Verowhite is a rigid plastic at room temperature and can be polymerized by an ink

consisting of isobornyl acrylate, acrylic monomer, urethane acrylate, epoxy acrylate, acrylic monomer, acrylic oligomer, and photo initiator. Similarly, Bodaghi et al. (2016) used TangoBlackPlus and VeroWhitePlus in a fiber and matrix structure. They also used Sup705a, which is a hydrophilic gel, as a sacrificial material for the manufacturing of complex geometries. This auxiliary material can be removed using a compressed water jet during the post-fabrication process, based on the preferential interactions between the hydrophilic gel and water.

Jamal et al. (2013) (Figure A-20) used photopatterned poly (ethylene glycol) (PEG)-based hydrogel bilayers. The two PEG bilayers contain two molecular weights with different swelling ratios and are crosslinked with conventional photolithography.

Villar et al. (2013) printed aqueous droplets in oil, which were connected by lipid bilayers and create a cohesive material.

Mao et al. (2015) used the same two base materials as Ge et al. (2014) did (Tangoblack and Verowhite). They combined these two materials at varying compositions, which was different from the conventional fiber and matrix structure in Ge et al. (2014). In fact, they fabricated seven compositions with various combinations of these two materials for seven hinges, as shown in Figure A-25.

Bakarich et al. (2015) used Alginate/PNIPAAm ionic covalent entanglement (ICE) gel with various concentrations of NIPAAm. In their experiments, the thermo-responsive crosslinked network of poly N-isopropylacrylamide (PNIPAAm) was utilized as the toughening agent and could also achieve reversible volume changes. The Alginate/PNIPAAm ICE gel contained α-Keto glutaric acid photoinitiator, acrylamide, alginic acid sodium salt, calcium chloride, ethylene glycol (as a rheology modifier), N-isopropylacrylamide and N, N'-methylenebisacrylamide crosslinker, and a commercial epoxy-based UV-curable adhesive (Emax 904 Gel-SC).

Kokkinis et al. (2015) used two cross-linked polymers with different swelling properties: a soft, highly swellable polymer and a solid polymer. The ink for these two polymers consists of PUA oligomers, which act as the base components of all inks. Two of them yield hard polymers, such as BR 302 and BR 571, and one of them yields a soft polymer, such as BR 3641 AJ. The ink for the two polymers also consists of reactive diluents to change the rheological and mechanical properties, photoinitiator (either Irgacure 907 with ultraviolet light or Irgacure 819 with a longer wavelength blue LED light), rheology modifier, and the alumina platelets. They used various concentrations of components for different objectives.

Mutlu et al. (2015) (Figure A-36) printed a thermoplastic elastomer (TPE) material that had viscoelastic behavior and was soft enough for the fabrication of a compliant finger.

Gladman et al. (2016) (Figure A-33) fabricated a composite hydrogel ink that mimicked the structure of plant cell walls. It consisted of a soft acrylamide matrix reinforced with the cellulose fibrils that had a high stiffness. The composite was printed using a viscoelastic ink that contained an aqueous solution of N, N-dimethylacrylamide, Irgacure 2959 (BASF), nanoclay, glucose oxidase, glucose, and nanofibrillated cellulose (NFC). Irgacure 2959 is the ultraviolet photoinitiator. The clay particles were used as a modifier for appropriate rheology and viscoelasticity, which was necessary for desirable ink printing. Larger amounts of clay lead to higher crosslink densities and therefore lower swelling ratios. Glucose oxidase and glucose scavenge the surrounding oxygen, which consequently can control oxygen during the UV curing process. The shape-shifting behavior of the material with the composition described above was irreversible. To achieve reversible shape-shifting behavior in hot and cold water, the poly(N, N-dimethylacrylamide) needed to be replaced with thermo-responsive N-isopropylacrylamide.

Zhang et al. (2016) printed polylactic acid (PLA) strips as the fibers on a fixed sheet paper. PLA strips have a glass transition temperature of $T_g \sim 60$ ℃ and an elastic modulus of 3.5 GPa in its glass state (Drumright et al., 2000; Cock et al., 2013). Zhang et al. (2016) assumed the elastic modulus of PLA to be 50 MPa when the temperature was above its T_g. In addition, they assumed the coefficient of thermal expansion of sheet paper to be negligible (Figure A-26).

Kuksenok et al. (2016) fabricated a composite that consisted of a thermo-responsive polymer gel with poly (N-isopropylacrylamide) (PNIPAAm), which was the host gel, and photo-responsive fibers functionalized with spirobenzopyran (SP) chromophores. The thermo-responsive gel has a lower critical solution temperature (LCST) and undergoes contraction at high temperature. With no light, the spirobenzopyran chromophores are in open ring form or in an equivalent protonated merocyanine McH form. Under the blue light, they are reversibly converted to the closed ring form or the equivalent spiro SP form (Kuksenok et al., 2016).

Wu et al. (2016) (Figures A-13, A-14, A-15, A-16, and A-17) used TangoBlack plus and Verowhite, which is similar to what Ge et al. (2014) and Mao et al. (2015) used. However, their composite contains two types of fibers. They used DM8530 (fiber 1) with $T_g \sim 57$ ℃ and DM9895 (fiber 2) with $T_g \sim 38$ ℃. These two fibers have SME in the temperature range between ~ 20 ℃ and ~ 70 ℃. The matrix is TangoBlack with $T_g \sim 2$ ℃.

Le Duigou et al. (2016) fabricated hygromorphic biocomposite, which was activated by moisture gradient. Their hygromorphic biocomposite consisted of polylactic acid (PLA) and polyhydroxyalkanoate (PHA) as the overall matrix, which was then reinforced with wood fibers. Natural fibers such as wood, flax, hemp, etc. usually exhibit hydro-elastic behavior. Biocomposites with natural fibers have a high-porosity microstructure (approximately 20 % volume percent). This structure enables swelling when subjected to moisture gradient.

Nadgorny et al. (2016) tried to achieve high quality, printable pH-responsive filaments for material extrusion 3D printing. They used poly (2-vinylpyridine) (P2VP) core material, and improved its mechanical properties by adding 12 %wt of acrylonitrile−butadiene− styrene (ABS) as the reinforcement material.

Zarek et al. (2016) produced a thermo-responsive shape memory tracheal stent based on semi-crystalline methacrylated polycaprolactone (PCL). PCL has great rheological and viscoelastic properties and can be easily manufactured into implants and medical devices. PCL has also been used in many drug delivery and tissue engineering applications (Woodruff & Hutmacher, 2010). Zarek et al. (2017) additionally used 2,4,6-trimethylbenzoyl-diphenyl-phosphineoxide (TPO) as the photoinitiator, in addition to vitamin E, to avoid premature crosslinking.

Naficy et al. (2016) used poly (N-isopropylacrylamide) (poly(NIPAM)) as the smart thermo-responsive polymer, along with a non-active poly (2-hydroxyethyl methacrylate) (poly(HEMA)) as the bilayer. Long polymer chains of polyether-based polyurethane (PEO-PU) are used to modify the rheology and viscosity. α-ketoglutaric acid serves as the UV initiator. N, N′-methylenebisacrylamide (BIS) is the crosslinking agent.

- **Discussions**

From analyzing existing studies, there are two requirements for materials in the 4D printing process: printability and intelligence (Figure 1-12). If the materials cannot be printed, the 4D printed structure cannot be manufactured. Many studies utilized a rheology modifier to provide a suitable material viscosity for extrusion-based printing processes. Similarly, the photo-initiator and the crosslinking and sacrificial agents are several other aspects that need to be considered for proper material printability. If the structure contains only non-active materials, it cannot achieve any targeted changes over time as a response to the stimulus. Schweiger et al. (2016) studied multilayered anterior teeth and defined "multi-material-3D-printing" as a 4D printing process. This

is not the 4D printing process discussed in this study because the structure does not contain any smart material.

Some applications require dual-responsive materials. For example, the shape-shifting behavior of a material can be triggered by both water and heat. Triple and other multi-responsive materials have not been considered in the 4D printing process so far and can be studied in the future. Another issue is the degree to which the smart materials can respond to stimulus. Some smart materials can sense stimulus but only provide minimal actuation or respond after a very long time. The responsivity of smart materials needs to be further studied as well.

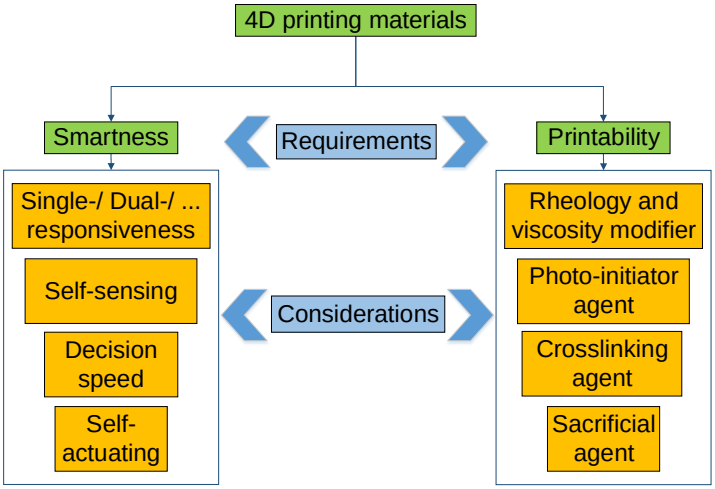

Figure 1-12. 4D printing materials.

1.4 Shape-shifting mechanisms and Stimuli

A 4D-printed structure can alter its shape, properties, or functionality based on one or more stimuli. However, an interaction mechanism needs to be identified, through which the printed smart structure can respond to stimulus in an appropriate way. The mechanisms can be divided into various categories. Campbell et al. (2014) explained two types of mechanisms in 4D printing: hydro-mechanics and thermo-mechanics. In this section, other mechanisms from the literature are organized and summarized, including unconstrained-hydro-mechanics, constrained-thermo-mechanics, unconstrained-thermo-mechanics, unconstrained-hydro-thermo-mechanics, unconstrained-pH-mechanics, unconstrained-thermo-photo-mechanics, osmosis-mechanics, and dissolution-mechanics.

- Unconstrained-Hydro-Mechanics

In this mechanism, a smart printed structure consists of an expandable hydrophilic active material and a passive material. Water is utilized as the external stimulus so that the structure can undergo shape-shifting under water and so that it can return to its original shape after being dried. This mechanism is driven by the different swelling ratios between the active and passive materials. The expansion of the smart material generates a force that leads to the shape change. When the expandable material is appropriately arranged with the passive material, complex shape-shifting behavior can be achieved. The magnitude and direction of the shape change depends on the spatial arrangements of the two materials (Tibbits et al. 2014). The mechanism is illustrated in Figure 1-13 and the entire cycle is unconstrained. Tibbits (2014), Tibbits et al. (2014), Raviv et al. (2014), and Jamal et al. (2013) used this type of mechanism in their experiments.

It should be noted that this mechanism is naturally reversible, i.e., the original shape can be recovered by drying the smart structure. However, the shape-shifting behavior can also be forced to be irreversible by using a special arrangement of passive and active materials. For example, Tibbits et al. (2014) reported that the structure in Figure A-31 will not unfold after being dried because of geometrical constraints.

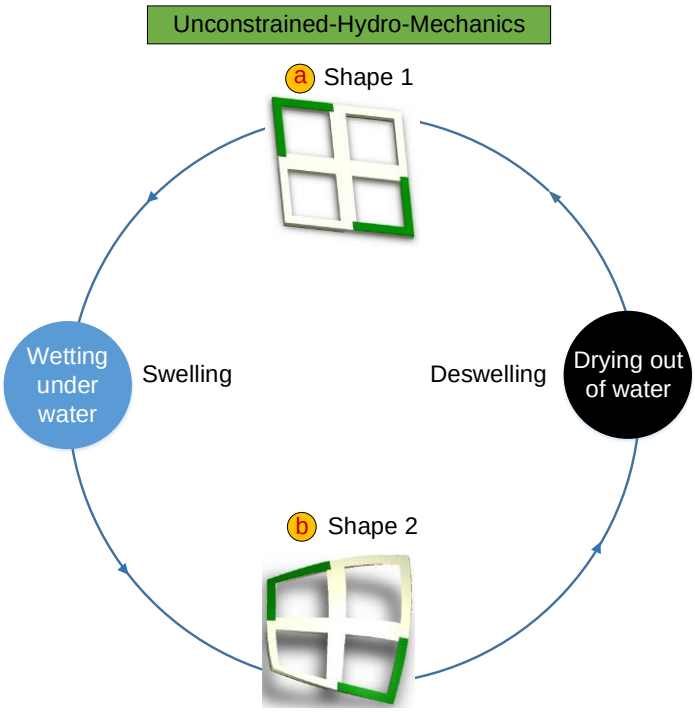

Figure 1-13. Schematic illustration of the unconstrained-hydro-mechanics mechanism in 4D printing. The green parts represent expandable materials.

- Constrained-Thermo-Mechanics

Two levels of temperature and one external load are required in this mechanism, as illustrated in Figure 1-14. One temperature is higher than the critical temperature of the smart material, such as its glass transition temperature or crystal-melt transition temperature ($T_H > T_C$). The other temperature should be lower than the critical temperature ($T_L < T_C$). In this mechanism, the printed structure is heated to T_H and the cycle starts at T_H in the following order. First, the original structure is stretched at T_H with a certain amount of strain depending on specific applications. Then, under external stress, the structure is cooled to T_L while the strain remains unchanged. Next, the external stress is removed at T_L, and the desired temporary shape is obtained at the end of this step. Finally, the structure can be reheated to T_H in a free stress condition to recover its original shape.

In this mechanism, temperature is the external stimulus. Ge et al. applied this mechanism in their experiments (Figures A-30 and A-24) (Ge et al., 2013; 2014). Wu et al. (2016) also employed this mechanism (Figures A-13, A-14, A-15, A-16, and A-17). They used water with different temperatures as a medium in order to transfer the heat to the printed structure. It should be noticed that the temperature is still the only stimulus in this cycle to trigger the shape-shifting behavior. Mao et al. (2015) applied this mechanism in their sequential self-folding multi-shape memory structure (Figure A-25). Yu et al. (2015) showed the feasibility of controlling the multi-shape-shifting sequence in a shape memory polymer based on this mechanism. Monzón et al. (2016) experimentally studied the correlations between the amount of recovery force and the mass/thickness/width of the printed shape memory polymers. These correlations can be effectively applied in the 4D printing process and should be the focus of future studies on interaction mechanisms.

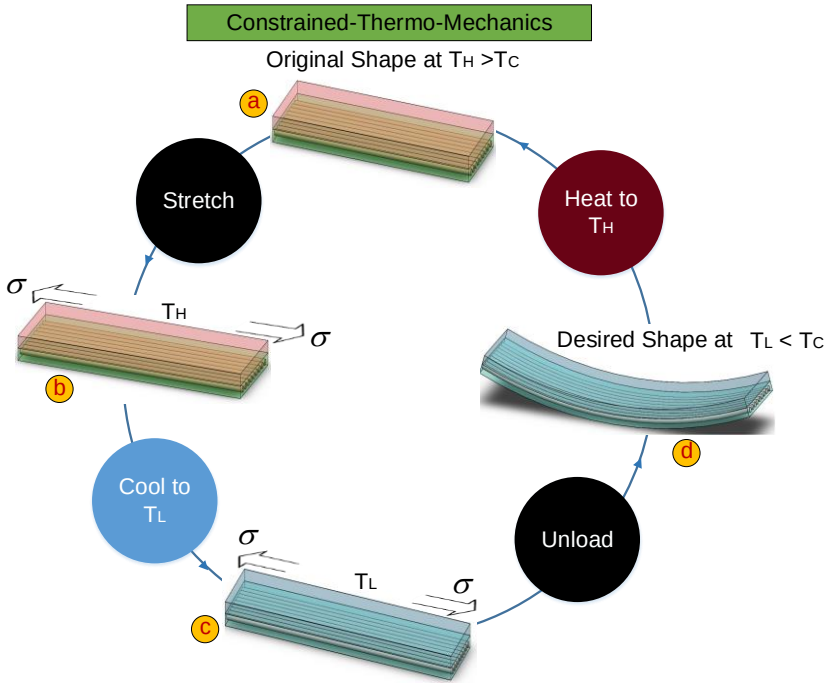

Figure 1-14. Constrained-thermo-mechanics mechanism in 4D printing.

- Unconstrained-Thermo-Mechanics

Unlike the previous mechanism, the external load is not included in the cycle of this mechanism. Only the two temperatures are required. One is higher than critical temperature of the active material involved in the structure ($T_H > T_C$), and the other one is lower than the critical temperature ($T_L < T_C$). As shown in Figure 1-15, the printed structure is first heated to T_H. The cycle then starts at T_H and proceeds in the following manner. First, the original structure is cooled to T_L, where the desired shape is achieved at the end of this step. Then, the structure can be heated to T_H to recover its original shape. In this mechanism, the external stimulus is temperature. Zhang et al. (2016) used this mechanism in their 4D printing studies (Figure A-26). They demonstrated several kinds of shape-shifting behaviors in smart, lightweight, and thin composite structures, such as transformation from a planar sheet to flower-like 3D structures, periodic 3D structures, and adaptive metamaterials.

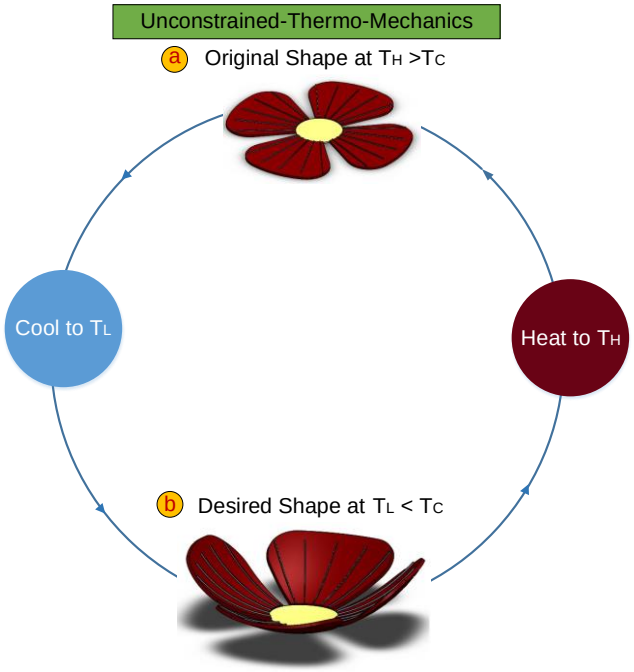

Figure 1-15. Unconstrained-thermo-mechanics mechanism in 4D printing.

- Unconstrained-Hydro-Thermo-Mechanics

This mechanism was shown by Bakarich et al. (2015), wherein the 4D printed structure undergoes two steps in the shape-shifting cycle. It first swells freely in cold water, and then deswells freely in hot water, as shown in Figure 1-16. This cycle can be repeated continuously. The swelling and deswelling processes are free and there are no constraints from external load. In this mechanism, both water and temperature are required as stimuli. Gladman et al. (2016) also employed this mechanism for reversible shape-shifting behavior (Figure A-33).

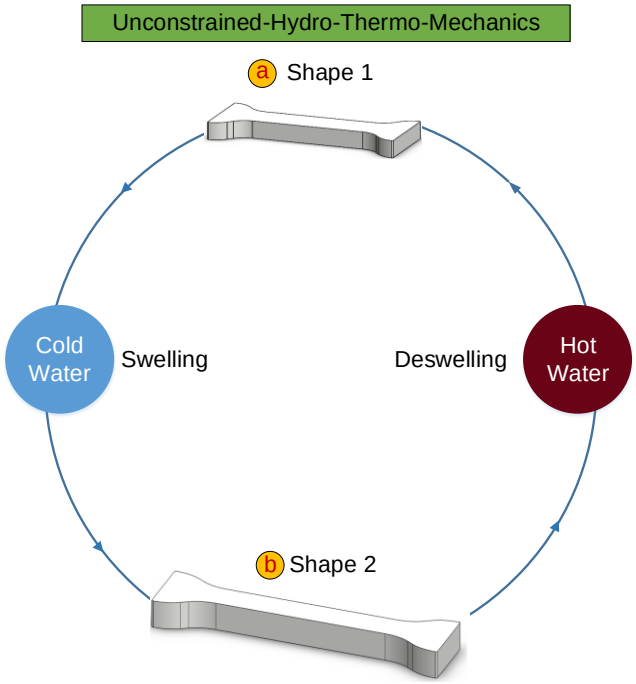

Figure 1-16. Unconstrained-hydro-thermo-mechanics mechanism in 4D printing.

- Unconstrained-pH-Mechanics

This mechanism was demonstrated by Nadgorny et al. (2016). In this mechanism, a 4D-printed, pH-responsive hydrogel can linearly swell at a specific pH level and then shrink at another designed pH level (Figure 1-17). This cycle is mainly conducted in an aqueous environment and is therefore suitable for the shape-shifting of hydrogels. Many studies on pH-responsive hydrogels have been conducted in available literature (Puranik et al., 2016; Frohm et al., 2015; Krogsgaard et al., 2013; Best et al., 2013; Gong et al., 2016). Nadgorny et al. (2016) provided pH-responsive hydrogels with a composition appropriate for printing.

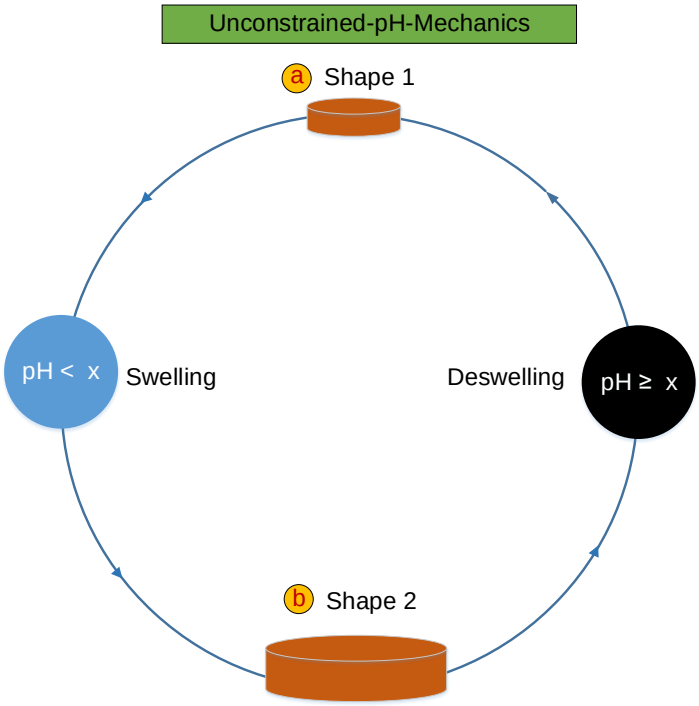

Figure 1-17. Unconstrained-pH-mechanics mechanism in 4D printing.

- Unconstrained-Thermo-Photo-Mechanics

This mechanism has been demonstrated by Kuksenok et al. (2016). In this mechanism, fibers were considered to be photo-responsive materials and the matrix was considered to be a thermo-responsive material. They showed that the application of light, heat, or a combination of both stimuli could yield printed structures with various morphologies. In their study, the gel has a lower critical solution temperature and shrinks at a high temperature. The spiro benzopyran (SP) chromophores functionalize elastic fibers, which can be converted into a hydrophobic form when subjected to blue light, and recover its hydrophilic form in dark environments.

Different behavior under exposure to light or heat is a result of local and global response. Light can be used to non-invasively enable local shape-shifting behavior in specific regions of the structures (Kuksenok et al. 2016). The original composite (Figure 1-18 (a)) shrinks like an accordion (Figure 1-18(b)) when heated freely (unconstrained) and bends like a caterpillar (Figure 1-18 (c)) when subjected to blue light. Figure 1-18(d) shows the behavior of the composite when both heat and blue light are applied.

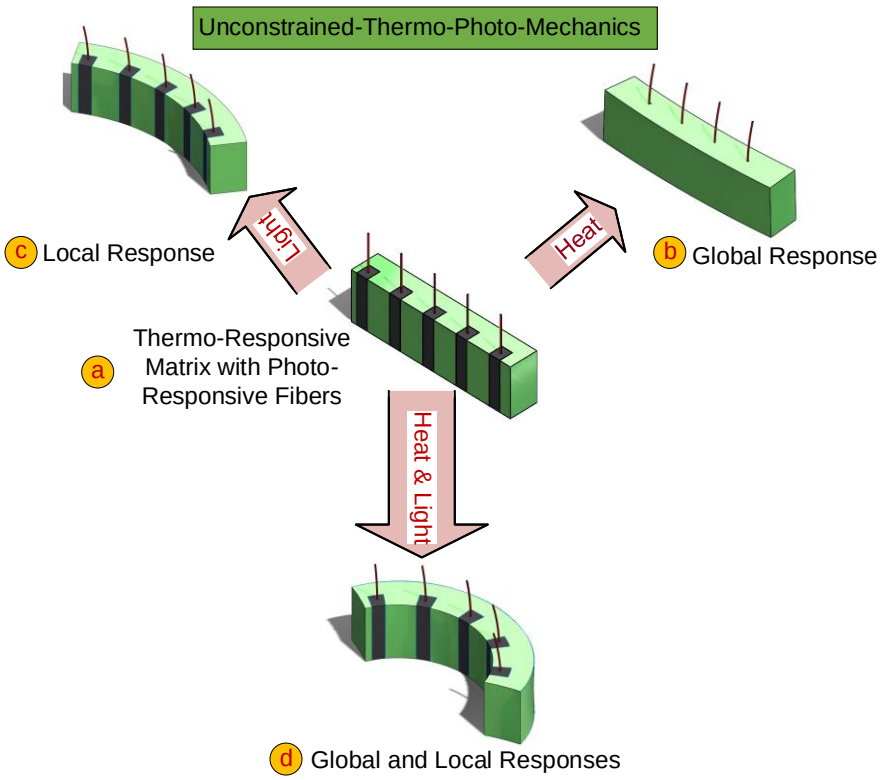

Figure 1-18. Illustration of the unconstrained-thermo-photo-mechanics mechanism.

- Osmosis-Mechanics

Villar et al. (2013) demonstrated this mechanism with a lipid interface bilayer, which joins two picoliter aqueous droplets with two different osmolarities. Water is the stimulus in this mechanism. The droplet with the higher osmolarity swells and the droplet with the lower osmolarity shrinks until they reach the same osmolarity (Figure 1-19(a)), which enables self-bending and is similar to the nastic movements of plants. At the macroscopic level, water flows through a network of droplets and causes the network to bend in a predetermined way, as shown in Figure 1-19(b). The final configuration of the network is determined based on the original geometry, the spatial arrangement of the droplets, and the ratio between their osmolarities.

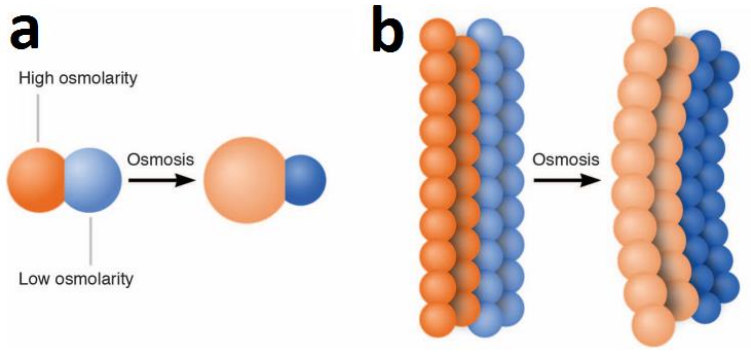

Figure 1-19 (a) Osmosis effect between two droplets, (b) Macroscopic deformation arising from osmosis effect (Villar et al. 2013).

- Dissolution-Mechanics

This mechanism was demonstrated by Kokkinis et al. (2015) in the field of bioprinting. In this mechanism, a printed structure is immersed in an appropriate solvent (ethyl acetate), based on the studied polymer structures. A change in shape occurs as a result of the loss of some non-crosslinked polymers when the structure is immersed in the solvent. After complete drying, the soft phase shrinks. This shape-shifting behavior is reversible by re-immersing the structure in the solvent. In this mechanism, the appropriate solvent is the stimulus.

As a summary of this section, all the shape-shifting mechanisms and stimuli are categorized in Figure 1-20, along with their related studies.

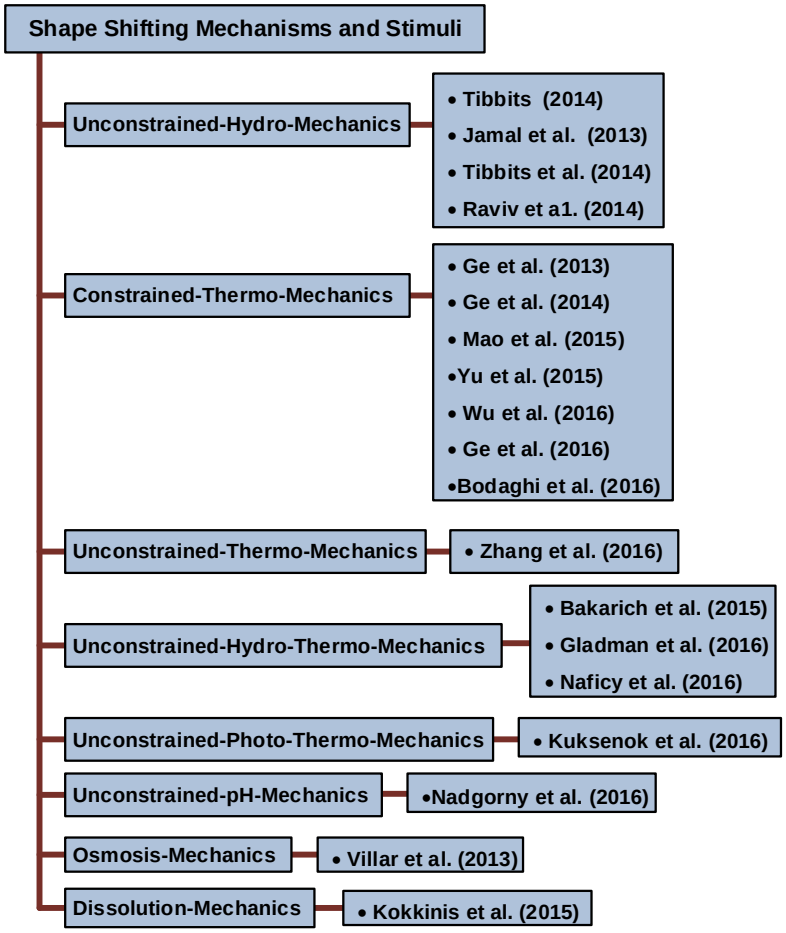

Figure 1-20. Shape-shifting mechanisms and stimuli which were used in 4D printing.

1.5 Mathematics

In this section, forward and inverse problems are defined for the 4D printing process, and one example is provided for each category. In addition, some studies focused specifically on the mathematics of 4D printing are discussed.

The development of the 4D printing process relies on appropriate mathematical modeling (Gladman et al., 2016). In fact, mathematics is necessary in 4D printing for the following reasons:

- It is needed to predict the shape evolution over time after printing.
- It provides the theoretical models needed to avoid collisions between components of the structure during the self-assembly operation.
- It reduces the number of trial-and-error experiments. Early experiments in 4D printing involve many repetitions for a specific structure to achieve the desired shape. For example, Tibbits et al. (2014) printed and repeated a series of experiments to identify the appropriate

material structure needed to reach the desired shape. This is shown in Figure 1-21. With mathematics and some theoretical models, the final shape can be predicted for a given material structure, material properties, and stimulus properties. Consequently, the number of test experiments can be reduced dramatically.

Several modeling experiments were conducted for 4D printing. The aforementioned experimental study by Tibbits et al. (2014) was quantified with mathematical models developed by Raviv et al. (2014), where the spring-mass concept was adopted, as shown in Figure 1-22. In addition, this spring-mass system for shape-memory materials was also used by Sun et al. (2012) and Yu et al. (2012). Sun et al. (2010) proposed a framework to illustrate the underlying physics in the thermo-responsive multi-shape memory effect (multi-SME). Their study qualitatively investigated the energy storage and release process achieved during the shape memory cycle. Yu et al. (2012) improved the previous qualitative study by proposing a quantitative analysis for multi-SME, as shown in Figure 1-23. They verified their model with the experimental results for perfluoro sulphonic acid ionomer (PFSA) from Xie (2010). Yu et al. (2012) employed the 1D standard linear solid (SLS) model proposed by Qi et al. (2010) to illustrate the multiple relaxation processes of the polymer chains in their multi-branch model. The SLS model has a parallel arrangement consisting of one elastic spring and one Maxwell element. The Maxwell element contains a serial arrangement of one spring and one dashpot. A previous study conducted on this subject yielded a four-element model developed by Tobushi et al. (1997), in which the creep phenomenon was incorporated through the fourth element, ε_s called the creep recovery strain (Figure 1-24).

Figure 1-21. Repeated tests to identify the appropriate material structure to reach the precise desired shape (Tibbits et al., 2014).

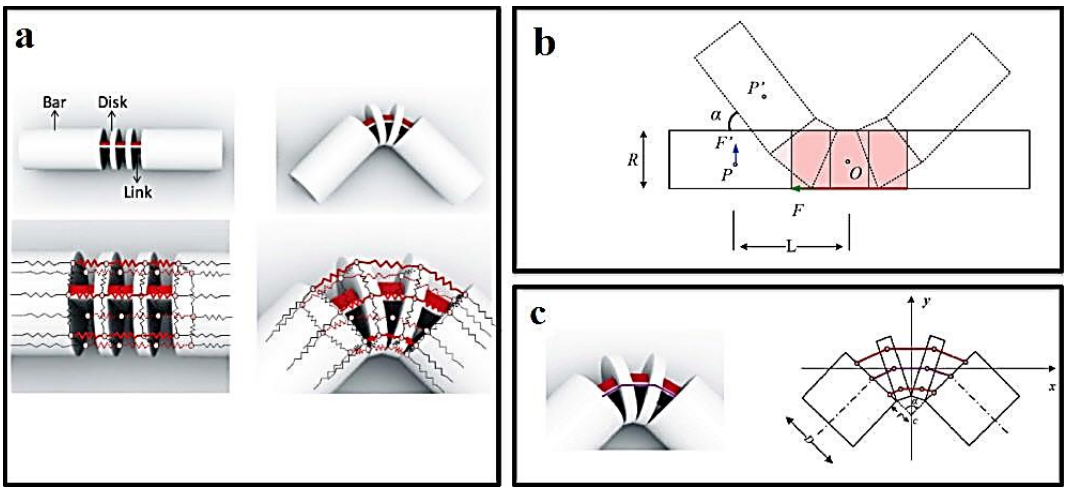

Figure 1-22. Mathematical modeling of the 4D-printed hinge that was introduced earlier by Tibbits et al. (2014) with the spring-mass concept (Raviv al. 2014).

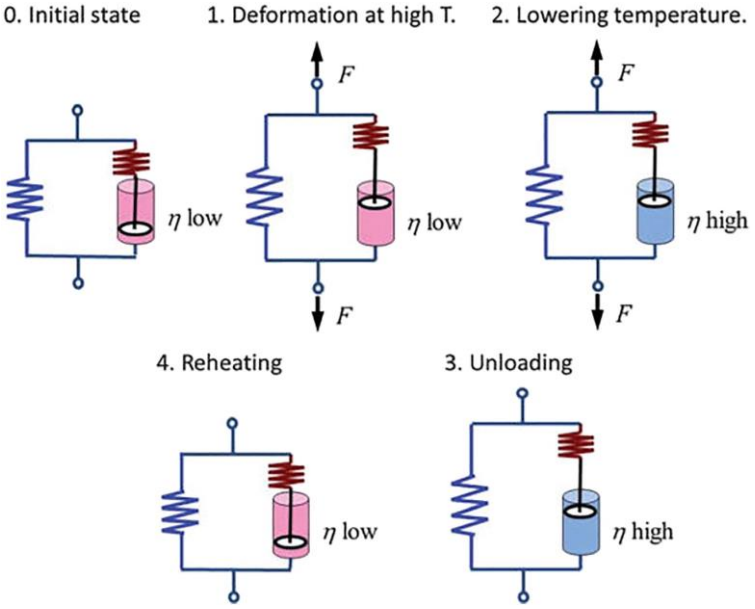

Figure 1-23. Standard linear solid (SLS) model to explain the mechanism of the shape memory effect in a shape memory polymer (Yu et al. 2012).

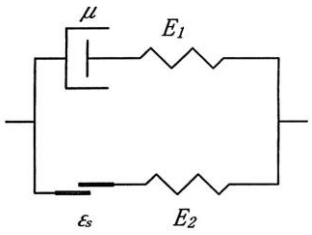

Figure 1-24. Four-element modeling of shape memory effect (Tobushi et al. 1997).

An appropriate theoretical model for 4D printing consists of four major components. The first is the final desired shape, which may include desired bending angle, twisting angle, length, etc. The next is material structure, such as the volume fractions of fibers and the matrix, filament size, orientation, spacing, anisotropy. Equivalently the material structure can be described by the size, shape and spatial arrangement of the voxels. From the perspective of the printing process, the material structure depends on print paths and nozzle sizes. Material properties makeup the third component, and they include shear modulus, Young`s modulus, and the interactive properties associated with the stimulus, such as glass transition temperature and swelling ratio. The final component is the stimulus properties, such as the temperature value and light intensity.

4D printing mathematics can be divided into two categories according to Gladman et al. (2016): the forward problem and the inverse problem. The categories are defined below:

Forward problem: Determination of the final desired shape given material structures, material properties, and stimulus properties.

Inverse problem: Determination of the material structure or the print paths and nozzle sizes given the final desired shape, material properties, and stimulus properties.

The studies on 4D printing related to the inverse problem are application-oriented, meaning that they are focused on achieving a desired functionality or shape. Studies related to the forward problem are mainly fundamental research aimed toward discovering concepts, theories, and relationships. These are illustrated in Figure 1-25.

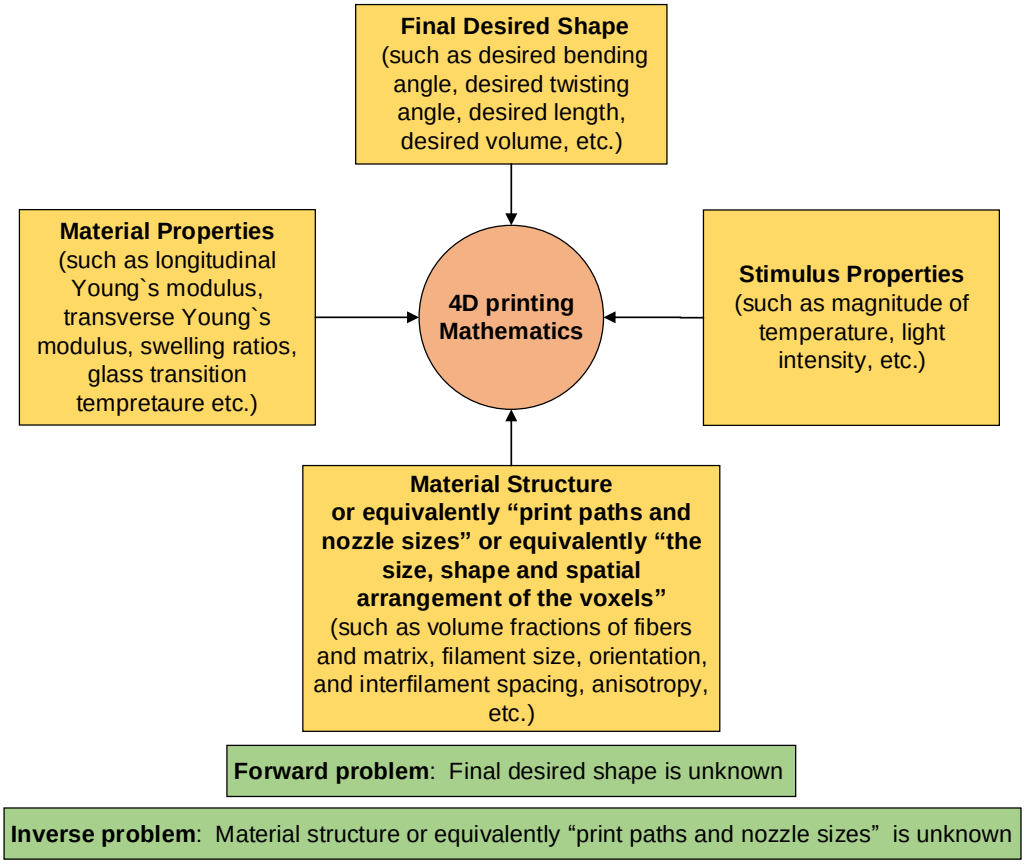

Figure 1-25. 4D printing mathematics allows theoretical models to connect the final desired shape, material structure (or equivalently the size, shape and spatial arrangement of the voxels or equivalently print paths and nozzle sizes), material properties, and stimulus properties.

The example with the spring-mass mathematical model shown above can be considered to be a forward problem. Gladman et al. (2016) studied a bilayer structure and utilized the mathematical relationships of coordinate system transformations to identify the print paths (Figure 1-29); this is an example of an inverse problem. As shown in Figure 1-26(a), the print path of the first layer aligns along the e_x direction (unit vector in x direction) and the print path of the second layer aligns along the direction of $\cos(\theta)\, e_x + \sin(\theta) e_y$, where θ is the angle between the two layers. The relationship between θ and the final desired shapes is then established, as given by the following equations:

$$H = c_1 \frac{\alpha_{\parallel} - \alpha_{\perp}}{h} \frac{sin^2(\theta)}{c_2 - c_3 \cos(2\theta) + m^4 \cos(4\theta)}$$

$$K = -c_4 \frac{(\alpha_{\parallel} - \alpha_{\perp})^2}{h^2} \frac{sin^2(\theta)}{c_5 - c_6 \cos(2\theta) + m^4 \cos(4\theta)}$$

where the final desired shapes are quantified by the curvature tensor $\boldsymbol{\kappa}$, mean curvature $H = \frac{1}{2}Tr(\boldsymbol{\kappa}) = \frac{1}{2}(\kappa_{xx} + \kappa_{yy})$ and Gaussian curvature $K = Det(\boldsymbol{\kappa}) = \kappa_{xx}\kappa_{yy} - {\kappa_{xy}}^2$, as shown in Figure 1-26(b). $\alpha_{\parallel}$ and $\alpha_{\perp}$ are the longitudinal and transverse swelling strains, respectively, as shown in Figure 1-26. $m = \frac{a_{bottom}}{a_{top}}$ is the ratio of layer thicknesses, $h = a_{top} + a_{bottom}$ is total thickness of the bilayer, and c_i are functions of longitudinal Young`s modulus, $E_{\parallel}$, transverse Young`s modulus, $E_{\perp}$, Poisson`s ratio, ν, and m. Based on final desired shape, the print paths can be calculated accordingly. As shown in Figure 1-27 and Figure 1-28, surfaces with positive Gaussian curvature can be produced with the concentric circles. Surfaces with negative Gaussian curvature or saddle-like surfaces can be produced with an orthogonal bilayer lattice structure. The combination of these two print paths can then yield a structure with varying Gaussian curvatures.

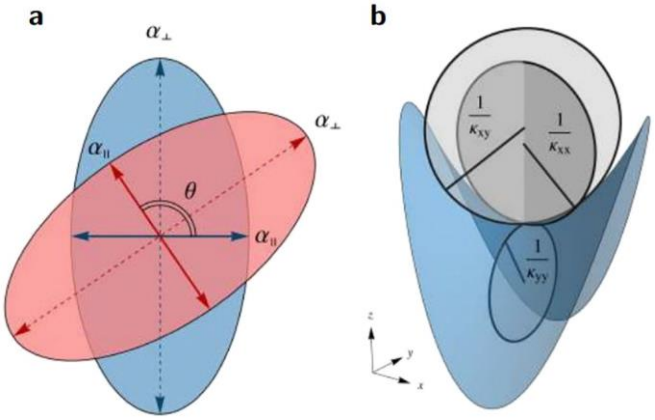

Figure 1-26. Mathematical modeling can make a connection between (a) print paths quantified by the angle θ between the two layers, and (b) final desired shape quantified by curvature tensor κ, mean curvature H, and Gaussian curvature K (Gladman et al., 2016).

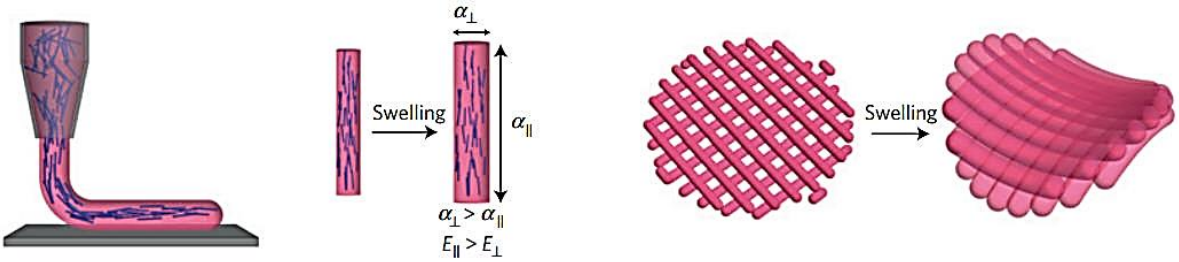

Figure 1-27. Longitudinal and transverse swelling strains ($\alpha_{\parallel}$ and $\alpha_{\perp}$) (Gladman et al., 2016).

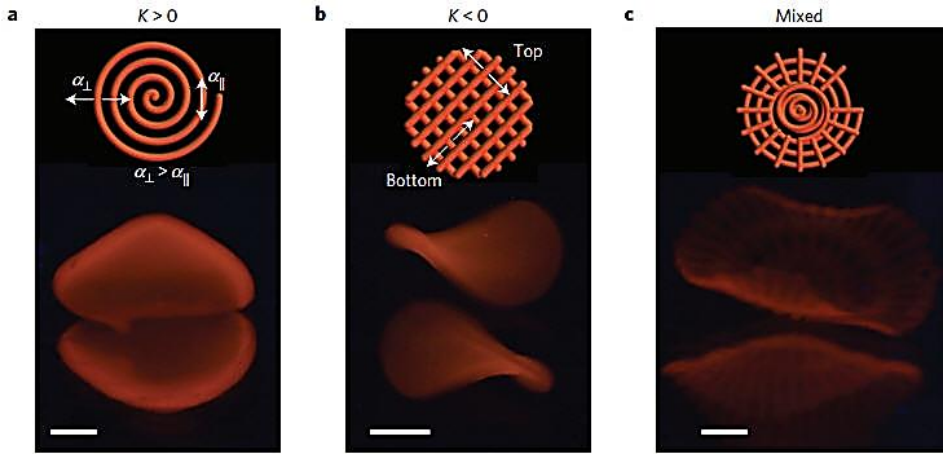

Figure 1-28. Print paths and final shapes (a) positive Gaussian curvature (b) negative Gaussian curvature (c) and varying Gaussian curvature (Gladman et al., 2016).

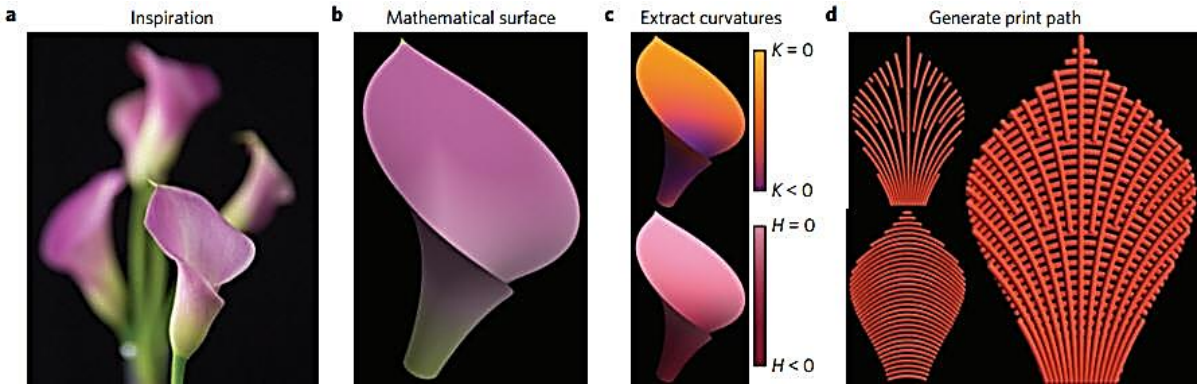

Figure 1-29. Using the concepts of the mean curvature, *H*, and Gaussian curvature, *K*, generates the print paths by knowing the final desired morphologies (Gladman et al., 2016).

Kowk et al. (2015) conducted design optimization of origami for freeform surfaces in 4D printing. According to them, the 3D structure needs to be flattenable to achieve self-folding shape-shifting. A flattenable 3D structure can be flattened into a 2D form without stretching. However, many designed parts are not flattenable. To address this issue, they provided a geometry optimization method, which can modify a non-flattenable pattern into a flattenable pattern. Wang et al. (2017) studied the mathematics of the single-loop foldable 8R (revolute joint) with multiple modes, which is also related to folding. They mathematically described that a self-folding structure can be folded into the same pattern through different methods and can also be folded to different patterns. These studies serve as the mathematical tools for the forward and inverse problems in 4D printing processes.

1.6 Conclusions

4D printing is the art of combining science with engineering technology. The scientific aspect of 4D printing is related to fundamental research into developing new smart materials, stimuli, and mathematical modeling. From the engineering aspect, the 4D printing process enables innovative and fascinating applications that can hardly be achieved with conventional manufacturing processes. The foundation of the 4D printing process includes the 3D printing process, stimulus, smart or stimulus-responsive materials, interaction mechanisms, and mathematical modeling. These features enable changes in shape/property/functionality after printing, as a function of time.

In addition, 4D printing has three main capabilities: self-assembly, self-adaptability, and self-repair. More studies need to be performed in the area of self-repair compared with the other two. Mathematical modeling is necessary in the 4D printing process primarily for three reasons: the prediction of the shape-shifting as a function of time; the prevention of collisions between components of the structure during self-assembly operations, and finally, the reduction of the number of trial-and-error experiments. The mathematical models used in the 4D printing process can be developed based on a desired shape, printing path, material properties, and stimulus properties. 4D printing can be utilized in various scales in interesting applications. To gain the potential applications of the 4D printing, a large amount of multidisciplinary research needs to be conducted in the future.

1.7 Problem statement and dissertation structure

After a comprehensive review of the 4D printing and related areas, three substantial gaps are identified in this emerging field. First, the main difference between 3D and 4D printed structures is one extra dimension that is smart evolution over “time”. However, currently, there is no general formula to model and predict this extra dimension. This gap is related to the design aspect of 4D printing. Second, 3D printing (additive manufacturing) is a manufacturing process with its known unique attributes. Now, 4D printing needs to be clearly underpinned as a new manufacturing process. Unique attributes of 4D printing as a new manufacturing process should also be identified. This gap is related to the manufacturing aspect of 4D printing. Third, various shape-morphing 4D printed structures have been illustrated in the literature. However, real applications and products, in which 4D printing can provide unique features still need to be demonstrated. 4D printing is not

just a concept, it is also a manufacturing paradigm that finally should lead to useful and applicable products or structures. Thus, real applications that can benefit from 4D printed structures should be addressed, continuously. This gap is related to the product development aspect of 4D printing.

To address the first gap (design), we have the second chapter, where we present general design principles of 4D printing that are required for understanding, modeling, and predicting the shape-shifting behaviors (the 4th D) of any multi-material 4D printed structure. To address the second gap (manufacturing), we have the third chapter, where we clearly underpin 4D printing as a new manufacturing process and specifically work on its energy-saving characteristic and obtain its theoretical limit. To address the third gap (product development), we have the fourth and fifth chapters, where we demonstrate two real applications (one in solar energy and one in wind energy), in which 4D printed products can provide unique benefits. These three main gaps and their corresponding chapters are related to design, manufacturing, and product development aspects of 4D printing.

CHAPTER 2

LAWS OF SHAPE-SHIFTING IN 4D PRINTING

The main difference between 3D and 4D printed structures is one extra dimension that is smart evolution over "time". However, currently, there is no general formula to model and predict this extra dimension. Here, by starting from fundamental concepts, we derive and validate a general bi-exponential formula that can model and predict the fourth D of 4D printed multi-material structures. 4D printing is a new manufacturing paradigm that utilizes stimuli-responsive materials in multi-material structures for advanced manufacturing (and construction) of novel products (and structures). It conserves the general attributes of 3D printing (such as the elimination of molds, dies, and machining) and further enables the fourth dimension of products and structures to provide intelligent behavior over time.

This intelligent behavior is encoded (usually by an inverse mathematical problem) into stimuli-responsive multi-materials during printing and is enabled by stimuli after printing. Here, we delve into the fourth dimension and reveal three general laws that govern the time-dependent shape-shifting behaviors of almost "all" (photochemical-, photothermal-, solvent-, pH-, moisture-, electrochemical-, electrothermal-, ultrasound-, enzyme-, etc.-responsive) multi-material 4D structures. We demonstrate that two different types of time-constants govern the shape-shifting behavior of almost all the multi-material 4D printed structures over time. Our results starting from the most fundamental concepts and ending with governing equations can serve as general design principles for future research in the 4D printing field, where the "time-dependent" behaviors should be understood, modeled, and predicted correctly. Future software and hardware developments in 4D printing can also benefit from these results.[2]

[2] This chapter is based on our journal article (under review), entitled "Laws of 4D printing", by Farhang Momeni and Jun Ni.

2.1 Introduction

Although some studies demonstrated single-material 4D printed structures, the future of 4D printing will lie in multi-material structures (Tibbits, 2014; Raviv et al., 2014; Ge et al., 2016; Pei & Loh, 2018; Kwok & Chen, 2017; Lind et al., 2017; News Staff, accessed 2018; Major, accessed 2018; Saunders, accessed 2018). The quiddity of 4D printing usually needs multi-material structures (Raviv et al., 2014). In the most fundamental case, the multi-material 4D printed structure has one active and one passive layer (Kwok & Chen, 2017). Performance improvement by allocating proper materials to related locations based on local necessities (Bandyopadhyay & Heer, 2018), multi-functionality by embeddable functions such as electronics (MacDonald & Wicker, 2016), combing rigid and flexible sections in an integrated structure (Lopes et al., 2018), and providing lightweight structures (Demir & Previtali, 2017) are only some of the advantages of multi-material structures.

In addition, to enable the shape memory effect (SME) (that is *not* an intrinsic property (Behl & Lendlein, 2007) of shape memory polymers (SMPs), a mechanical force is required in addition to heat (thermomechanical cycles). This force is usually provided externally. However, 4D printing can help us to arrange active and passive materials in a multi-material structure and utilize their internal mismatch-driven forces to enable the SME autonomously, with no need of external load for training (Mao et al., 2016; Momeni et al., 2019). In this study, we focus on multi-material 4D printed structures.

Aspects of 4D printing have been explored in the literature. Several studies worked on beam and plate theories (e.g., refer to the supplementary information of ref. (Gladman et al., 2016). However, the missing piece in the literature is modeling of "time-dependent" behaviors (the 4th D) of 4D structures. Especially, the time-dependent behavior is the critical part of 4D (stimuli-responsive) materials, whether fabricated by additive manufacturing and thus called 4D *printed* structures or created by other manufacturing processes. More importantly, a huge number of studies on 4D materials used the Timoshenko bimetal model (Timoshenko, 1925) (that is linear with time) to analyze the time-*dependent* behaviors of their experiments. Here, we will see that, in general, the Timoshenko bimetal model cannot capture the true time-*dependent* behaviors of 4D materials (except for some special cases or selected linear regions), although it provides useful insights on time-*independent* behaviors. In fact, the purpose of Timoshenko bimetal model was

not to model the time-*dependent* behavior (the 4th D) of 4D materials. Thus, there is an urgent need for qualitative and quantitative analysis on the 4th D of 4D materials.

The main part of 4D printed structures is the 4th D; however, currently, there is no general formula to model and predict this extra dimension. Here, by developing fundamental concepts and from the equilibrium and compatibility conditions, we derive a bi-exponential formula that "is needed" for modeling and predicting the 4th D of any multi-material 4D printed structure. We further validate our bi-exponential formula by various experimental data from separate studies in the literature and show that it is a general formula that is useful for any type of 4D multi-material structure (photochemical-, photothermal-, solvent-, pH-, moisture-, electrochemical-, electrothermal-, ultrasound-, enzyme-, etc.-responsive). This generality happens, because we build the bases of our bi-exponential formula, comprehensively.

2.2 Definitions, derivations, and discussions

There are many materials and stimuli. Consequently, most of the ongoing studies in the 4D printing field are case-specific. The time-dependent behavior (the 4th D) of any 4D printed structure needs to be predicted. A detailed, but systematic, study on 4D printing and related areas helped us to reveal three universal laws that govern the "shape-shifting" behaviors of almost all the multi-material 4D printed structures, although there are many materials and stimuli (Figure 2-1).

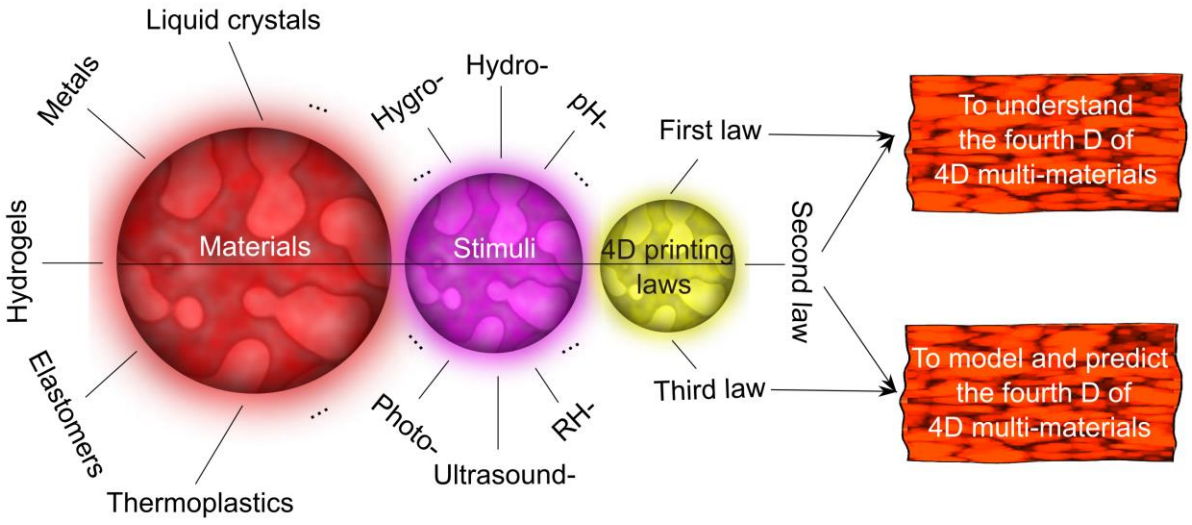

Figure 2-1. Toward the laws of shape-shifting in 4D printing.

2.2.1 First law

Almost all the shape-shifting behaviors (photochemical-, photothermal-, solvent-, pH-, moisture-, electrochemical-, electrothermal-, ultrasound-, enzyme-, hydro-, thermo-, etc.-responsive) of the multi-material 4D printed structures originate from one fundamental phenomenon that is "relative expansion" between active and passive materials.

This "relative expansion" is the origin of almost all the complicated 4D printing shape-shifting behaviors such as twisting, coiling, curling, etc., that are enabled by encoding various types of anisotropy between active and passive materials and fabricating different heterogeneous structures.

2.2.2 Second law

The shape-shifting behaviors of almost all the multi-material 4D printed structures have four different types of physics: mass diffusion, thermal expansion/contraction, molecular transformation, and organic growth. They all (discussed and quantified below) lead to the relative expansion between active and passive materials and consequent shape-shifting behaviors under stimuli (the stimulus is usually provided externally, but it can be internal).

2.2.2.1 Quantifying the second law

Here, we describe and quantify the four underlying physical concepts that lead to relative expansions between active and passive materials in multi-material 4D structures, resulting in various shape-shifting behaviors, with or without shape memory effect.

2.2.2.1.1 Mass Diffusion

In this category, a matter transport leads to the relative expansion.

Mass change due to sorption (absorption or adsorption) of a guest matter (here is mainly a stimulus such as water, ion, etc.) in a host matter can be modeled as below (Kim et al., 2003; Berens & Hopfenberg, 1978; Czugala et al., 2014):

$$\frac{\Delta M}{M}(t) = C\left[1 - \exp\left(-\frac{t}{\tau}\right)\right], \tag{2-1}$$

where t is time and M is mass. C and τ are usually obtained by curve fitting to experimental data and depend on host matter relaxation and guest matter diffusion. However, models can be developed for these two parameters. The exponential model above captures the correct behavior of mass diffusion for short- to long-time processes. There is also one other model called power

function (kt^n), which is not accurate for long-time processes of mass diffusion (Kim et al., 2003). However, we know that the main part of 4D printing is the intelligent behavior over "time" that can be short or long.

The exponential model above has been mainly introduced for $\frac{\Delta M}{M}$ and $\frac{\Delta V}{V}$ (volumetric strain). However, we have

$$\frac{\Delta V}{V} = \frac{V_2 - V_1}{V} = \frac{(L_x + \Delta L_x)\big(L_y + \Delta L_y\big)(L_z + \Delta L_z) - L_x L_y L_z}{L_x L_y L_z} \cong \varepsilon_x + \varepsilon_y + \varepsilon_z, \tag{2-2}$$

where V is volume, L is length, ε is strain, and the second- and third-order differential quantities are neglected.

For an isotropic material,

$$\varepsilon_x = \varepsilon_y = \varepsilon_z = \varepsilon \Rightarrow \varepsilon = \frac{1}{3}\frac{\Delta V}{V}. \tag{2-3}$$

In addition, mass and volume have a linear relationship. Therefore,

$$\varepsilon_{\text{Mass Diffusion}}(t) = C_1\left[1 - \exp\left(-\frac{t}{\tau_1}\right)\right], \tag{2-4}$$

where C_1 and τ_1 are constants that depend on the previous parameters.

We quantify all the four categories in terms of strain. One reason is that for example, if we want to quantify them in terms of mass, then we do not have any mass change in the next category (Thermal Expansion/Contraction). Similarly, we do not have temperature change in this category, while we have it in the next category.

In this category, several stimuli can be used such as hydro-, solvent-, moisture-, pH-, enzyme-, photochemical-, and electrochemical-responsive mechanisms. All of these stimuli finally cause a matter transport, leading to relative expansion in multi-material 4D structures, resulting in various shape-shifting behaviors.

2.2.2.1.2 Thermal Expansion/Contraction

In this category, a temperature change will increase (or decrease) the average distance between atoms and molecules (with constant mass), leading to the relative expansion in multi-materials.

Strain due to temperature change is (Pytel & Kiusalaas, 2012):

$$\varepsilon_{\text{thermal}} = \alpha\Delta T, \tag{2-5}$$

where α is thermal expansion coefficient and T is temperature. Because we need to predict the behavior of 4D printed structures over *time*, we convert this temperature-based equation to time-based form.

On the other hand, by applying a thermal stimulus with temperature T_2 to a structure with temperature T_1, and assuming a uniform temperature in the structure, the temperature of the structure changes over time as below (Kaviany, 2011):

$$T_1(t) = T_2 + [T_1(t=0) - T_2]\exp\left(-\frac{t}{\tau}\right) + R(\dot{S}_1 - Q_1)\left[1 - \exp\left(-\frac{t}{\tau}\right)\right], \quad (2\text{-}6)$$

where t is time, $T_1(t=0)$ is the initial temperature of the structure, $\dot{S}_1$ is energy conversion in the structure, Q_1 is the heat transferred between the structure and environment (other than the stimulus), and R is thermal resistance. τ is a time-constant that depends on density, heat capacity, volume of the structure, and thermal (and thermal contact) resistance, and can be modeled in a specific application (Kaviany, 2011).

By working on the above equation, we have

$$T_1(t) - T_1(t=0) = [T_2 - T_1(t=0)] - [T_2 - T_1(t=0)]\exp\left(-\frac{t}{\tau}\right) + R(\dot{S}_1 - Q_1)\left[1 - \exp\left(-\frac{t}{\tau}\right)\right],$$

$$\Rightarrow T_1(t) - T_1(t=0) = [T_2 - T_1(t=0)]\left[1 - \exp\left(-\frac{t}{\tau}\right)\right] + R(\dot{S}_1 - Q_1)\left[1 - \exp\left(-\frac{t}{\tau}\right)\right],$$

$$\Rightarrow T_1(t) - T_1(t=0) = \left[T_2 - T_1(t=0) + R(\dot{S}_1 - Q_1)\right]\left[1 - \exp\left(-\frac{t}{\tau}\right)\right],$$

$$\Rightarrow \Delta T_1 = \left[T_2 - T_1(t=0) + R(\dot{S}_1 - Q_1)\right]\left[1 - \exp\left(-\frac{t}{\tau}\right)\right]. \quad (2\text{-}7)$$

By combining the above equation and the initial equation (i.e., $\varepsilon = \alpha\Delta T$), we will have

$$\varepsilon_{\text{Thermal Expansion/Contraction}}(t) = C_2\left[1 - \exp\left(-\frac{t}{\tau_2}\right)\right], \quad (2\text{-}8)$$

where C_2 and τ_2 are constants that depend on the previous parameters.

In this category, several stimuli can be used such as photothermal-, electrothermal-, and ultrasound- responsive mechanisms. All of these stimuli finally raise the temperature of the structure and consequently, increase the average distances between atoms and molecules. For example, in electrothermal-responsive structures, the movement of a current through a resistance provides heat (so-called Joule or Ohmic heating), this heat increases the temperature, and finally, the expansion happens. Similarly, contraction is obtained by cooling. It should be noted that some

materials will shrink (contract) upon heating. In these cases, α (the thermal expansion coefficient) would be negative in the equations above and the final equation, i.e., $\varepsilon_{\text{Thermal Expansion/Contraction}}(t) = C_2\left[1 - \exp\left(-\frac{t}{\tau_2}\right)\right]$ will remain intact. Nevertheless, the key point is the "relative" thermal expansion/shrinkage in multi-materials to enable various shape-shifting behaviors in this category.

2.2.2.1.3 Molecular Transformation

In this category, a molecular transformation (e.g., trans-to-cis change in azobenzene) with constant mass and temperature leads to the relative expansion. The constant-temperature feature of this category indicates that the relative expansion is not due to the thermal expansion/contraction, even though some thermal fluctuation may happen in the structure due to bond cleavage or formation.

The molecular transformation is usually accomplished by photochemical responsivity mechanism that is different from photothermal responsivity (Naumov et al., 2015). The kinetics of photoinduced transformation is (Naumov et al., 2015):

$$D(t) = D_0\left[1 - \exp\left(-\frac{t}{\tau}\right)\right], \tag{2-9}$$

where t is time and $D(t)$ is the degree of transformation. D_0 and τ are constants that depend on the irradiation flux intensity, quantum yield of the transformation, etc., and can be modeled in a specific application (Naumov et al., 2015).

On the other hand, subsequent volume change (expansion or contraction) is proportional to the degree of transformation (Naumov et al., 2015). In addition, we have already seen that the volumetric strain ($\frac{\Delta V}{V}$) and linear strain ($\varepsilon = \frac{\Delta L}{L}$) are proportional. Therefore,

$$\varepsilon_{\text{Molecular Transformation}}(t) = C_3\left[1 - \exp\left(-\frac{t}{\tau_3}\right)\right], \tag{2-10}$$

where C_3 and τ_3 are constants that depend on the previous parameters.

The main stimulus for this category is the photochemical-responsive mechanism.

2.2.2.1.4 Organic Growth

In this category, there is a living layer (organism) and its growth over time can lead to the relative expansion between active and passive materials. The organic growth can be defined as the increase of an organic system in weight or length (Von Bertalanffy, 1938). This usually happens

in bioscience and bioengineering dealing with cells, soft tissues, organs, scaffolds, and so on that can be 4D printed and are generally called 4D bioprinting.

Kinetics of the organic growth is (Von Bertalanffy, 1938):

$$L(t) = L_\infty - (L_\infty - L_0)\exp\left(-\frac{t}{\tau}\right), \tag{2-11}$$

where t is time, $L(t)$ is the length of the organic system, L_∞ is the final length, and L_0 is the initial length. τ is usually a curve-fitting time-constant that depends on the metabolism of the living organism, environment, and so on. Nevertheless, models can be developed for it. It should also be noted that τ affects L_∞ (Von Bertalanffy, 1938). This formula shows the growth of *individual* organisms in a population that is different from *population* growth. The population growth is the growth in the number of individuals in a population and is modeled by other formulas (Malthus, 1798; Verhulst, 1838).

On the other hand, based on the definition of strain, $\varepsilon = \frac{L(t)-L_0}{L_0}$, we have

$$\begin{aligned}\varepsilon = \frac{L(t)-L_0}{L_0} &= \frac{(L_\infty - L_0) - (L_\infty - L_0)\exp\left(-\frac{t}{\tau}\right)}{L_0} \\ &= \left(\frac{L_\infty - L_0}{L_0}\right)\left[1 - \exp\left(-\frac{t}{\tau}\right)\right].\end{aligned} \tag{2-12}$$

Therefore,

$$\varepsilon_{\text{Organic Growth}}(t) = C_4\left[1 - \exp\left(-\frac{t}{\tau_4}\right)\right], \tag{2-13}$$

where C_4 and τ_4 are constants that depend on the previous parameters.

In this category, one of the main stimuli that can trigger a living organism would be the electrical signal (electrochemical mechanism). In addition, various stimuli such as pH, light, heat, and enzyme can be used to tune the growth rate.

2.2.2.2 Unified model of the second law

By quantifying the second law, we found that

$$\begin{cases} \varepsilon_{\text{Mass Diffusion}}(t) = C_1\left(1 - e^{-\frac{t}{\tau_1}}\right) \\ \varepsilon_{\text{Thermal Expansion/Contraction}}(t) = C_2\left(1 - e^{-\frac{t}{\tau_2}}\right) \\ \varepsilon_{\text{Molecular Transformation}}(t) = C_3\left(1 - e^{-\frac{t}{\tau_3}}\right) \\ \varepsilon_{\text{Organic Growth}}(t) = C_4\left(1 - e^{-\frac{t}{\tau_4}}\right) \end{cases}, \tag{2-14}$$

where C_i and τ_i $(i = 1,2,3,4)$ all are constants. However, they depend on different factors as described.

2.2.3 Third law

Time-dependent shape-shifting behavior of almost all the multi-material 4D printed structures is governed by two "different types" of time-constants. For the most fundamental case of a multi-material 4D printed structure having one active and one passive layer (Figure 2-2), the time-dependent behavior (in terms of "curvature" that is a building block concept for shape-shifting) is

$$\begin{aligned} \kappa(t) = \frac{1}{\rho}(t) &= \frac{H_I\left(1 - e^{\frac{-t}{\tau_I}}\right) + H_{II}\left(1 - e^{\frac{-t}{\tau_{II}}}\right)}{\frac{h}{2} + \frac{2(E_1 I_1 + E_2 I_2)}{h}\left(\frac{1}{E_1 a_1} + \frac{1}{E_2 a_2}\right)} \\ &= K_I\left(1 - e^{\frac{-t}{\tau_I}}\right) + K_{II}\left(1 - e^{\frac{-t}{\tau_{II}}}\right), \end{aligned} \tag{2-15}$$

where t is time, $\kappa(t)$ is the curvature induced by the relative expansion, ρ is the radius of curvature, h and a_i are thicknesses identified in Figure 2-2, E_i is Young`s modulus, and $I_i$ is the second moment of area. The passive and active layers are denoted by numbers 1 and 2, respectively. $H_I$ is a constant that depends on Young`s moduli of the active and passive layers and the amount of the mismatch-driven stress generated at the interface. τ_I is a time-constant that depends on the viscosity induced at the interface and Young`s moduli of the active and passive layers. The viscosity induced at the interface needs to be measured or modeled for a specific active-passive composite. The exact format of H_I and τ_I can be developed in a specific application depending on the active-passive composite and by using parallel and series rules of springs (elasticity elements)

and dashpots (viscosity elements). H_{II} and τ_{II} are respectively equivalent to C_i and τ_i $(i = 1,2,3,4)$ of the unified model in the previous section.

2.2.3.1 Proof of the third law

To derive equation (2-15), we start from the equilibrium and compatibility conditions that are the starting point for any problem in mechanics of materials (Pytel & Kiusalaas, 2012). We also consider the Timoshenko bimetal model (Timoshenko, 1925) (and its basic assumptions).

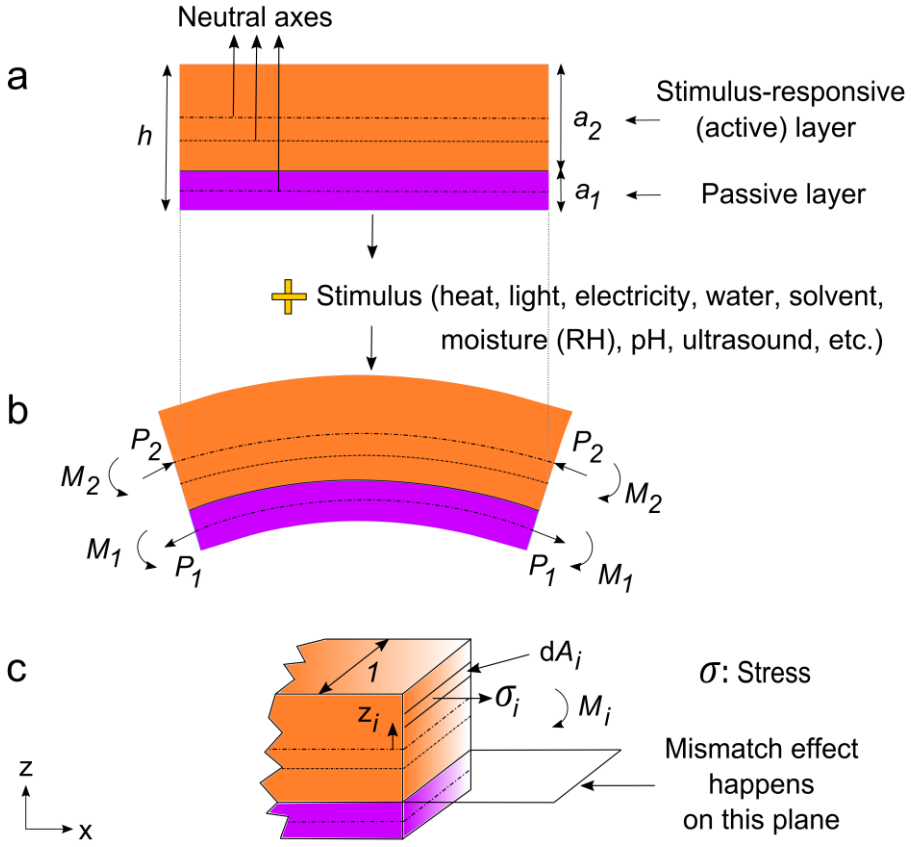

Figure 2-2. Toward the third law by analyzing the most fundamental multi-material 4D structure.

Equilibrium:

First, we must have balances of forces and moments in Figure 2-2. Therefore (Timoshenko, 1925),

$$Balance\ of\ forces: \sum \boldsymbol{F} = 0 \Rightarrow P_1 = P_2 = P \tag{2-16}$$

$$Balance\ of\ moments: \sum \boldsymbol{M} = 0 \Rightarrow \frac{P_1 a_1}{2} + \frac{P_2 a_2}{2} = M_1 + M_2 \xrightarrow[a_1+a_2=h]{P_1=P_2=P} \frac{Ph}{2} = M_1 + M_2, \tag{2-17}$$

where P_i and M_i are forces and moments, respectively (shown in Figure 2-2).

Compatibility:

Second, *at the interface* of the two layers, the lengths of the two layers are the same after applying the stimulus. Because their initial lengths are also the same, their strains must be equal and thus (Timoshenko, 1925; Pytel & Kiusalaas, 2012),

$$At\ the\ interface: \varepsilon_1 = \varepsilon_2.$$

The strain in each of the two layers has three main contributors as below (Timoshenko, 1925; Matsumoto, 2016).

$$\left(\varepsilon_{curvature} + \varepsilon_{stress} + \varepsilon_{expansion}\right)_1 = \left(\varepsilon_{curvature} + \varepsilon_{stress} + \varepsilon_{expansion}\right)_2. \tag{2-18}$$

Strain from curvature: $\varepsilon_{curvature}$

$$\begin{cases} (\varepsilon_{curvature})_1 = \frac{a_1}{2\rho} \\ (\varepsilon_{curvature})_2 = -\frac{a_2}{2\rho} \end{cases} \text{(Timoshenko, 1925).} \tag{2-19}$$

Strain from stress: ε_{stress}

$$\begin{cases} (\varepsilon_{stress})_1 = \frac{P_1}{E_1 a_1} \\ (\varepsilon_{stress})_2 = -\frac{P_2}{E_2 a_2} \end{cases} \text{(Timoshenko, 1925).} \tag{2-20}$$

$$\xrightarrow{\text{(2-18),(2-19),and (2-20)}} \frac{a_1}{2\rho} + \frac{P_1}{E_1 a_1} + \left(\varepsilon_{expansion}\right)_1 = -\frac{a_2}{2\rho} - \frac{P_2}{E_2 a_2} + \left(\varepsilon_{expansion}\right)_2. \tag{2-21}$$

Now, in the following, we develop ε_{stress} and $\varepsilon_{expansion}$ for 4D multi-materials and incorporate them in the equilibrium and compatibility equations.

Here, we note that ε_{stress} is the strain due to the *mismatch-driven stress* at the interface of the active and passive materials. The mismatch-driven stress naturally leads to opposing resistive forces in the two layers (in general). We include the resistive effect by expanding the well-known moment equation for each layer, M_i. By considering Figure 2-2(c),

$$M_i = \int \boldsymbol{r_i} \times d\boldsymbol{F_i} = \int \boldsymbol{z_i}\sigma_i dA_i = \left(\int \boldsymbol{z_i}\sigma_i dA_i\right)_{except\ interface} + \left(\int \boldsymbol{z_i}\sigma_i dA_i\right)_{interface}. \tag{2-22}$$

Because the integral is the same as the summation, i.e., it is continuous summation, we could separate the integral above into two terms as equation (2-22). The second term on the right-hand side of (2-22) shows the integral over an *infinitesimal* cross-sectional area, dA_i (Figure 2-2(c)) that is close to the interface. Therefore, equation (2-22) can be written as

$$\begin{cases} M_1 = \dfrac{E_1 I_1}{\rho} + m_1 \\ M_2 = \dfrac{E_2 I_2}{\rho} + m_2 \end{cases}. \tag{2-23}$$

The first terms on the right-hand side of (2-23) are similar to those proposed by Timoshenko (1925) and the second terms (m_1 and m_2) arise from the resistive (mismatch) effect at the interface of the active and passive materials. At this stage, the nature of m_1 and m_2 is moment. Let us keep them as black-box terms.

Strain from expansion that is enabled by stimulus: $\varepsilon_{expansion}$

By analyzing almost all types of shape-shifting mechanisms in multi-material 4D structures, the relative expansions induced under stimuli can be categorized into four main groups elaborated in the second law. We demonstrated that almost all types of strains due to expansions induced by stimuli have the same format as below:

$$\varepsilon_{expansion}(t) = C\left(1 - e^{\frac{-t}{\tau_{II}}}\right). \tag{2-24}$$

We use τ_{II} as the time-constant of $\varepsilon_{expansion}$ to distinguish it from τ_I that will be introduced for the strain due to the *mismatch-driven* stress (ε_{stress}).

By combining equations (2-16), (2-17), and (2-21),

$$\frac{h}{2\rho} + \frac{2(M_1 + M_2)}{h}\left(\frac{1}{E_1 a_1} + \frac{1}{E_2 a_2}\right) = \left(\varepsilon_{expansion}\right)_2 - \left(\varepsilon_{expansion}\right)_1 \overset{(2\text{-}23)}{\Longrightarrow}$$

$$\frac{h}{2\rho} + \frac{2(E_1 I_1 + E_2 I_2)}{h\rho}\left(\frac{1}{E_1 a_1} + \frac{1}{E_2 a_2}\right) + Nm_1 + Nm_2 = \underbrace{\left(\varepsilon_{expansion}\right)_2 - \left(\varepsilon_{expansion}\right)_1}_{\varepsilon_{relative\ expansion}},$$

where $N = \frac{2}{h}\left(\frac{1}{E_1 a_1} + \frac{1}{E_2 a_2}\right)$. Now, we assume that the active (stimuli-responsive) material is usually responsive under stimulus, and the passive material is not usually responsive under stimulus, as their names imply (nevertheless, the relative expansion is important for shape-shifting). Therefore, by applying equation (2-24) to the above equation,

$$\frac{h}{2\rho}+\frac{2(E_1I_1+E_2I_2)}{h\rho}\left(\frac{1}{E_1a_1}+\frac{1}{E_2a_2}\right)+Nm_1+Nm_2=C\left(1-e^{\frac{-t}{\tau_{II}}}\right).$$

Now, each term in the above equation is strain. Therefore, the nature of Nm_1 and Nm_2 is strain. On the other hand, these two terms reflect the mismatch (viscosity) effect of the interface into each layer. The viscoelastic *strain* over *time* can be modeled by an exponential term as below (Duffy, 2010).

$$\frac{h}{2\rho}+\frac{2(E_1I_1+E_2I_2)}{h\rho}\left(\frac{1}{E_1a_1}+\frac{1}{E_2a_2}\right)+A_1\left(1-e^{\frac{-t}{B_1}}\right)+A_2\left(1-e^{\frac{-t}{B_2}}\right)=C\left(1-e^{\frac{-t}{\tau_{II}}}\right),$$

where A_1 and A_2 are constants that depend on Young`s moduli of the active and passive layers and the amount of the mismatch-driven stress generated at the interface. This stress is affected by the stimulus power (such as light intensity, pH value, etc.). B_1 and B_2 are constants that depend on the viscosity induced at the interface (that is related to the active-passive composite) and Young`s moduli of the active and passive layers. It should be noted that the Young`s modulus and viscosity are affected by the fabrication process (Momeni et al., 2019) and its conditions (such as printing resolution).

On the other hand, because the two layers are attached at the interface during the shape-shifting, B_1 and B_2 (time-constants of strains in each layer due to the mismatch-driven stress at the interface) are equal ($B_1=B_2=\tau_I$). Thus,

$$\frac{h}{2\rho}+\frac{2(E_1I_1+E_2I_2)}{h\rho}\left(\frac{1}{E_1a_1}+\frac{1}{E_2a_2}\right)+A_1\left(1-e^{\frac{-t}{\tau_I}}\right)+A_2\left(1-e^{\frac{-t}{\tau_I}}\right)=C\left(1-e^{\frac{-t}{\tau_{II}}}\right).$$

By using new uniform notations H_I and H_{II},

$$\frac{h}{2\rho}+\frac{2(E_1I_1+E_2I_2)}{h\rho}\left(\frac{1}{E_1a_1}+\frac{1}{E_2a_2}\right)=H_I\left(1-e^{\frac{-t}{\tau_I}}\right)+H_{II}\left(1-e^{\frac{-t}{\tau_{II}}}\right).$$

Finally, by re-arranging,

$$\frac{1}{\rho}=\frac{H_I\left(1-e^{\frac{-t}{\tau_I}}\right)+H_{II}\left(1-e^{\frac{-t}{\tau_{II}}}\right)}{\frac{h}{2}+\frac{2(E_1I_1+E_2I_2)}{h}\left(\frac{1}{E_1a_1}+\frac{1}{E_2a_2}\right)}=K_I\left(1-e^{\frac{-t}{\tau_I}}\right)+K_{II}\left(1-e^{\frac{-t}{\tau_{II}}}\right),$$

which is the same as equation (2-15).

2.2.3.2 Stimulus-on versus stimulus-off

Equation (2-15) is used when the stimulus is "on", and a curvature happens in the structure. However, when the stimulus is "off", the structure can return to its original shape by starting from

the final curvature of the previous part (i.e., the stimulus-on region). Therefore, the governing equation for the second region can be found as below:

$$\left(\frac{1}{\rho}\right)_{\text{off}} = \left\{ \lim_{\substack{t\to\infty \\ (\text{or large } t)}} \left[K_I\left(1-e^{\frac{-t}{\tau_I}}\right)+K_{II}\left(1-e^{\frac{-t}{\tau_{II}}}\right)\right]\right\} - \left[K_I\left(1-e^{\frac{-t}{\tau_I}}\right)+K_{II}\left(1-e^{\frac{-t}{\tau_{II}}}\right)\right]$$

$$= (K_I + K_{II}) - \left[K_I\left(1-e^{\frac{-t}{\tau_I}}\right)+K_{II}\left(1-e^{\frac{-t}{\tau_{II}}}\right)\right]$$

$$= K_I e^{\frac{-t}{\tau_I}} + K_{II} e^{\frac{-t}{\tau_{II}}}. \quad (2\text{-}25)$$

It should be noted that in some applications, a self-locking mechanism could be devised by special arrangements of active and passive materials so that when the stimulus is off, the structure does not return to its original shape.

2.2.3.3 General graph

Based on equations (2-15) and (2-25), the general graph is rendered in Figure 2-3. Some applications need only one cycle, and some others require multiple cycles. In some applications, only one of the two regions of the graph happens and in some other applications, both the regions are present. In some cases, the shape-shifting behavior can occur with memory (SME), and in some other cases, it can take place without memory.

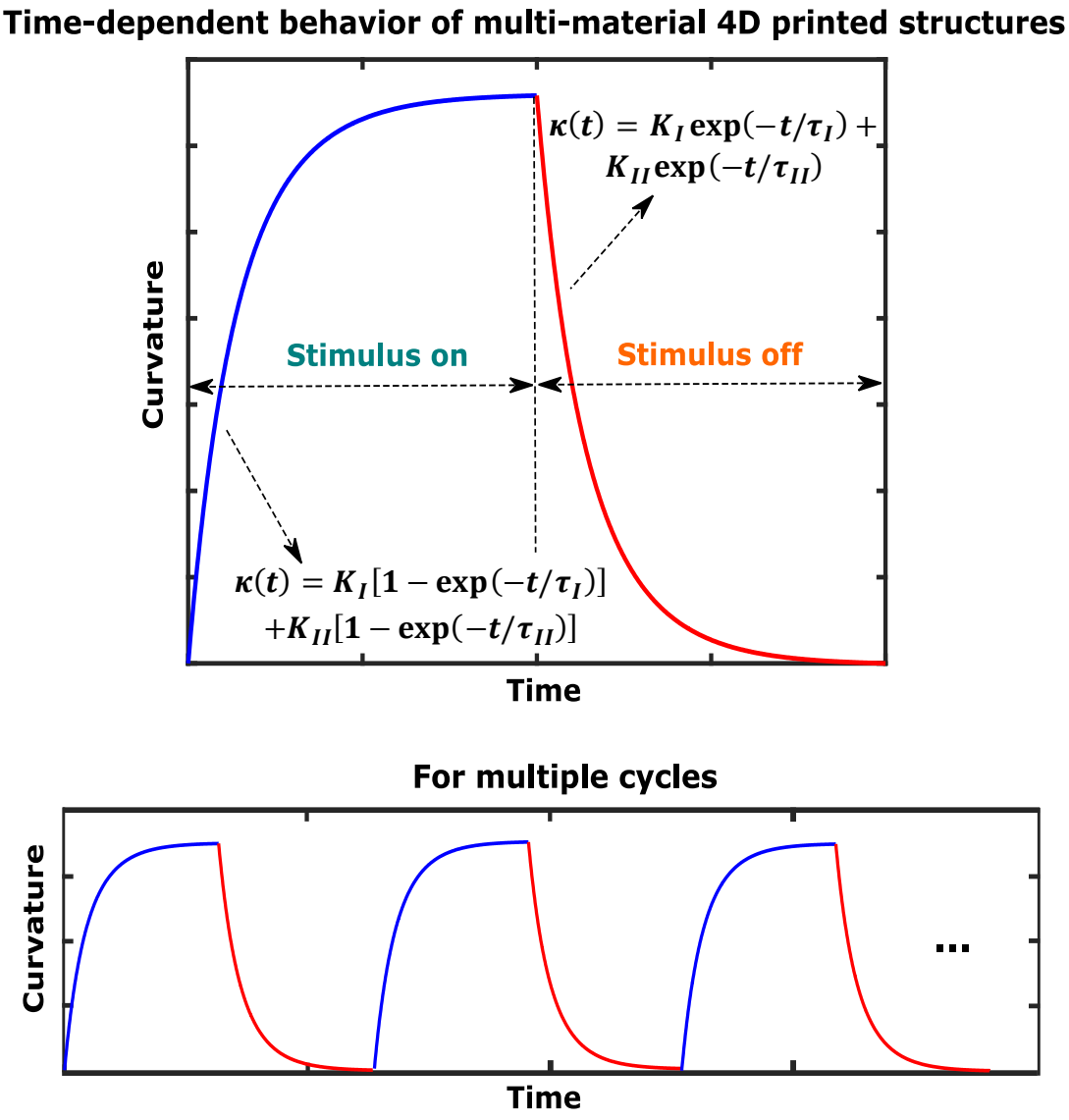

Figure 2-3. The general graph that exhibits the time-dependent behavior of almost all the multi-material 4D printed structures (photochemical-, photothermal-, solvent-, pH-, moisture-, electrochemical-, electrothermal-, ultrasound-, enzyme-, hydro-, etc.-responsive).

2.2.3.4 Analyzing the proposed formula by using real data

Here, we analyze our derived bi-exponential formula by using real data. For completeness, we also consider the Timoshenko bimetal (Timoshenko, 1925) and mono-exponential models. As seen in Figure 2-4, unlike the Timoshenko bimetal and mono-exponential models, the developed bi-exponential model perfectly captures the correct time-dependent behavior of various experimental data from separate studies in the literature. Therefore, in general, the time-dependent behavior of 4D multi-materials is nonlinear (with time) and has the specific format as equation

(2-15). Some of the following studies presented experimental data for time-dependent curvature, and some others provided experimental data for time-dependent angle of rotation (deflection angle). However, the curvature and deflection angle have a linear relationship. Consequently, if one of them has bi-exponential behavior, the other one will have bi-exponential behavior. All the six items in Figure 2-4 have one active material and one passive material. The active component has responsivity to the desired stimulus, whether with or without shape memory effect. We performed the curve fitting by Levenberg-Marquardt (Levenberg, 1944; Marquardt, 1963) method. We also tried other least-squares algorithms and obtained similar results. The axes units are eliminated, as the absolute values are not essential to convey the idea.

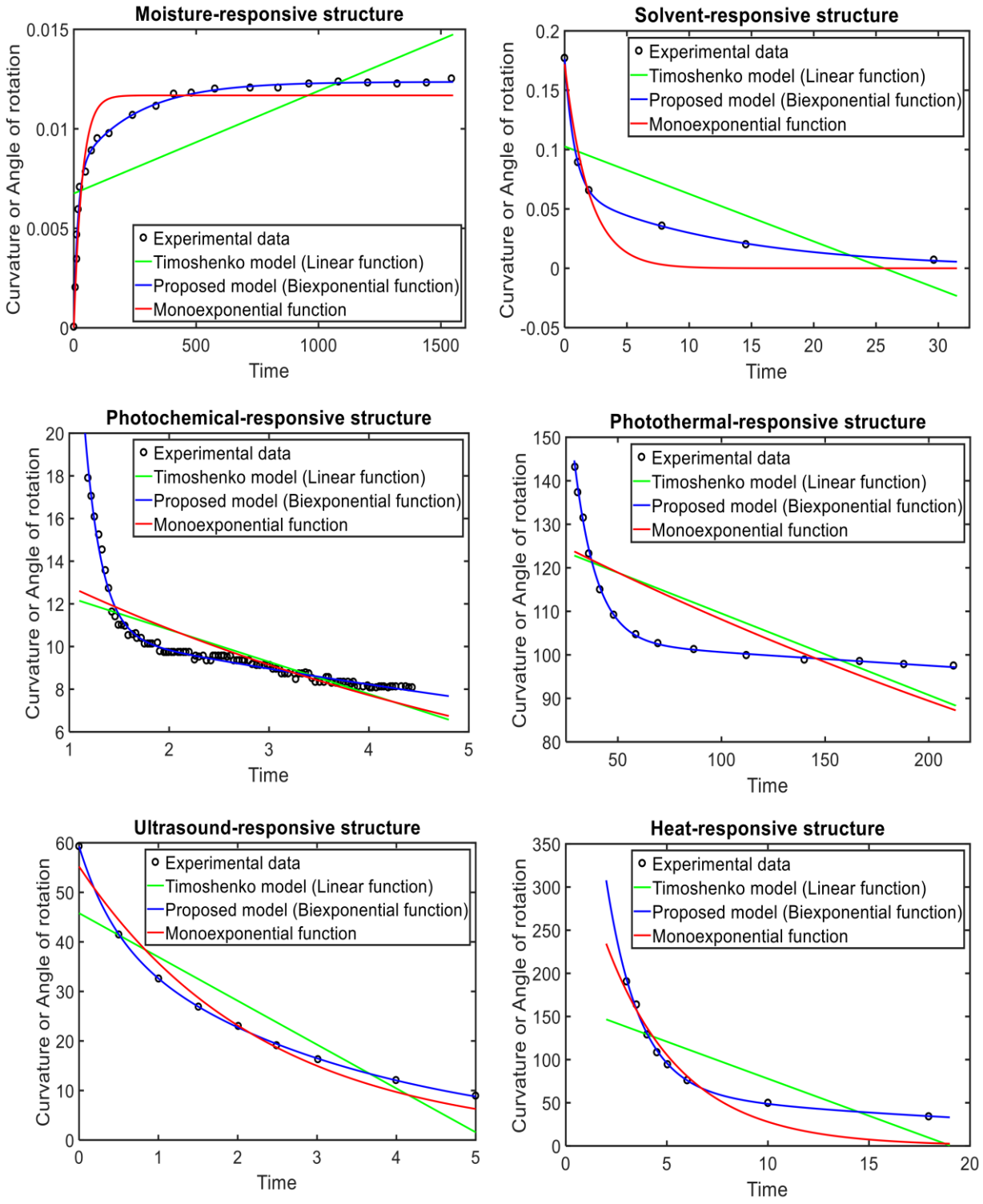

Figure 2-4. Analysis of the proposed model by experimental data from separate studies in the literature (Le Duigou et al., 2016; Alipour et al., 2016; Nath et al., 2014; Zhou et al., 2016; Li et al., 2015; Zhang et al., 2016), for both the on and off regions and various stimuli such as moisture (Le Duigou et al., 2016), solvent (Alipour et al., 2016), photochemical (Nath et al., 2014), photothermal (Zhou et al., 2016), ultrasound (Li et al., 2015), and heat (Zhang et al., 2016).

Remark 1. True time-dependent behavior of 4D printed multi-material structures. The results show that generally speaking, two different time-constants govern the time-dependent shape-shifting behaviors of multi-material 4D structures. Nevertheless, in some cases, the two time-constants (τ_I and τ_{II}) may be approximately equal, and the time-dependent behavior can be modeled by a mono-exponential equation. In some cases, the resistive (viscosity) effect at the interface of the active and passive materials (that is reflected in τ_I) is negligible, and the first exponential term vanishes. In addition, sometimes, the two time-constants are large, and the proposed bi-exponential formula tends to the linear (Timoshenko) model. That is, if τ_I and $\tau_{II} \rightarrow$ large values, then $K_I\left(1-e^{\frac{-t}{\tau_I}}\right)+K_{II}\left(1-e^{\frac{-t}{\tau_{II}}}\right) \cong bt$, where b is a constant. This point can be realized by analyzing the related graph or by using Taylor series. Thus, in linear cases, both the proposed bi-exponential model and Timoshenko bimetal model work.

It should be noted that in the heat- and ultrasound-responsive structures of Figure 2-4, the mono- and bi-exponential models are relatively close to each other.

Remark 2. Final shape versus instantaneous shape. We found that the Timoshenko bimetal model (Timoshenko, 1925), as well as the mono-exponential function, cannot capture the correct time-dependent (instantaneous) behavior. However, when the final shape is achieved ($t \rightarrow$ large values), both the Timoshenko bimetal model (Timoshenko, 1925) and our formula (equation (2-15)) would be

$$\kappa_{final} \propto \frac{1}{\frac{h}{2}+\frac{2(E_1 I_1+E_2 I_2)}{h}\left(\frac{1}{E_1 a_1}+\frac{1}{E_2 a_2}\right)}. \tag{2-26}$$

Two points should be discussed in this regard. First, the above outcome implies that both the Timoshenko bimetal model and our formula provide similar analyses for time-*independent* behaviors (such as the effect of thickness on curvature). Second, in the literature, some experimental studies reported the decrease of maximum (final) curvature with an increase of layer thickness, while some others reported the increase of maximum (final) curvature with an increase of layer thickness. It is worth digging into this point by an analytical study as the following.

Equation (2-26) depends on two quantities, Young`s moduli (E_i) and layers thicknesses (a_i), as h and I_i are functions of layers thicknesses ($h=a_1+a_2$, $I_i=\frac{1}{12}{a_i}^3$; based on the basic assumptions of the Timoshenko bimetal model, the width of the strip was assumed to be small and specifically was taken unity as seen in Figure 2-2). Therefore, we have

$$\kappa_{final} \propto \frac{1}{\frac{a_1+a_2}{2}+\frac{2}{a_1+a_2}\left(\frac{E_1}{12}{a_1}^3+\frac{E_2}{12}{a_2}^3\right)\left(\frac{1}{E_1 a_1}+\frac{1}{E_2 a_2}\right)}. \quad (2\text{-}27)$$

By analyzing equation (2-27), we can find that the curvature first increases and then decreases with increase in a_1. Because equation (2-27) is symmetric in terms of a_1 and a_2, the curvature has a similar trend with respect to a_2. The region, in which the increase or decrease of the curvature happens, depends on relative values of a_1 and a_2, as well as E_1 and E_2. Here, we generate some possible scenarios as shown in Figure 2-5. A similar result to scenario (c) in Figure 2-5 was proposed by Timoshenko (Timoshenko, 1925). Due to the symmetry of (2-27), the same results as Figure 2-5(a)-(b) are valid if we switch a_1 and a_2 in these two plots.

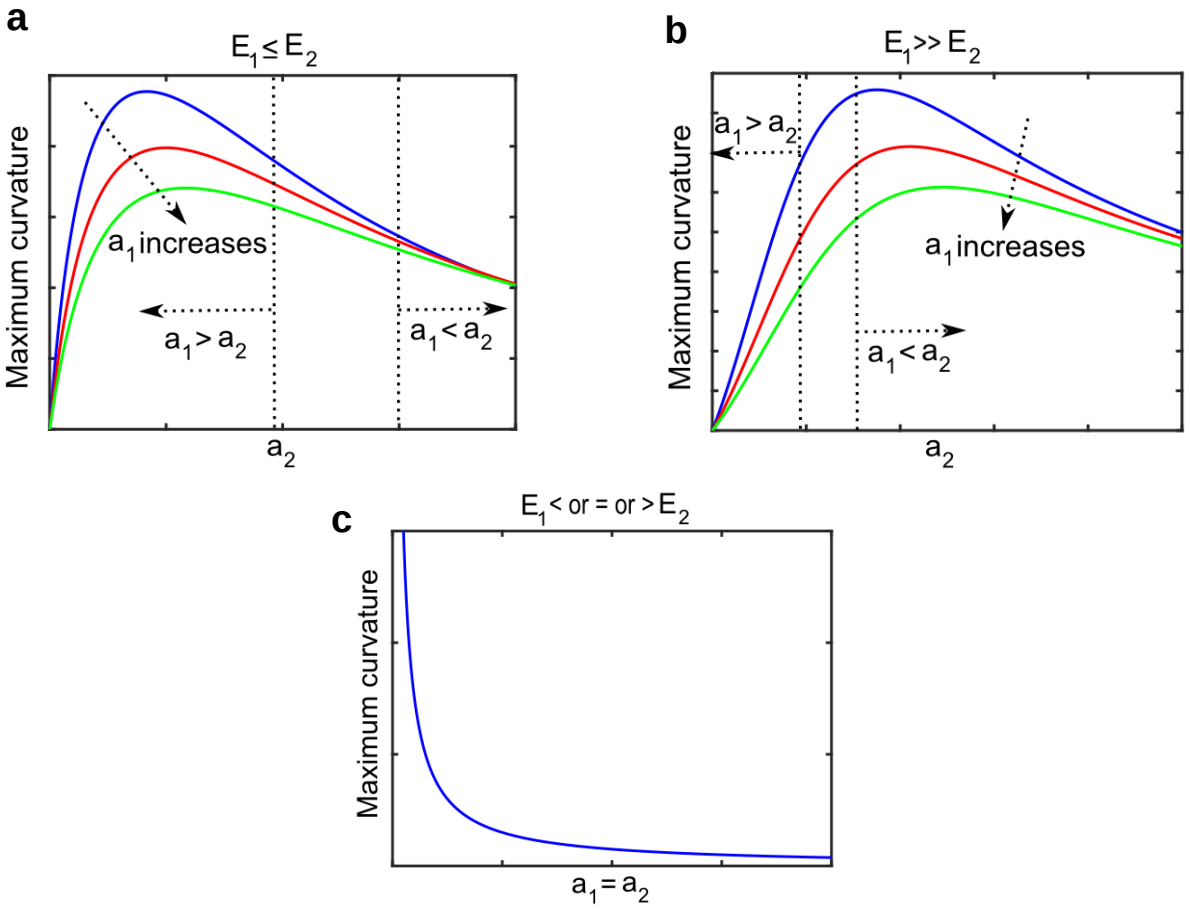

Figure 2-5. Depending on the relative values of a_1, a_2, E_1, and E_2, the relationship between curvature and layers thicknesses would be different (it can be decreasing, increasing, or a mixed behavior). This figure is based on equation (2-27).

Remark 3. Shape-shifting speed. The shape-shifting speed is important almost in any application performing dynamic intelligent behavior over time, and becomes more crucial in some

applications such as autonomous deployment in space missions, drug delivery systems, detection devices, and so on. By taking derivatives of equations (2-15) and (2-25), the magnitude of the shape-shifting speed for both the on and off regions would be

$$(shape\ shifting\ speed)_{on} = (shape\ shifting\ speed)_{off} =$$

$$\frac{d\kappa(t)}{dt} = \frac{\frac{H_I}{\tau_I}\left(e^{\frac{-t}{\tau_I}}\right) + \frac{H_{II}}{\tau_{II}}\left(e^{\frac{-t}{\tau_{II}}}\right)}{\frac{h}{2} + \frac{2(E_1I_1 + E_2I_2)}{h}\left(\frac{1}{E_1a_1} + \frac{1}{E_2a_2}\right)} = \frac{K_I}{\tau_I}\left(e^{\frac{-t}{\tau_I}}\right) + \frac{K_{II}}{\tau_{II}}\left(e^{\frac{-t}{\tau_{II}}}\right). \quad (2\text{-}28)$$

As seen in equation (2-28), the shape-shifting speed is time-dependent with the specific format above. However, the Timoshenko bimetal model (Timoshenko, 1925) gives a constant shape-shifting speed over time.

Based on equation (2-28), for a large amount of time (i.e., when the final shape is going to be achieved), the shape-shifting speed tends to zero for both the on and off regions. This point can also be captured from Figure 2-3 as both the on and off regions becomes flat (constant) for $t \rightarrow$ large values, and the derivative of a constant function is zero.

Remark 4. Stimulus power. Here, we analyze the effect of stimulus power on the time-dependent behavior. By the expression "stimulus power", we mean light intensity, temperature magnitude, pH value, moisture (RH) content, enzyme concentration, current magnitude, solvent concentration, and so on. By analyzing the various parameters of equation (2-15) (and considering the concepts associated with the second and third laws), we can find that the stimulus power will affect three parameters, H_I, H_{II}, and τ_{II}. Therefore, the time-dependent behaviors of two different stimulus powers would be

$$\begin{cases} \kappa^{(1)}(t) = \dfrac{H_I{}^{(1)}\left(1-e^{\frac{-t}{\tau_I}}\right)+H_{II}{}^{(1)}\left(1-e^{\frac{-t}{\tau_{II}{}^{(1)}}}\right)}{\frac{h}{2}+\frac{2(E_1I_1+E_2I_2)}{h}\left(\frac{1}{E_1a_1}+\frac{1}{E_2a_2}\right)} \\ \quad = K_I{}^{(1)}\left(1-e^{\frac{-t}{\tau_I}}\right)+K_{II}{}^{(1)}\left(1-e^{\frac{-t}{\tau_{II}{}^{(1)}}}\right) \\ \kappa^{(2)}(t) = \dfrac{H_I{}^{(2)}\left(1-e^{\frac{-t}{\tau_I}}\right)+H_{II}{}^{(2)}\left(1-e^{\frac{-t}{\tau_{II}{}^{(2)}}}\right)}{\frac{h}{2}+\frac{2(E_1I_1+E_2I_2)}{h}\left(\frac{1}{E_1a_1}+\frac{1}{E_2a_2}\right)} \\ \quad = K_I{}^{(2)}\left(1-e^{\frac{-t}{\tau_I}}\right)+K_{II}{}^{(2)}\left(1-e^{\frac{-t}{\tau_{II}{}^{(2)}}}\right) \end{cases}. \tag{2-29}$$

To illustrate the effect of stimulus power on time-dependent behaviors, we consider five different stimulus powers. The related formulas would be

$$\begin{cases} \kappa^{(1)}(t) = K_I{}^{(1)}\left(1-e^{\frac{-t}{\tau_I}}\right)+K_{II}{}^{(1)}\left(1-e^{\frac{-t}{\tau_{II}{}^{(1)}}}\right) \\ \kappa^{(2)}(t) = K_I{}^{(2)}\left(1-e^{\frac{-t}{\tau_I}}\right)+K_{II}{}^{(2)}\left(1-e^{\frac{-t}{\tau_{II}{}^{(2)}}}\right) \\ \kappa^{(3)}(t) = K_I{}^{(3)}\left(1-e^{\frac{-t}{\tau_I}}\right)+K_{II}{}^{(3)}\left(1-e^{\frac{-t}{\tau_{II}{}^{(3)}}}\right), \\ \kappa^{(4)}(t) = K_I{}^{(4)}\left(1-e^{\frac{-t}{\tau_I}}\right)+K_{II}{}^{(4)}\left(1-e^{\frac{-t}{\tau_{II}{}^{(4)}}}\right) \\ \kappa^{(5)}(t) = K_I{}^{(5)}\left(1-e^{\frac{-t}{\tau_I}}\right)+K_{II}{}^{(5)}\left(1-e^{\frac{-t}{\tau_{II}{}^{(5)}}}\right) \end{cases} \tag{2-30}$$

and the general graph would be similar to Figure 2-6(a). The general trend observed in Figure 2-6(a) is consistent with the experimental data found in the literature (Zhang et al., 2014; Hirano et al., 2017; Zhou et al., 2016; Nath et al., 2014).

There might be some applications, in which faster response without any change in the final shape (unlike Figure 2-6(a)) is desirable. To this end, smaller time-constant (τ) with the same coefficient (K) is required. For five different scenarios, the related formulas would be

$$\begin{cases} \kappa^{(1)}(t) = K_I\left(1 - e^{\frac{-t}{\tau_I}}\right) + K_{II}\left(1 - e^{\frac{-t}{\tau_{II}^{(1)}}}\right) \\ \kappa^{(2)}(t) = K_I\left(1 - e^{\frac{-t}{\tau_I}}\right) + K_{II}\left(1 - e^{\frac{-t}{\tau_{II}^{(2)}}}\right) \\ \kappa^{(3)}(t) = K_I\left(1 - e^{\frac{-t}{\tau_I}}\right) + K_{II}\left(1 - e^{\frac{-t}{\tau_{II}^{(3)}}}\right), \\ \kappa^{(4)}(t) = K_I\left(1 - e^{\frac{-t}{\tau_I}}\right) + K_{II}\left(1 - e^{\frac{-t}{\tau_{II}^{(4)}}}\right) \\ \kappa^{(5)}(t) = K_I\left(1 - e^{\frac{-t}{\tau_I}}\right) + K_{II}\left(1 - e^{\frac{-t}{\tau_{II}^{(5)}}}\right) \end{cases} \tag{2-31}$$

and the general graph would be similar to Figure 2-6(b). In order to tune the response speed without interfering with the final shape, separate studies are needed. Carbon nanotubes (CNTs) (De Volder et al., 2013) may be a possible solution, as they can be incorporated into stimuli-responsive materials to tune their response speed (He et al., 2016).

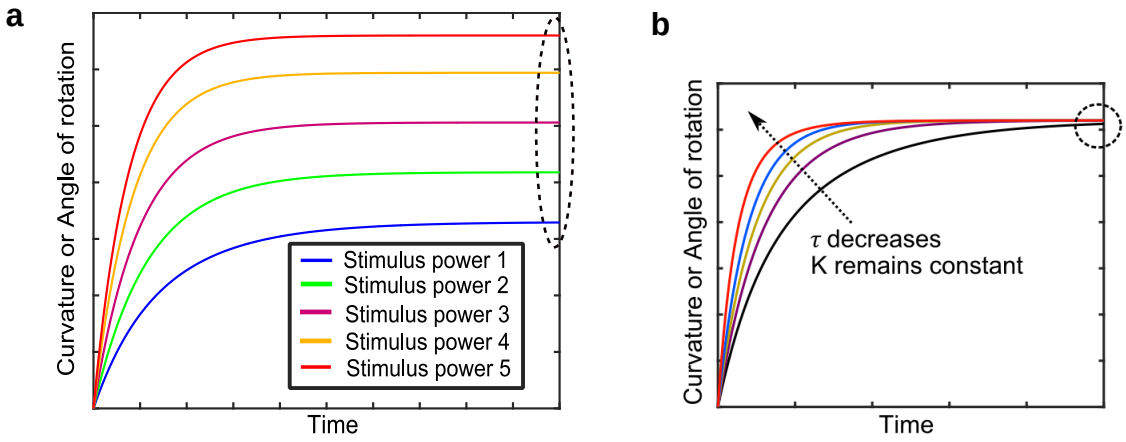

Figure 2-6. (a) The general effect of stimulus power (e.g., light intensity, pH value, temperature magnitude, and so on) on time-dependent behavior. This plot is based on equation (2-30). (b) Tuning the response speed, without changing the final shape. This plot is based on equation (2-31).

Remark 5. Extension of the developed concepts to complicated multi-material 4D structures. Based on the concepts developed here, one can analyze, predict, and tune the time-dependent behaviors of multi-material 4D structures almost at any level of complexity. Let us consider one example exhibited in Figure 2-7. This case has four different types of materials, two of which are active materials. For the top two layers, we have one exponential term of type I and one exponential term of type II. Similarly, we can consider the middle two layers, and the bottom

two layers. By superposing these terms, this multi-material structure has three exponential terms of type I and three exponential terms of type II (nevertheless, some of these exponential terms can be equal in a specific case, as discussed in Remark 1). In addition, this case will have the same general graph shown in Figure 2-3, as its governing equation is a summation of exponential terms. However, the slope of its graph would be different at various points (i.e., it will have steeper slopes in some regions).

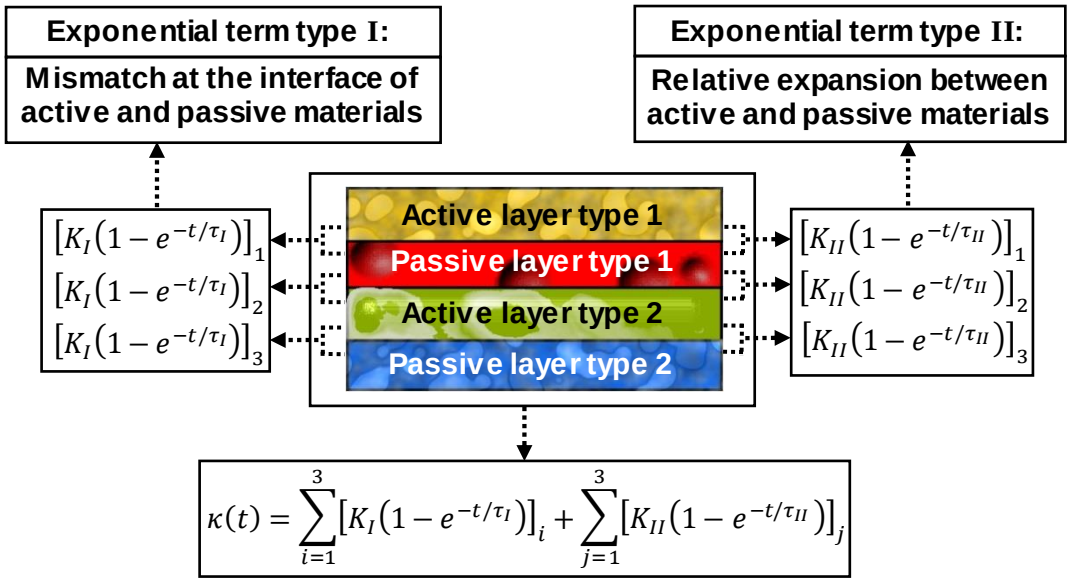

Figure 2-7. A 4D structure with more than two types of materials.

To realize the complicated 4D structures, in addition to the multi-material (rather than two-material) structures discussed above, two more important points should be taken into consideration. First, our model provides the time-dependent behavior of the "curvature" that is a fundamental building block of shape-shifting in multi-material structures. Other higher-level shape-shifting quantities such as curling, twisting, coiling, and their combinations originate from this quantity. Second, we have discussed the time-dependent behavior of the curvature in one direction (narrow strip). For a plate having the same materials as the original narrow strip, the curvature would be the same in any direction (this point can be concluded by analyzing the discussions made by Timoshenko, 1925), and can be modeled by the same two exponential terms of the original (parent) narrow strip. For a plate that has different materials in different directions, the curvature would be different in each direction. However, the same two types of time-constants and exponential terms proposed in this study can be used to model the time-dependent curvature in a specific direction,

accordingly. Future studies may incorporate the proposed two time-constants in extensions to plates and so on.

It should also be noted that the concepts have been developed for multi-*material* structures that may not necessarily be multi-*layer*. In some cases, the boundary between active and passive layers may not be as clear as Figure 2-2. However, in these cases, eventually, the active and passive materials will have contact in some regions, and the same concepts developed here will be present.

Remark 6. Shape memory effect (SME). As we touched on earlier, SME is *not* an intrinsic property (Behl & Lendlein, 2007). The readers are referred to ref. (Behl & Lendlein, 2007) for more information on the SME and shape memory polymers. The four shape-shifting mechanisms discussed and quantified in the second law can take place with or without SME. The key point is that these four shape-shifting mechanisms are the underlying physical concepts for relative expansion and subsequent shape-shifting in multi-material 4D structures. For example, the "heat-responsive structure" of Figure 2-4 illustrates a typical shape memory polymer in a bilayer with a passive material, and its shape-shifting in the multi-material structure is enabled by the relative "thermal expansion" of the active and passive materials as mentioned by Zhang et al. (2016).

Because of the aforementioned discussion, we did not put SME as one category of fundamental physical concepts in the second law. Nevertheless, the following discussion can be useful.

Most of the shape memory polymers are thermo-responsive, and to enable their shape memory effect, their temperature should go beyond a critical temperature, e.g., glass transition temperature (whether by direct heat or other stimuli such as light, electricity, and electromagnetic field to change the temperature, indirectly) (Behl & Lendlein, 2007). It is worth mentioning that the researchers (Bonner et al., 2010) reported that the "strain-time" relationship of a shape memory polymer above its glass transition temperature could be modeled by the exponential formula $\varepsilon(t) = C\left[1 - \exp\left(-\frac{t}{\tau}\right)\right]$.

Remark 7. Other manufacturing processes. We distilled three laws that govern the shape-shifting behaviors of almost all the 4D multi-materials, whether fabricated by additive manufacturing (AM) and so-called 4D printed structures or made by other manufacturing processes.

Stimuli-responsive multi-materials can be made by various manufacturing processes; however, AM has some benefits. Two general advantages are discussed here. First, the same

reasons that motivate us to use AM for conventional (passive) materials, will be motive for utilizing AM for stimuli-responsive (active) materials. In other words, 4D printing conserves the general advantages of AM (such as material waste reduction, elimination of molds, dies, and machining (Ligon et al., 2017), and providing complex geometries) that are not present in other manufacturing processes. In addition, unlike other manufacturing processes, 4D printing provides an encoded multi-material smart structure in a single run. Second, AM helps us to manipulate the "structure" of multi-materials, precisely, to enable various shape-shifting behaviors. In other words, 4D "printing" enables encoding local anisotropy (Gladman et l., 2016) in multi-materials.

In fact, before the initiation of the 4D printing idea, researchers were *not* usually trying to find a specific printing path by mathematics that could yield a predictable and desired shape-shifting over time. 4D printing is a new manufacturing paradigm that combines smart materials, mathematics, and multi-material additive manufacturing, as we organized it in a systematic way in Chapter 3 (see the simplified version of Figure 3-1, in Figure 2-8).

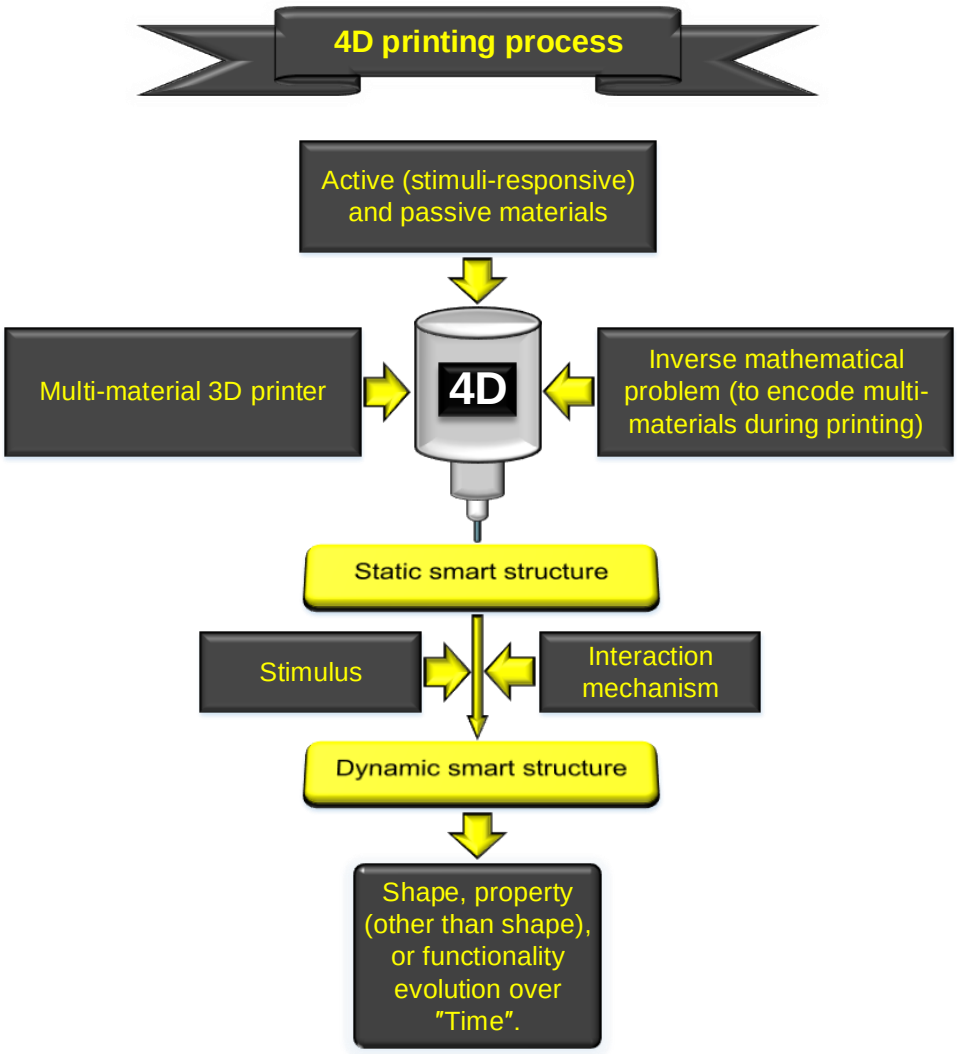

Figure 2-8. The simplified version of Figure 3-1, illustrating 4D printing process.

Remark 8. Scope and exceptions. Throughout this work, we did not make any specific assumption regarding the types of materials, stimuli, and length scales, for which these three laws are valid.

However, three points should be mentioned about the scope of this study. First, these three laws aimed at "shape-shifting" behaviors that are currently the focus of studies in the 4D printing field. The evolutions of other properties such as color or thermal resistance have not been discussed in this study, although they are of interest. Nevertheless, the shape-shifting behavior can provide evolutions in other properties or functionality. As an example, the researchers (Athanasopoulos & Siakavellas, 2018; 2017) demonstrated smart patterned surfaces that can alter their geometry in a manner that leads to changes in their effective emissivity to eventually control the satellite temperature, without using controllers and energy supplies. Second, these laws are associated with

"multi-material" structures having active and passive materials. Third, simple linear expansion/contraction shape-shifting behaviors are excluded from this study, because in these cases, there is no curvature (they may be considered as zero-curvature, for which the radius of curvature is infinity).

In science and engineering, laws are flexible and can have exceptions. We have reviewed more than 200 related published works, whether stimuli-responsive structures fabricated by printing or made by other manufacturing processes. However, we could not find any exception (counterexample) for our laws (considering the remarks and scope of this study). Nevertheless, we put the expression "almost all" in our three laws for possible exceptions in the future. By the way, our results are general and also important, as they target the 4th D of 4D multi-materials. Some of the exiting works, at the first glance, may seem counterexample for these three laws. However, by in-depth analysis and considering their fundamental physics, their compliance with these three laws will be comprehended. For example, the built-in (direct) 4D printing proposed by some researchers (Ding et al., 2017; van Manen et al., 2017) has the same "underlying physics" of conventional shape memory polymers. As we touched on earlier, to enable the SME of SMPs a mechanical force is required in addition to heat (the thermomechanical (thermo+mechanics) cycles of SMPs indicate this point, as well). In the built-in (direct) shape memory effect (Ding et al., 2017; van Manen et al., 2017), this mechanical force (that is used for programming) is provided during the printing, i.e., the printing and programming steps are integrated. A similar concept has been discussed in the introduction and has also been mentioned by some other studies (Mao et al., 2016; Zhang et al., 2016). The underlying physics of shape-shifting of these examples in multi-material structures is the same as "heat-responsive structure" of Figure 2-4 that has been discussed in Remark 6.

Sometimes, a formula is derived and validated; however, it is valid and applicable only for a specific range of cases. The bi-exponential formula derived and validated here is a universal governing equation that can model and predict the 4th D of any 4D multi-material structure as seen in Figure 2-4, this is because we built its bases, comprehensively. We use the word "law", because the related results are general and are also required for understanding, modeling, and predicting the shape-shifting behaviors of multi-material 4D printed structures.

Remark 9. Closing. As a summary of the proposed three laws, Figure 2-9 is presented.

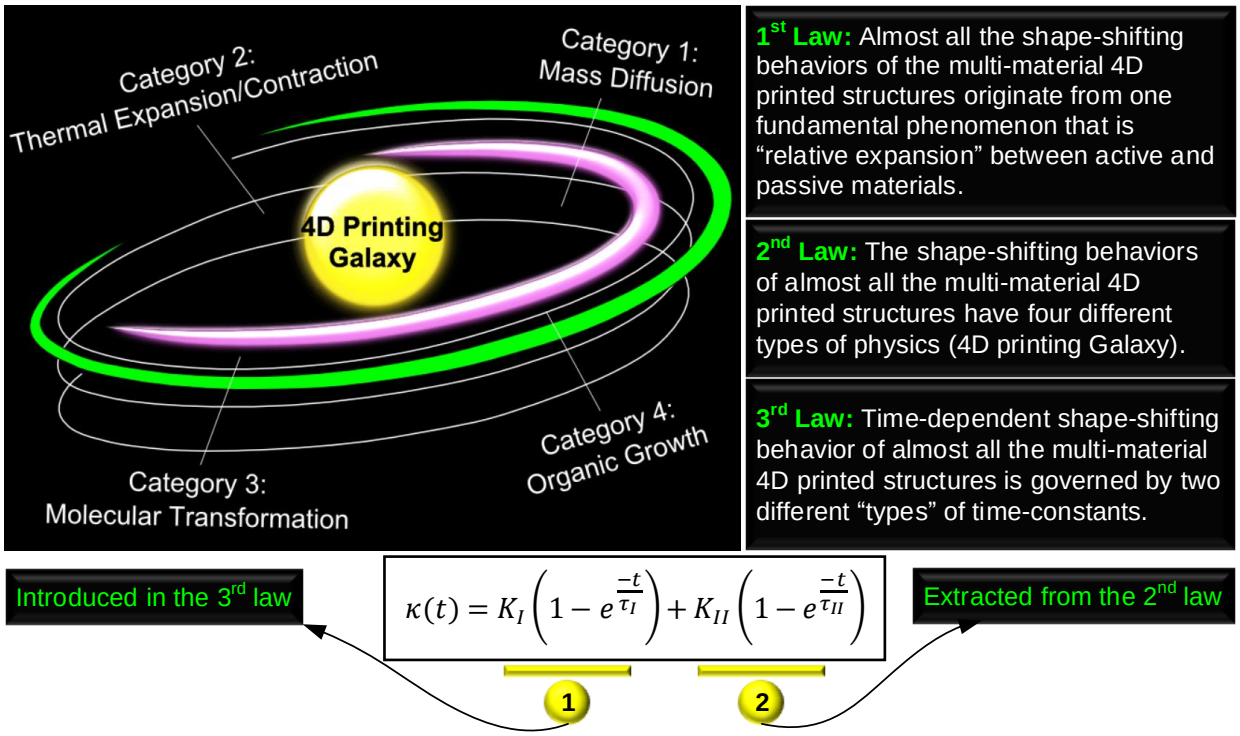

Figure 2-9. A summary of our laws. (the galactic shape of this figure has been inspired by a display designed by Rod Hill, showing advancements in Reconfigurable Manufacturing Systems, and installed on the wall of the ERC-RMS Center at the University of Michigan.)

2.3 Conclusions

Stimuli-responsive materials have demonstrated their promising applications. Any emerging application that is enabled by functional and stimuli-responsive materials can be elaborated in the field of 4D printing due to the unique attributes of the multi-material additive manufacturing process. Here, by a detailed, but systematic, qualitative and quantitative study, we generated a bi-exponential formula that governs the shape-shifting behavior of almost all the multi-material 4D structures over time. We showed that two different types of time-constants *are needed* to capture the correct time-dependent behavior of 4D multi-materials. The purpose of the first and second laws was to understand the 4th D of 4D printed multi-material structures, and the purpose of the second and third laws was to model and predict the 4th D. The results of this study can serve as a guideline and general design principles for the future. They can also be incorporated into future software and hardware developments. We should note that pure experimental study might not be able to generate a general conclusion for the relationship between two quantities, as the experimental study may not cover all the possible regions of the relationship in various cases.

Drawing a systematic conclusion is the strength of analytical study (validated by experimental data) as done here.

CHAPTER 3

4D PRINTING AS A NEW PARADIGM FOR MANUFACTURING WITH MINIMUM ENERGY CONSUMPTION

In this chapter, as a first attempt, we consider the energy aspect of 4D printing. By a thermodynamic analysis, we obtain the theoretical limit of energy consumption in 4D printing and prove that 4D printing can be the most energy-efficient manufacturing process. Before that, we clearly underpin 4D printing as a new manufacturing process and identify its unique attributes.[3]

3.1 Introduction

Manufacturing industries consume about one-third (31%) of the global energy and are also responsible for approximately one-third (36%) of CO_2 emissions (Bunse et al., 2011; IEA, 2007a; ElMaraghy et al., 2017; Saygin et al., 2010). Energy availability and costs are the next issues in addition to environmental impacts (Rahimifard et al., 2010; Seow & Rahimifard, 2011). Therefore, energy efficiency has been the focus of many studies recently, and its eminence has been highlighted more than ever (Nilakantan et al., 2015; Liu et al., 2014).

On the other hand, 4D printing provides a situation for using random (free) energy to make non-random structures (Tibbits, 2013). As discussed and illustrated in various examples in Appendix A, self-assembling components are first encoded and fabricated by the 4D printing process. Then, the components are self-assembled by applying free environmental energy like heat or water to get the desired complex shape.

[3] This chapter is based on our journal article (under review), entitled "4D printing as a new paradigm for manufacturing with minimum energy consumption", by Farhang Momeni and Jun Ni.

In fact, rather than making the final complex desired structure thoroughly by 3D printing (and spending more electrical energy), simpler components can be made that later transform into the desired shape under free environmental energies (or stimuli). The initial self-assembling components can be made as separate components or an integrated structure (like a flat sheet that transforms into a cube), depending on a specific application. These goals are achieved by encoding smart (stimuli-responsive) materials in multi-material structures. Thus, 4D printing may revolutionize manufacturing and construction industries as said by Tibbits (2013).

In the following, first, we underpin 4D printing as a new manufacturing process and identify its unique attributes. Then, we obtain the theoretical limit of minimum energy consumption in manufacturing that can be approached by 4D printing.

3.2 4D printing as a new manufacturing process with unique attributes

3D printing (additive manufacturing) is a well-known manufacturing process with its unique attributes. Now, 4D printing needs to be clearly defined and described as a new manufacturing process and its unique attributes should also be proved.

By analyzing natural shape morphing materials and structures (Oliver et al., 2016), in addition to stimuli and stimuli-responsive materials, one other thing is observed that is encoded anisotropy (Oliver et al., 2016). To enable complicated shape-shifting behaviors required for accomplishing various tasks in natural structures such as the pinecone, nature programs a specific arrangement of active and passive elements (Oliver et al., 2016). This encoded anisotropy is required to direct the response into the desired direction (Oliver et al., 2016). Now, 4D printing is a good paradigm to meet this type of encoding in synthetic shape morphing structures. By considering the aforementioned point in natural shape morphing structures and based on the 4D printing concepts discussed in the first chapter, we underpin 4D printing as a new manufacturing process as shown in Figure 3-1, and identify attributes of 4D printing as in Figure 3-2. As we have seen in the first chapter, almost all applications enabled by 4D printing can be categorized into self-assembly, self-adaptability, and self-repair that we call them here as “3S of 4D printing applications”. 4D printing conserves the advantages of 3D printing and further adds new features. The “complexity-free geometry” attribute was introduced as the unique feature of structures made by 3D printing (Kruth et al., 1998; Mahajan et al., 2012; Jin et al., 2016; Costabile et al., 2017). Here, we introduce “complexity-free geometry change” as the unique attribute of 4D printed

structures. One of the key goals of 3D printing is movement from form to functionality (Lewis, 2015). 4D printing goes further and provides multi-functionality. Furthermore, 4D printing possesses the material-saving characteristic arising from the general advantages of 3D printing and further adds the energy-saving trait (that is the focus of this study).

Proposal for future: it should be highlighted that future "4D printers" should possess an integrated inverse mathematics (as a software/hardware added to the current multi-material 3D printers) to predict the shape-shifting behaviors for various (or categories of) materials and stimuli. The term "4D printer" has already been mentioned in various studies in the literature of 4D printing. However, "4D printer" is *not* simply achieved by extending a single-material 3D printer to a multi-material 3D printer, or by combining several printing techniques (e.g., FDM and inkjet) in one 3D printer. *"4D printer" should be able to analyze and predict the "4th D"*. To achieve a 4D printer, an "intelligent head" should be developed and added to the current printers (Figure 3-3). This head (as an integrated software/hardware added to the existing multi-material 3D printers) should be able to analyze and predict the 4th D. It should be able to predict the appropriate arrangement of active and passive materials (an encoded anisotropy) for the desired evolution after printing. As we elaborated in the first chapter, 4D printing mathematics is a link between four main factors: printing path (arrangement of active and passive voxels), desired shape after printing, stimulus properties, and materials properties. 4D printing mathematics is required to predict the shape-shifting behavior after printing over time, prevent internal collisions, and decrease or even eliminate trial-and-error tests for getting the desired shape-shifting. Currently, 4D printing process utilizes the inverse mathematical modeling in an offline manner (passively), as seen in Figure 3-1. However, the inverse mathematical modeling can systematically be incorporated into current 3D printers to yield 4D printers that can analyze and predict the 4th D. Our general bi-exponential formula derived and validated in the second chapter can be used in future 4D printers. That equation is the starting point and the proposed two time-constants can be further extended to complicated cases.

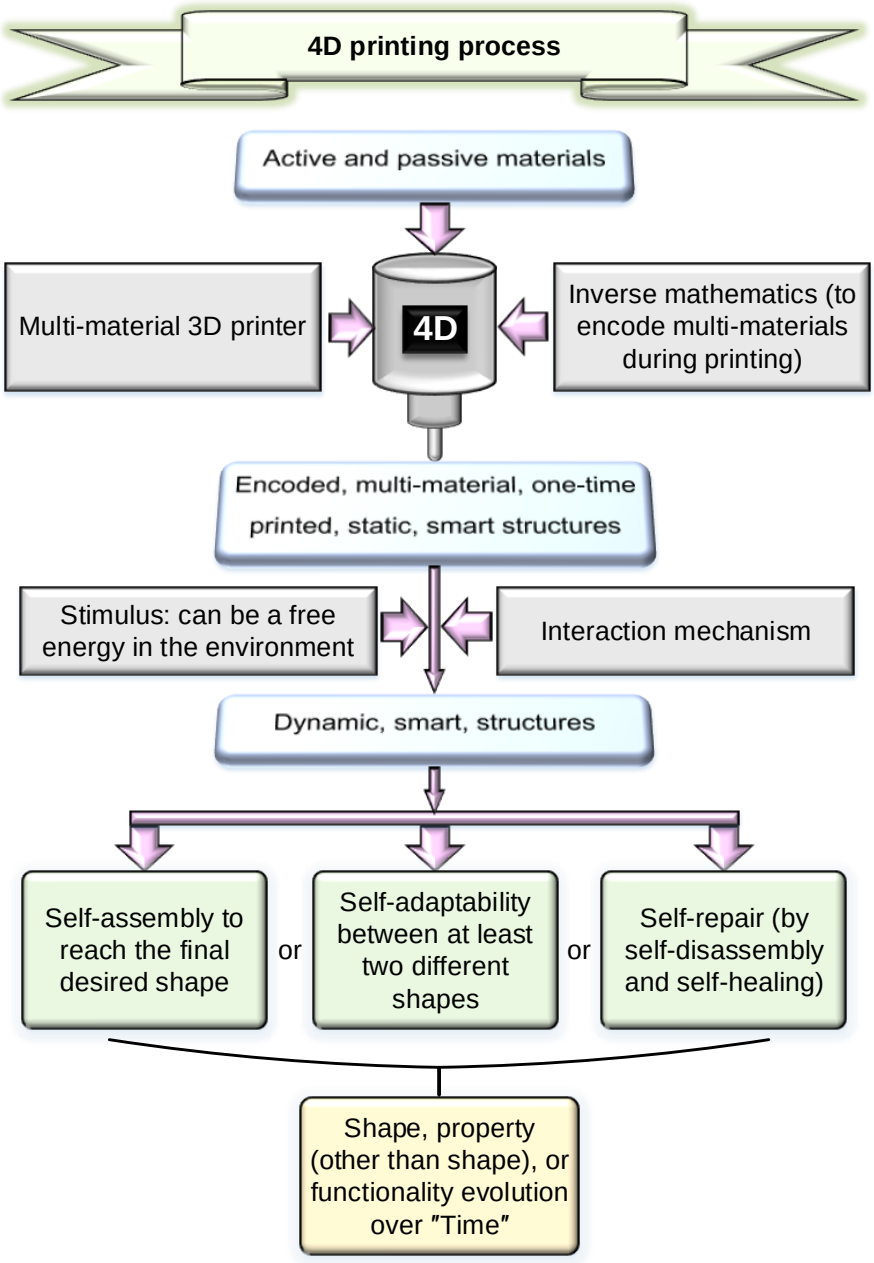

Figure 3-1. 4D printing process.

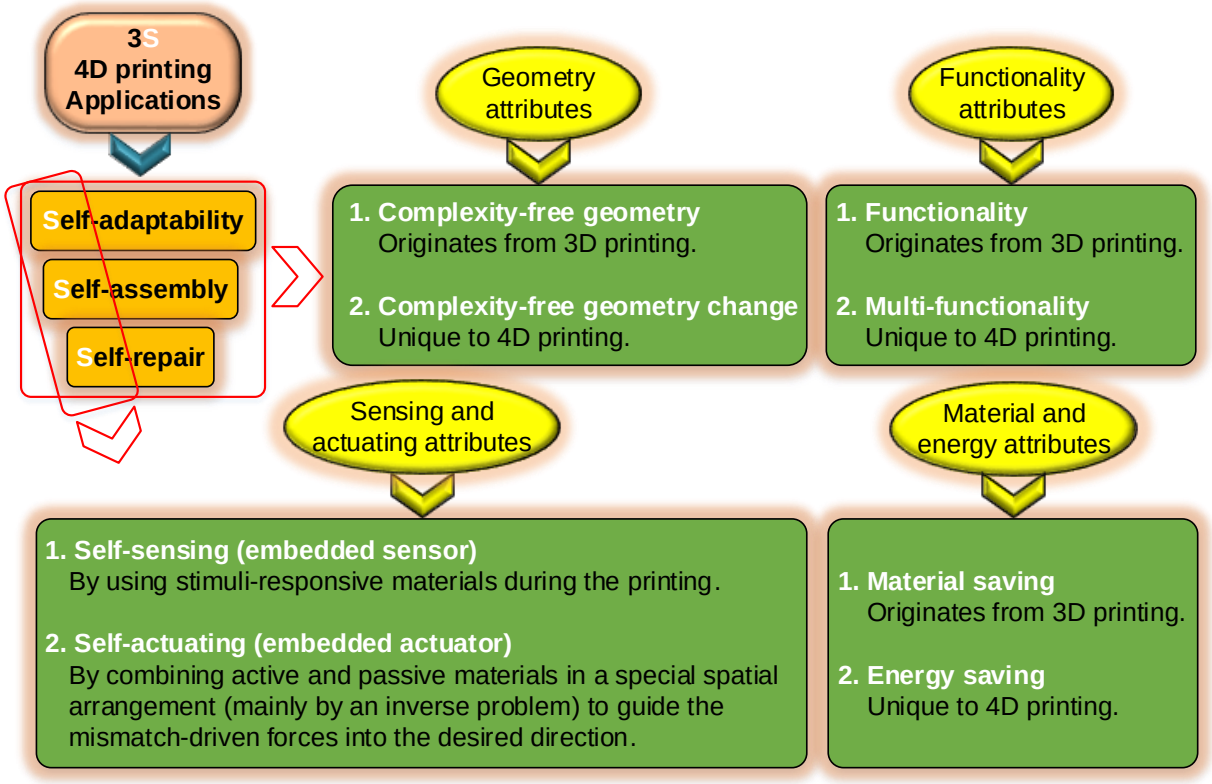

Figure 3-2. "3S of 4D printing applications" and 4D printing attributes.

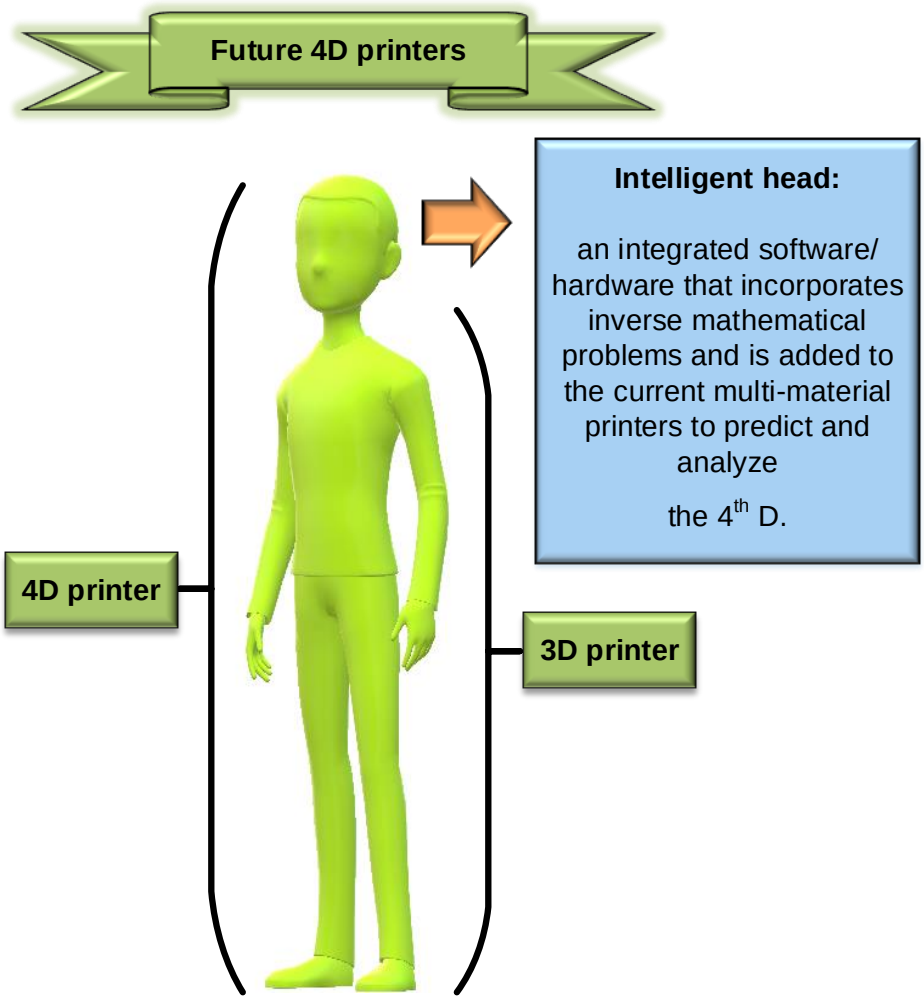

Figure 3-3. Future 4D printers. To achieve a 4D printer, an "intelligent head" (i.e., an integrated software/hardware that incorporates inverse mathematical problems of Figure 3-1) should be developed and added to the current multi-material 3D printers.

3.3 Energy aspect of 4D printing as a new process for self-assembly at manufacturing scale

A manufacturing process, in the most general form, can be modeled as Figure 3-4 (Gyftopoulos & Beretta, 2005; Gutowski et al., 2006; 2007; 2009; Branham et al., 2008). There are three types of energy transfer mechanisms between a system and its surroundings: *heat*, *work*, and *mass flow* (in fact, mass is energy and mass flow is present in open thermodynamic systems) (Cengel & Boles, 2015). The energy transfer between a system and its surroundings causes entropy transfer between them so that $\dot{S}_{heat} = \frac{\dot{Q}}{T}$, $\dot{S}_{work} = 0$, and $\dot{S}_{mass} = \dot{m}s$ (there is no entropy transfer by work) (Cengel & Boles, 2015). Energy is conserved (i.e., it cannot be destroyed or generated), while entropy can be generated (Cengel & Boles, 2015). The first and second laws of

thermodynamics deal with energy and entropy, respectively, and in the most general forms are (Cengel & Boles, 2015):

$$\begin{cases} \text{Energy balance: } E_{in} - E_{out} = \Delta E_{sys} \xrightarrow{\text{rate form}} \dot{E}_{in} - \dot{E}_{out} = \dfrac{dE_{sys}}{dt} \\ \text{Entropy balance: } S_{in} - S_{out} + S_{gen} = \Delta S_{sys} \xrightarrow{\text{rate form}} \dot{S}_{in} - \dot{S}_{out} + \dot{S}_{gen} = \dfrac{dS_{sys}}{dt} \end{cases}. \tag{3-1}$$

By ignoring kinetic and potential energies (and other macroscopic forms of energy), the two thermodynamics laws are (Bejan, 2016):

$$\begin{cases} \text{Energy balance: } \dot{Q}_{in} - \dot{Q}_{out} + \dot{W}_{in} - \dot{W}_{out} + \sum_{in} \dot{m}h - \sum_{out} \dot{m}h = \dfrac{dE_{sys}}{dt} \\ \text{Entropy balance: } \sum_{H} \dfrac{\dot{Q}_{in}}{T_H} - \sum_{L} \dfrac{\dot{Q}_{out}}{T_L} + \sum_{in} \dot{m}s - \sum_{out} \dot{m}s + \dot{S}_{gen} = \dfrac{dS_{sys}}{dt} \end{cases}. \tag{3-2}$$

Here, we adopted subscripts H and L to indicate high and low temperatures, respectively (Figure 3-4).

By applying equation (3-2) to a general manufacturing process (Figure 3-4) operating under steady conditions ($\frac{d}{dt} = 0$), we have

$$\begin{cases} \text{Energy balance: } \dot{Q}_{in} - \dot{Q}_{out} + \dot{W}_{in} - \dot{W}_{out} + (\dot{m}h)_{in} - (\dot{m}h)_{out} = 0 \\ \text{Entropy balance: } \dfrac{\dot{Q}_{in}}{T_H} - \dfrac{\dot{Q}_{out}}{T_L} + (\dot{m}s)_{in} - (\dot{m}s)_{out} + \dot{S}_{gen} = 0 \end{cases}. \tag{3-3}$$

By multiplying both sides of the entropy balance equation by T_L and equating the left-hand sides of the energy balance and the resulting entropy balance equation, we arrive at

$$\dot{W}_{in} = \dot{W}_{out} + \left(\frac{T_L}{T_H} - 1\right)\dot{Q}_{in} + (\dot{m}h)_{out} - (\dot{m}h)_{in} - T_L[(\dot{m}s)_{out} - (\dot{m}s)_{in}] + T_L\dot{S}_{gen}. \tag{3-4}$$

Equation (3-4) is a more general form of the required input work than that obtained in the literature (Branham et al., 2008; Gutowski et al., 2009), which further considers the output work. Up to here, we followed the same approach devised by Gutowski et al. (2006; 2007; 2009) and Branham et al. (2008) and further extended their input work equation.

Now, the required input power (energy rate) would be

$$\dot{E}_{in} = \dot{W}_{in} + \dot{Q}_{in} \Rightarrow$$

$$\dot{E}_{in} = \dot{W}_{out} + \frac{T_L}{T_H}\dot{Q}_{in} + (\dot{m}h)_{out} - (\dot{m}h)_{in} - T_L[(\dot{m}s)_{out} - (\dot{m}s)_{in}] + T_L\dot{S}_{gen}. \tag{3-5}$$

This equation can also be written in non-rate form as

$$E_{in} = W_{out} + \frac{T_L}{T_H} Q_{in} + (mh)_{out} - (mh)_{in} - T_L[(ms)_{out} - (ms)_{in}] + T_L S_{gen}. \quad (3\text{-}6)$$

Equation (3-6) is a general equation that gives the required input energy for any manufacturing process.

Now, for 4D printing as a manufacturing process that enables self-assembly at manufacturing scale, this equation can be further analyzed and simplified. Let us consider the following key-points:

Key-point 1. Self-assembly is a spontaneous and reversible process (Bergström, 2011; Steed et al., 2007; Frewer et al., 2011; Whitesides & Grzybowski, 2002; Bensaude-Vincent, 2006; 160. Whitesides & Boncheva, 2002). For such a process, the central thermodynamic equation is $\Delta G_{process} = 0$ (Bergström, 2011; Cengel & Boles, 2015).

Key-point 2. In a reversible process, the system is in thermodynamic equilibrium with its surroundings. One of the necessities of thermodynamic equilibrium is thermal equilibrium. When two bodies are in thermal equilibrium, their temperatures are the same. Therefore, during a reversible process, $T_{sys} \approx T_{surr}$ (Sears & Salinger, 1975; Zumdahl & DeCoste, 2016; Cengel & Boles, 2015) ("sys" and "surr" stand for system and surrounding, respectively).

Key-point 3. For a reversible process, $S_{gen} = 0$ (Cengel & Boles, 2015) ("gen" stands for generation).

By considering Key-point 2, for any manufacturing process in the reversible condition, equation (3-6) can be written as (we emphasize that from the first equation, the convention is $\Delta ◎ = ◎_{in} - ◎_{out}$):

$$E_{in} = W_{out} + \frac{T_L}{T_H} Q_{in} - \Delta G + T_L S_{gen}, \quad (3\text{-}7)$$

where $\Delta G = \Delta H - T\Delta S$ and G is the Gibbs free energy. Then, by using key-points 1 and 3, we have the following equation for 4D printing that enables self-assembly at manufacturing scale:

$$E_{in} = W_{out} + \frac{T_L}{T_H} Q_{in}. \quad (3\text{-}8)$$

Equation (3-8) is the minimum theoretical limit of required input energy for 4D printing as a new process that enables self-assembly at manufacturing scale. In addition, generally, $\Delta G \leq 0$ and $S_{gen} \geq 0$ and thus both terms $-\Delta G$ and $T_L S_{gen}$ are positive or zero (≥ 0). Therefore, by

comparing equations (3-7) and (3-8), it can be concluded that 4D printing can have the minimum energy consumption among various manufacturing processes.

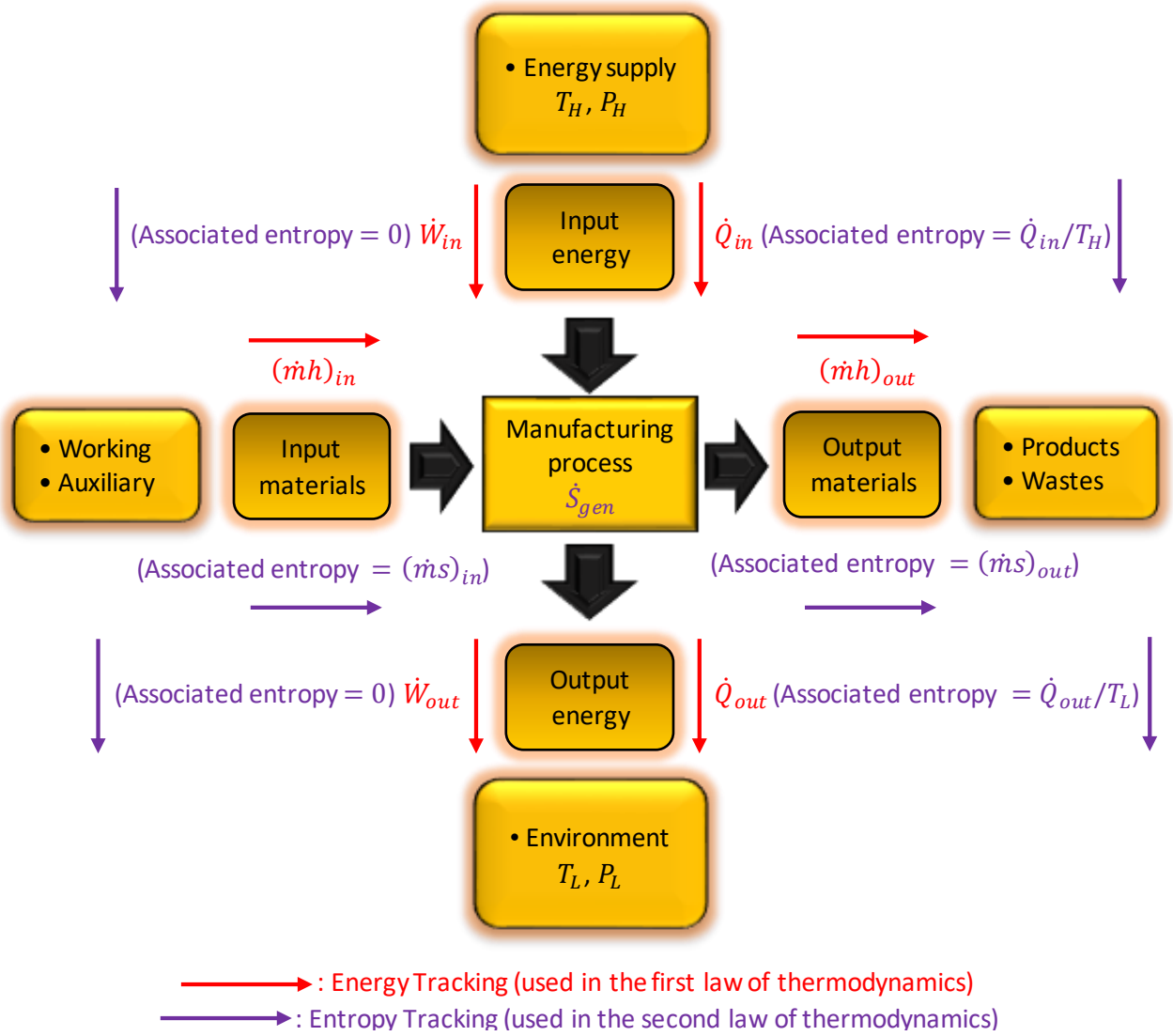

Figure 3-4. A manufacturing process in the most general thermodynamic model (this figure has been drawn based on the concepts in (Gyftopoulos & Beretta, 2005; Gutowski et al., 2006; 2007; 2009; Branham et al., 2008). The energy and entropy flows have also been illustrated.

3.4 Conclusions

We derived the theoretical limit of minimum energy consumption in 4D printing as a manufacturing process and proved that 4D printing could be the most energy-efficient process among various manufacturing processes. This minimum energy consumption limit in

manufacturing obtained here can be *approached* by 4D printing process and future 4D printers. It does not necessarily mean that this limit is practically achieved in 4D printing processes. One of the main reasons is that, currently, in 4D printing, although the self-assembly process can be triggered by environmental free energy, fabrication of the initial self-assembling components requires electrical energy for running the printers. Nevertheless, future 4D printers may somehow incorporate environmental free energy for the whole manufacturing process (that is, fabrication of the self-assembling components and then self-assembly of them). Sadi Carnot worked on the energy efficiency of "heat engines" and the Carnot cycle gives the theoretical limit in heat engines. Here, we worked on the energy efficiency of "manufacturing processes" and obtained the theoretical limit of minimum energy consumption in manufacturing that can be approached by 4D printing. In this study, we have also clearly underpinned 4D printing as a new manufacturing process with unique attributes.

CHAPTER 4

PLANT LEAF-MIMETIC SMART WIND TURBINE BLADES BY 4D PRINTING

Scientists have reported that plant leaf veins grow into an optimized architecture not only to accomplish their biological and physiological functions but also to sustain the environmental loads (Steele, 2000; Somerville et al., 2004; Liu & Gong, 2011). Researchers showed that the wind blade mimicking the leaf architecture could always have relatively lower internal strain energy, better static strength and stiffness, smaller stress intensity, and higher fatigue life compared with the conventional blade structures (Liu et al., 2006; 2009; 2010; 2011). However, the plant leaf-mimetic wind blade has so far remained at the level of simulations. Here, a new paradigm for the design and fabrication of wind blades is demonstrated by 4D printing process, which combines several beneficial attributes in one blade. The proposed blade having the plant leaf structure can show reversible bend-twist coupling (BTC). It does not rely on conventional electromechanical systems such as sensors and actuators to determine proper deflection and change its shape. Additionally, the existing blades capable of BTC through passive methods have inherent flutter instability since they need to be flexible. The proposed blade may solve the flutter challenge. Lastly, this multi-functional blade can lead to eco-friendly wind turbines. Wind-tunnel tests and performance analysis are performed on the proposed blade to demonstrate its applicability.[4]

[4] This chapter is based on our journal article published in *Renewable Energy 130 (2019)*, entitled "Plant leaf-mimetic smart wind turbine blades by 4D printing", by Farhang Momeni, Seyedali Sabzpoushan, Reza Valizadeh, Mohammad Reza Morad, Xun Liu, and Jun Ni.

4.1 Introduction

Earth`s winds have enough capacity to become a primary resource for near-zero-emission electricity generation (Marvel et al., 2013). In 2016, MacDonald et al. (2016) mentioned that about 80% reduction of CO_2 emissions could be achieved from the US electricity sector, compared with 1990 levels, by using the wind and solar energies with no penalty in the levelized cost. By assessing the wind power costs, whether long-term (Zhang et al., 2016) or short-term (Girard et al., 2013), it was drawn that the wind electricity had a promising future and market (Esteban et al., 2011). Wind resources are free and carbon-free (Zhang et al., 2016).

One of the apparent challenges in the wind energy exploitation is saturation. The power extraction from the wind increases linearly with increasing the number of wind turbines in the beginning but then approaches saturation (Jacobson & Archer, 2012). Several studies analyzed the limits that govern power extraction from wind kinetic energy (Marvel et al., 2013; Miller et al., 2015; Jacobson & Archer, 2012; and Miller & Kleidon, 2016). In this regard, Marvel et al., 2013 mentioned that the Earth's winds have enough capacity to become a primary resource for electricity generation and wind power growth is limited by economic, political, environmental, and technical constraints, instead of global geophysical limits.

Historically, wind turbines originate about 200 BC from Persia (Iran) and also the first practical windmills (named the Sistan windmills) were designed and utilized by Persians in the 7th century that were vertical axis (Tummala et al., 2016; Eriksson et al., 2008; Kaldellis & Zafirakis, 2011; Musgrove, 2010 and Dodge, 2006). One of the first endeavors to produce electricity from the wind energy was made by Charles Brush in the US in 1888 (Eriksson et al., 2008).

Many studies are pursued in the renewable energy field to improve the current wind turbine blades from various perspectives. To convey the whole relevant studies, we organize the important concepts as the following sub-sections by considering four main advancements in wind turbine blades, including adaptability, bend-twist coupling shape-shifting, flexibility and plant leaf-mimetic wind blade.

4.1.1 Adaptive wind turbine blades

Two types of adaptability have been considered in wind turbine blades so far, bend-twist coupling (Lobitz et al., 1996; Veers et al., 1998; De Goeij et al., 1999; Lobitz et al., 2001; Griffin, 2002; Veers & Lobitz, 2003; Bottasso et al., 2013; Nicholls-Lee et al., 2013; Fedorov & Berggreen,

2014; Hayat & Ha, 2015; Zhou et al., 2015; Hayat et al., 2016; Stäblein et al., 2017), and sweeping (Liebst, 1986; Zuteck, 2002; Larwood & Zutek, 2006; Ashwill et al., 2010; Verelst & Larsen, 2010; Hansen, 2011; Picot et al., 2011; Larwood et al., 2014; Pavese et al., 2017). The adaptive wind turbine blade can be defined as a blade capable of shape-shifting between the original blade shape and the final shape. In this regard, the bend-twist coupling and sweeping are two common strategies that their final effect would be similar. Bend-twist coupling (BTC) has one flap-wise (span-wise) out-of-plane bending coupled with one chord-wise out-of-plane twisting (Figure 4-1(a)). Sweeping shape-shifting is in the direction of rotation, edge-wise and in-plane (Riziotis et al., 2010) as shown in Figure 4-1(b). Both types of these adaptabilities have been proven to be effective in load reductions on the wind turbine blades and improved energy gain (Lobitz et al., 1996; Veers et al., 1998; De Goeij et al., 1999; Lobitz et al., 2001; Griffin, 2002; Veers & Lobitz, 2003; Bottasso et al., 2013; Nicholls-Lee et al., 2013; Fedorov & Berggreen, 2014; Hayat & Ha, 2015; Zhou et al., 2015; Hayat et al., 2016; Stäblein et al., 2017; Liebst, 1986; Zuteck, 2002; Larwood & Zutek, 2006; Ashwill et al., 2010; Verelst & Larsen, 2010; Hansen, 2011; Picot et al., 2011; Larwood et al., 2014; Pavese et al., 2017).

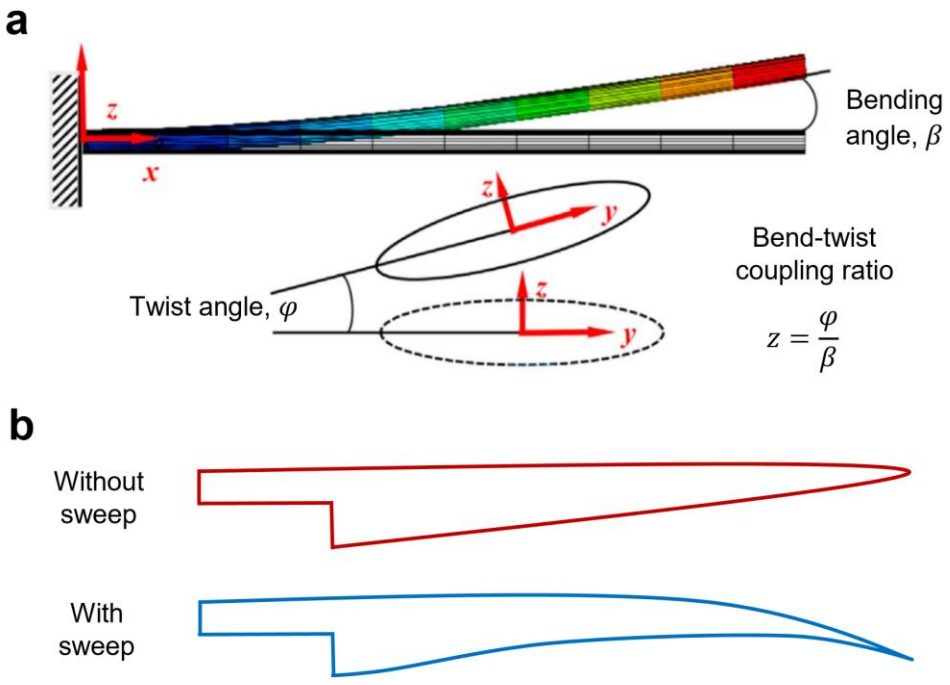

Figure 4-1. Adaptability in wind turbine blades. (a) Bend-twist coupling adaptability (Hayat et al., 2016) and (b) Sweeping adaptability (Sandia lab presentations, 2012).

4.1.2 Bend-twist coupling in wind turbine blades

The bend-twist coupling (BTC) was proven to be effective in fatigue and extreme loads alleviation and energy conversion improvement (Lobitz et al., 1996; Veers et al., 1998; De Goeij et al., 1999; Lobitz et al., 2001; Griffin, 2002; Veers & Lobitz, 2003; Bottasso et al., 2013; Nicholls-Lee et al., 2013; Fedorov & Berggreen, 2014; Hayat & Ha, 2015; Zhou et al., 2015; Hayat et al., 2016; Stäblein et al., 2017). Bend-twist coupling is also known as aero-elastic tailoring (Veers et al., 1998; Veers & Lobitz, 2003 and Hayat & Ha, 2015). The BTC is currently achieved in active and passive manners. In the active manner, controllers and electromechanical systems are required to change the blade shape. In the passive manner, anisotropic mechanical properties of a composite structure is utilized such that during operations (under wind loads), the wind blades display the BTC shape-shifting. The passive way has attracted more interests, because it can be more effective and economical and does not need sensors, actuators, and moving parts that may fail (Lobitz et al., 1996; Veers et al., 1998; De Goeij et al., 1999; Lobitz et al., 2001; Griffin, 2002; Veers & Lobitz, 2003; Bottasso et al., 2013; Nicholls-Lee et al., 2013; Fedorov & Berggreen, 2014; Hayat & Ha, 2015; Zhou et al., 2015; Hayat et al., 2016; Stäblein et al., 2017). Thus, most of the current works are focused on BTC through the passive manner. However, one related issue is the flutter instability. This is because this type of blade needs to be flexible to achieve the BTC through the passive manner under the wind loads. Higher flexibility leads to higher risk of flutter instability (Hayat et al., 2016; Bir & Jonkman, 2007; Politakis et al., 2008 and Cognet et al., 2017).

4.1.3 Flexible wind turbine blades

Human being can always be inspired and benefit from nature and living things, even from those that are apparently useless and harmful. Unexpected changes in wind turbines power have been reported in California wind farms, in which the power declined to half after 26 July at the same speeds compared with the days before 11 July (Corten & Veldkamp, 2001). The reason was found to be contamination and roughness of the leading edge of blades caused by insects, resulting in flow separation increase, sooner stall and lift lost. However, the insect wing`s flexibility has been inspired recently to increase the power generation of the wind turbine by expanding the desired working zone, which is a narrow region in rigid blades (Shultz, 2017 and Cognet et al., 2017).

Flexible wind blades are elastic and can be deformed in the direction of the wind. This deformation falls into two categories, pre-bending deformation (Sartori et al., 2016; Bazilevs et al., 2012; Riziotis et al., 2010) and pitch- angle change (Bongers et al., 1991; Hoogedoorn et al., 2010; Krawczyk et al., 2013; MacPhee & Beyene, 2011; MacPhee et al., 2015; MacPhee & Beyene, 2016; Su & Song, 2015; Cognet et al., 2017). Pre-bend deformation is in the direction of the wind, flap-wise (span-wise) and out-of-plane (Riziotis et al., 2010) as shown in Figure 4-2. Pitch-angle change is in the direction of the wind, chord-wise, and out-of-plane (Cognet et al., 2017) as illustrated in Figure 4-3. Moreover, the pitch- angle change can involve blade airfoil camber change (Figure 4-3(a)) or can keep the camber constant and only adjust the pitch angle (Figure 4-3(b)).

Pre-bending deformation is one of the solutions for the tower clearance problem in wind turbine blades to ensure enough distance between the blades and the tower during operations (Bazilevs et al., 2012). Moreover, the pre-bending can reduce the blade loads during operations and improve aero-structural efficiency (Riziotis et al., 2010; Sartori et al., 2016).

Pitch-angle change (whether with constant or adjustable airfoil camber) is one of the solutions to increase the efficient working zone (envelope) of wind turbines (Krawczyk et al., 2013; Hoogedoorn et al., 2010; Schubel & Crossley, 2012 and Cognet et al., 2017). This type of flexibility can also delay the stall compared with the rigid counterparts (Hoogedoorn et al., 2010 and MacPhee & Beyene, 2011).

In the literature, the difference between the adaptive and flexible wind turbine blades was ambiguous, and they were used interchangeably sometimes. These two phrases are distinguished in this study. An adaptive blade has the capability to change its shape from shape 1 (the original shape) to shape 2 (bend-twist coupled or swept form). However, both the original and final shapes can be rigid or flexible. These will be further discussed in section 4.3.1.4.

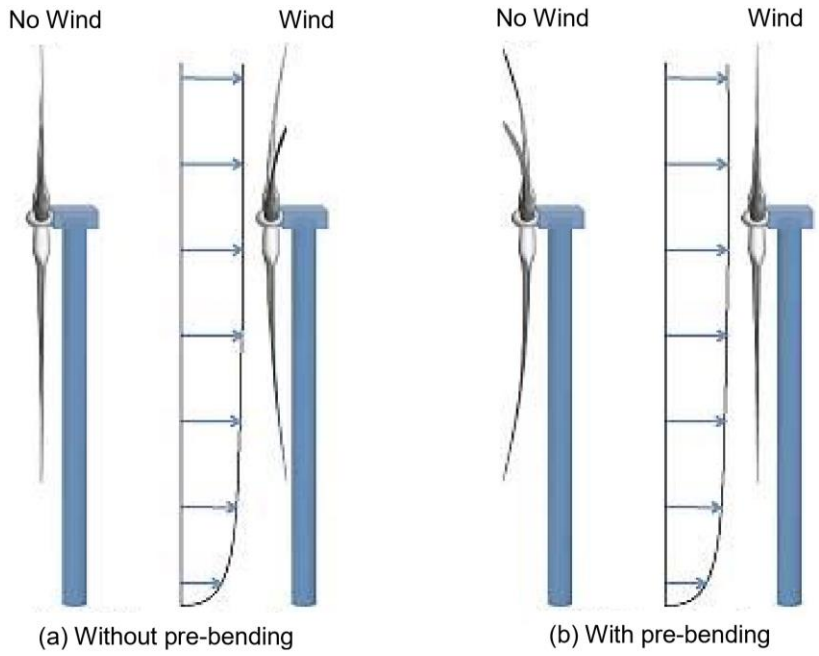

Figure 4-2. Pre-bending deformation in flexible wind turbine blades to ensure tower clearance (Bazilevs et al., 2012).

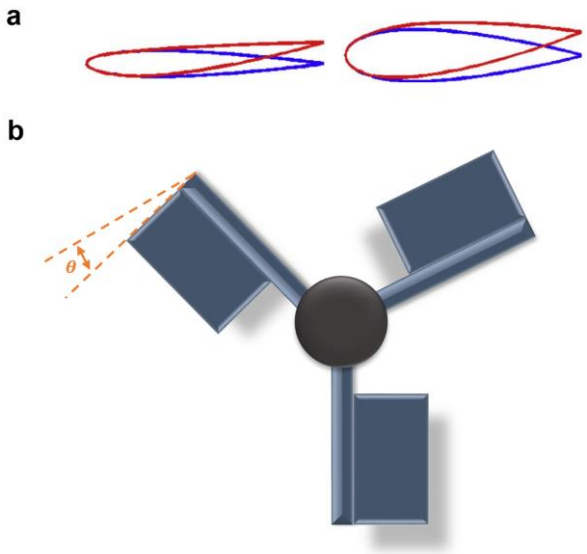

Figure 4-3. Pitch-angle change in flexible wind turbine blades. (a) airfoil with variable camber (Hoogedoorn et al., 2010). (b) airfoil with constant fixed camber (Cognet et al., 2017).

4.1.4 Plant leaf-mimetic wind turbine blades

Plant leaves grow in a manner not only to perform their physiological functions but also to accommodate and adapt to the environmental stresses (Steele, 2000; Somerville et al., 2004 and Liu & Gong, 2011). Veins of plant leaves grow into a steady architecture with global optimal

performance, and this self-optimization capability arises from their genes (Li et al., 2013). There are several similarities between the wind turbine blade and plant leaf. Both of them have similar working environment; both are cantilever (fixed-free beam) structures and both need to sustain the environmental loads (Liu & Gong, 2011). Inspired by natural optimum laws of the plant leaf growth, bionic design mimicking the plant leaf structure can be applied to wind turbine blades (Liu et al., 2006; 2009; 2010; 2011). Liu et al. (2006; 2009; 2010; 2011) showed that the blade structures based on the plant leaf network could always have relatively lower internal strain energy, better static strength and stiffness, smaller stress intensity, and higher fatigue life (Liu et al., 2006; 2009; 2010; 2011).

However, most of the studies in wind turbine blades inspired by the plant leaf remained at the level of simulations such as geometry optimization (Figure 4-4). One reason is that the vein network has a complex and subtle geometry and its fabrication can hardly be achieved by the conventional manufacturing processes. Especially, more difficulties are raised in traditional manufacturing processes with fabrication of complex geometries by using smart (active) materials such as shape memory polymers (Choong et al., 2017). This will be resolved in this study by 4D printing process.

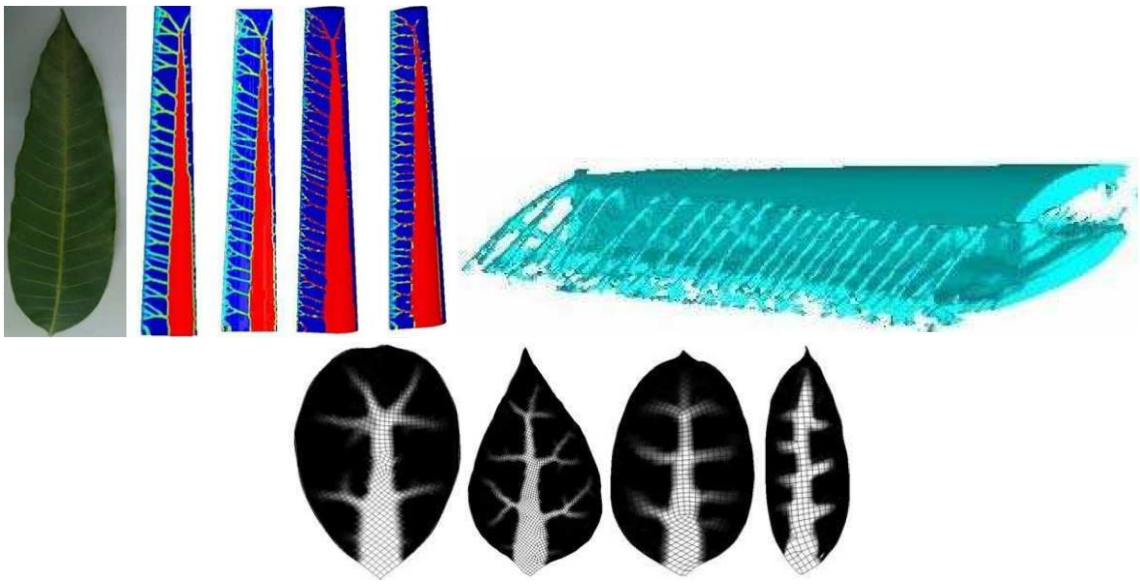

Figure 4-4. The simulations such as geometry optimizations performed by Liu et al. (2006; 2009; 2010; 2011) , demonstrated that wind blades based on the plant leaf structure had better mechanical and structural properties such as the stiffness, static strength, and fatigue life compared to the conventional structures (Liu et al., 2006; 2009; 2010; 2011).

By analyzing the related literature described so far, various shape-shifting behaviors in wind turbine blades are organized and summarized in Figure 4-5.

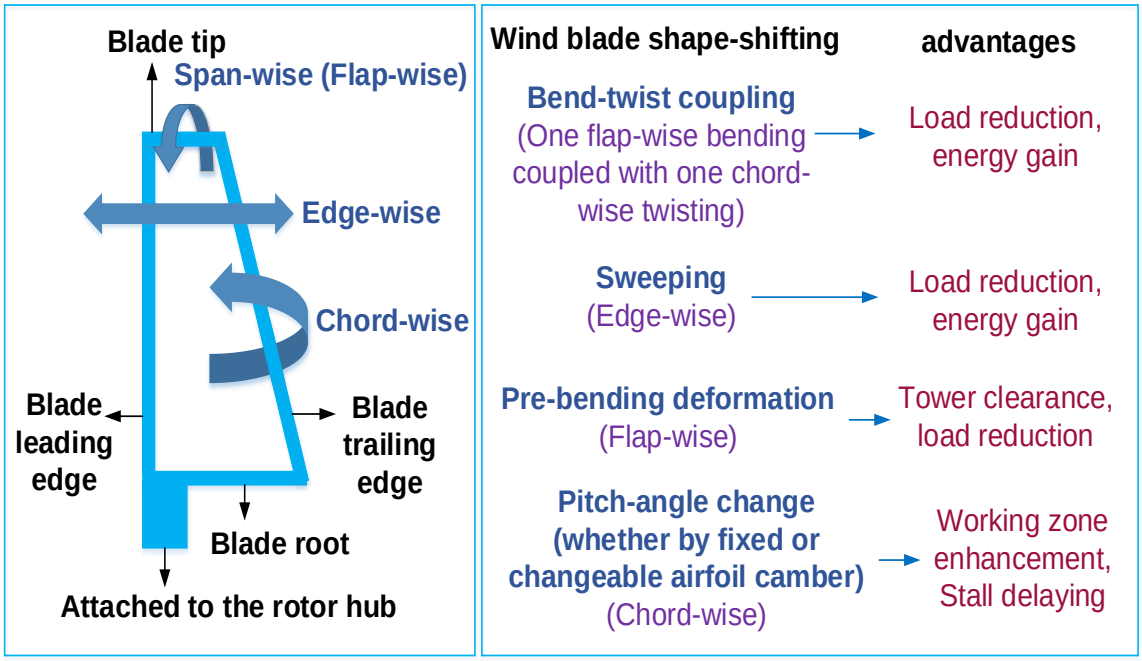

Figure 4-5. Various shape-shifting behaviors in wind turbine blades, and their advantages.

The 3D printing presents unique characteristics regarding geometry complexity and specific functionality in renewable energy applications (Ruiz-Morales, 2017). 4D printing conserves the attributes of 3D printing and adds the fourth dimension to provide shape, property (other than shape), or functionality evolution over "time" (Momeni et al. 2017; 2018). In this study, we explore the 4D printing in the wind energy field and demonstrate its advantages.

The smart material used in this study is Polylactic acid (PLA), which is a thermo-responsive, biodegradable shape memory polymer. The shape-shifting dimension is 2D flat blade to 3D deformed blade, and the shape-shifting type is bend-twist coupling.

4.2 Mathematical modeling of the proposed blade

4D printing relies on a desired arrangement of active (smart) and passive (non-smart) materials in space such that the mismatch-driven forces enable the required dynamics of the structure. The arrangement is calculated from mathematical modeling. Based on the properties of materials and stimuli, the printing paths will determine the final desired shape, which is referred to as a forward problem. In contrary, if the final desired shape is known, while the printing path is unknown, it is called an inverse problem (Gladman et al., 2016 and Momeni et al., 2017).

In this study, a mathematical model is developed to establish the relationship between the printing paths and the final desired bend-twist coupling shape. Here, the bending of the blade is from the global bending associated with the main vein as well as the local bending of the lateral veins. Overall twist of the blade originates from the local bending of each lateral vein. After the bend-twist coupling shape-shifting, the deformed blade would have one bend angle (β) and one twist angle (α) as shown in Figure 4-6. Here, PLA is the smart material, and a membrane of paper is the passive material.

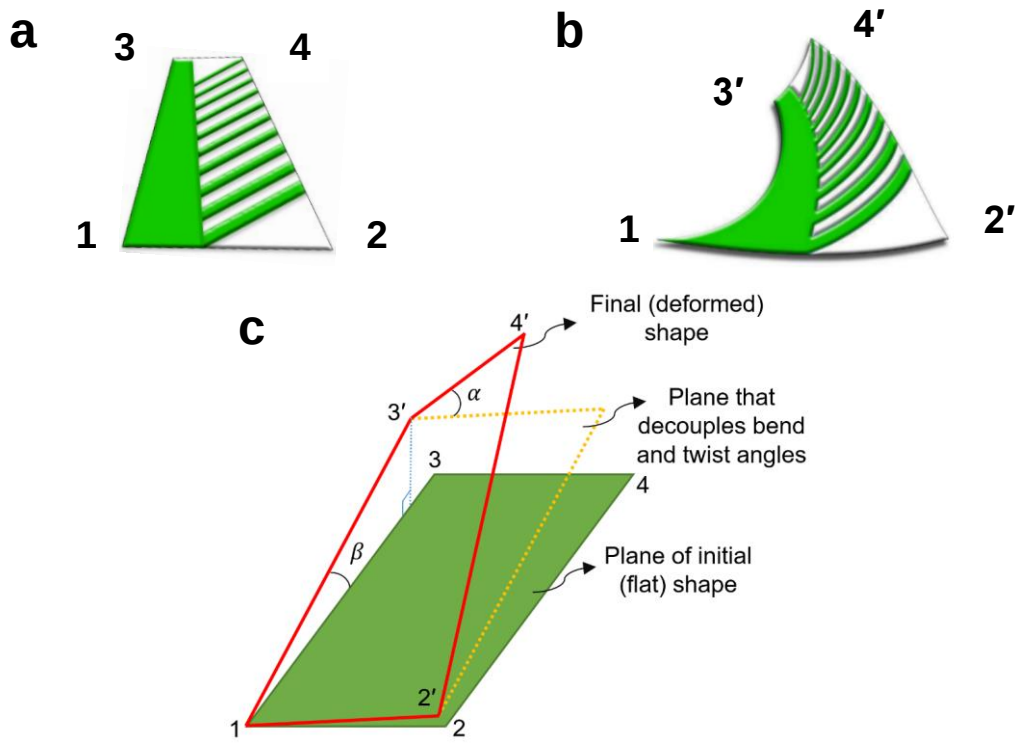

Figure 4-6. Schematic illustrations of the desired bend-twist coupling in the proposed 4D printed wind turbine blade based on the leaf structure: (a) Original flat blade, (b) Desired deformed blade, and (c) bend angle (β) and twist angle (α) in the deformed blade.

Since both the bending and twisting of the blade are from the *bending* of the main and lateral veins, the mathematical model can be developed by treating the main and lateral veins as composite bending beams, which consist of one layer of PLA and one membrane layer of paper.

In Chapter 2, we found that when the final shape was achieved, both the Timoshenko model and our formula would converge and provide similar analyses for time-independent behaviors (such as the effect of thickness on curvature). Here, we are interested in the final shape (rather than instantaneous shapes). In this regard, Zhang et al., 2016 had already worked on the Timoshenko

model, simplified it, and provided the values of parameters for the PLA/paper composite. As described by Timoshenko and Gere (1973) and Zhang et al., (2016), after heating this composite structure to a certain temperature greater than the glass transition temperature, T_g of the smart layer, and then reaching equilibrium at room temperature, about 25 ºC, the final bend angle would be:

$$\theta(x,t') = -6\alpha_{eff}\dot{T}t'(1-\kappa')\frac{x}{h_m}\frac{E'_{pm}h_{pm}b_{pm}(h_{pm}+1)}{(E'_{pm}h_{pm}+1)(E'_{pm}b_{pm}{h_{pm}}^3+1)} \quad (4\text{-}1)$$

where $\dot{T}$ is the heating rate; $h_{pm} = h_p/h_m$, and h_p and h_m are the thickness of the printed polymer and paper, respectively; $b_{pm} = b_p/b_m$, and b_p and b_m are the widths of the printed polymer and paper, respectively; $E'_{pm} = E_{pe}/E_m$, where E_{pe} is the elastic modulus of the polymer above the T_g, and E_m is the elastic modulus of the paper. $x \in [0, l]$, where l is the composite strip length. $t' = t - t_0$, where t is the total time and t_0 is the amount of time between the initial temperature and the glass transition temperature. $\kappa' = \alpha_m/\alpha_{eff}$, where α_m is the coefficient of thermal expansion (CTE) of the paper. The equivalent linear CTE (α_{eff}) for the printed composite is calculated based on the equation below (Zhang et al., 2015; 2016), which is derived from the Kelvin–Voigt model that consists of a spring and a dashpot arranged in parallel:

$$\alpha_{eff} = -\frac{\varepsilon_r}{\dot{T}t'}\left(1 - e^{-\frac{t'}{\tau_f}}\right) \quad (4\text{-}2)$$

where ε_r is the stored internal strain and τ_f is the relaxation time, both of which are constants related to the printed PLA/paper composite and ε_r is also affected by the printing speed (Zhang et al., 2015; 2016). When the final shape is the goal, t' will be large and the exponential term will vanish. Here, our goal is the final shape and eventually, we consider t' as a large number.

The above two equations are employed to develop mathematical model of the vein network structure in this study. For a plant leaf-mimetic blade consisting of *N* lateral veins and 1 main vein, the length (l), width (b), and thickness (h) of each vein, as well as the angle between the main vein and lateral veins (γ) are illustrated in Figure 4-7.

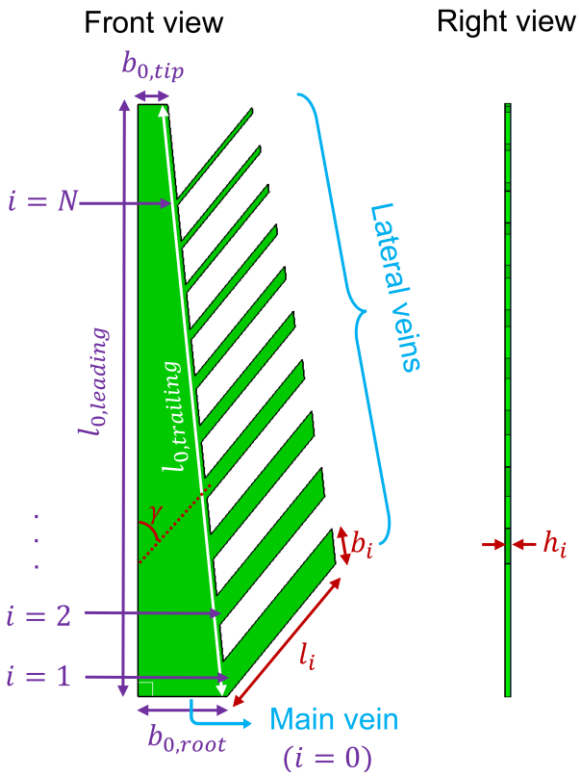

Figure 4-7. Illustration of the veins dimensions and the angle between the main and lateral veins.

Based on this figure, the required printing paths for the desired blade bending and twist angles can be determined as the following:

$$\theta_i(l_i,t') = -6\alpha_{eff}\dot{T}t'(1-\kappa')\frac{l_i}{h_{m,i}}\frac{E'_{pm}h_{pm,i}b_{pm,i}(h_{pm,i}+1)}{(E'_{pm}h_{pm,i}+1)(E'_{pm}b_{pm,i}{h_{pm,i}}^3+1)} \quad (4\text{-}3)$$

Equation (4-3) expresses the relationship between the final desired shape (θ_i), printing paths (l_i, h_i, b_i), materials properties (E_i, α_i) and stimulus property($\dot{T}$). Number $i = 0$ is the main vein and $1 \leq i \leq N$ denote the lateral veins, where $i = 1$ is the lateral vein nearest to the root and $i = N$ corresponds to the nearest one to the tip. $\theta_i(l_i,t')$ is the bending angle of the *tip* for each of the lateral or main veins.

The bending angle (β) in the final deformed blade can be approximated by the following equation:

$$\beta = \theta_0(l_0,t') + \cos(\gamma) \times \left(\theta_1(l_1,t') + \theta_2(l_2,t') + \cdots + \theta_N(l_N,t')\right) \quad (4\text{-}4)$$

On the right side, the first term is the contribution of the bending angle from the main vein and the second term is the contributions from the lateral veins. For the blade twist angle (α), similar

correlation can be obtained considering the individual $\theta_i(l_i, t')$. However, the inverse mathematical modeling for determining the printing path based on the desired twist angle is more complicated. Instead, forward appoach is employed for the twist angle. Three angles of 45°, 65°, and 90° between the main and lateral veins are experimentally (in the next section) investigated to obtain a smooth and incremental twist from root to tip.

In our structure, the smart material is PLA, and the passive material is a paper membrane. According to Zhang et al. (2015; 2016), $\varepsilon_r = 0.0155$ (assuming that the increase in printing speed from 30 mm/s to 50 mm/s has an insignificant effect on ε_r), $\tau_f = 1.89\ s$, $E_m = 5 \times 10^9\ (Pa)$, $\alpha_m = 0\ \left(\frac{1}{K}\right)$. The elastic modulus of the printed PLA at different temperatures is measured and the value well above T_g is around $E_{pe} = 2 \times 10^8\ (Pa)$. The measurement of this critical material parameter is elaborated in the section of DMA test. For the final bending angle (rather than instantaneous bending angles), t' is generally in the range of hours and much larger compared with the relaxation time τ_f, therefore $1 - e^{-\frac{t'}{\tau_f}} \cong 1$. Consequently, the heating rate will be cancelled out. Based on these values and the discussions above, printing paths of several plant leaf-mimetic structures are designed and listed in Table 4-1. The experiments were carried out with three angles 45°, 65°, and 90° between the main vein and the lateral veins. For each angle, two sets of the lateral veins widths are investigated to compare the shape-shifting behavior between the constant-width and varying-width lateral veins. Accordingly, there are a total of six conditions for one specific thickness. These six conditions were further studied with three levels of veins thicknesses for the analysis of the blade flexibility.

Table 4-1. Designed veins dimensions and the angle between the main and lateral veins for printing.

Veins lengths	Value (mm)	Veins widths	Value (mm)	Veins thicknesses	Value (mm)
$l_{0,leading}$	100	$b_{0,tip}$	5	h_0	0.2, 0.4, 1
$l_{0,trailing}$	100.5	$b_{0,root}$	15		
l_1	29	b_1	6 (in V.W.), 2 (in C.W.) *	h_1	0.2, 0.4, 1
l_2	28	b_2	5 (in V.W.), 2 (in C.W.)	h_2	0.2, 0.4, 1
l_3	27	b_3	4.2 (in V.W.), 2 (in C.W.)	h_3	0.2, 0.4, 1
l_4	26	b_4	3.4 (in V.W.), 2 (in C.W.)	h_4	0.2, 0.4, 1
l_5	25	b_5	2.8 (in V.W.), 2 (in C.W.)	h_5	0.2, 0.4, 1
l_6	24	b_6	2.2 (in V.W.), 2 (in C.W.)	h_6	0.2, 0.4, 1
l_7	23	b_7	1.8 (in V.W.), 2 (in C.W.)	h_7	0.2, 0.4, 1
l_8	22	b_8	1.4 (in V.W.), 2 (in C.W.)	h_8	0.2, 0.4, 1
l_9	21	b_9	1.2 (in V.W.), 2 (in C.W.)	h_9	0.2, 0.4, 1
l_{10}	20	b_{10}	1 (in V.W.), 2 (in C.W.)	h_{10}	0.2, 0.4, 1

Angle	Value (degrees)
γ	45°, 65°, 90°

*V.W. stands for varying-width lateral veins and C.W. stands for constant-width lateral veins.

To demonstrate the capability of the mathematical modeling in the prediction of the blade bending angle (β), one specific case of Table 4-1 shown in Figure 4-12 is analyzed in detail. The geometric specifications of this case are listed in Table 4-2. Based on equation (4-4), the calculated bending angle is 16°. The actual bending angle of the deformed blade is determined based on Figure 4-6 (c), and the measured value is 15 ± 2°, which shows a good agreement with the mathematical modeling result.

Table 4-2. Dimensions of PLA/paper composite in the blade structure demonstrated in Figure 4-12.

Description	Length	Value (mm)	Width	Value (mm)	Thickness	Value (mm)
Main vein	l_0†	100.3± 0.1	b_0†	10 ± 0.1	h_0	1 ± 0.1
Lateral vein 1 (closest one to the root)	l_1	29 ± 0.1	b_1	6 ± 0.1	h_1	1 ± 0.1
Lateral vein 2	l_2	28 ± 0.1	b_2	5 ± 0.1	h_2	1 ± 0.1
Lateral vein 3	l_3	27 ± 0.1	b_3	4.2 ± 0.1	h_3	1 ± 0.1
Lateral vein 4	l_4	26 ± 0.1	b_4	3.4 ± 0.1	h_4	1 ± 0.1
Lateral vein 5	l_5	25 ± 0.1	b_5	2.8 ± 0.1	h_5	1 ± 0.1
Lateral vein 6	l_6	24 ± 0.1	b_6	2.2 ± 0.1	h_6	1 ± 0.1
Lateral vein 7	l_7	23 ± 0.1	b_7	1.8 ± 0.1	h_7	1 ± 0.1
Lateral vein 8	l_8	22 ± 0.1	b_8	1.4 ± 0.1	h_8	1 ± 0.1
Lateral vein 9	l_9	21 ± 0.1	b_9	1.2 ± 0.1	h_9	1 ± 0.1
Lateral vein 10 (closest one to the tip)	l_{10}	20 ± 0.1	b_{10}	1 ± 0.1	h_{10}	1 ± 0.1
Paper membrane	l_m	$= l_i$	b_m	$= b_i$	h_m	0.105± 0.001 *
Angle			Value (degrees)			
γ			45°			

† l_0 was calculated as the average of $l_{0,leading}$ and $l_{0,trailing}$ and b_0 was accounted as the average of $b_{0,tip}$ and $b_{0,root}$.

* Measured by a Mitutoyo micrometer with 0.001 *mm* resolution and ±1 μm accuracy.

Here, we were interested in the final shape and thus we had the simplified (linear) equation. Now, we want to utilize our biexponential equation to analyze the time-dependent (instantaneous) behaviors of the same materials used here (a bilayer of PLA/paper). The purpose is to generate the time-dependent behavior of this bilayer by our own biexponential equation in a step-by-step example and then to see whether the generated behavior is similar to the actual time-dependent behavior of this bilayer in practice or not. For the actual behavior, we use the data from Zhang et al. (2016). They used PLA strips with the size of 60 × 0.8 × 0.12mm (length × width × thickness) (based on which the values of a_1, a_2, I_1, I_2, and h of our formula are identified) and a heat plate with a temperature of 90 ºC.

The physics of this bilayer structure lies in category 2 of our second law (Thermal Expansion/Contraction). Thus, $\tau_{II} = (\rho c_p V)R$ and $H_{II} = \alpha[T_2 - T_1(t=0) + R(\dot{S}_1 - Q_1)]$,

where $\rho = 1240\ \frac{\text{Kg}}{\text{m}^3}$ (density of PLA is well-known), $c_p = 1800\,\frac{\text{J}}{\text{Kg.K}}$ (heat capacity of PLA is well-known). $V = 60\,\text{mm} \times 0.8\,\text{mm} \times 0.12\,\text{mm} = 5.76 \times 10^{-9}\ \text{m}^3$. The thermal resistance of a rectangular slab is $R = L/Ak$, where L is the length of the slab in the direction of heat flow (and thus $L = 0.12 \times 10^{-3}$ m), A is the area of the slab perpendicular to the direction of heat flow (and thus $A = 60 \times 0.8 = 48 \times 10^{-6}\ \text{m}^2$), and k is thermal conductivity ($k = 0.13\,\frac{W}{m \cdot K}$ that is well-known for PLA). Therefore, $\tau_{II} = 0.25$ (s). The quantities $\dot{S}_1$ and Q_1 can be assumed zero in heat transfer, $T_1(t = 0) = 25$ ºC, $T_2 = 90$ ºC, and $\alpha = 41 \times 10^{-6}\ \left(\frac{1}{K}\right)$ (this is the thermal expansion coefficient of the active layer, PLA, which is well-known. The passive layer has $\alpha_m = 0\ \left(\frac{1}{K}\right)$ as mentioned earlier, which is consistent with the fact that the passive layer is not usually responsive under stimuli). Therefore, $H_{II} = 2.67 \times 10^{-3}$ (unitless). $E_2 = 2 \times 10^8\ (Pa)$ (measured in our DMA test as discussed earlier). $E_1 = 5 \times 10^9\ (Pa)$ (this is Young`s modulus of the paper as noted earlier).

To find H_I and τ_I, we need the following discussion. PLA is a typical viscoelastic material. For such a material, there is a famous model in solid mechanics as $E'' = \frac{E\tau\omega}{\tau^2\omega^2+1}$, where $\tau = \frac{\eta}{E}$, η is viscosity, E'' is loss modulus, E (or equivalently written as E') is Young`s (storage) modulus, $\omega = 2\pi f$ and f is the frequency in DMA test. In a typical single-material shape memory polymer, to enable the shape memory effect, the required force is applied externally. However, in a multi-material having active and passive elements, the force is generated internally between the active and passive materials. In this bilayer, we can assume that the passive layer (paper) has the role of a mechanism that applies the required force to the active layer (PLA). Therefore, the above equation that is used for a single-material shape memory polymer, can be used for the PLA in the PLA/paper bilayer in this example. Thus, τ_I in our formula would be equivalent to τ in the above formula. To find τ_I, we can do the shear test by DMA machine to find the shear storage and loss moduli (G', G'') and then viscosity, or we can re-write the above equation as ${\tau_I}^2 - \frac{E}{2\pi f E''}\tau_I + \frac{1}{\omega^2} = 0$ and solve it by knowing the involved parameters. The value of storage modulus has been measured in our DMA test (Figure 4-31) as discussed earlier in the mathematical modeling. The value of loss modulus (E'') has also been measured in DMA test. It is illustrated here in Figure 4-8. To find τ_I from the equation above, we need the ratio of storage and loss modulus. The value

of f from the DMA section is 1 Hz. Therefore, the value of τ_I is obtained. Finally, the value of H_I has already been measured in the literature (Zhang et al., 2015; 2016) for this example. Now, the values of all parameters in our biexponential equation are present (Table 4-3).

The generated behavior is seen in Figure 4-9. This behavior impressively has the same trend of real behavior reported in the literature (Zhang et al., 2016). However, some gaps happen between theory and practice. One immediate reason is that we obtained the result for one strip, while the real behavior is related to multiple strips (the number of strips is not clear in the related study). The coupling effect between several strips is also the next important reason for the difference. By the coupling effect, we mean that the behavior of a PLA/paper strip with width w is not similar to the behavior of n PLA strips each of which having a width of w/n printed on paper with some spacing between PLA strips. Nevertheless, the general trend is nicely generated. If we just change the value of one of τ_I, τ_{II}, H_I, H_{II}, the trend is totally corrupted as seen in Figure 4-10. This implies that this step-by-step analysis of our formula led us to the appropriate values of parameters. Any deviation from these values, cannot lead to the correct behavior (even through the biexponential formula).

It should be noted that, in chapter 2, we presented three laws. Laws are different from theories. Law is the starting point and reveals something that exists. By further analysis, laws can lead to theories. Theories are much more complicated expressions. The step-by-step example analyzed here can show the way for future theories in 4D printing that can be built based on the proposed laws. These laws capture and show the big picture and future theories can delve into more details to find some models for τ_I, τ_{II}, H_I, H_{II} of our biexponential formula.

Table 4-3. Values of parameters of our biexponential formula for a bilayer of PLA/paper composite. Number 1 indicates the passive layer (paper) and number 2 indicates the active layer (PLA).

Parameter	Value (Unit)
E_1	5×10^9 (Pa)
E_2	2×10^8 (Pa)
a_1	0.105 (mm)
a_2	0.12 (mm)
I_1	7.72×10^{-5} (mm^4)
I_2	1.15×10^{-4} (mm^4)
h	0.225 (mm)
H_I	0.0155 (unitless)
H_{II}	2.67×10^{-3} (unitless)
τ_I	0.6 (s)
τ_{II}	0.25 (s)

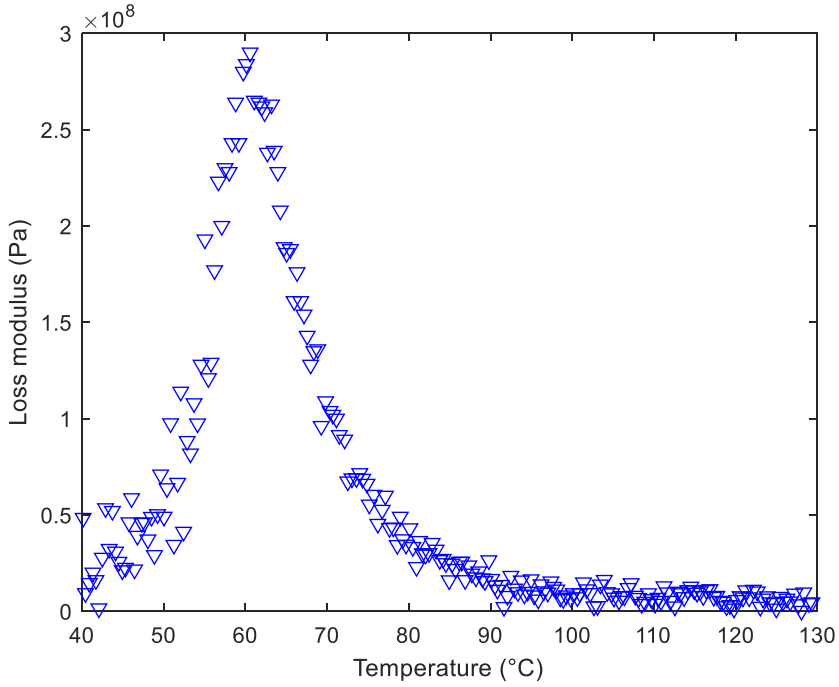

Figure 4-8. The behavior of the loss modulus of the PLA from DMA test (with the same conditions considered for storage modulus in Figure 4-31).

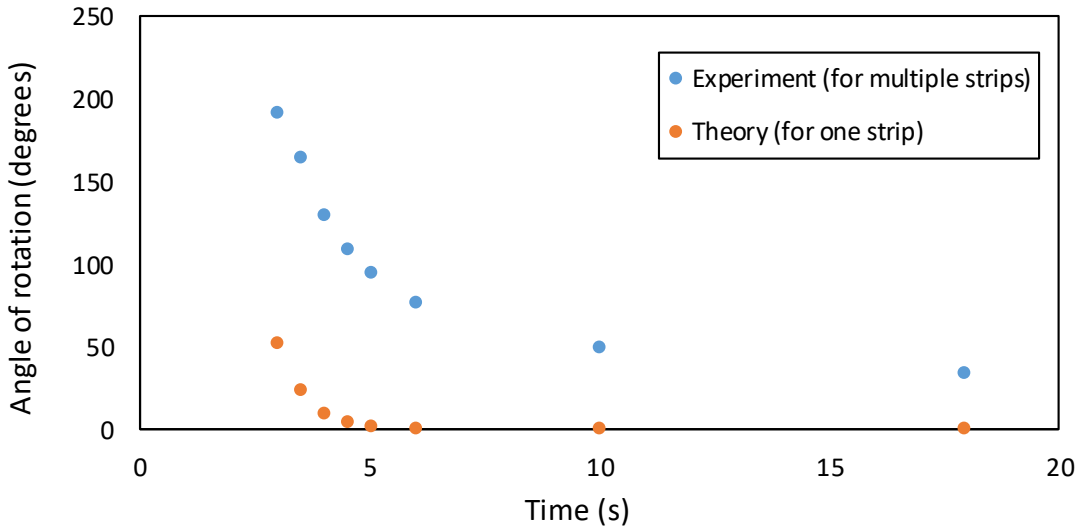

Figure 4-9. The generated behavior of our biexponential formula for one strip and the real behavior for multiple strips from Zhang et al. (2016). The exact number of strips was not given in that experimental study (Zhang et al., 2016).

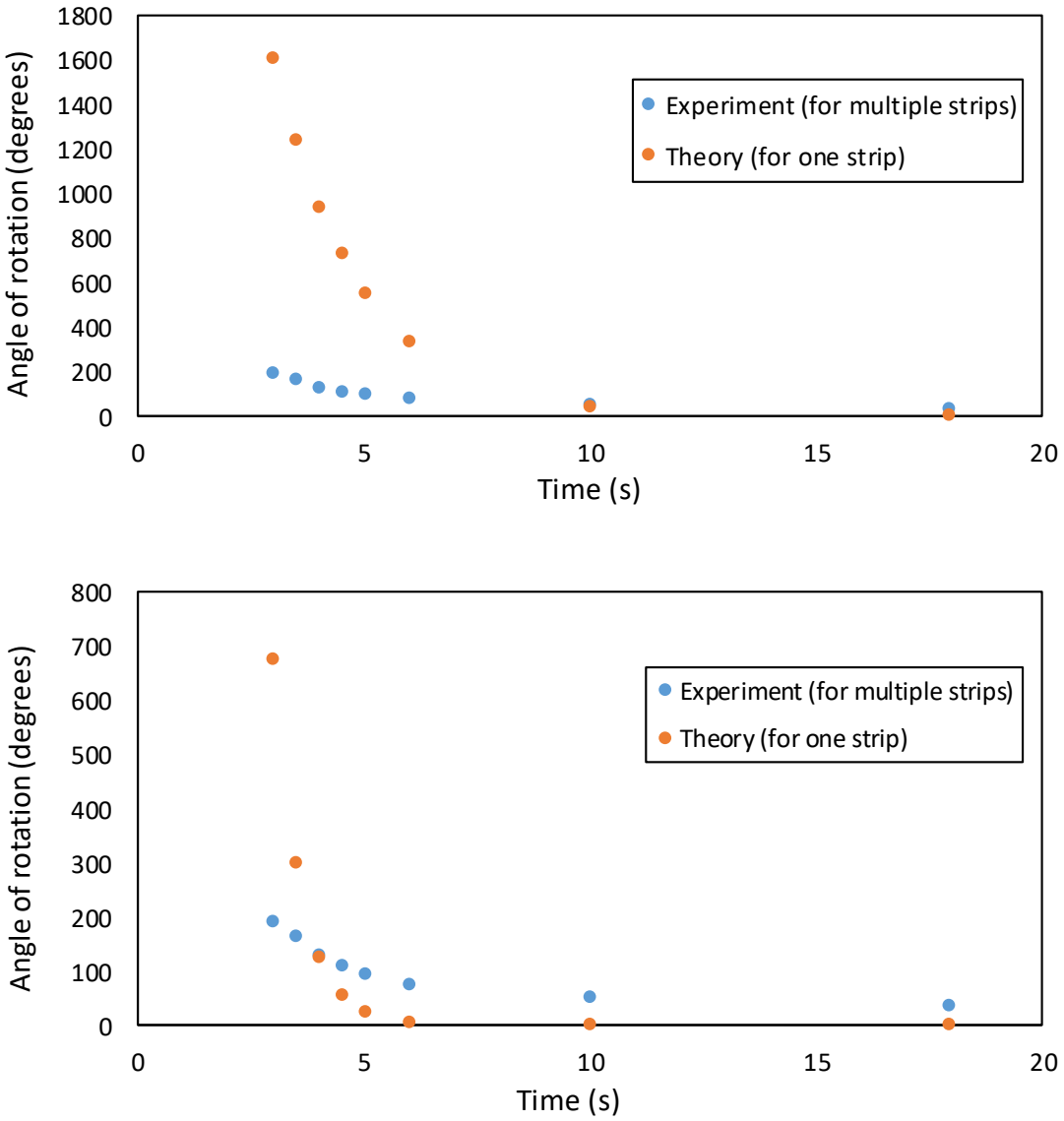

Figure 4-10. Any deviation from the generated parameters in the step-by-step example, cannot give the correct behavior. The experimental data are from Zhang et al. (2016).

4.3 Fabrications and shape-shifting demonstrations

The wind turbine blade structures in Table 4-1 are fabricated by printing PLA filaments onto a piece of paper, which resembles the structure of plant leaves. The CAD models were transformed from STL format to G-code by Cura software and imported to the printer (LulzBot, TAZ 5). The printer was run under the following condition: printing resolution was set to 100 microns; nozzle temperature was adjusted to 205 ℃; bed temperature was considered as 60 ℃, and printing speed was tuned to 50 mm/s (Figure 4-11). PLA is a shape memory polymer having a T_g (glass transition

temperature) of 60 ºC. After printing process, each structure was heated to 110 ºC and maintained at that temperature for 10 min to reach the equilibrium. It was then cooled down to the room temperature in the atmospheric condition, and the desired bend-twist coupling shape-shifting was achieved.

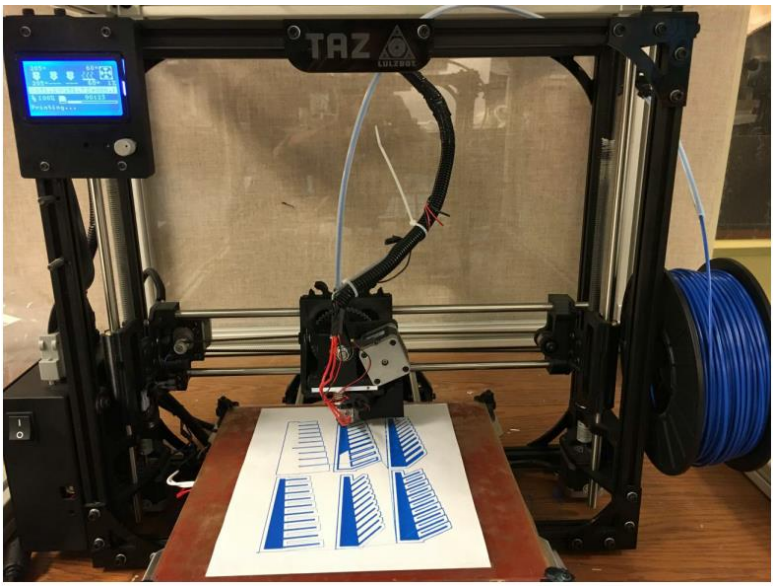

Figure 4-11. Printer TAZ 5 test setup for printing the plant-leaf mimetic architectures.

4.3.1 Results and discussions

Here, we have six items. In the first four items, we analyze the technical advantages of the proposed wind blade. In item 5, we discuss eco-friendly attributes of the proposed blade. In item 6, we discuss the unique advantages of the proposed blade compared to other blades capable of BTC through passive methods.

4.3.1.1 Plant leaf-mimetic structure

As shown in Figure 4-11, the proposed structure mimics the pattern of the plant leaf. The plant leaf-mimetic structure proposed in the literature remained mainly at the level of simulations including geometry optimization. Its fabrication was challenging.

This is because, first, the vein network has a complex and subtle geometry and its fabrication can hardly be achieved by the conventional manufacturing processes. In addition to the first-level veins, there are second- and third-level veins (smaller branches) that support structural and mechanical properties and can be explored in the future. Second, more difficulties are raised in traditional manufacturing processes with the fabrication of complex geometries by using smart

materials such as shape memory polymers (Choong et al., 2017). This is resolved in this study by 4D printing process that is the convergence of additive manufacturing and smart materials (as well as mathematics). This study demonstrates the plant leaf-mimetic wind blade structure *in practice*. In addition, it has simultaneously other advantageous attributes. This feature of the proposed blade is in favor of structure durability as discussed in the introduction.

4.3.1.2 Reversible bend-twist coupling shape-shifting

The architecture with an angle of 45° between the main and lateral veins had more twisting in the tip than in the root, which was desirable. The angle of 90° had more twisting in the root than the tip for both constant-width and varying-width cases, which was unsuitable. The angle of 65° had similar twisting from tip to root for both constant-width and varying-width cases, which was also unsuitable. Based on simulations, Liu et al. (2010; 2011) showed that the best fatigue life happened in blades having angles of 45°-65° between their main and lateral veins. This is not only coincident with the related angle of most natural plant leaves seen in the environment, but also increasing the blade fatigue life remarkably (Liu et al., 2010; 2011).

Additionally, the blade structure with varying width that mimics more accurately the actual pattern of plant leaf shows a better and more uniform twisting overall. The bend-twist coupling shape-shifting behavior was reversible by re-heating. This feature of the proposed blade is in favor of aero-elasticity (load reduction and energy gain) as discussed in the introduction. Figure 4-12 shows the structure for the desired bend-twist coupling shape-shifting, which has the angle of 45°, 1 mm thickness, and varying-width lateral veins.

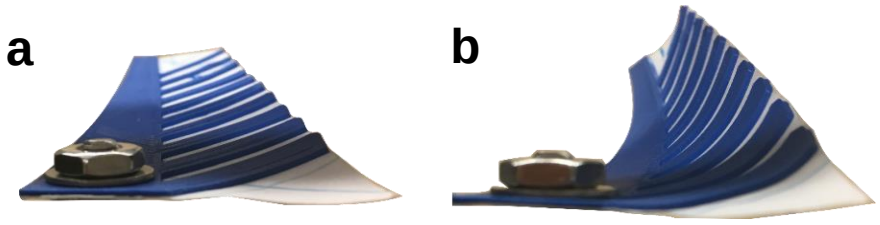

Figure 4-12. (a) Originally printed flat blade without heat treatment (b) Bend-twist coupling after heat treatment.

4.3.1.3 No need for electromechanical and moving parts

The structures can demonstrate the desired bend-twist coupling shape-shifting only by providing the stimulus (heat), which removes the requirement of moving parts and traditional electromechanical systems such as external sensors and actuators that are required in the active

control. The necessity of the conventional sensor is eliminated by employing the smart (active) material during the printing. The need for the conventional actuator is removed by printing the active and passive materials in a special spatial arrangement based on mathematical modeling to guide the mismatch-driven forces into the desired directions to provide the BTC shape-shifting. This feature of the proposed blade is in favor of control simplicity.

4.3.1.4 Decoupled flexibility and adaptability

It should be emphasized that the flexibility is different from adaptability. An adaptive blade can change its shape from shape one to shape two. However, shapes one and two can be either rigid or flexible. In the literature, the bend-twist coupling (BTC) shape-shifting in wind turbines is achieved either by using controllers (active method) or by utilizing the anisotropic mechanical properties of a composite structure (passive method). The passive method is currently the focus of the studies owing to its advantages (Lobitz et al., 1996; Veers et al., 1998; De Goeij et al., 1999; Lobitz et al., 2001; Griffin, 2002; Veers & Lobitz, 2003; Bottasso et al., 2013; Nicholls-Lee et al., 2013; Fedorov & Berggreen, 2014; Hayat & Ha, 2015; Zhou et al., 2015; Hayat et al., 2016; Stäblein et al., 2017). However, the BTC through the existing passive methods has one big issue that is flutter instability. This issue occurs because the blade needs to be flexible to demonstrate the BTC under wind loads through the current passive methods. A more flexible blade has a higher risk for flutter instability (Hayat et al., 2016; Bir & Jonkman, 2007; Politakis et al., 2008; Cognet et al., 2017). We demonstrated a blade that could show the BTC without the need of flexibility such that both the initial and deformed shapes could be as much rigid as needed. It would become soft and flexible only during the shape-shifting process, when it is above the glass transition temperature. It can be rigid during the usual operation. Its rigidity can be adjusted to any degree that is desired depending on a specific application by changing the thickness of the smart material. This feature of the proposed blade may solve the flutter instability and can be explored in a separate study, quantitatively.

It should be noted that during the shape-shifting, the structure is not too flexible to cause a failure under the external loads. In addition, the flexibility of PLA can be tuned depending on a specific need by incorporating some additives into PLA or by suitable synthesis processes on pure PLA (Mittal et al., 2015; Wang et al., 2018). However, the effect of external loads on the shape-shifting angles in a specific application should be considered and incorporated in the mathematical equations to have accurate predictions of shape-shifting behaviors.

In the proposed blade design, a thickness of 1 mm for the veins showed an adaptive blade, in which both the flat and deformed shapes were rigid under the wind loads in the wind tunnel. However, the blade with a thickness of 0.2 mm (and 0.4 mm) displayed adaptive blade with flexible flat and deformed states.

The technical advantages of the developed wind blade in this study are summarized in Figure 4-13.

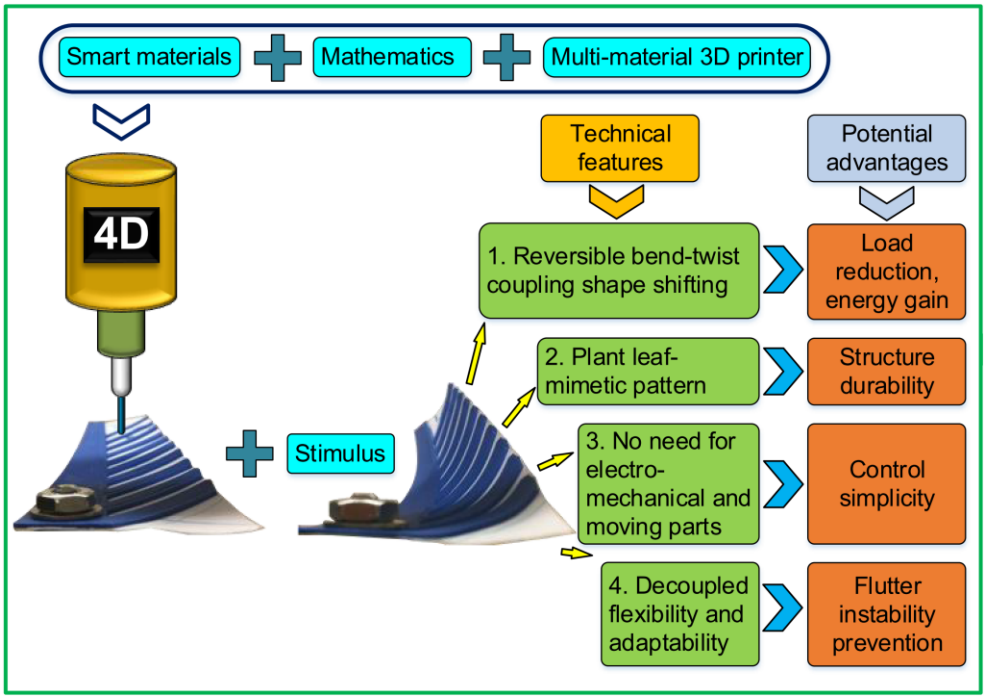

Figure 4-13. The technical advantages of the proposed wind turbine blade.

4.3.1.5 Eco-friendly attributes

To pave the ways for the future sustainable world, several advancements such as novel eco-friendly wind turbines are needed in the near future (Figure 4-14). The eco-friendly attributes of the proposed blade are:

1. **Biodegradable materials:** The smart material employed in the proposed blade is PLA, which is biodegradable that can lead to eco-friendly wind turbines. PLA is a bio-based polymer generated from natural resources such as corn and is one of the cheapest biodegradable polymers to supersede petroleum-based plastics (Dong et al., 2014; Mallegni et al., 2018). It is currently utilized in rigid bottles for beverage, yogurt and so on (Mallegni et al., 2018) and has potential applications in many other industries such as

automotive (Dong et al., 2014). PLA is usually degraded by hydrolysis (Garlotta, 2001). Recent industrial technologies could produce PLA with high molecular weights suitable for structural applications with enough lifetime and no rapid hydrolysis (Avella et al., 2009). An experiment showed that, in air, PLA begins to degrade at 300 ℃ (Sombatdee et al., 2018). Nevertheless, depending on biodegradability needs in a specific application, the biodegradability of PLA can be tuned through several ways such as coating with beeswax to decrease water vapor permeability and biodegradability (Reis et al., 2018) or cold plasma treatment to increase the biodegradability (Song et al., 2016).

2. **Low mass:** The low mass of the proposed blade is the next benefit. Blade mass minimization is one of the four main objective functions engaged to optimize wind turbine performance (Chehouri et al., 2015)
3. **Low carbon emission:** Ji & Chen (2016) analyzed the overall carbon footprint in the full life cycle of a representative wind farm by considering construction, operation, and dismantling phases. They showed that the most carbon emission was related to the construction phase and in this phase, "smelting and pressing of metals" has the highest share of carbon emissions. The proposed blade is not involved in such concern.

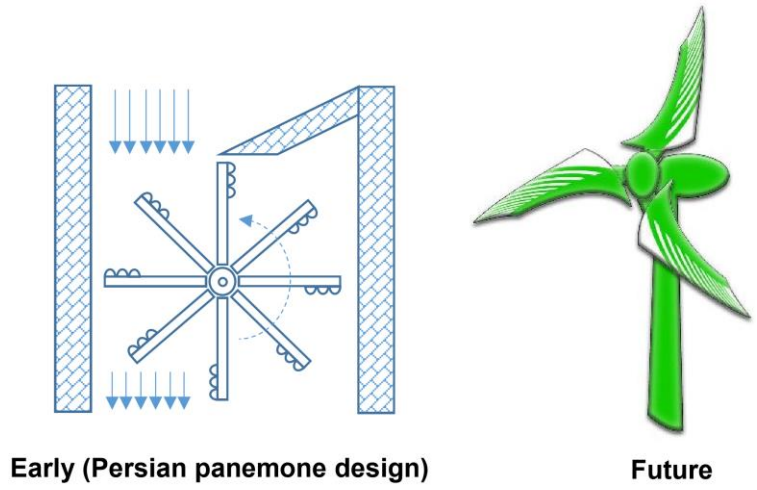

Figure 4-14. From purely rigid ancient wind turbines (such as Persian panemone (Dodge, 2006)) toward the future plant leaf-mimetic, smart, and eco-friendly wind turbines.

4.3.1.6 Comparison between the proposed blade and other blades capable of bend-twist coupling through passive manners

The overall advantages of the proposed blade were discussed in the previous sections. Now, the unique advantages of this blade compared with the existing blades capable of BTC through the passive manners can be summarized as three main benefits. These are the plant leaf-mimetic structure that improves the mechanical and structural properties, decoupled flexibility and adaptability that may solve the flutter issue, and the eco-friendly features that may pave the way for the future sustainable world. Additionally, the optimization of the proposed paradigm can be studied in future investigation to explore the energy and power gains improvement.

4.4 Wind tunnel tests

Based on the above results, the blade structure with the angle of 45° between the main and lateral veins, 1 mm thickness and varying-width lateral veins is selected for the following wind tunnel test. Aerodynamics and performance of the originally printed flat blade and the final deformed blade that has been exposed to the thermal stimulus, as shown in Figure 4-12(a) and (b), are compared.

In this experiment, a wind tunnel was assembled by a fan (Model No. #122 "FC" HD Arr 9H, IAP Inc.), a direct current permanent magnet motor (Model C4D17FK10, LEESON Electric Corporation), a manometer (Model No. 400-, Dwyer Instrument Inc.), and subminiature load cells (Model 11 with tension/compression, Honeywell). The wind tunnel setup was connected to a PC with LabVIEW software (version 2014, National Instruments) through an NI-cDAQ chassis. The ambient temperature and pressure were 21.4 ± 0.1°C and 99.63 ± 0.05 kPa measured by a Wireless Weather Forecaster (model TE688W, Meade Instruments) with temperature resolution of 0.1°C, pressure resolution of 0.01 kPa, negligible temperature accuracy error, and pressure accuracy error of 0.05 kPa.

The ambient temperature and pressure are for determining the density and viscosity of air. Viscosity is used in Reynolds number calculations. Density is for calculating Reynolds number as well as wind speed based on the Bernoulli equation. The drag and lift are measured by the subminiature load cells that have ± 0.5% accuracy. The precision error of the lift and drag forces is obtained from the LabVIEW program by considering a 95%-confidence-interval. The wind speeds are calculated by using the pressure data from the manometer and the Bernoulli equation. The manometer has 1 Pa resolution error, ± 2% accuracy error and the precision error obtained by

repeated measurements. These three types of errors (resolution, accuracy and precision errors) are combined to determine the uncertainties and error bars. Figure 4-15 shows the wind tunnel test setup.

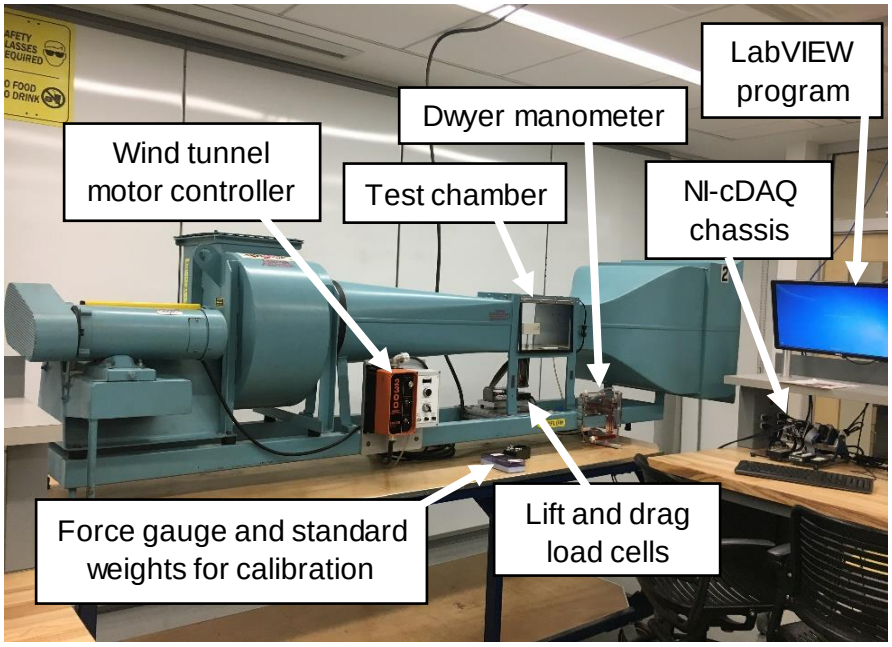

Figure 4-15. Wind tunnel test setup.

4.4.1 Results and discussions

4.4.1.1 Calibration curves

The output of subminiature load cells of the wind tunnel is in mV/V. The wind tunnel load cells need to be calibrated to find the conversion factor between the load cell output (in mV/V) and the desirable drag and lift forces in Newton (*N*). To this end, we used several calibration masses (10 g, 20 g, 50 g, 100 g, and 150 g) and one Correx tension gauge (model 1001681, 500 g CNP KM) with an accuracy of ±0.01 × (maximum dial reading + actual test reading) and the resolution error of 0.05 *N*. For a stationary object in the wind tunnel, the drag force is in the same direction as the wind, while the lift force can be either upward or downward depending on the shape of the object. Therefore, we consider only one horizontal direction for the drag force calibration by using the Correx force gauge. However, we consider both the vertical directions for the lift force by using the calibration masses for the downward force and Correx force gauge for the upward force. The force gauge can be used to calibrate the downward lift as well, but the calibration masses are used for this direction, as they are more accurate compared to the force

gauge. The sample for the calibration is a rectangular cuboid Balsa wood with the dimensions (51 ± 1 mm) × (51 ± 1 mm) × (102 ± 1 mm). The calibration curves are presented in Figure 4-16. The horizontal and vertical error bars have been calculated by combining all the three types of errors including resolution error (e_r), precision error (e_p), and accuracy error (e_a) based on the following equation:

$$Uncertainty = \pm\sqrt{e_r^2 + e_p^2 + e_a^2} \tag{4-5}$$

A best-fit line was plotted for both the calibration curves and the slope of these curves was the conversion factors. These conversion factors can be used for the test on the blades, in which the raw data in mV/V are multiplied by these factors to yield the lift and drag forces in *N*. The uncertainty in each of these conversion factors is twice the error in slope with 95%-confidence-interval uncertainty. The error in slope can be obtained by the following formula (Heald, 1992) for a line ($y = ax + b$) that is fitted to data,

$$error\ of\ slope = \sigma_a = a\sqrt{\frac{\frac{1}{R^2} - 1}{N - 2}} \tag{4-6}$$

Where a is the slope, R^2 is the correlation factor and N is the number of data points. The conversion factors are obtained as 0.256 ± 0.017 for the drag force and 0.254 ± 0.004 for the lift force. The vertical error bars for the downward lift (negative lift) are smaller than the upward lift (positive lift). This is consistent with the assumption that the standard masses used for the downward lift calibration have less uncertainty than the Correx force gauge.

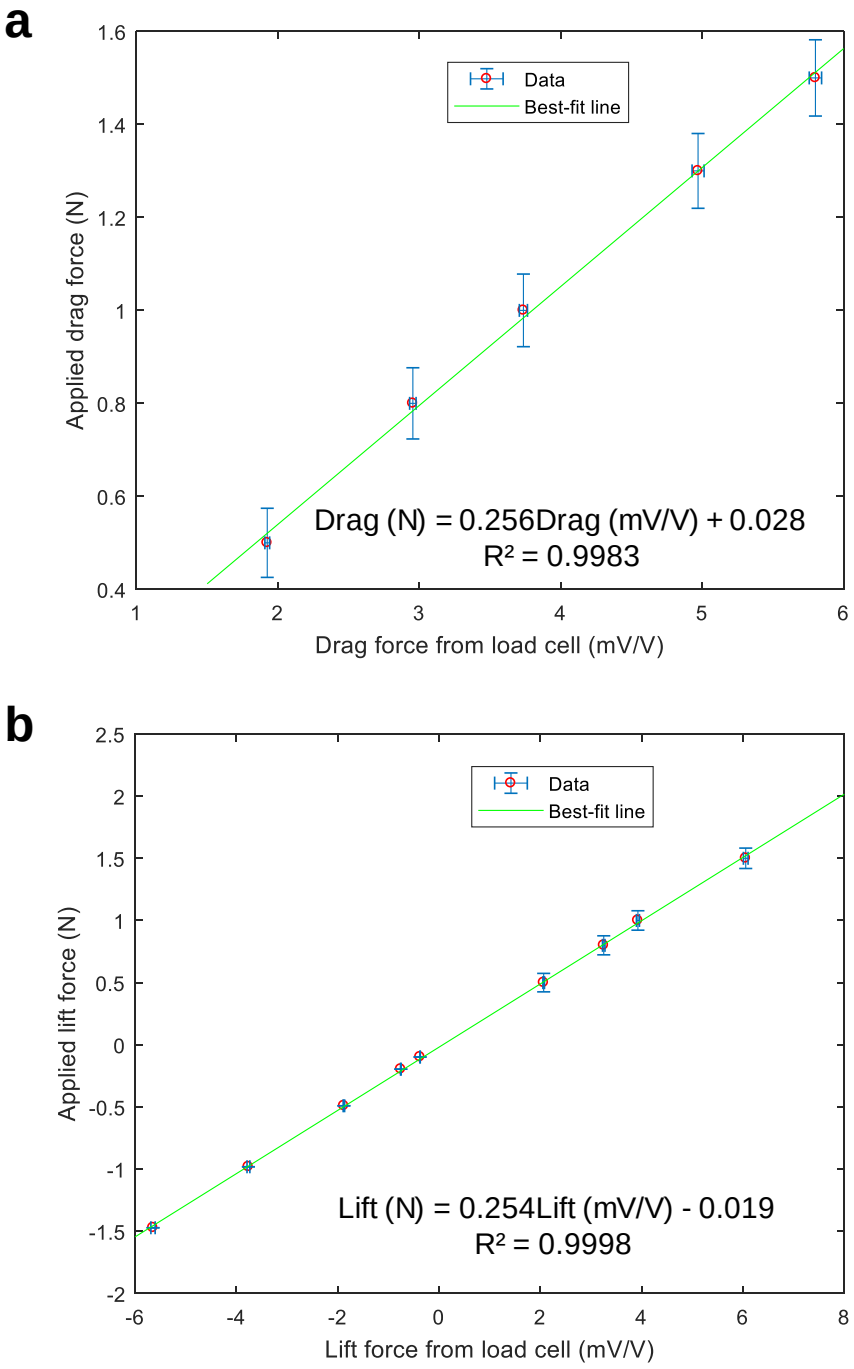

Figure 4-16. (a) Drag load cell calibration, only for one horizontal direction. (b) Lift load cell calibration, for both upward and downward vertical directions.

4.4.1.2 Aerodynamics of the flat blade versus deformed blade

The two flat and deformed blades (Figure 4-12) are tested in the wind tunnel chamber (Figure 4-17). The lift and drag forces at various speeds are measured based on the conversion coefficients

from the previous calibrations, and the results are shown in Figure 4-18. The speed values were gained by using the Bernoulli equation and the pressure data from manometer. To convert the pressure data from manometer to wind speed, the following simplified equation (Dwyer Instruments Inc., 2010) derived from Bernoulli equation was used:

$$V = 1096.7\sqrt{\frac{P_V}{\rho}} \tag{4-7}$$

Where, P_V is the pressure measured by manometer in inch-of-water, ρ is the air density in lb/ft^3 and V is the wind speed in ft/min.

The resolution, accuracy and precision errors in forces gained from the load cells construct the vertical error bars, while these three errors in wind speeds obtained from the manometer data underpin the horizontal error bars in Figure 4-18. The sample is mounted to a sting installed inside of the test chamber. The other end of the sting is attached to the load cells for force measurements as shown in Figure 4-17. The lift and drag forces from the sting are measured as well, which is then subtracted for determining the lift and drag forces due to the samples only. It should be noted that for the vertical direction, along which the blades were mounted to the sting shown in Figure 4-17 (a), (b) and (c), the lift is in the downward direction (negative), and the results in Figure 4-18 illustrate the absolute values of the lift forces. If we install the blades upside down, the lift would be upward.

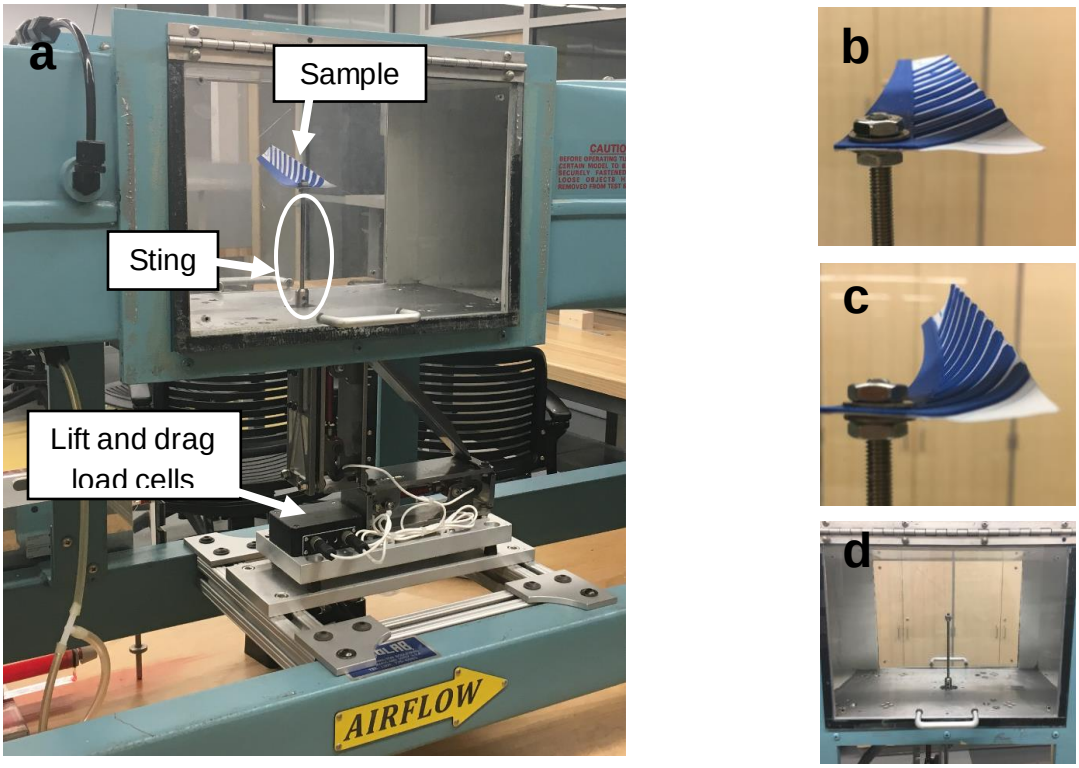

Figure 4-17. (a) Wind tunnel test on the samples installed on the sting, (b) flat sample attached to the sting, (c) deformed sample connected to the sting and (d) wind tunnel test on the pure sting.

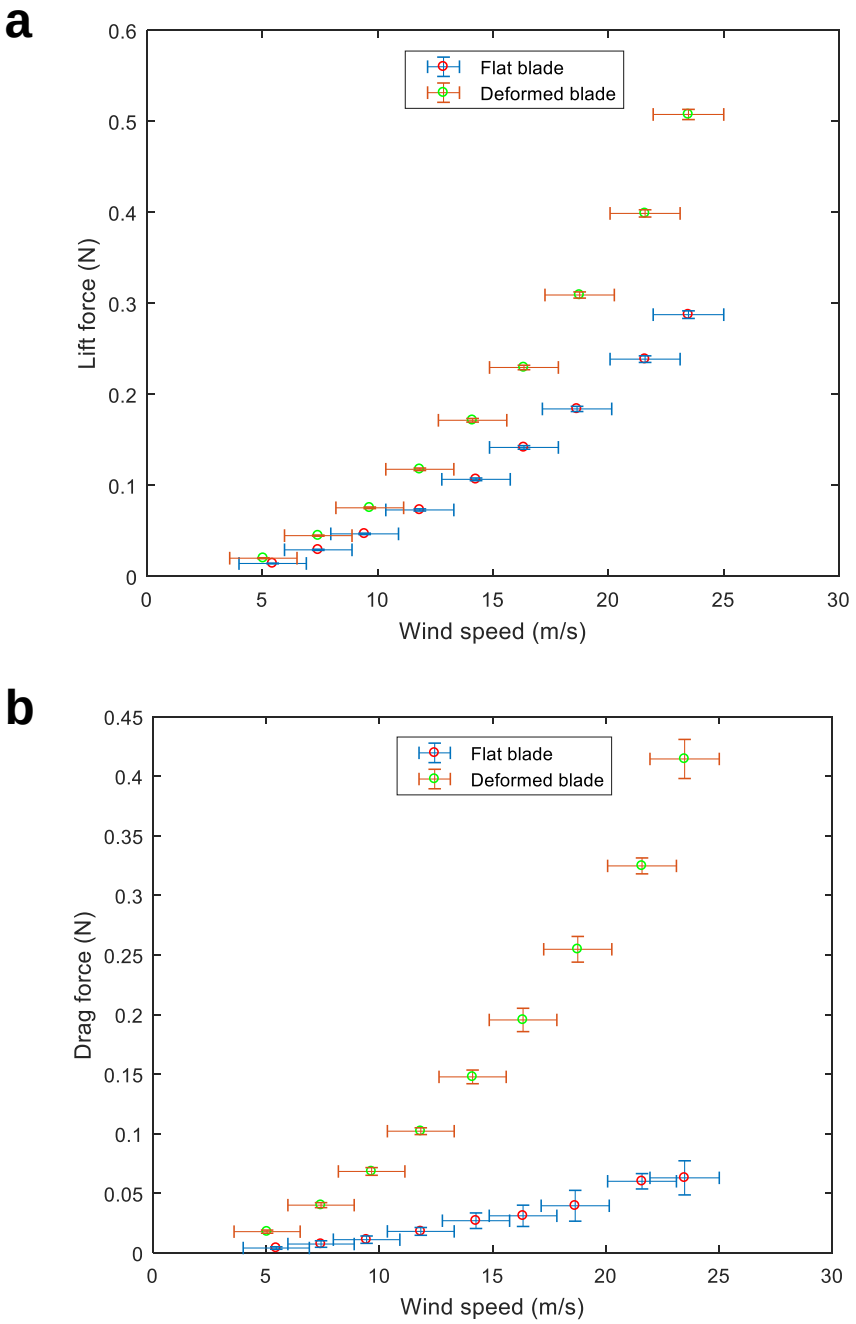

Figure 4-18. (a) Comparison of the lift force for the flat and deformed blades. (b) Comparison of the drag force for the flat and deformed blades.

For further comparisons, dimensionless quantities including the drag coefficient (C_D), the lift coefficient (C_L) and Reynolds number (Re) are calculated based on the following equations (Kuethe & Chow, 1976). These three quantities can also be used to scale up the results.

$$C_D = \frac{F_D}{\frac{1}{2}\rho V^2 A} \tag{4-8}$$

$$C_L = \frac{F_L}{\frac{1}{2}\rho V^2 A} \tag{4-9}$$

$$Re = \frac{\rho V L}{\mu} \tag{4-10}$$

Where F_D, F_L, ρ, V, μ, L and A are the drag force, lift force, air density, air speed, air dynamic viscosity, characteristic length and the reference area of the sample, respectively. The drag coefficients are calculated based on the frontal area of the samples and the lift coefficients are calculated based on the top area of the samples. The top and frontal areas of the deformed blade are calculated based on a CAD reconstruction of the experimentally obtained blade, which is explained in more details in the next section. Corresponding parameters for calculations of C_D and C_L are listed in Table 4-4 and the results are shown in Figure 4-19 (a) and (b). The error bars in Figure 4-19 are calculated based on the sequential perturbation method by using equations (4-8), (4-9), and (4-10) and the measurements of the lift force, drag force, and wind speed (Figure 4-18).

Table 4-4. Values of parameters for calculating C_D, C_L and Re.

Parameter (Symbol)	Value (Unit)
Temperature (T)	21.4 ± 0.1 (°C)
Pressure (P)	$99628 \pm 50 (Pa)$
Dynamic Viscosity (μ)	$1.84\text{E}-5 \pm 0.00E-5 \left(\frac{kg}{m.s}\right)$
Density (ρ)	$1.17 \pm 0.00 \left(\frac{kg}{m^3}\right)$
Characteristic length (L)	$0.1 \pm 0.0\ (m)$
Deflected Frontal Area ($A_{F,Def.}$)	$0.0013 \pm 0.0002\ (m^2)$
Deflected Top Area ($A_{T,Def.}$)	$0.0024 \pm 0.0002\ (m^2)$
Flat Frontal Area ($A_{F,Flat}$)	$0.00010 \pm 0.00004\ (m^2)$
Flat Top Area ($A_{T,Flat}$)	$0.0029 \pm 0.0002\ (m^2)$

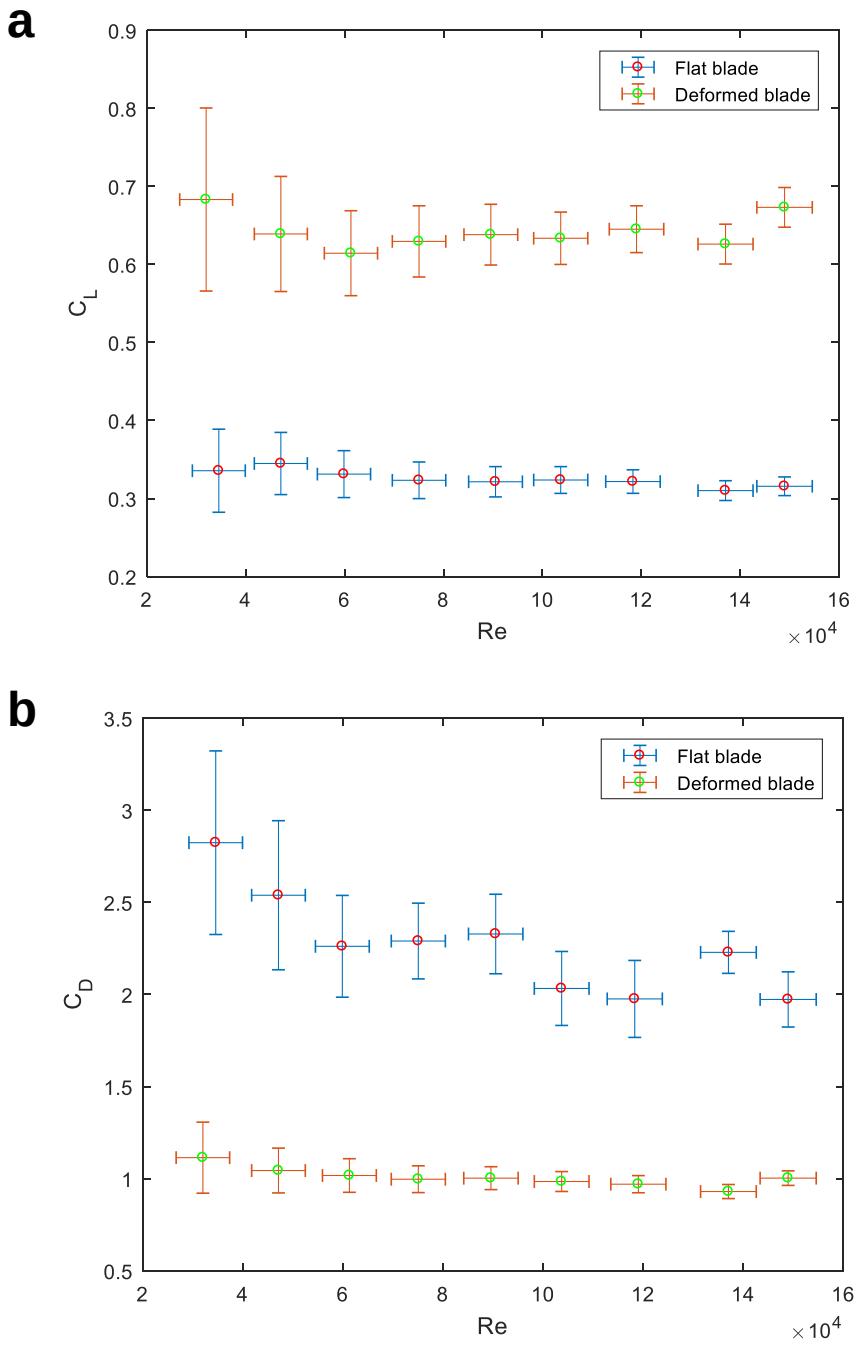

Figure 4-19. (a) Comparison of the lift coefficient for the flat and deformed blades. (b) Comparison of the drag coefficient for the flat and deformed blades.

The C_D and C_L show that the deformed blade has a higher non-dimensional lift force and lower non-dimensional drag force compared with the flat blade, which demonstrate the better aerodynamics in the bend-twist coupled blade. It should be noted that based on the physics of the problem, the pressure drag is of much greater magnitude and importance than the other types of

drag. Hence, in order to normalize the drag force, one can use the blade frontal area, from which the dominant term of drag (pressure drag) originates (NASA Glen research center page, accessed 2018; Hedenstrom & Liechti, 2001). Due to larger frontal area of the deformed blade in comparison to the flat blade, its drag coefficient is smaller than that of the flat one, although the numerator of the drag coefficient (that is drag force) may increase itself. Hence, although Figure 4-18 (b) shows that the deformed blade has a higher drag force, but its drag coefficient is lower as can be seen in Figure 4-19 (b).

4.4.1.3 Blockage ratio

Blockage ratio is the ratio of the cross-section of the sample that is normal to the flow direction divided by the cross-section of the wind tunnel test section (test chamber) normal to the flow direction. In this experiment, the test chamber cross-sectional area normal to the airflow was 203 ± 1mm by 203 ± 1mm. Consequently, the blockage ratio for the deformed blade, flat blade, and the calibration rectangular cuboid sample are 3.2 ± 0.5 %, 0.2 ± 0.1 % and 6.3 ± 0.2 %, respectively. According to the literature (Howell et al., 2010), the blockage ratio should be less than about 7% to ensure that the flows around the samples are unaffected by the walls.

4.5 CFD simulations and performance analysis

In this section, CFD analyses are performed to study additional characteristics of the 4D-printed blade that could not be investigated in wind tunnel tests. It should be mentioned that the dimensions of the simulated blade are the same as the tested blade in wind tunnel. Advantages of the proposed blade can be further revealed. First, the simulation is validated with available experimental data. Performance study is then carried out for various conditions including different wind speeds, rotational speeds, etc. The wind speed interval of approximately 5 to 24 m/s is rational, which lays between cut-in and cut-off speeds for small-scale wind turbines due to their intrinsically high rotational speeds (Drumheller et al., 2015; Wan et al., 2015).

In the wind tunnel test as well as performance calculations, the amounts of the top and frontal areas are needed in order to calculate aerodynamic coefficients (especially lift and drag coefficients) (NASA Glen research center page, accessed January 2018; Hedenstrom & Liechti, 2001). These areas can be easily obtained in a CAD software as shown in Figure 4-20. The top and frontal areas of the deformed blade are calculated of about 0.0024 ± 0.0002 (m^2) and 0.0013 ± 0.0002 (m^2), respectively. The uncertainties in the top and frontal areas arise from the reconstruction of the deformed blade in the software based on the measured (x, y, z) coordinates of some specific points

of the deformed blade. The main and lateral veins are not shown in this figure because only the aerodynamic shape of the blade (bend-twist coupled form) due to the deflection of these smart veins is important and the veins themselves have only structural roles.

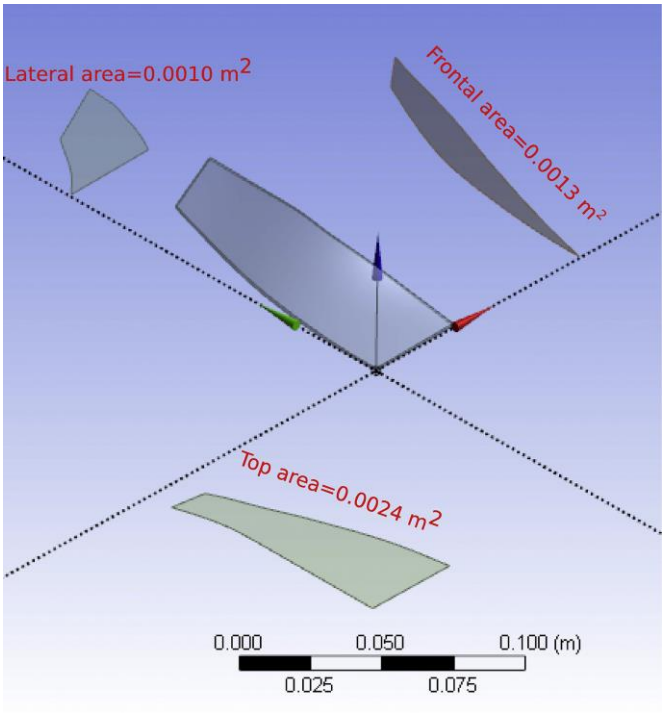

Figure 4-20. The top, frontal and lateral projections of the deflected 4D-printed blade.

As a validation of CFD simulations method, lift and drag forces on the fixed (stationary) deformed blade are compared between wind tunnel data and numerical results at different wind speeds. These comparisons are shown in Figure 4-21 and Figure 4-22, respectively, where the horizontal axis is the wind speed, the primary vertical axes are lift or drag forces exerted on the blade, and the secondary vertical axis is the percentage of error of numerical results with respect to corresponding experimental data. The errors are in 5% to 10% from lower wind speeds to higher wind speeds. This implies that the CFD simulations are in good accuracy and valid in order to be implemented for further investigations on the proposed blade.

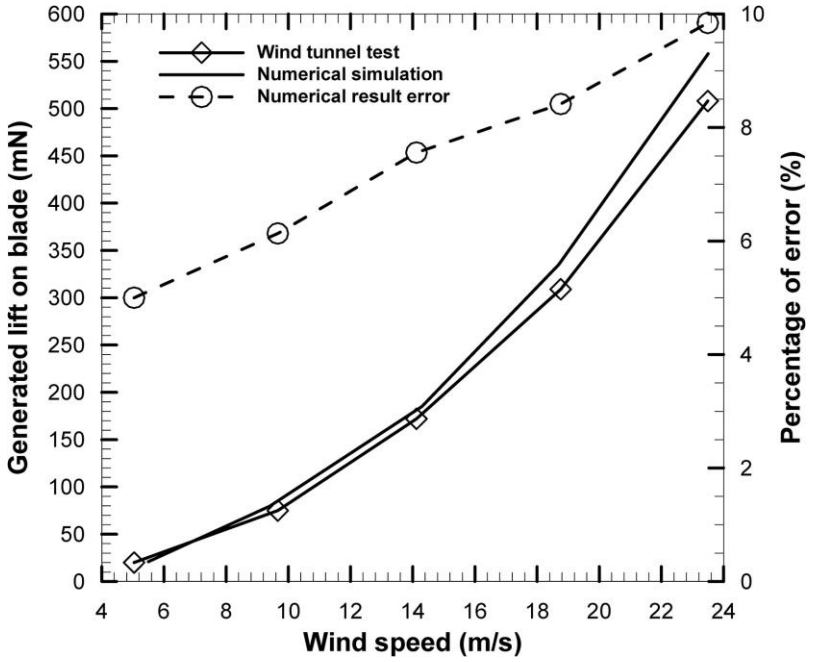

Figure 4-21. Comparison of lift force on a fixed deformed blade as a function of wind speed between results of the wind tunnel tests and CFD simulations.

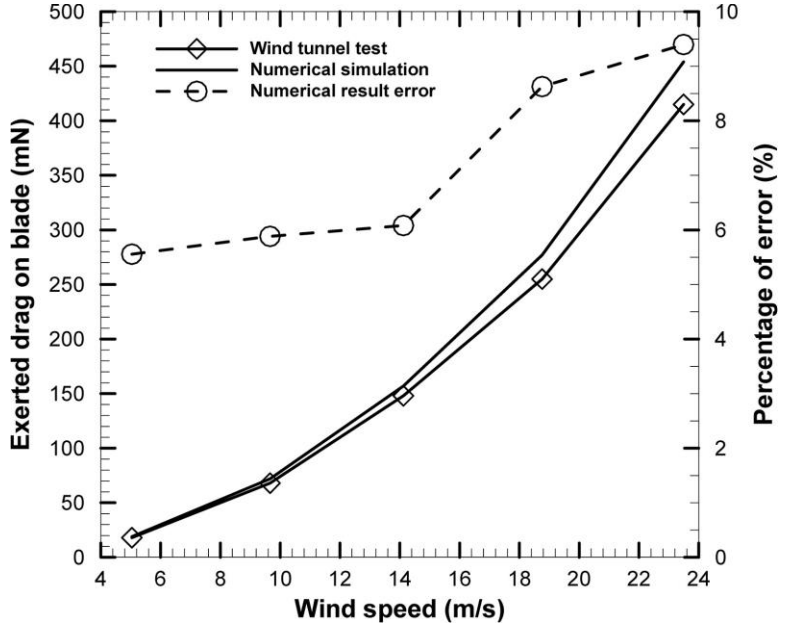

Figure 4-22. Comparison of drag force on a fixed deformed blade as a function of wind speed between results of the wind tunnel tests and CFD simulations.

After validation of the numerical results, the rotational speed of blade in a rotor disk at different wind speeds is determined, which is also helpful for future design criteria. This value is determined by two groups of opponent moments. One is the driving torque from the wind

generated due to lift force on the blade, and the others are the opposite moments, including the friction from bearings and preventer torque from the generator. Here, no study is going to be done on bearing and generator selection and hence, their effects can be neglected to obtain an upper limit for ideal working conditions. The rotational speed of the rotor disk increases until the velocity triangles of different sections of the rotor blade change in such a way that their resultant yields a zero net lift force (driving torque). Therefore, in general, as the wind speed goes up, turbine rotor disk rotational speed increases. This behavior is shown in Figure 4-23 for the proposed 4D-printed blade in a rotor disk. The rotor disk is chosen to have 6 blades and a hub radius of 5 cm. 6-bladed rotor disk will be shown to be optimum from a certain point of view in a few paragraphs later. The value of the rotational speeds in Figure 4-23 can be implemented for the future structural design of the wind turbine (bearings, spars, etc.).

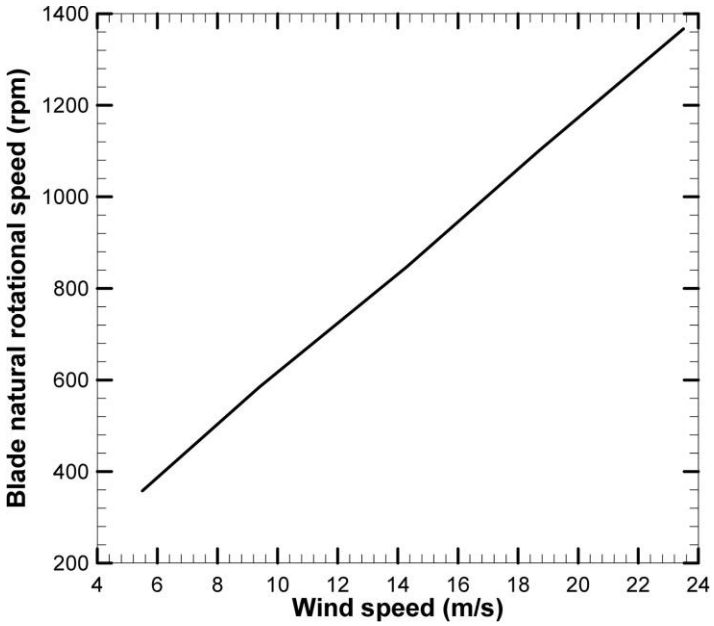

Figure 4-23. The increment of deformed blade RPM as the wind blows in higher speeds.

One crucial performance parameter of a wind turbine blade is its generated torque (due to lift) as a function of wind speed. In order to verify the advantages of the proposed 4D-printed blade (with outer geometry same as the tested blade in wind tunnel), its generated lift force at different wind speeds is provided in Figure 4-24. The result is compared with the flat (non-heated) blade at an angle of attack (AOA) slightly less than the stall value. According to the simulations on the flat blade at different angles of attack, the stall angle is about 12.6° at the Reynolds number of about 23000. Hence, in order to avoid flat blade stall at higher Reynolds numbers (higher wind speeds),

it has been simulated at an AOA of 12.4°. The lift forces in this figure are from conditions wherein both the deflected and flat blades were stationary. The higher values of lift force at various wind speeds in Figure 4-24 show the superiority of the deformed blade over the flat one, albeit the flat blade has an AOA (12.4°) just before its stall AOA (12.6°). Physically, in the pre-stall region, higher AOA of the blade will lead to higher lift generation. Through wind tunnel tests, we have already observed that the deformed blade has more lift generation than the flat blade when both have the same angles of attack equal zero at the root. Here, we captured an interesting point that the deformed blade with zero AOA at the root even has more lift compared with the flat blade almost having its maximum pre-stall AOA at the root.

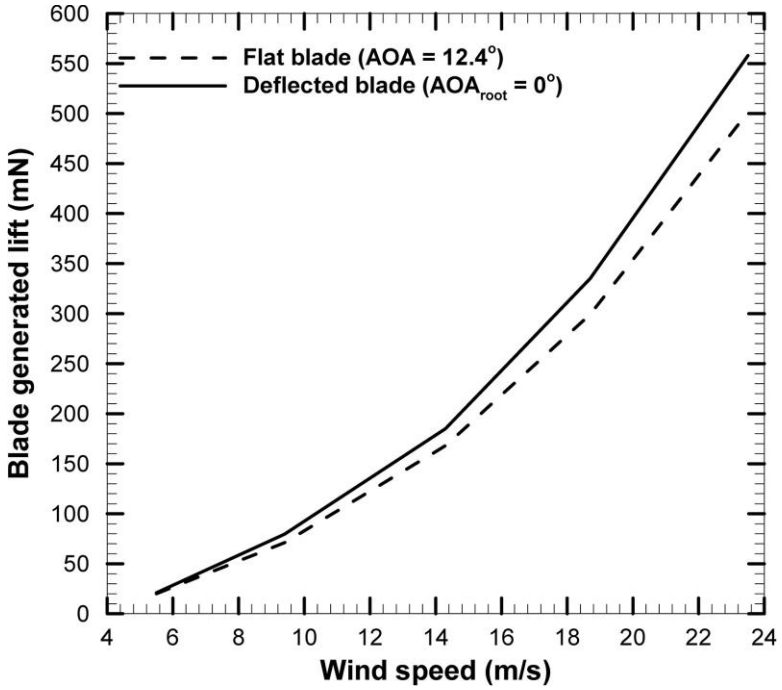

Figure 4-24. Generated lift on deflected shape of the proposed 4D-printed blade and its flat shape at different wind speeds.

In addition, the optimum number of deformed blades in a full rotor disk is determined. In this regard, rotor disks with different numbers of blades (3, 4, 6, 8, 10 and 12) have been simulated for sliced-periodic disks (1/3, 2/4, 2/6, 2/8, 2/10 and 2/12) at a fixed position. As an example, the corresponding sliced-periodic domain with 2 out of 6 blades of a rotor disk is shown in Figure 4-25. The hub radius is 5 cm as specified before. Inlet boundary and the imaginary shaft are also shown in this figure.

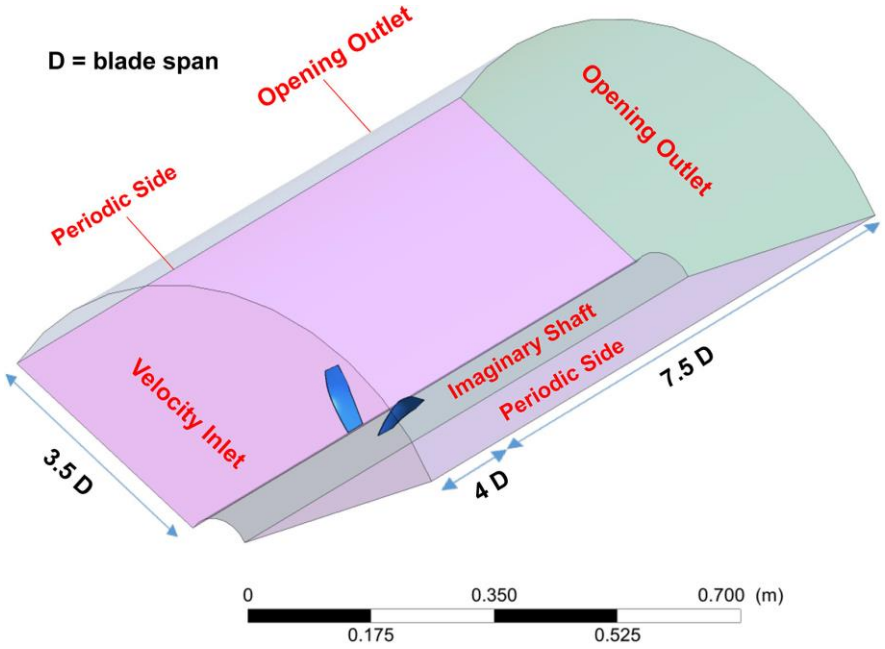

Figure 4-25. The sliced-periodic domain used for simulation of a rotor disk with 6 blades, containing only a couple of those blades.

In the next step, the amount of generated torque is selected as the criterion for performance evaluation. Due to different blockage ratios and interactive effects of adjacent blades, the drag and lift forces and consequently, the generated torque per blade depends on the number of blades in a rotor disk, as shown in Figure 4-26 for a wind speed of 9.4 m/s. The maximum torque per blade occurs at a rotor disk with 6 deformed blades. The values of this curve depend on wind speed. However, the optimum number of blades for generating the maximum torque per blade remains at 6 by varying the value of air stream velocity.

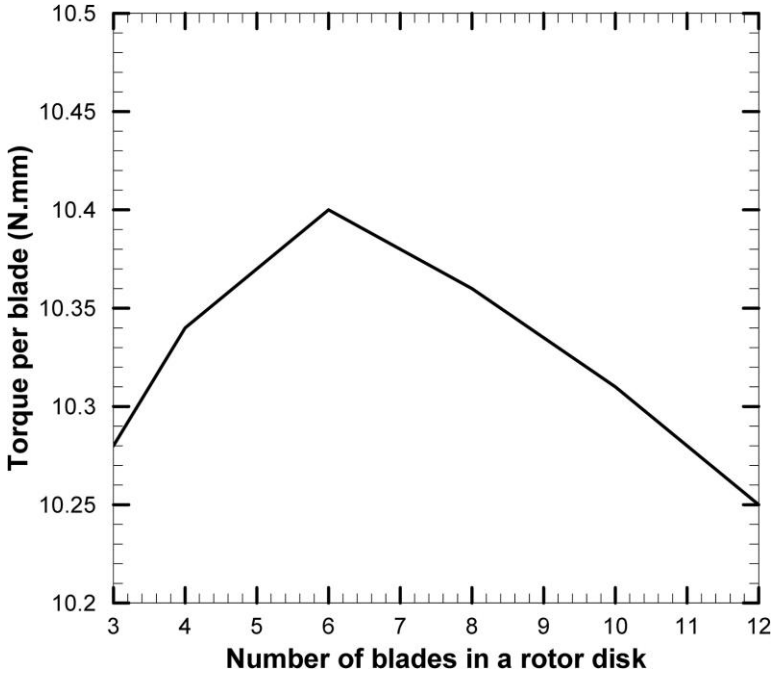

Figure 4-26. Variation of generated torque per blade as a function of the total number of blades in a full rotor disk (at the wind speed of 9.4 m/s).

Some important performance parameters for wind turbine blade are generally studied with certain theories like Blade Element Momentum (BEM). However, the BEM method can only predict these parameters accurately for large-scale turbines (Tummala et al., 2016). Due to these limitations, in this study, numerical simulation is employed. As one of the most important performance parameters, the power coefficient is calculated using equations (4-11), (4-12) and (4-13) and plotted as a function of tip speed ratio (TSR) in Figure 4-27. It should be noted that the trend of variation of the power coefficient with TSR depends on the incidence angle (the angle between the root's chord line and the rotor axis) of the rotor blades (Tummala et al., 2016).

$$TSR = \frac{r_{tip}.\omega}{V_{wind}} \tag{4-11}$$

$$C_p = \frac{T.\omega}{\frac{1}{2}\rho A {V_{wind}}^3} \tag{4-12}$$

$$A = \pi {r_{tip}}^2 \tag{4-13}$$

In the formulas above, r_{tip} is equal to 15 cm considering a hub radius of 5 cm for the blade with 10 cm of span (length) and ω is rotational speed of the rotor disk. T is the generated torque on the blade rotating with the corresponding rotational speed (ω) at wind velocity of V_{wind}. ρ is air density equal to its value during wind tunnel tests (1.17 $\frac{kg}{m^3}$) and A is area of a circle encompassing the rotor disk. For each wind speed, different rotational speeds have been considered for the rotor disk, which yields in different values of TSR. Having the amounts of the generated torque on the blade for all the wind speed-RPM couples from CFD, variation of power coefficient versus TSR is achievable. The ratio of the hub radius to the blade tip radius of the proposed blade may seem too small in comparison to that of the large-scale turbines. However, it should be noted that for small-scale (micro) wind turbines, this ratio becomes smaller and some examples of such small values can be found in some references (Sedaghat et al., 2012; Kishore et al., 2013).

In real operations, by utilizing different generator and bearings, they may have different friction coefficients. The rotor disk would then be subjected to different amounts of opponent moments. Therefore, at a certain wind speed, the rotor can have different rotational speeds and consequently different TSRs depending on the utilized generator and bearings, which then change the value of the power coefficients, accordingly. In this regard, Figure 4-27 compares the relationship between the TSR and the power coefficient at different wind speeds for a rotor disk with 6 deformed blades. It can be observed that the TSR value that maximizes the power coefficient is independent of wind speed. Not only the maxima, but also the entire curve of power factor versus TSR is independent of wind speed (Tummala et al., 2016). Figure 4-27 indicates these independencies very well. Using the proposed 4D-printed blade, the maximum power coefficient occurs at the TSR of about 0.6.

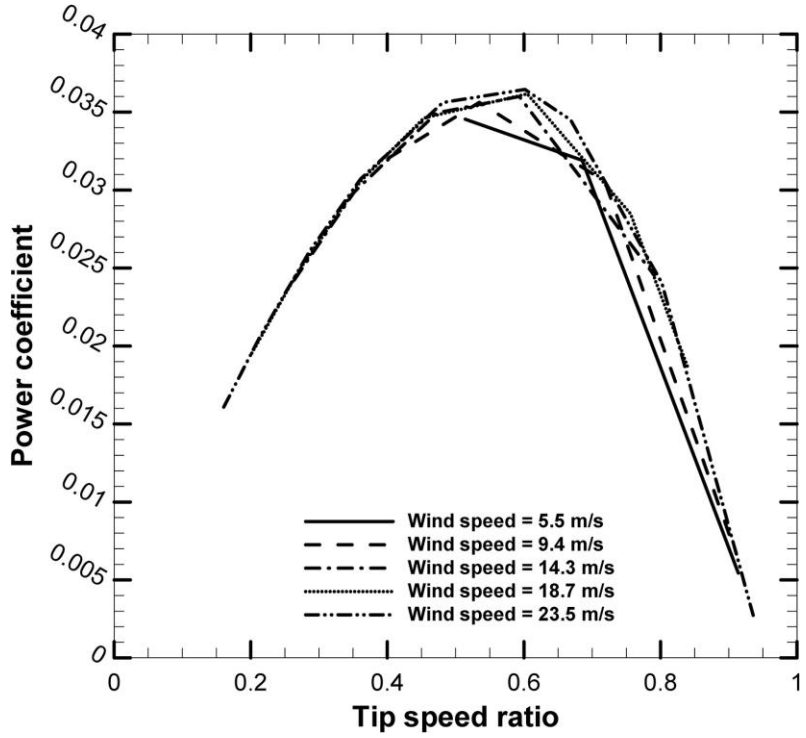

Figure 4-27. Performance curve of the 6-bladed rotor disk power coefficient vs. tip speed ratio in five different wind speeds.

In addition to the above outcomes in CFD part, some qualitative analyses on numerical results are provided. Figure 4-28 shows velocity contour lines at four different sections of the deformed blade when it is rotating with an induced rotational speed of about 580 rpm due to the wind speed of 9.4 m/s. Except a tiny partial flow separation occurs at the root of the blade, the flow is fully attached to the blade surface especially near the tip (no tip stall is observed), which has a more important effect on the aerodynamic performances compared with the root (Wetzel, 2005).

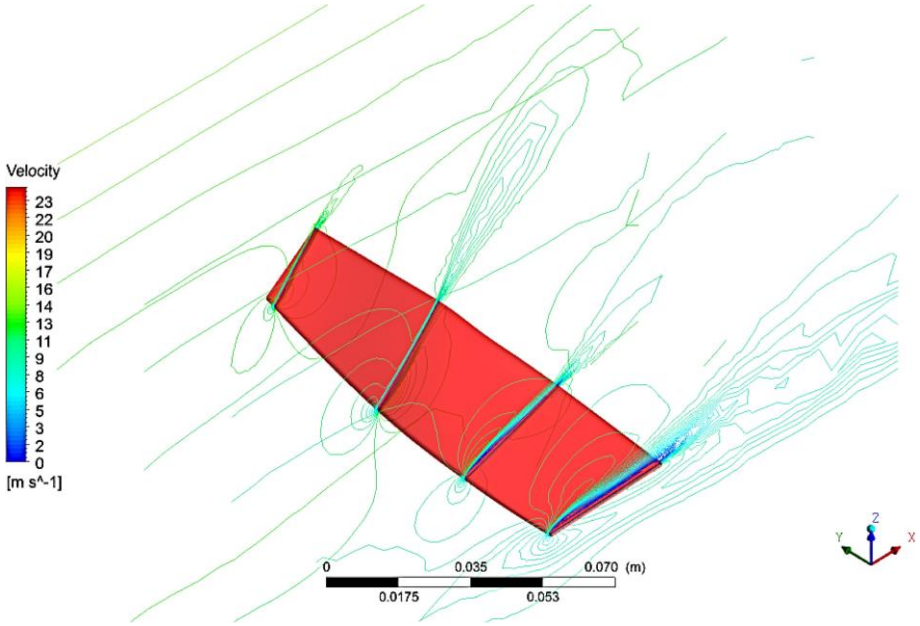

Figure 4-28. Velocity contours in 4 different chord-wise cross sections along the blade span (0.01, 0.3, 0.6 and 0.9 of span).

Figure 4-29 and Figure 4-30 show the air streamlines and static pressure contours at those four chord-wise sections at the same wind conditions, respectively. These reaffirm the good quality of the airflow around the blade. Almost no flow separation exists around the blade, and the pressure distributions are favorable (there is almost no reverse flow on the blade surface). A tiny partial flow separation occurs at the root of the blade, which is due to a relatively high local angle of attack. This arises from some structural constraints, which can be explained as follows: The blade is subjected to a couple of perpendicular moments due to lift and drag forces. The moment from the drag force is usually more crucial because the blade may not have any rotational motion in the direction of drag force. Indeed, the maximum bending moment occurs at the root. The cross-section of the root should, therefore, have a large I_{zz} in order to withstand the moment exerted by the drag force, which can be achieved by aligning of the chord of root parallel to the air stream. This causes a relatively high local angle of attack at the root of the blade. However, the small amount of flow separation at this region can have no considerable effect on the blade performance.

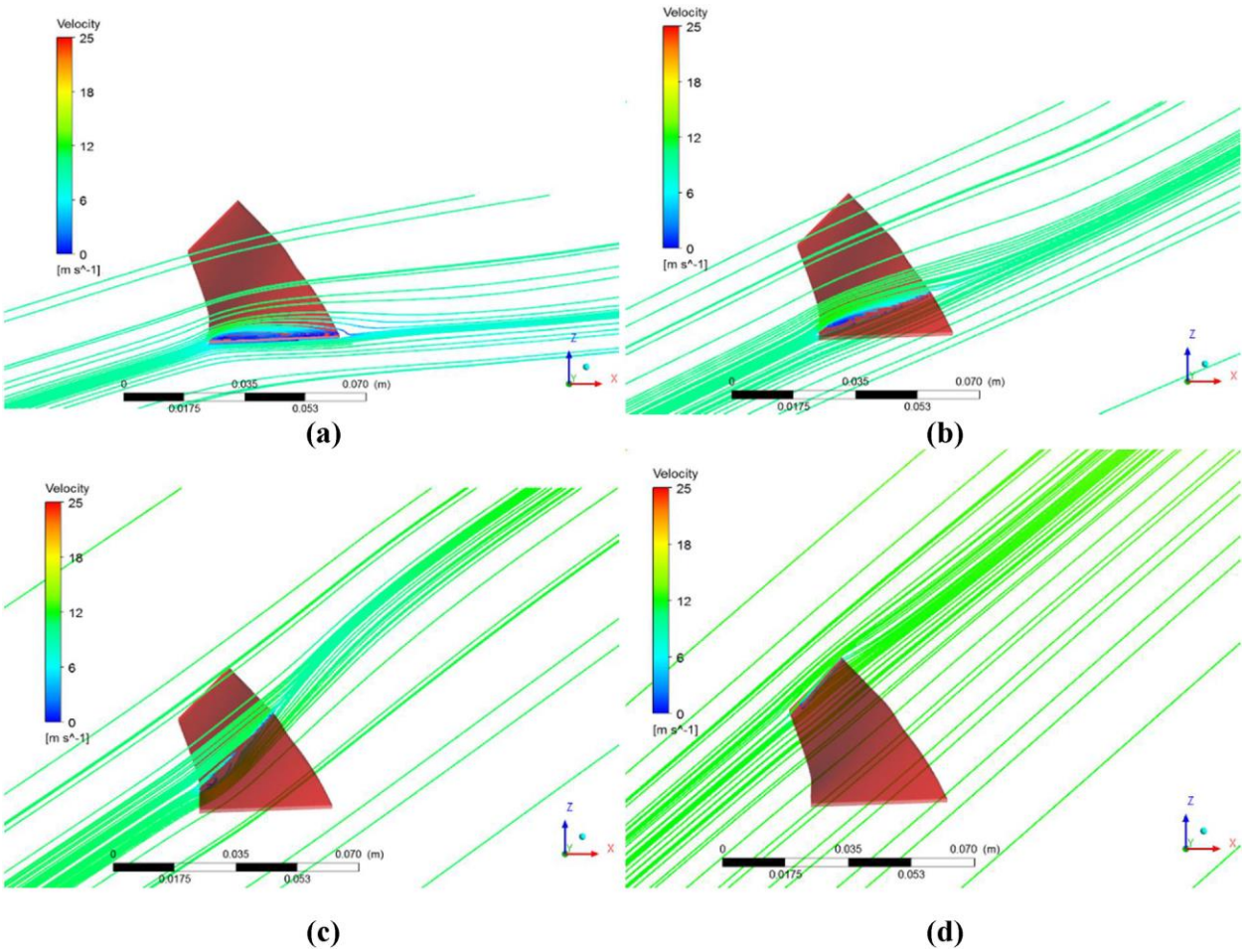

Figure 4-29. Air streamlines passing around the stationary 4D-printed blade in four different chord-wise cross sections along the blade span. (a) 0.01, (b) 0.3, (c) 0.6 and (d) 0.9 of span.

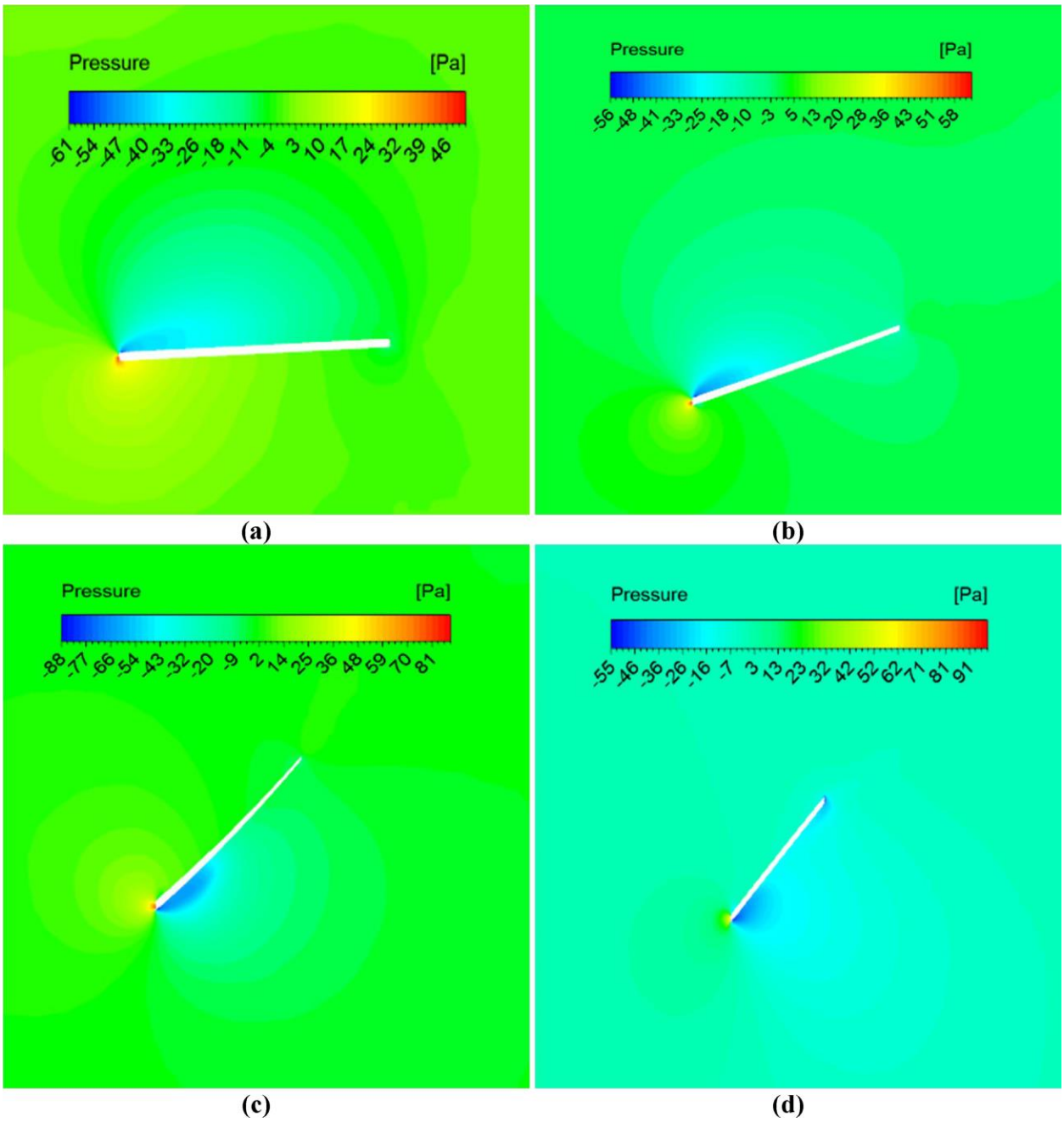

Figure 4-30. Static pressure (gauge) contours in 4 different chord-wise cross sections along the blade span. (a) 0.01, (b) 0.3, (c) 0.6 and (d) 0.9 of span.

In the CFD part of the present study, a novel 4D-printed blade is compared to a simple flat plate. In other words, the 4D-printed deformed blade is considered as a thin flat plate which is deformed and curved. Therefore, the whole present analysis is about the improvement gained by 4D deformation of a thin plate inspired by leaf structure, so the performance is also compared with a flat plate as presented in CFD part. The present cross-section may be the camber of any arbitrary

airfoil section profile for upper and lower surfaces. In fact, there is a high potential for future investigations to improve both aerodynamic and structural performance of the leaf-mimetic 4D-printed blades with airfoil cross-sections. Apart from aerodynamic performance, structural characteristics (strength to weight ratio, etc.), manufacturing expenses, and attainability of desirable shape deformation are other concepts, which must be investigated in separate studies.

Along with the CFD simulations and in order to compare the power range quantitatively, a 6-bladed commercially-used small-scaled wind turbine with a rotor disk diameter of 91 cm is considered (Marlec Eng. Co. Ltd.). Referring to the performance curves, its power production varies from almost 2 to 222 Watts in the operating range of wind speed from 3 to 15 m/s. The present 4D-printed blade, with 5 cm hub radius and blade length of 10 cm, has a rotor disk with a diameter of 30 cm. According to a simple scaling law (Amano & Sundén 2014; Manwell et al., 2010), the power of the turbine is proportional to the square of the diameter of its rotor disk. This proportionality is also examined numerically in the present study. Consequently, after scaling the 4D-printed rotor disk diameter from 30 to 90 cm, its power (obtained from present CFD results) lies between 2.2 to 174 Watts for wind speeds of 5.5 to 23.5 m/s. A result which is comparable to that of commercially-used small-scaled turbines with conventional blades.

The main purpose of these simulations, however, is to evaluate the performance of the 4D-printed blade in more details and complement some limitations of experimental tests and analytical solutions. In fact, these analyses serve to implement the proposed design and fabrication paradigm in this study for advanced 4D-printed wind turbine blades in future works.

4.6 Dynamic Mechanical Analysis (DMA) tests

One of the critical material properties that needs to be determined in the mathematical model in equation (4-3) is the elastic (storage) modulus of the polymer above the glass transition temperature T_g. The shape memory polymers have a temperature-dependent elastic modulus, especially around the T_g and it can be measured from Dynamic Mechanical Analysis (DMA) test.

Some of the studies in the literature used the results of the DMA test on molded structures for analyzing the deformation behavior in 4D printed structures, which is conceivably inaccurate. To verify this statement, DMA tests were performed on a treated printed PLA.

The test was performed in the tensile mode with a DMA machine under the following condition: the strain oscillation had a frequency of 1 *Hz* with a maximum amplitude of 0.01%. The

temperature ranged from 40 to 130 ℃ at an increasing rate of 2 ℃/min. A static preload of about $0.1g$ $(0.001N)$ was considered to maintain the specimen straight during the whole experiment as was done in some of the previous studies (Wu et al. 2016).

It is seen that some researchers use the materials properties of molded or annealed structures to model the behavior of their 4D printed structures. Here, we measure the desired property of our 4D printed structure (Figure 4-31) and observe that the manufacturing process affects materials properties. It should be noted that our smart blade will have multiple shape-shifting behaviors (cycles) rather than only one cycle. Therefore, we consider this point and measure the desired property of a printed structure that has already gone one shape-shifting cycle. We just call this structure as "treated printed" structure to distinguish it from "just printed" structure. After the first shape-shifting cycle, the structure would behave as a "treated printed" structure for the rest of the shape-shifting cycles, rather than the "just printed" structure. Therefore, the "treated printed" structure is closer to reality than the "just printed" structure.

Comparing the measured results in Figure 4-31 with the properties of a molded PLA from Cock et al. (2013) in Figure 4-32, the elastic modulus shows an entirely different behavior as a function of temperature. The elastic modulus for the molded PLA has a local minimum value and then increases after the glass transition temperature. On the other hand, the elastic modulus in a treated printed PLA uniformly decreases as the temperature increases. This shows that the manufacturing process directly influences these material properties not only on their absolute values (especially around the T_g) but also on their general trends. This difference can lead to tremendously different results in predicting the behavior of the 4D printed structures. Based on Figure 4-31, the elastic modulus well above T_g of the treated printed PLA is 2×10^8 Pa, which was used in the mathematical modeling. In contrary, Figure 4-32 shows that the value of the elastic modulus for molded PLA well above T_g is around 5×10^7 Pa.

Therefore, for accurate mathematical modeling and prediction of the shape-shifting behavior over time, the actual material properties of the 4D printed structure should be used.

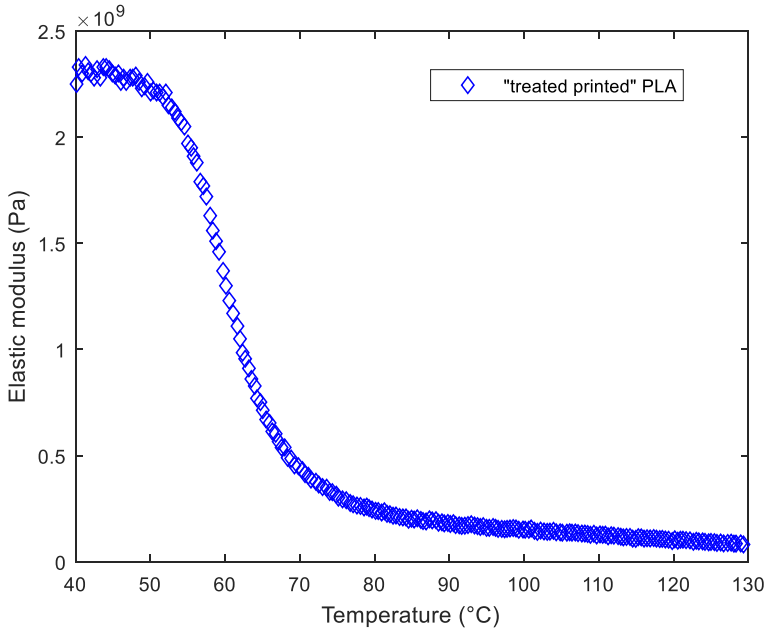

Figure 4-31. The behavior of the elastic (storage) modulus of the "treated printed" PLA from DMA test.

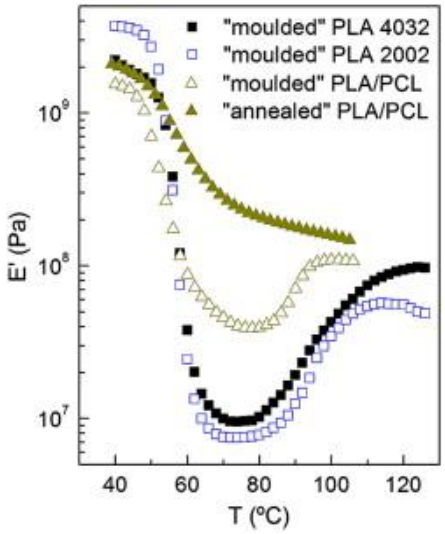

Figure 4-32. The behavior of the elastic (storage) modulus of the "molded" and "annealed" PLA from DMA test (Cock et al., 2013).

4.7 Discussions

4.7.1 Mechanisms for applying stimulus

In this study, we utilized a hot plate (CIMAREC, model SP131325) to provide heat in the lab. The mechanisms that can supply heat in real operations can be studied, separately. For example,

a connection can be made between the environmental temperature and the desired shape changes, instantaneously; or some hot wires can be embedded through the smart parts (PLA) of the blade to apply heat locally. This heat can be provided by electricity or even by a mechanism that incorporates the free energy of sunlight. In addition, photo-responsive smart materials can be used in our design rather than the current heat-responsive smart material. In this case, the desired shape can be achieved directly by light (i.e., photochemical mechanism) without reliance on heat and temperature change (as seen in photothermal mechanism).

The frequency of the shape-shifting should also be considered in a specific application. According to the Probability Density Function (PDF) and Cumulative Frequency (CF) of wind speed and also wind rose graph of its direction in the region of installation site (Chen et al., 2016), the materials compositions and layers directions can be set in the printing process. Then, depending on these features and by dividing the wind speed range into some intervals, it can be determined for the blade to shift its shape at certain wind speed and direction milestones. The required energy for blade deflection is then dependent on the materials and structural characteristics of the blade, as well as wind intensity (speed) and direction. One main parameter that determines the amount of the required heat is the glass transition temperature (T_g) of the smart material that can be tuned by some additives, blends, and even using some other types of smart materials. However, one of the ultimate goals of 4D printing is using random free energy to provide non-random structures and shape-shifting behaviors (Tibbits, 2013). It should be also noted that if the number of shape-shifting is too many, then the 4D printed structure may not be able to totally recover its initial and final shapes and this fact should be considered and monitored (Momeni et al., 2016).

The next consideration is related to seasonal variations in temperature that cause the blade surface temperature to vary. The smart material used here has a glass transition temperature (T_g) of about +60 ℃, above which the shape-shifting occurs. Therefore, at any temperature below this point, there is no unwanted shape-shifting. By the way, the T_g can be decreased or increased as discussed above.

4.7.2 Small-scale and large-scale applications

Here, we demonstrated the proof-of-concept of a new blade followed by wind tunnel tests and performance analysis. The proposed paradigm can be explored for both small-scale and large-scale applications. The three unique advantages of the proposed blade compared to the existing

blades capable of BTC through the passive methods (discussed in section 3.1.6), would be present in both the small and large scales. In addition, the energy gain can be studied by optimizing the proposed blade from various perspectives. It should be noted that, for large-scale applications, the widths of main and lateral veins will increase. Thus, to avoid unwanted shape-shifting along the width of a vein, the smart material should be printed as several small-width strips with some spacing between strips, rather than a continuous large-width vein. Moreover, for the large-scale wind turbines, the mechanical properties of the materials should be considered as the following.

4.7.3 Materials considerations

First of all, composite materials have been recognized as the best materials for wind blades (compared to metals (primarily aluminum) and wood) (El Alaoui et al., 2016; Mishnaevsky et al., 2017; Swolfs, 2017; Sutherland, 1999; Brøndsted et al., 2005; Jespersen & Mikkelsen, 2017; Dai & Mishnaevsky, 2014). Moreover, if green composites (Dicker et al., 2014; Schledjewski et al., 2017; Murdani et al., 2017) are used, then it will be eco-friendlier. For composite materials, fiber and matrix should be analyzed separately. For matrix portion, two types of materials are usually used; thermosets and thermoplastics. Compared to thermosets, thermoplastics are recyclable and have higher fracture toughness, as well as larger elongation at fracture. Nevertheless, thermoplastics have more difficult manufacturing processes due to their higher viscosity and larger processing temperature compared to thermosets (Mishnaevsky et al., 2017). However, this difficulty can be resolved by additive manufacturing. Here, we used PLA that is a biodegradable thermoplastic. It can be reinforced by carbon fibers. PLA-carbon fiber blends are commercially available for additive manufacturing. In addition, natural fibers such as Bamboo have been reported as good alternatives to glass and carbon fibers for both the small- and large-scale wind turbines (Mishnaevsky et al., 2017; Holmes et al., 2009; Pozo Morales et al., 2017). Nevertheless, research on green composites suitable for large-scale wind turbine blades is ongoing.

4.7.4 Other plant-mimetic approaches useful for wind turbines

There was a different plant-mimetic approach for wind turbines, where the researchers (Loth et al., 2017; Ichter et al., 2016; Noyes et al., 2018) were inspired by downstream bending of the palm tree trunk in high winds leading to load reduction. In their design, the blades had the same conventional structures (rather than leaf structure). However, they had a segmented structure close to their rotor hub and could bend from that part, in the direction of the wind, similar to the palm

tree (and in contrast to the oak tree). This leads to load reduction and is suitable for extreme-scale wind turbines (Loth et al., 2017; Ichter et al., 2016; Noyes et al., 2018). This approach can be combined with our proposed blade mimicking the leaf vein network.

4.8 Conclusions

A new paradigm for the design and fabrication of the wind turbine blades has been demonstrated by the 4D printing process. This can integrate several advantageous attributes into one structure, simultaneously. Other materials can be incorporated. The results can be scaled up, and the methodology can be adjusted and customized to a particular need. We demonstrated a plant leaf-mimetic wind turbine blade in practice that is capable of reversible bend-twist coupling behavior. This blade does not rely on traditional electromechanical systems, moving parts, sensors and actuators. We have also separated the adaptability and flexibility concepts in wind turbine blades and demonstrated this difference in practice. This may solve the flutter issue seen in blades capable of BTC through passive methods. The proposed multi-functional blade can finally lead to eco-friendly wind turbines. Our blade only relies on heat to show its shape memory effect, in contrast to the usual shape memory materials that need both the heat (thermal part) and force (mechanical part) to achieve the shape memory effect. This is because we combined active and passive materials and designed their arrangement so that their mismatch-driven force serves as the required mechanical force in the required direction. Finally, it should be noted that certain materials properties of 4D printed structures, for example, the elastic (storage) modulus are different from those of the molded/annealed structures. The actual materials properties of "4D printed" structures should be applied in the corresponding mathematical models for predicting the shape-shifting behaviors over time.

CHAPTER 5

NATURE-INSPIRED SMART SOLAR CONCENTRATORS BY 4D PRINTING

Currently, solar concentrators, whether in solar PV or solar thermal applications are designed and utilized as a fixed shape such as elliptic, parabolic, V-shape, hyperbolic, and multi-stage forms. Here, we are inspired by diurnal and nocturnal flowers and their differences and propose a smart solar concentrator that can increase the overall light collection efficiency by more than 25% compared with its non-smart counterparts. We introduce the concept of smart solar concentrators inspired by nature and enabled by 4D printing and illustrate its necessity and advantages. We found that most of the diurnal flowers have parabolic and most of the nocturnal flowers have hyperbolic petals. Our proposed multi-functional concentrator has a parabolic shape for a portion of the day that parabola dominates all the other shapes in terms of the optical efficiency, then it can reversibly change its shape to hyperbola for another portion of the day that the hyperbola beats all the other geometries. By using this design, the optical efficiency trend will move from peak-and-valley form toward constant-at-peak format, resulting in overall efficiency improvement. The proposed biomimetic structure is an example of smart origami. It is simple and low-mass. It demonstrates the desired shape-shifting without reliance on cumbersome and expensive electromechanical systems.[5]

[5] This chapter is based on our journal article published in *Renewable Energy 122 (2018)*, entitled "Nature-inspired smart solar concentrators by 4D printing", by Farhang Momeni and Jun Ni.

5.1 Introduction

Both the solar PV and solar thermal modules can have three main elements, a receiver (mandatory), a concentrator (optional) and a tracking mechanism (optional). The primary reason for using concentrators is to converge the sunlight and obtain the same efficiency by using less solar cell materials in solar PV applications (Parida et al., 2011) and increase the receiver temperature in solar thermal applications (Tian & Zhao, 2013). Currently, the solar concentrators are designed as a fixed shape, and most of the existing solar concentrators are parabolic. Elliptic, V-trough, and hyperbolic concentrators have been studied in few specific cases, and the parabolic concentrators have been recognized as a suitable form for general purposes and usual operations (Madala & Boehm, 2017; Khamooshi et al., 2014; Ghasemi & Ranjbar, 2017; Marefati et al., 2018; Kasaeian et al., 2018; Bellos & Tzivanidis, 2017; Rabl, 1976; Khakrah et al., 2017).

On the other side, the reason for using the tracking mechanism is to keep perpendicular sunlight incidence by tracking the apparent motion of the sun (Apostoleris et al., 2016). However, the current tracking mechanisms are heavy, large, and expensive (due to the installation, operation, auxiliary energy, and maintenance costs) (Madala & Boehm, 2017; Apostoleris et al., 2016). These factors cause hurdles for the commercialization of concentrating photovoltaic (CPV) systems (Apostoleris et al., 2016). This issue is going to be solved through several ways such as integrated-tracking systems (Apostoleris et al., 2016; Duerr et al., 2011; Lamoureux et al., 2015) and/or proposing simple, lower-mass and cheap tracking mechanisms by novel solutions, such as kirigami technique (Lamoureux et al., 2015), and so on. Kirigami (‘kiru’: cut; ‘kami’: paper) and origami (‘ori’: fold) can provide novel solutions for engineering applications by combing mathematics and art (Blees et al., 2015; Rafsanjani & Bertoldi, 2017; Wang-Iverson et al., 2016; Ge et al., 2014). By 4D printing, *smart* origami (Ge et al., 2014) and kirigami are achievable, in which the shape is evolved by intelligence rather than mechanically-driven alterations by pure pushing and pulling.

Optical efficiency is one of the primary efficiencies in solar PV and solar thermal applications, and in some cases, the overall efficiency of concentrating photovoltaic/thermal (CPVT) collectors is limited by optical efficiency (Karathanassis et al., 2017; Daneshazarian et al., 2018). This means that, in these cases improving factors other than optical efficiency, cannot give a net improvement in the overall efficiency until this bottleneck (optical efficiency) is improved. In optical efficiency analysis, ray-tracing simulation is a useful technique for the design, analysis, and optimization of solar concentrators (Riveros-Rosas et al., 2011), especially by using TracePro

software (TracePro User's Manual, 2017) that has attracted a growing level of attention (Wang et al., 2017).

The design, analysis, and optimization of the four concentrators above have been explored in several studies by numerical, experimental, and analytical approaches (Zhang et al., 2017; Tina & Scandura, 2012; Ali et al., 2013; Tang & Wang, 2013; Sellami et al., 2012; Al-Shohani et al., 2016; Mohsenzadeh & Shafii, 2017; Chaves, 2015; Gorjian et al., 2014). Here, we show the necessity and advantages of a smart solar concentrator that has the desired reversible shape-shifting in one specific case. We demonstrate the proof-of-concept for a low concentration (Amanlou et al., 2016), one-stage, and compound concentrator. However, 4D printed solar concentrators can be further analyzed in all the four shapes, in simple or compound, one- or multi-stage concentrators, in the low, medium, or high concentration systems, in the solar PV or solar thermal applications, etc. Moreover, it can be considered in various optimizations schemes.

Natural living things have evolved, self-corrected, self-adapted, and self-optimized to the environmental conditions over a long time. Nature usually accomplishes a function with the least amount of energy. Hence, biomimetic approaches can provide one of the most efficient, and most robust solutions for human-made systems (Li et al., 2013; Vincent, 2006; Speck et al., 2017). Here, we show how a biomimetic inspiration paves the way for a more efficient solar energy utilization.

5.2 Design concept

There are three types of flowers. Some flowers are always open, some of them open in the morning and close in the afternoon that is named diurnal flowers, and some others open in the afternoon and close in the next morning that is called nocturnal flowers. The diurnal and nocturnal flowers open and close for several reasons such as pollination and the type of pollinators (some pollinators are night-flying, and some are day-flying), avoiding unwanted attention from other harmful insects whether during the day or night, managing the internal temperature & humidity, metabolism, etc. Nevertheless, one of the main growing requirements of both the diurnal and nocturnal flowers is capturing as much sunlight as possible. However, the interesting point is that the total performance (fruit or seed set) of these two categories are comparable in many cases (Young, 2002; van Doorn & van Meeteren, 2003; ProFlowers, 2011; UCSB ScienceLine, accessed 2017; Shamoon, accessed 2017; Carter, accessed 2017; Avid, accessed 2017; Palermo, 2013; Villazon, 2009). Therefore, we can say that there should be some competitive advantages in nocturnal flowers that can yield the same performance, albeit they receive only the inclined portion

of the sunlight of a day and are closed around noon. We propose *one* competitive advantage, demonstrate an impressive result based on this inspiration, utilize it in our smart solar concentrator design, and show the efficiency gain.

We organize several popular nocturnal and diurnal flowers in Figure 5-1. A fascinating result can be captured by analyzing the geometries of these two categories. The diurnal flowers have *mainly* parabolic petals, while the nocturnal flowers have *mainly* hyperbolic (trumpet-shaped) petals.

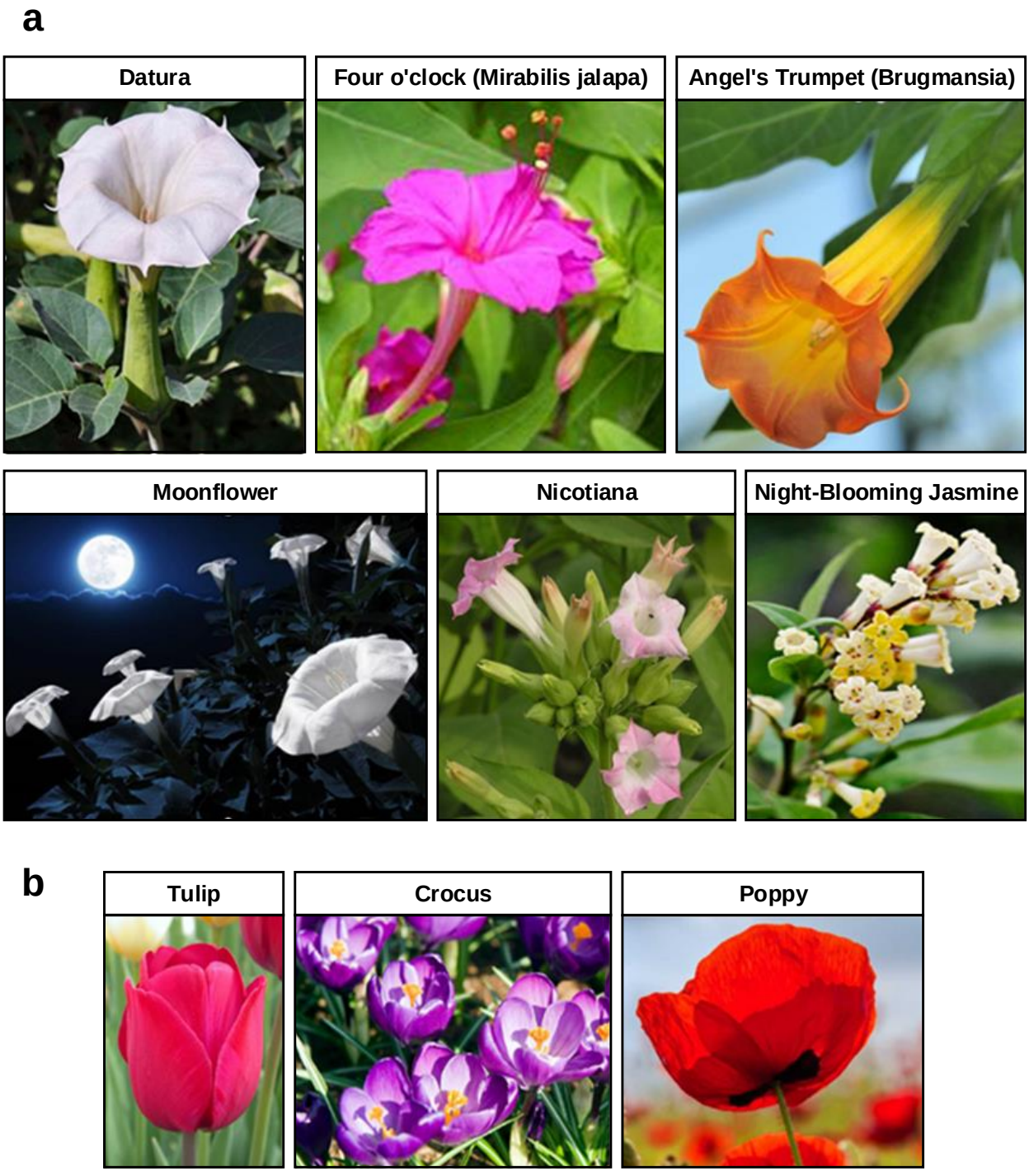

Figure 5-1. Comparing the configurations of petals in diurnal and nocturnal flowers. Category (a) shows some popular nocturnal flowers. They are closed around noon and are open far from noon. Category (b) illustrates some popular diurnal flowers. They are open around noon and are closed far from noon (Palermo, 2013; Villazon, 2009; Taylor, 2017; Wikipedia. Mirabilis jalapa, accessed 2017; Waluyo, 2015; Wikipedia. Nicotiana tabacum, accessed 2017; Taylor, 2017; Wooden Shoe Tulip Farm, accessed 2017; Gardenia, accessed 2017).

Before we proceed to simulations, we discuss the reflectivity of the flowers` petals. The flowers` petals have a combination of specular (mirror-like) and diffuse reflections (Moyroud et al., 2017; Grant, 1987; Vogelmann, 1993; Hohmann-Marriott, 2014; Barthlott et al., 2017; McClendon, 1984; Wehner & Bernard, 1993; Xie et al., 2017; Foster et al., 2014; Fritz et al., 2017). The specular reflection generally results from the air-petal interface (Moyroud et al., 2017; Grant, 1987; Vogelmann, 1993). More interestingly, in some flowers such as Buttercup (*Ranunculus* species), the specular reflection totally dominates the diffuse one, and the flowers` petals, perfectly reflect the sunlight toward the reproductive organs (van der Kooi et al., 2017) (Figure 5-2). The highly specular reflection in *Ranunculus* is due to an incredibly smooth epidermal layer (van der Kooi et al., 2017; Kooi et al., 2014; Parkin, 1928), and the presence of an air layer beneath the epidermal layer (i.e., between the epidermal and starch layers) (Vignolini et al., 2011; van der Kooi et al., 2017). The highly specular reflection has been reported in some other flowers (such as *Gorteria diffusa)* that helps the pollination (Ellis & Johnson, 2010; Vignolini et al., 2012). Even, metallic-mirror like surfaces were found in the mirror orchid *Ophrys speculum* (Barthlott et al., 2017). The extremely specular reflection in the mirror orchid is due to an unusually smooth cuticle layer (ultrastructure) resided on top of a very flat epidermal layer (Vignolini et al., 2012).

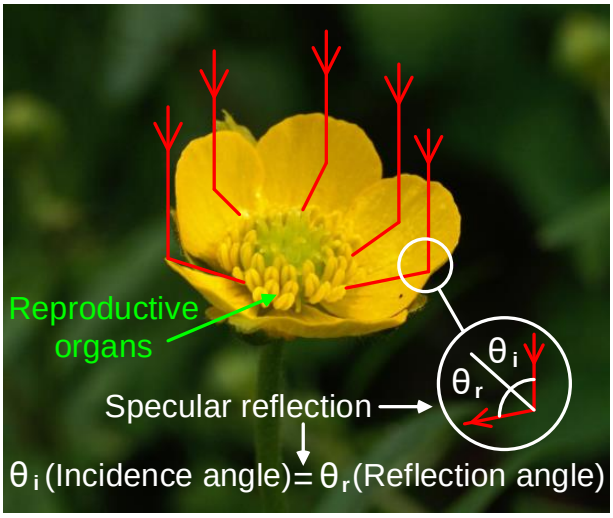

Figure 5-2. The specular reflection in flowers` petals. The flower photo of this figure was taken by Dekker (accessed 2017).

5.3 Simulation

Now let`s analyze these two geometries observed in the nocturnal and diurnal flowers (hyperbola and parabola), by a ray tracing simulation software, TracePro. The general concepts and procedures of ray tracing simulation by TracePro are shown in Figure 5-3. In Figure 5-3, θ is

the solar incidence angle. Light is beam and monochromatic with an average wavelength of 0.5461 µm (green color light). Concentrators have about 95% specular reflectance (standard mirror), and the receiver is a perfect absorber (blackbody). Figure 5-3 also shows the irradiance maps of the receiver surface that indicate the pattern and amount of absorbed flux. Both the black-white and color maps show the absorbed flux by the receiver that is equal to the incident flux on the receiver, as the reflected flux is zero for the perfect absorber. The color map is for better realization, and further illustrates the incoming rays, concentrators, and receiver.

At this point, rather than comparing only parabola and hyperbola, we follow a recent work (Madala & Boehm, 2016) and similarly consider all of the four shapes, elliptic, parabolic, V-shape, and hyperbolic concentrators. The results are illustrated in Figure 5-4.

In Figure 5-4 the heights (H) and (geometric) concentration ratios (CR) of the four shapes are the same, and each data point shows one particular simulation that illustrates the optical efficiency at a specific irradiance angle. This figure implies two main points. First, we can find that why most of the diurnal flowers have parabolic shape and most of the nocturnal flowers have the hyperbolic shape as *one* reason. It shows that the parabolic shape is better in terms of optical efficiency for perpendicular irradiance angles around noon and the hyperbolic shape is better for inclined angles far from noon. Second, it can be understood that why most of the existing studies worked on parabolic concentrators. They try to capture the perpendicular irradiations around noon, as much as possible. In addition, it should be noted that the parabolic concentrator has easier fabrication through the conventional manufacturing processes compared with the hyperbolic counterpart.

Now, we propose 4D printed smart solar concentrators, which specifically in our case, can be parabolic as long as parabola beats all other shapes in terms of optical efficiency and can reversibly change its shape to hyperbola for another portion of the day that hyperbola has the best performance among all the four shapes. To show the gain, let`s consider three different scenarios (cases) as seen in Figure 5-5. In this figure, we consider the overall (average) optical efficiency (i.e., considering all irradiance angles) of a day for three cases. CPC and CHC stand for the compound parabolic concentrator, and compound hyperbolic concentrator, respectively. Case 1 has a non-smart (static) parabolic concentrator for the whole day. Case 2 has a non-smart hyperbolic concentrator for the entire day. However, case 3 has a 4D printed smart concentrator that is parabolic for a portion of the day (i.e., between the two intersection points in Figure 5-4)

and can change to hyperbola for another portion of the day (i.e., outside of the intersection points). The overall efficiencies of these three cases have been calculated based on Figure 5-4 by considering all the irradiance angles. The overall efficiency of case 3 was obtained by considering the efficiency of the CPC between the two intersection points, and the efficiency of the CHC outside of the intersection points. It is observed that case 3 improves the overall optical efficiency by more than 25% compared to cases 1 and 2. By further optimizations of concentrators, this gain can be enhanced as well. It should be noted that the equality of the overall efficiencies of the CPC and CHC is accidental. For example, if we change the present geometry of the CHC (in Figure 5-4 and Figure 5-5) and keep the same geometry for the CPC, then their overall efficiencies would become different.

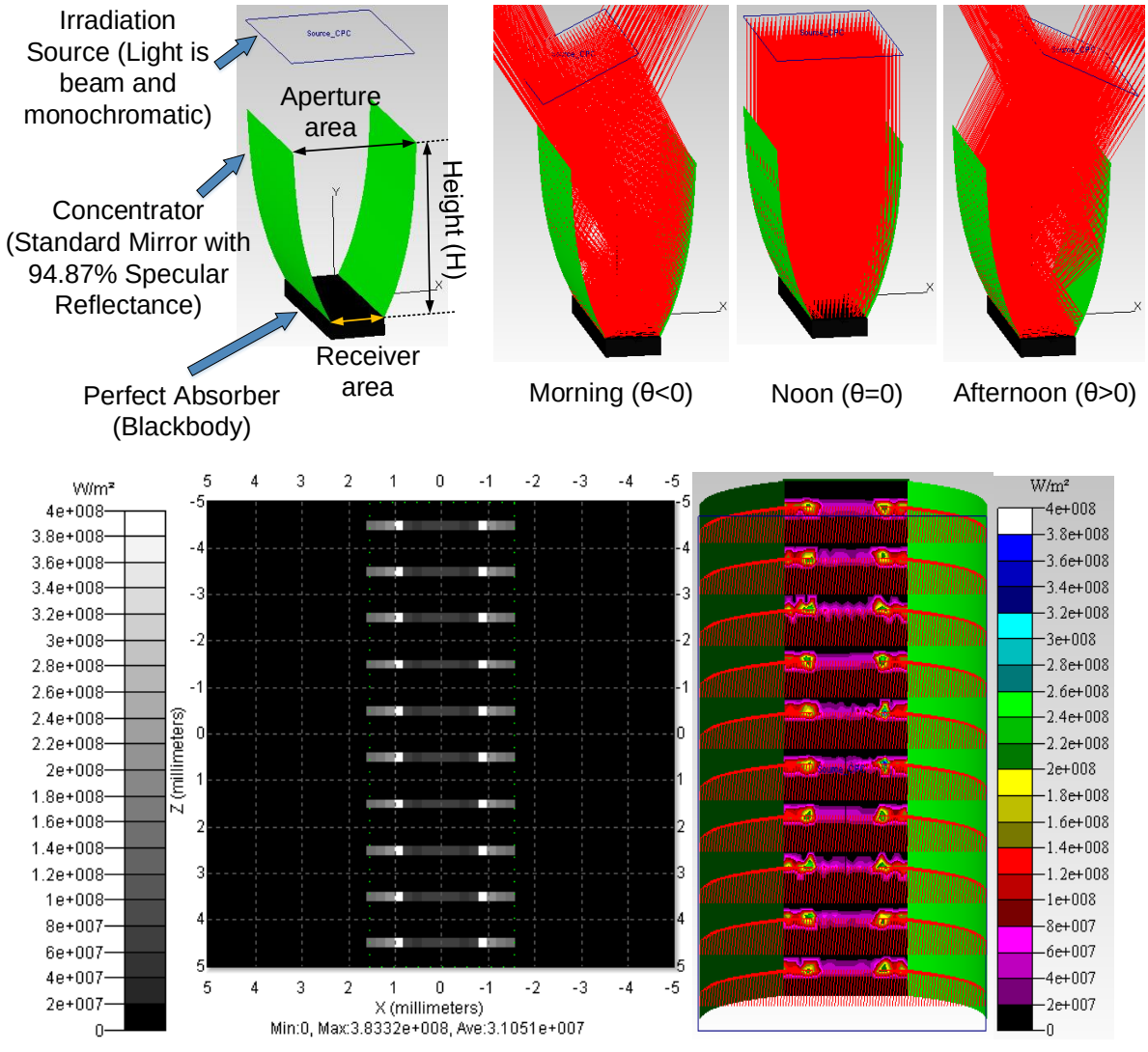

Figure 5-3. Concepts and procedures of Ray tracing simulations and optical analysis using TracePro.

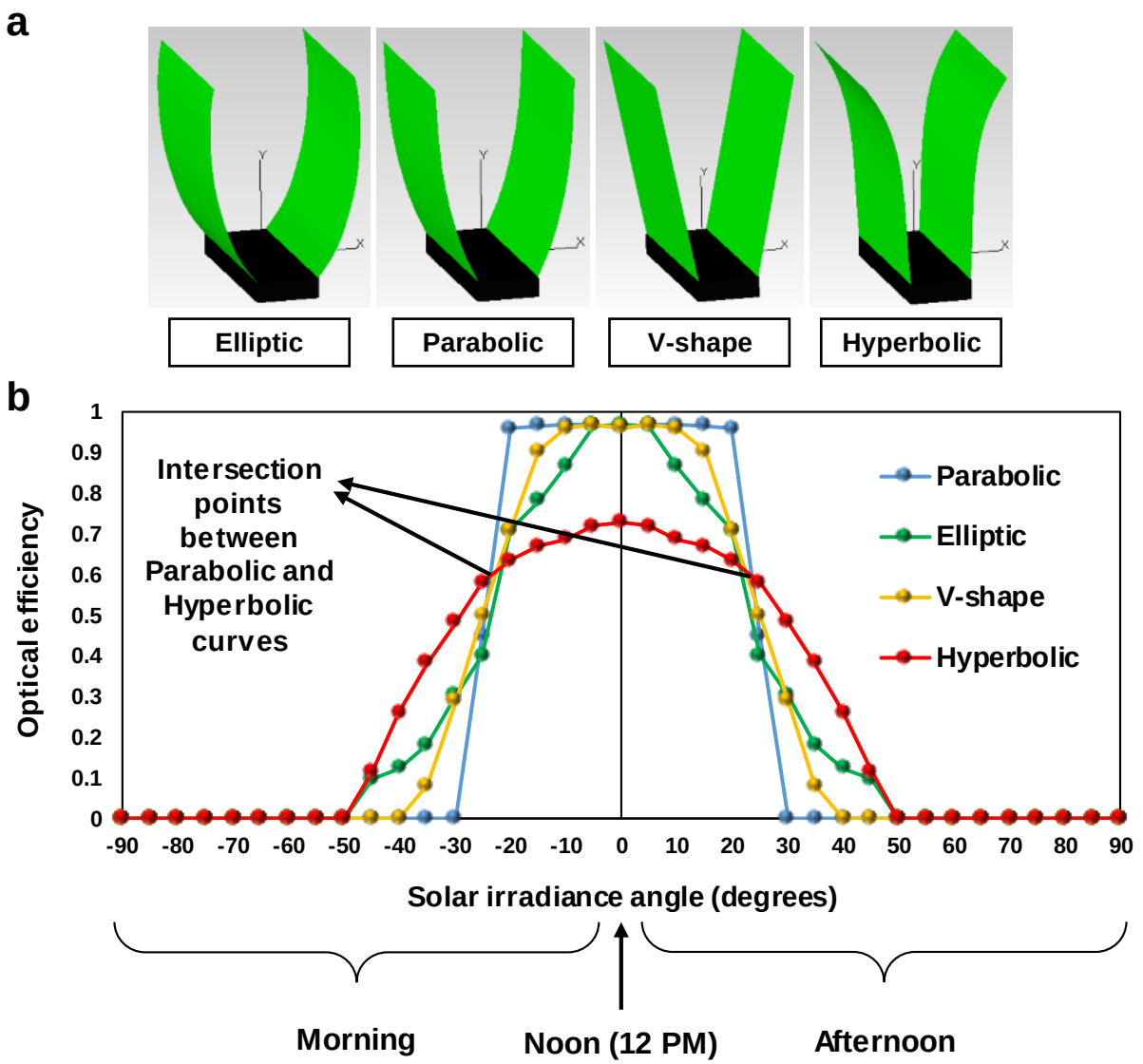

Figure 5-4. Comparison of the optical efficiency in four well-known concentrators, i.e., elliptic, parabolic, V-shape, and hyperbolic. All the four concentrators have equal heights and concentration ratios (H=10 mm and CR=2.35). (a) shows CAD (Computer-Aided Design) models of the four concentrators that were simulated in ray tracing software. (b) exhibits the optical efficiency of the four shapes illustrated in part (a), over various irradiation angles.

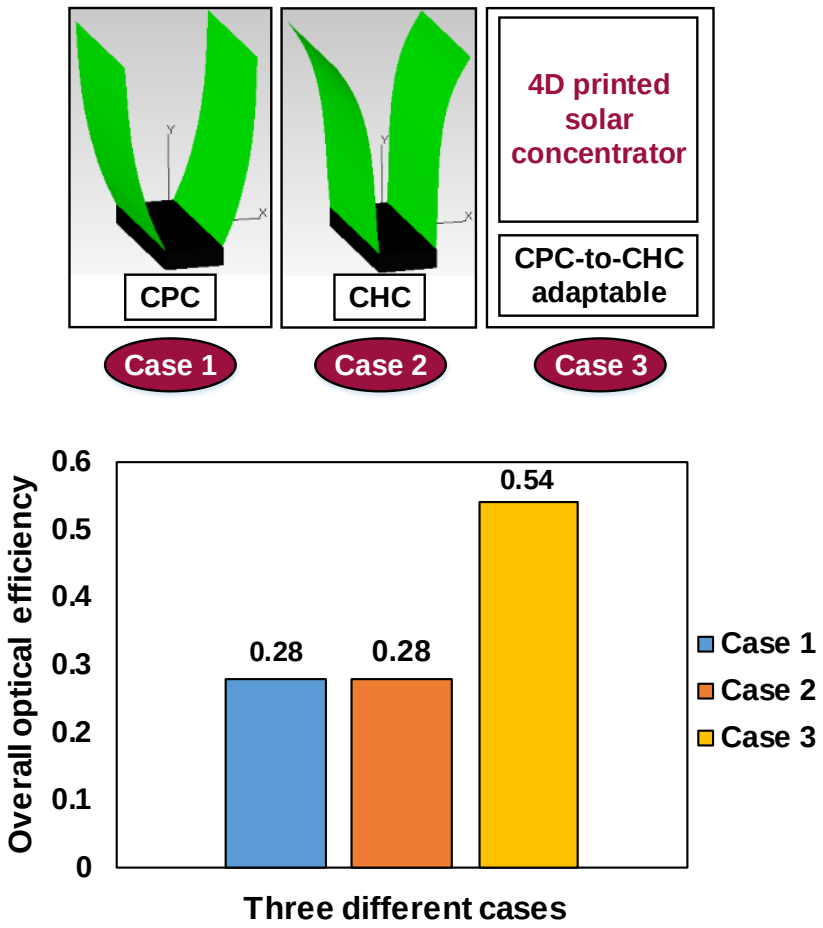

Figure 5-5. Overall optical efficiency in three different cases.

Now, we have the proposed idea in our mind and can proceed to further analysis. The studies on hyperbolic concentrators, usually try to improve their optical efficiency around noon similar to all other types of concentrators. However, we are not worried about the performance of hyperbolic concentrators around noon. We are interested in a better performance of hyperbolic concentrators far from noon that solar irradiations are inclined. Because our concentrator would be parabolic between the two intersection points specified in Figure 5-4 (i.e., around noon) and will become hyperbolic far from noon. The optical efficiency around noon is high enough and outside of the intersection points needs improvements.

In the following, we investigate four design principles including height, concentration ratio, trapping zone, and entry curvature in CHC to improve its optical efficiency far from noon. After that, we demonstrate the design, fabrication and the desired shape-shifting.

The first design principle (Figure 5-6), indicates that by increasing the concentrator`s height in CHC, the optical efficiency decreases at all irradiation angles. By further analysis, the reason is unveiled as shown in Figure 5-7. This figure indicates that higher heights would cause ray flux reductions arising from more reflections. It should be noted that this result cannot be captured in simulations having concentrators with perfect mirror (perfect reflector). In the cases with standard mirrors having a reflectivity less than 100% (as shown in Figure 5-3), after each reflection, some ray flux is lost, the thing that happens in real applications.

The second design (Figure 5-8) indicates that higher concentration ratio will usually cause lower optical efficiency at all solar incidence angles. Similar results about the effect of concentration ratio on optical efficiency were obtained in the literature (Maatallah et al., 2018; Ota et al., 2017; Reddy et al., 2014; Kim & Dutta, 2012).

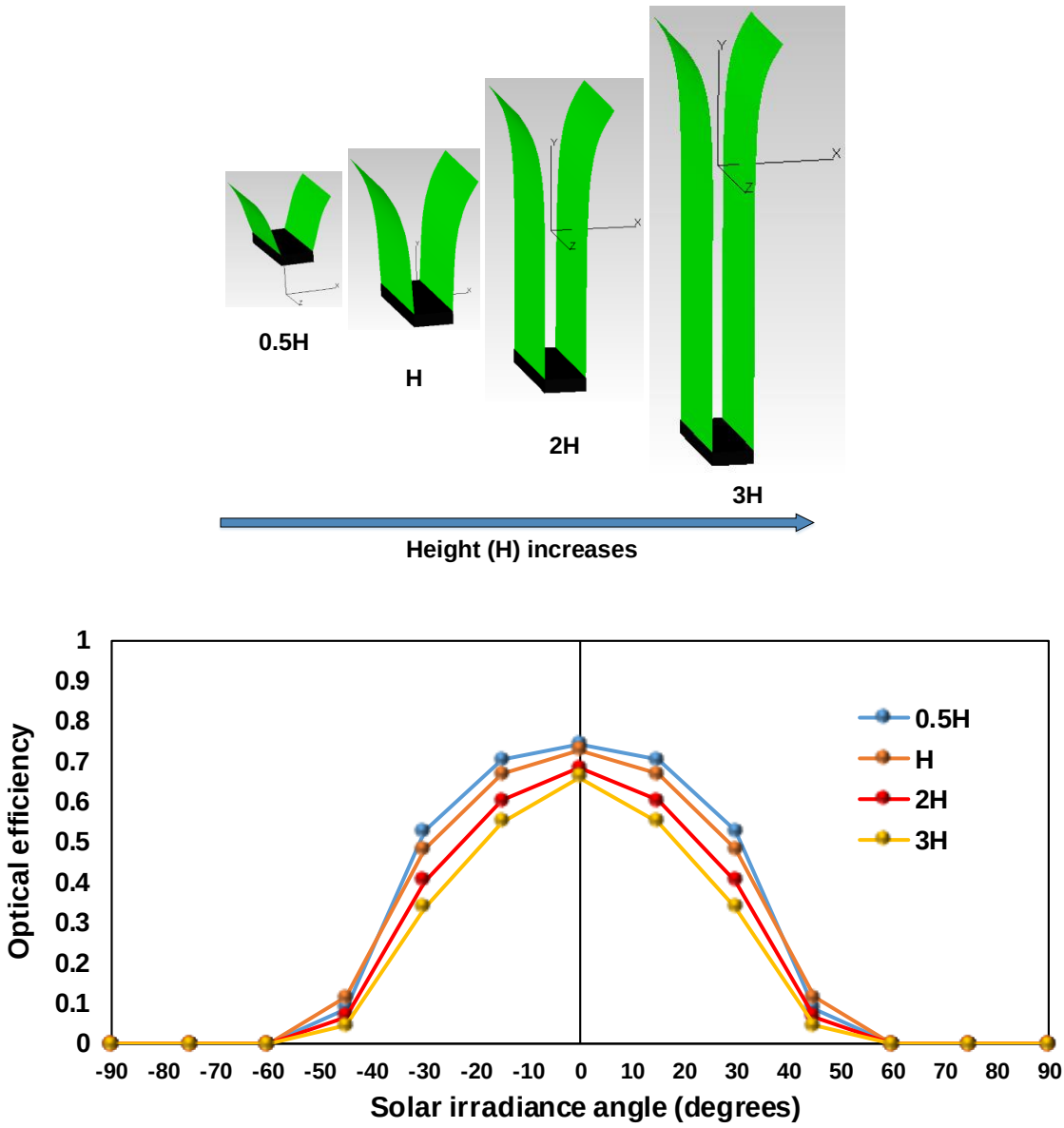

Figure 5-6. The effect of concentrator`s height on the optical efficiency of CHC at various solar irradiance angles. H= 10 mm is the reference value that was used in Figure 5-4. The concentration ratio and head configuration are kept constant at all various heights. This result indicates that higher height usually leads to lower optical efficiency at all incidence angles.

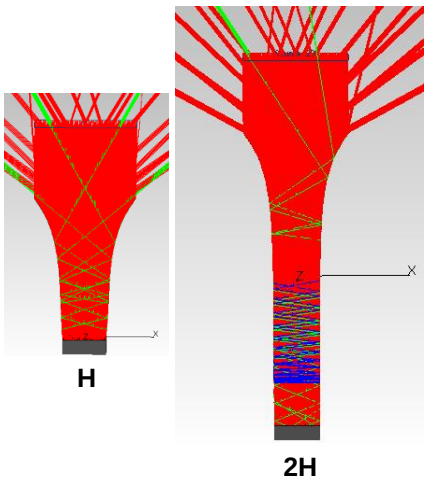

Flux-based ray colors

From	To	Color
0.666	1	
0.333	0.666	
0	0.333	

Figure 5-7. The reason of less optical efficiency in concentrators with higher heights by flux-based ray color analysis. The concentration ratio and head configuration are the same in both cases.

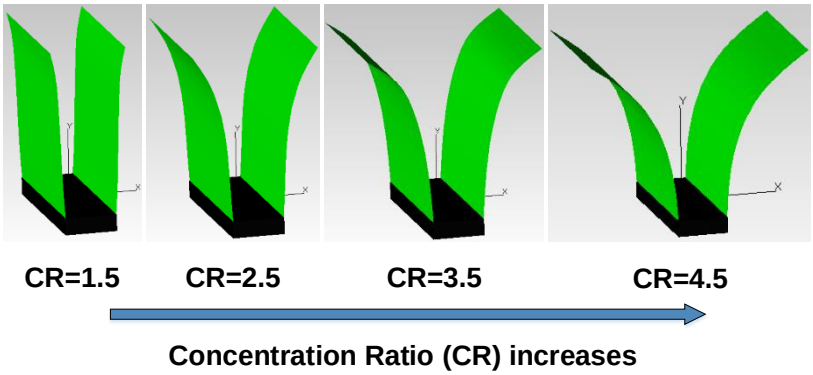

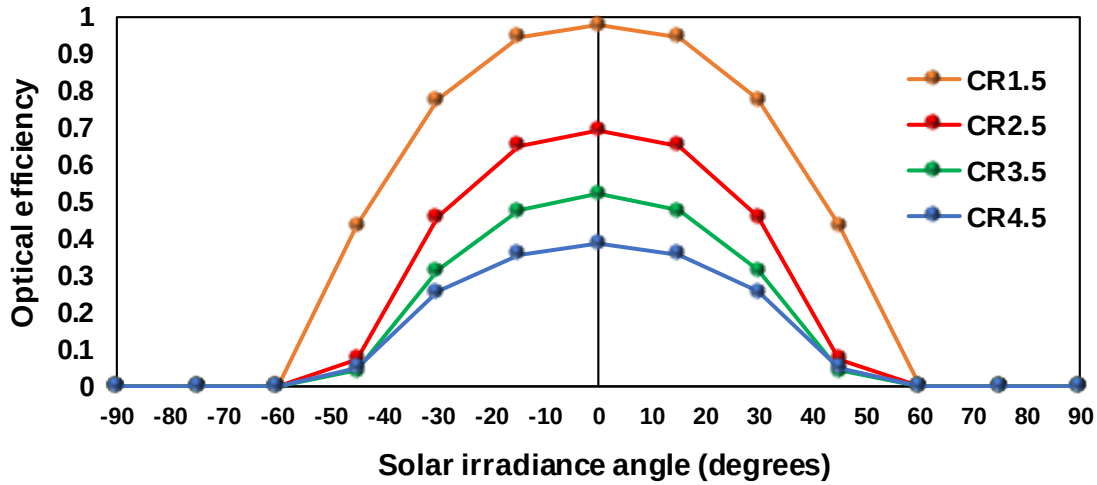

Figure 5-8. The effect of concentration ratio (CR) on the optical efficiency of CHC at various solar irradiance angles. The height is similar in all cases. This result indicates that higher CR leads to lower optical efficiency at all incidence angles.

Now, we consider the third design principle. We realized that similar to some nocturnal trumpet-shaped flowers if we have a concave area near to the receiver (concentrator`s exit), the optical efficiency can be improved for inclined solar irradiations (far from noon) as seen in Figure 5-9. For example, at an angle of 45°, more than 10% improvement in optical efficiency is obtained. We call this design as "Trapping Zone". This design will decrease the efficiency of CHC around noon. However, it does not matter as the concentrators would be the usual CPC rather than CHC in that portion of the day. The gain in optical efficiency can be improved by systematic optimizations in separate studies.

Achieving this geometry will not be a drawback, by using 4D printing process, that provides shape-shifting at any level of complexity.

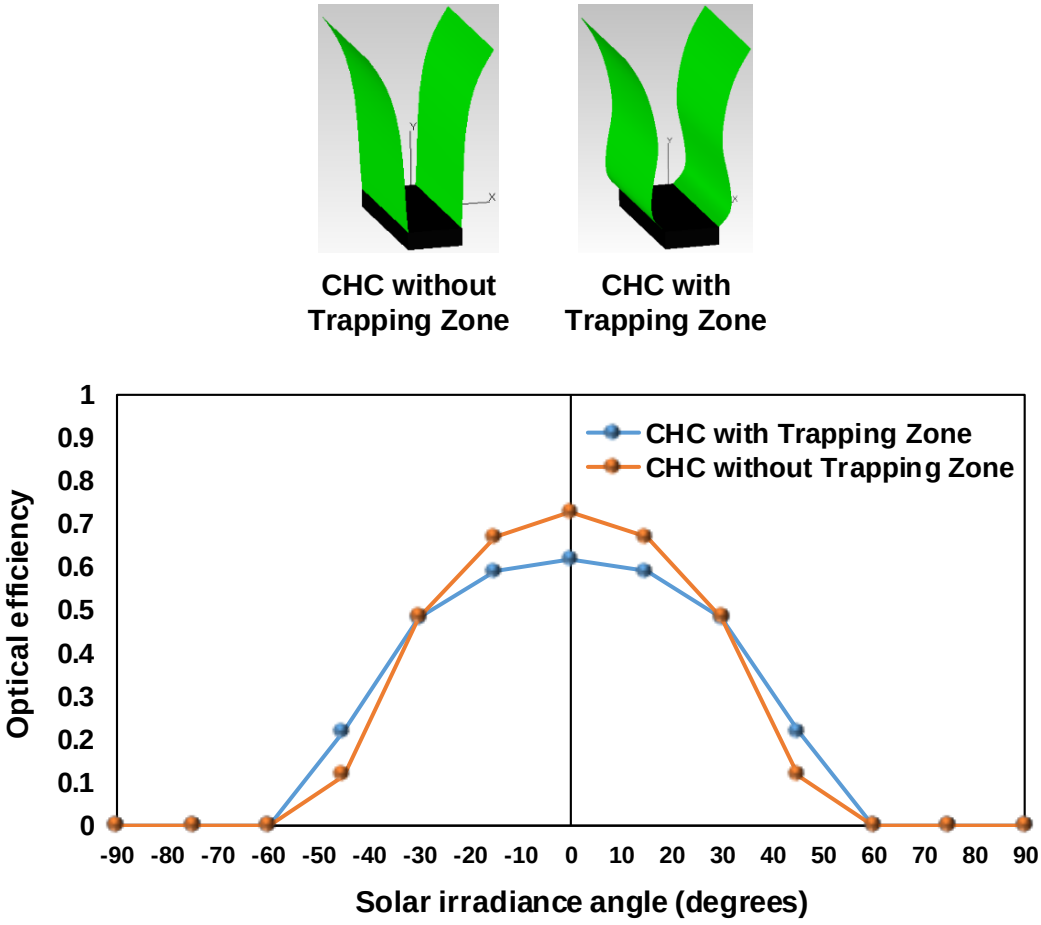

Figure 5-9. The effect of our so-called Trapping Zone on the optical efficiency of CHC at various solar irradiance angles. The concentration ratio, height, and head configuration are kept constant in both of the cases.

Finally, our last design principle deals with our so-called "Entry Curvature" in concentrator`s head. We found that similar to some trumpet-shaped nocturnal flowers if we have a curvature in the entry of concentrators (aperture area), the optical efficiency is improved for inclined irradiations far from noon, in which we are interested (Figure 5-10). For example, at an angle of 45°, about 20% improvement in optical efficiency is obtained. This design will decrease the optical efficiency around noon, but it is not an issue as the structure would be CPC around noon. By further optimizations in separate studies, the gain would become more.

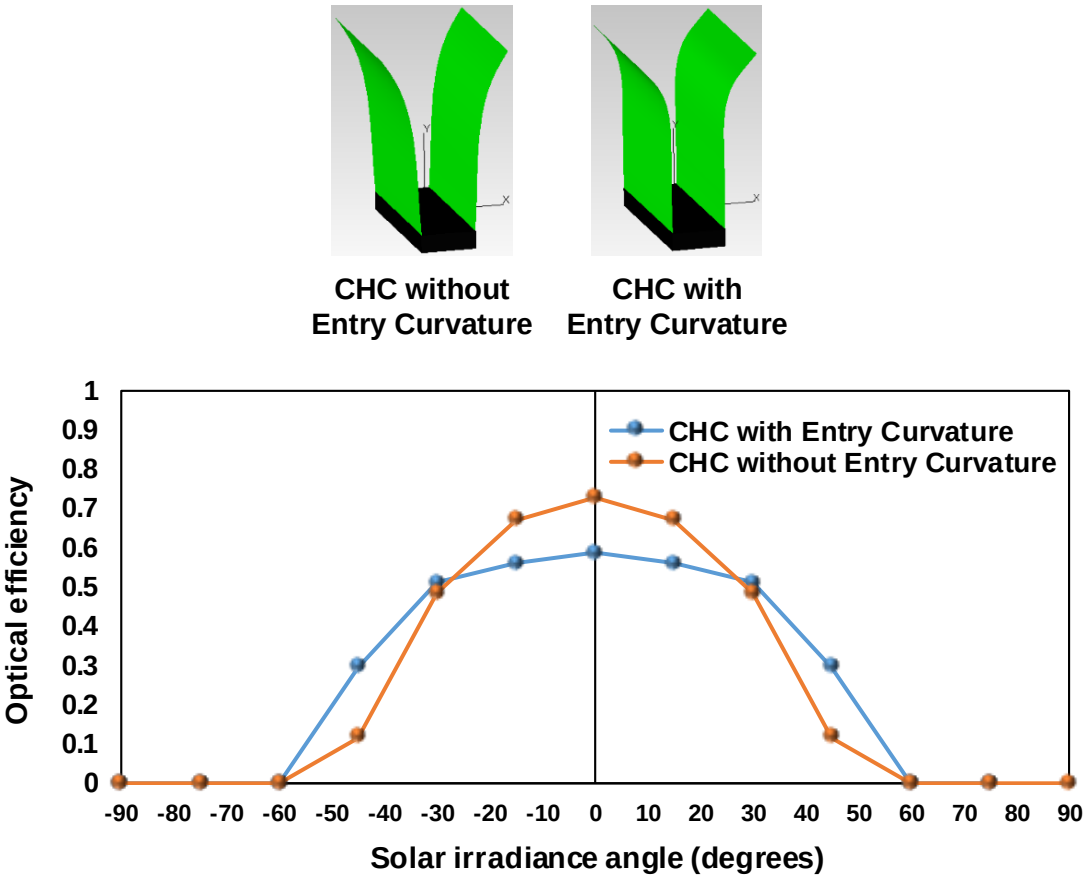

Figure 5-10. The effect of our so-called Entry Curvature on the optical efficiency of CHC at various solar irradiance angles. The concentration ratio and height are kept constant in both the cases.

5.4 Experiment

In the following, we demonstrate the design, fabrication and the desired shape-shifting of the proposed 4D printed solar concentrator based on the results of Figure 5-4 and Figure 5-5. The steps are presented in Figure 5-11. We need a smart concentrator that is parabolic at high

temperatures (because it needs to be parabolic around noon) and is hyperbolic at low temperatures (because it needs to be hyperbolic far from noon). As seen in Figure 5-11 (c), by considering the geometry of the two ends of the concentrator, the proposed concentrator meets this requirement. Here, we used a hot plate (CIMAREC, model SP131325) to apply heat. However, the mechanisms that provide heat can be explored, separately. For example, heat can be provided directly by making a connection between the sunlight`s energy and the desired geometry change, instantaneously; or by storing the sunlight`s energy and releasing it at a designed rate. To this end, other smart materials whether thermo-responsive materials with low glass transition temperature (T_g) or photo- responsive ones should be studied as well.

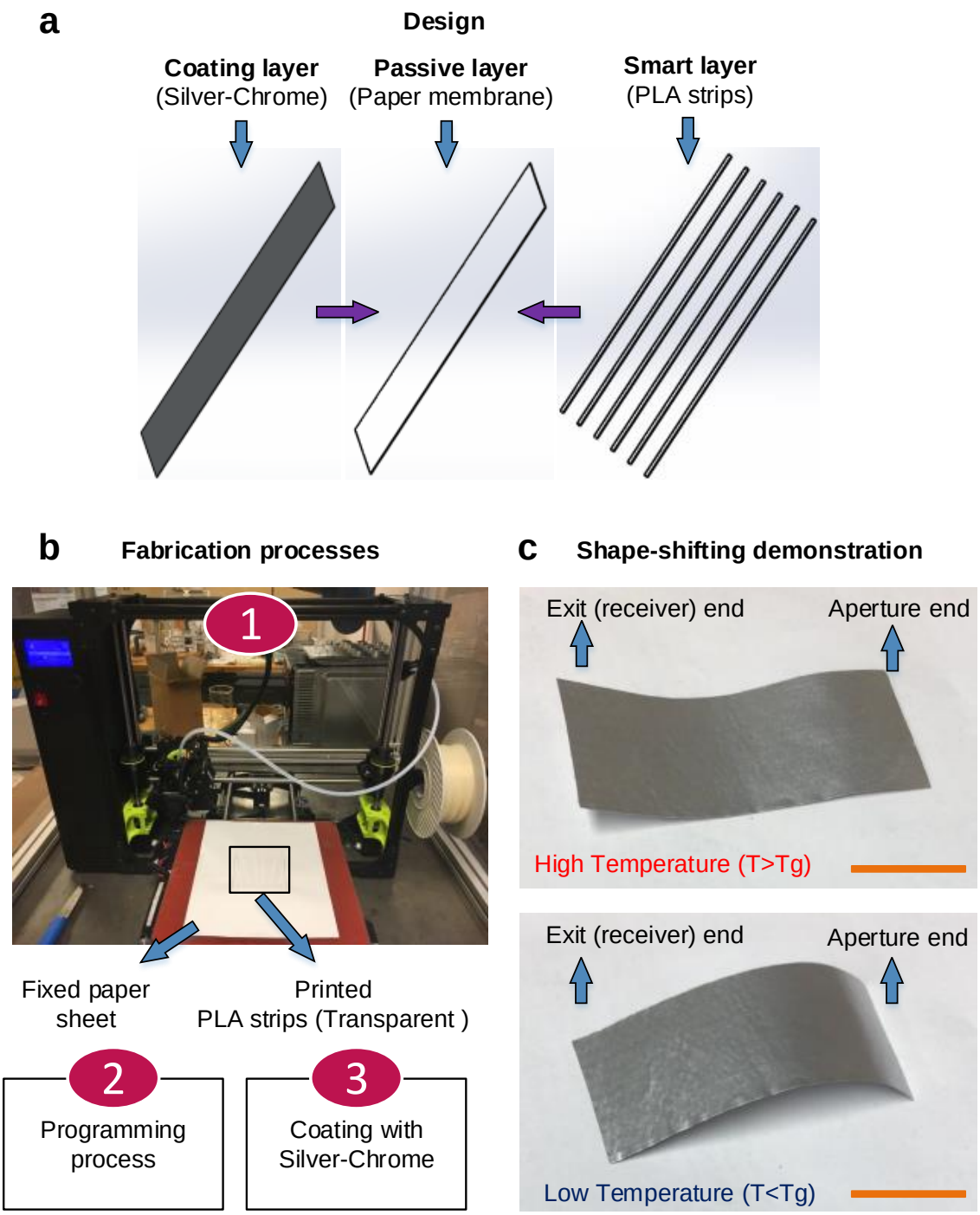

Figure 5-11. Design, manufacturing, and desired shape-shifting. (a) illustrates the design process. (b) exhibits the fabrication steps that consist of three processes. Process 1 shows one example of the PLA printing on a paper sheet. (c) shows the desired reversible shape-shifting between hyperbola at low temperatures (consistent with the weather conditions far from noon) and parabola at high temperatures (consistent with the weather conditions around noon). Scale bars are 3.5 cm.

The proposed structure contains three layers including PLA (polylactic acid), paper sheet, and silver-chrome. PLA is a thermo-responsive shape memory polymer with a glass transition temperature of around 60 ºC. The PLA layer plays the role of the smart (active) layer. The paper sheet plays the role of the passive (non-smart) layer. The silver-chrome portion is a coating layer serves as the reflector. The PLA layer has been modeled by a CAD software (Solidworks 2016) and consists of 6 strips, each of which has 80mm length, 1mm width, and 0.2mm thickness (these four numbers were flexible, and other values for the design parameters worked, as well). The spacing between adjacent PLA strips is 5mm (2mm to 5mm worked for the desired shape-shifting of this structure). The CAD model was converted from STL file to G-code format by Cura 20.01 software. The PLA filaments (transparent color) were printed onto a paper sheet by using LuzBot, TAZ 6 printer that operates with FDM (Fused deposition modeling) method. The printer was used with a printing speed of 50mm/s, a bed temperature of 60 °C, a nozzle temperature of 205 °C, and a resolution of 100 microns (z-direction).

After printing process and before coating, we need to perform the programming step of the structure. Programming is a process in the shape memory polymers, in which we embed a memory of the desired shape (by applying mechanical force in the desired direction) in the structure during the thermomechanical cycle, which can be activated upon exposure to the right stimulus. Without the programming step, the PLA/paper composite will uniformly bend toward the PLA layer after heat treatment (exposing to a temperature higher than the T_g of smart layer for a few minutes and then putting at room temperature) as done by Zhang et al. (2016).

Uniform bending is not suitable for our goal by considering the geometry of concentrators. Moreover, without the programming step, the structure would become totally flat at high temperatures that again is not suitable. Thus, without the programming step, the structure will have a reversible shape-shifting between a uniform bending (arc shape) at low temperatures and flat shape at high temperatures. However, with programming, the structure will have the desired shape-shifting as seen in Figure 5-11 (c). Here, we only need to program one end of the concentrator (the end that is close to the receiver) so that this end will bend toward the silver-chrome layer at high temperatures (to provide parabola) and becomes flat at low temperatures (to provide hyperbola). The low and high temperatures are specified as lower and higher than the T_g of the smart layer, respectively. In the proposed structure, after we reach the suitable shape-shifting by programming step, for the subsequent cycles there is no need for programming step and heat is the only

requirement for the desired reversible shape-shifting. The coating process was the last step to avoid the negative effects of printing and programming steps. For the coating step, we sprayed silver-chrome (NC.FORMULA, SPRAY PAINT, MONTANA.CANS) on the other side of the paper sheet so that the paper sheet was the middle layer as shown in Figure 5-11 (a).

The mathematical modeling of the solar concentrator of this chapter is similar to the mathematical modeling of the wind blade of the previous chapter, as the bilayer structure has the same materials discussed in previous chapter. This mathematical modeling makes a connection among four main elements involved in 4D printing mathematics: (1) printing paths (which in this study are identified by width, length, and thickness of PLA strips); (2) final desired shape (which in this study is identified by bending angle of the structure); (3) materials properties (which in this study are Young`s modulus and thermal expansion coefficient), and (4) stimulus properties (which in this study is the heating rate). The effect of the coating layer on bending angle is neglected in this work.

This structure is an example of smart origami (considering the folding concept as local bending). The proposed concept and paradigm can be further explored for various cases in future. Other smart and passive materials can also be incorporated. The accuracy of the coating layer can be improved by other techniques such as E-beam deposition. Solar simulators can be utilized to study the total efficiency improvement in solar PV applications. The robustness of the proposed structure to environmental conditions can be tuned by adjusting the thickness of the PLA layer to produce as much rigid structure as needed. This rigid structure becomes soft only above the T_g, during the shape-shifting. The next consideration is related to the degradation of the 4D printed structure (Momeni et el., 2016) so that the smart structure will gradually degrade after some cycles and the lifespan of a 4D printed structure should be monitored as well. These considerations regarding new materials, and fabrication processes can be explored in future studies.

5.5 Conclusions

Here, we introduced the general concept of smart solar concentrators inspired by nature and enabled by the 4D printing process. Based on the difference that we observed between diurnal and nocturnal flowers, we devised a study and showed that this biomimetic inspiration unveiled an exciting result in engineering side and could further help us to propose a novel smart solar concentrator. The proposed 4D printed solar concentrator is multi-functional and takes advantages of both types of flowers discussed above. It shows the desired reversible shape-shifting from

parabolic to hyperbolic shape that can improve the overall optical efficiency (day-average) by more than 25% compared with the non-smart solar concentrators. In future studies, this efficiency can be enhanced by various optimizations. The proposed smart solar concentrator does not rely on external sensors and actuators. Moreover, the proposed concept and its design & fabrication processes can be scaled up or down (in microarray applications) for a particular need.

CHAPTER 6

CONCLUSIONS AND FUTURE WORKS

6.1 Conclusions

In history, some topics are coined and enter into research communities and become popular, then after a short period, they lose the broad interests. However, it is expected that 4D printing remains attractive and useful for a long period because stimuli-responsive materials have already demonstrated their promising applications in various fields. Furthermore, 4D printing helps us to locally and precisely encode the stimuli-responsive multi-materials by leveraging the strengths of multi-material additive manufacturing and mathematics that are the elements of 4D printing.

The purpose of this work was to address three main gaps in the emerging field of 4D printing. After a comprehensive review of 4D printing and related areas, we identified three important gaps in this field that were respectively related to design, manufacturing, and product development aspects of 4D printing (details in "Problem statement and dissertation structure", Section 1.7). Our contributions are:

In Chapter 1, by an extensive review, we systematically studied and organized the 4D printing field for future research. We explored, identified, and framed various elements and unsought aspects of the 4D printing (e.g., we framed 4D printing mathematics). We provided a general guideline for the reader by deconstructing the 4D printing process into several main sections. These sections include definition, scope, motivation, shape-shifting behaviors, material structures, materials, shape-shifting mechanisms and stimuli, mathematics, and applications.

In Chapter 2, we revealed three laws that govern the time-dependent shape-shifting behaviors of almost all the multi-material 4D printed structures. Our laws starting from the most fundamental concepts and ending with general equations are essential for future research in the 4D printing field, where the time-dependent behaviors should be comprehended, modeled, and

predicted, correctly. The main part of 4D printed structures is the 4th D; however, currently, there is no general formula to model and predict this extra dimension. Here, by starting from the equilibrium and compatibility conditions and developing some concepts, we derived a bi-exponential formula that "is needed" for modeling and predicting the 4th D of any multi-material 4D printed structure. We further validated our bi-exponential formula by various experimental data from separate studies in the literature and showed that it was a general formula for any type of 4D multi-material structure (photochemical-, photothermal-, solvent-, pH-, moisture-, electrochemical-, electrothermal-, ultrasound-, enzyme-, etc.-responsive). This generality happens, because we built the bases of our bi-exponential formula, comprehensively. The overall results of this chapter can serve as general design principles. Future software and hardware developments in 4D printing can benefit from these results, as well.

In Chapter 3, first, we underpinned 4D printing as a new manufacturing process and identified its unique attributes. Then, as a first attempt, we considered the energy aspect of 4D printing. By a thermodynamic analysis, we proved that 4D printing could be the most energy-efficient manufacturing process, and obtained its theoretical limit.

In Chapter 4, we demonstrated plant leaf-mimetic wind blade in *practice* that *simultaneously* is capable of bend-twist coupling shape-shifting. Our proposed smart blade can demonstrate reversible BTC, with no need for electromechanical systems and moving parts. Moreover, we separated adaptability and flexibility concepts in wind blades, based on which our proposed paradigm may solve the flutter instability issue seen in blades capable of BTC through passive methods. The above four advantageous blade features were integrated into one structure by the 4D printing process. Our multi-functional blade can also lead to eco-friendly wind turbines. Wind tunnel tests and performance analysis showed the applicability of the proposed blade.

In Chapter 5, we introduced the general concept of smart solar concentrators inspired by nature and enabled by 4D printing. Our smart concentrator can increase the overall optical efficiency by more than 25% compared with its non-smart counterparts. In addition, we introduced Trapping Zone and Entry Curvature design principles for solar concentrators enabled by 4D printing.

6.2 Future works

A market study announced on the Reuters website (Costello, 2018) indicates that 3D printing market will have a CAGR (compound annual growth rate) of 30.20% from 2017 to 2022, while

4D printing market will have a CAGR of 40.30% from 2017 to 2022. Definitely, the total investment on 3D printing is more than 4D printing, at the present time. However, the aforementioned statistics compare the growth (the future perspective) between 3D and 4D printing.

3D printing, by itself, is considered a multi-disciplinary field. Thus, more research areas will be involved in the 4D printing field. This diversity can increase the strength of 4D printing.

Future works can consider several topics. One of the main topics is the compatibility of materials in multi-material structures. The materials should form a strong bond at their interface. Their bond should also remain strong under stimuli. The other topic is the measurement and modeling of critical parameters in the bi-exponential formula such as the time-constants. Some of the parameters should be measured for active-passive materials, while models (whether case-specific or general) can be developed for some of them. Experimental studies can be conducted to find the exact values or the ranges of parameters for categories of materials.

The next topic lies in software and hardware developments and their "integration". Future 4D printing software should have some levels of predictions. It can also provide a situation for tuning the behavior over time. Future 4D printing hardware developments require some controls strategies that can handle multi-material printing. Assume that ten different materials are going to be encoded in a single-piece structure, in its various locations (voxels), through ten different nozzles that are going to work, simultaneously. As we proposed in chapter 3, future "4D *printers*" need to have an "intelligent head" with a built-in inverse mathematical problem (an integrated software/hardware added to current multi-material 3D printers) to predict evolutions over time (the 4th D). Printability of smart materials is the next work. There are many smart materials; however, they need to become printable. Tuning the response speed is also an important topic.

The next point is related to product development by 4D printing. In fact, 4D printing is not a concept in physics, chemistry, or medicine. It is a new manufacturing process, as 3D printing (additive manufacturing) is a manufacturing process. Manufacturing is always connected with design and their integration leads to a product. Therefore, new products or applications that can have unique features by 4D printing, should continuously be considered and addressed.

Recently, many exciting works have been demonstrated by 4D printing that can hardly be achieved by other processes. However, more collaborations between scientists and engineers from various fields are needed to move from lab to fab and unveil full potentials of 4D printing.

APPENDIX A

Details of our review on 4D printing

A.1 Shape-shifting behaviors

The shape-shifting behaviors considered in 4D printing include folding, bending, twisting, linear or nonlinear expansion/ contraction, surface curling, and the generation of surface topographical features. These features include wrinkles, creases, and buckles. The shapes can be shifted from 1D to 1D, 1D to 2D, 2D to 2D, 1D to 3D, 2D to 3D, and 3D to 3D. It should be noted that a structure that shows 1D-to-1D shape-shifting over time is also considered to be a 4D printed structure. This is because this structure is initially 3D printed and then evolves over time. Before analyzing the shape-shifting types and dimensions, some relevant definitions are presented first.

A.1.1 Shape-changing vs. Shape-memory materials

Zhou et al. (2016) explained that shape-shifting materials could be divided into two sub-classes: shape-changing materials and shape-memory materials. A shape-changing material changes its shape immediately after a stimulus is applied, and returns to its permanent shape immediately after the stimulus is removed. On the other hand, the shape-memory effect (SME) involves a two-step cycle. Step 1 is the programming step in which a structure is deformed from its primary shape then held in a metastable temporary shape, and Step 2 is the recovery step in which the original shape can be recovered with an appropriate stimulus (Zhou et al., 2015; 2016; Sun et al., 2010). The SME can be further classified into two subsets: (1) One-way shape memory materials, and (2) Two-way shape memory materials (Zhou et al., 2016).

One issue with classical one-way SME is irreversibility (Hager et al., 2015). After the original shape is recovered, a new programming step is needed to re-create the temporary shape. This issue can be avoided with two-way SME, which can alter shape in a reversible manner (Hager et al., 2015). This concept is illustrated in Figure A-1.

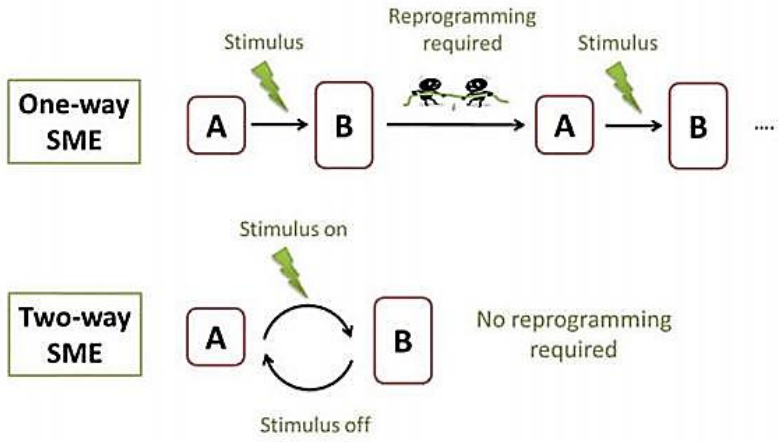

Figure A-1. Illustration of the difference between one-way and two-way shape memory materials (Hager et al., 2015).

A.1.2 Dual, triple, and multi shape memory effects

Shape memory materials belong to the category of stimulus-responsive materials shown in Figure 1-4. Hager et al. (2015) described that in shape memory materials, the permanent shape was "memorized" by the material and alterations between a permanent and a temporary shape occurred. A dual-SME material includes one permanent shape and one temporary shape, while a triple-SME material has one permanent shape and two temporary shapes (Figure A-2). Similarly, a multi (n)-SME material has one permanent shape and $(n-1)$ temporary shapes (Hager et al., 2015). Multi-SME materials were discussed by Xie (2010), Yu et al. (2012), Sun et al. (2010), Therien-Aubin et al. (2013), and Li et al. (2016).

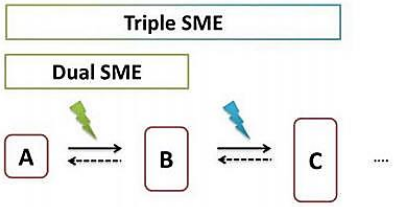

Figure A-2. Illustration of dual and triple SME (Hager et al., 2015), where A is the permanent shape.

A.1.3 Folding vs. bending

The difference between folding and bending is nuanced. Bending is a global deformation associated with smoother curvatures, while folding is localized deformation that is associated with

sharp angles occurring in a narrow hinge area (Ryu et al., 2012; Peraza-Hernandez et al., 2014). A series of local folding results in bending (Liu et al., 2016). In other words, bending relates to a distributed curvature, whereas folding is more localized (Lauff et al., 2014). These concepts are shown in Figure A-3 (Peraza-Hernandez et al., 2014; Liu et al., 2016).

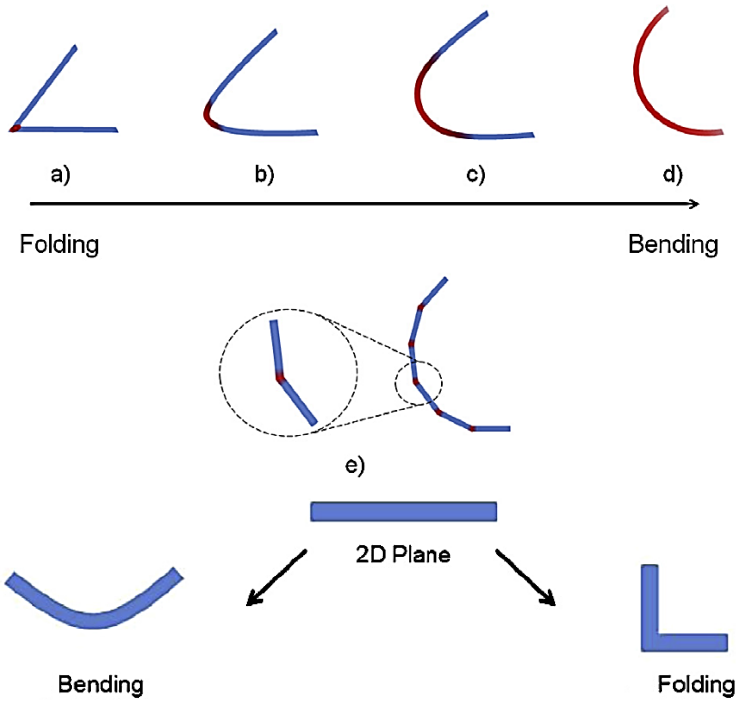

Figure A-3. The difference between folding and bending (Liu et al., 2016).

A.1.4 Surface topography

Surface topography is the representation of local deviations of a surface from a flat plane. Typical features include wrinkling, creasing, and buckling, as shown in Figure A-4. These features usually occur under compressive loading conditions (Wang & Zhao, 2014) and have been quantitatively studied by Wang and Zhao (2014). They allow for an approach based on the Maxwell stability criterion to predict the initiation and growth of various types of these features.

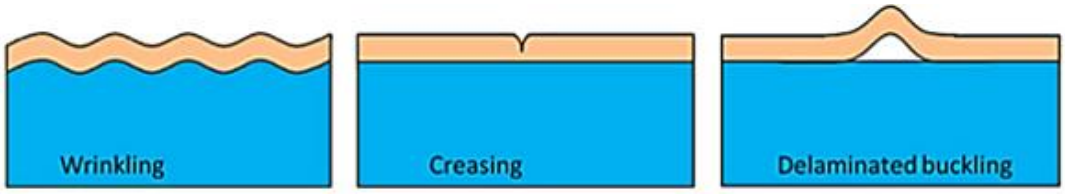

Figure A-4. Surface topography: wrinkling, creasing, and buckling (Wang & Zhao, 2014).

A.1.5 Shape-shifting types and dimensions

- **1D-to-1D expansion/contraction:**

Raviv et al. (2014) and and Yu et al. (2015) demonstrated the linear expansion/contraction from 1D to 1D through a 4D printing process. The research from Raviv et al. is shown in Figure A-5. The stimulus is water and the 4D printed structure contains alternating layers of passive discs and active hydrogels. After the structure is immersed in water, the hydrogel parts will swell while the passive discs remain the same. By adjusting the ratio of expandable hydrogels to passive discs, the structure can show linear shape-shifting behavior with a desirable final length (Raviv et al., 2014). On the other hand, in the structure obtained by Yu et al., the stimulus is heat, as shown in Figure A-6. Its linear shape-shifting behavior is obtained based on a shape memory cycle, which includes the usual programming and recovery steps for thermoresponsive shape memory polymers (SMP).

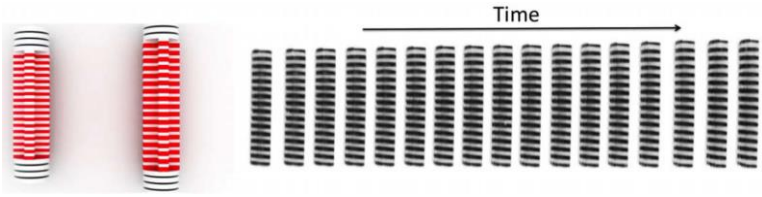

Figure A-5. The illustration of 1D-to-1D shape-shifting by linear expansion/contraction adapted from (Raviv et al., 2014).

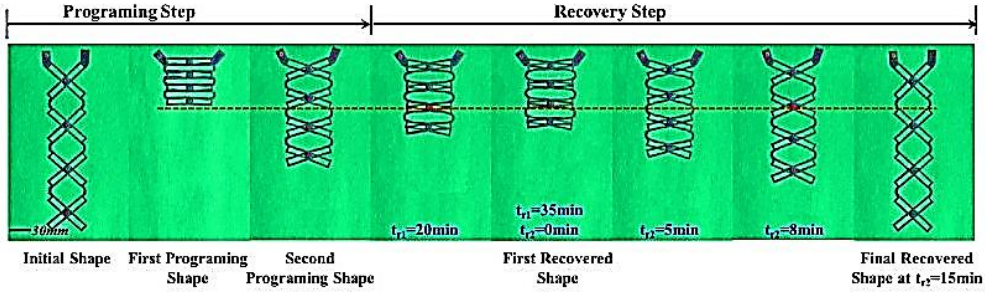

Figure A-6. The illustration of 1D-to-1D shape-shifting by linear expansion/contraction adapted from (Yu et al., 2015).

- **1D-to-2D Folding:**

Tibbits (2014) printed a single strand structure that can transform into the letters "MIT" when subjected to water. This is a demonstration of 1D to 2D shape-shifting by self-folding mechanism (Figure A-7). There are two types of materials involved in the structure: passive and active. The active material is a hydrogel that can swell when immersed in water while the passive parts remain intact. This difference provides a stress mismatch and enables the overall shape to be

changed toward a specific direction. The position and volume of the active and passive materials in the structure can be designed to achieve different shape-shifting directions.

Figure A-7. The illustration of 1D-to-2D shape-shifting by self-folding (Tibbits, 2014).

- **1D-to-2D Bending:**

Tibbits et al. (2014) then created a linear strip structure with alternating sections of the passive and active materials described above. This structure can transform into a precise sinusoidal shape when immersed in water (Figure A-8). This is a demonstration of 1D-to-2D shape-shifting using the self-bending mechanism.

Figure A-8. An illustration of 1D-to-2D sinusoidal shape-shifting by self-bending (Tibbits et al., 2014).

- **1D-to-3D Folding:**

Tibbits (2014) also created a single strand structure that could transform into a 3D-cube wireframe when subjected to water (Figure A-9). The structure contains the same two materials described above. This is an illustration of 1D-to-3D shape-shifting by self-folding mechanism. For each wireframe hinge, two passive discs are embedded in the hydrogel part, which connects the two passive strands. This is shown in Figure A-10. These two passive discs can limit the maximum degree of free shape-shifting. For example, in order to stop the deformation of the two strands at 90° to create a cubic shape, the two passive discs can be placed to touch each other at this final position, which prevents additional folding. The amount of folding is determined by the size of the two discs and the distance between them. According to Tibbits (2014), increasing the diameter of the discs or decreasing the distance between the discs will reduce the final folding angle amount.

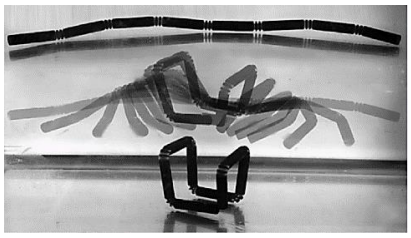

Figure A-9. The self-folding of 1D strand to 3D wireframe cube (Tibbits, 2014).

Figure A-10. Two passive discs to tune the final folding angle (Tibbits, 2014).

In another study, Tibbits et al. (2014) demonstrated shape-shifting from a 1D strand to a 3D structure of Crambin protein, based on the self-folding mechanism (Figure A-11). This shape-shifting behavior is again enabled by the stress mismatch between the passive and active materials from their different swelling properties.

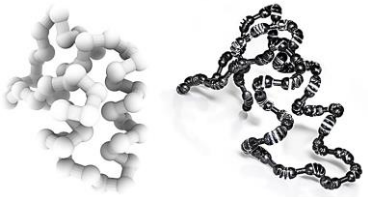

Figure A-11. Shape-shifting from a 1D strand to a 3D structure of Crambin protein based on self-folding (Tibbits et al., 2014).

- **2D-to-2D Bending:**

Villar et al. (2013) illustrated 2D-to-2D self-bending in a 4D bio-printed networks of droplets. As shown in Figure A-12, a rectangular network could be bent into a circle. This shape-shifting behavior is based on the differences in osmolarity of the droplets. The droplets with higher osmolarity swell and the droplets with lower osmolarity shrink. The shape continues to change until the osmolarity gradient becomes zero.

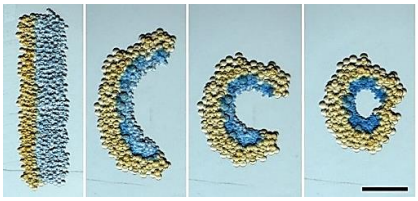

Figure A-12. 2D-to-2D self-bending in which a rectangular network transforms into a circle. Scale bar, 200 μm (Villar et al., 2013).

- **2D-to-3D Bending:**

Wu et al. (2016) applied multi-shape memory effect for 2D-to-3D transformations in various structures, such as the active trestle (Figure A-13), active helix shape (Figure A-14), active wave shape (Figure A-15), smart insect-like structure (Figure A-16), and smart hook (Figure A-17). Heat was the stimulus and these shape-shifting behaviors were achieved in the usual shape memory cycles with well-known programming and recovery steps.

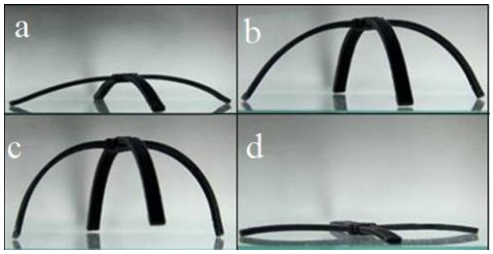

Figure A-13. Multi-shape memory effect from 2D to 3D by self-bending in a smart trestle (Wu et al., 2016).

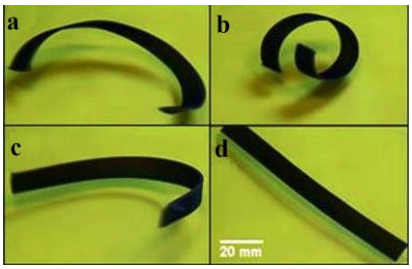

Figure A-14. Multi-shape memory effect from 2D to 3D by self-bending in an active helix shape (Wu et al., 2016).

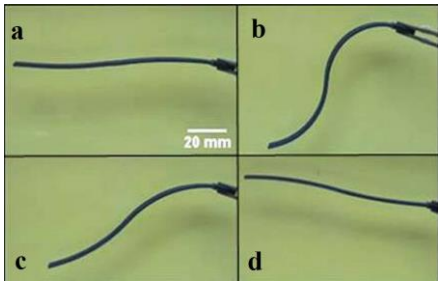

Figure A-15. Multi-shape memory effect from 2D to 3D by self-bending in an active wave shape (Wu et al., 2016).

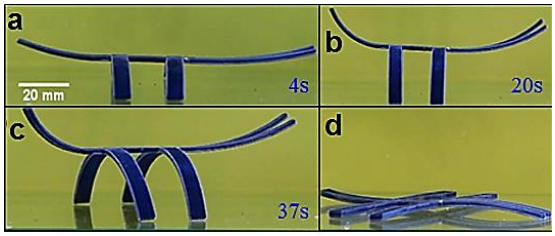

Figure A-16. Multi-shape memory effect from 2D to 3D by self-bending in a smart insect-like structure (Wu et al., 2016).

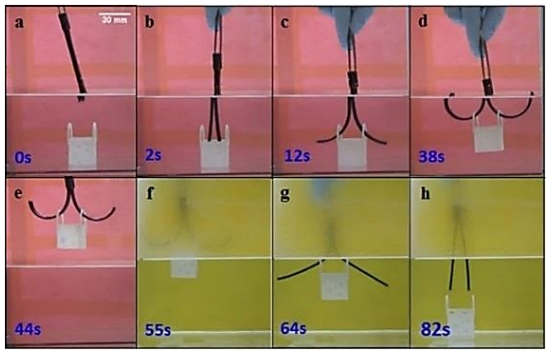

Figure A-17. Multi-shape memory effect from 2D to 3D by self-bending in a smart hook (Wu et al., 2016).

Zhang et al. (2016) demonstrated 2D-to-3D self-bending behavior by creating a flower-like structure. This is shown in Figure A-18(a) and (b). In Figure A-18(c), a complex structure was created by tearing paper off the flower-like 3D structure. Heat is the stimulus in this shape-shifting behavior. However, their experiment is different from the regular shape memory cycles with programming and recovery steps. In this mechanism, there is no need to apply external force at a high temperature and cool down to a low temperature while maintaining the previously applied force. The shape-shifting behavior is enabled by different thermal expansion coefficients of the active and non-active materials.

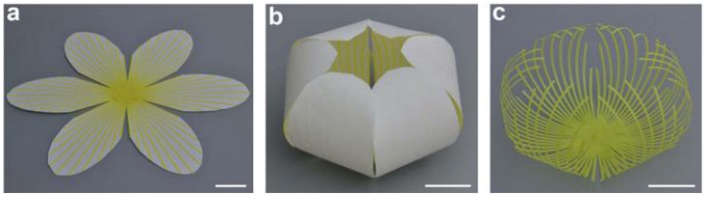

Figure A-18. Flower-like 4D structure. (a) The original flat sheet. (b) The final flower-like structure. (c) A complex structure created by tearing paper off the flower-like 3D structure (Zhang et al. 2016).

In another experiment performed by Zhang et al. (2016), a 3D periodic structure was achieved from a 2D sheet consisting of four periodic cells in a square arrangement. Each cell included one central region and four rectangular neighbors, as shown in Figure A-19. The mechanism of this shape-shifting behavior is similar to that exhibited in the previous experiment.

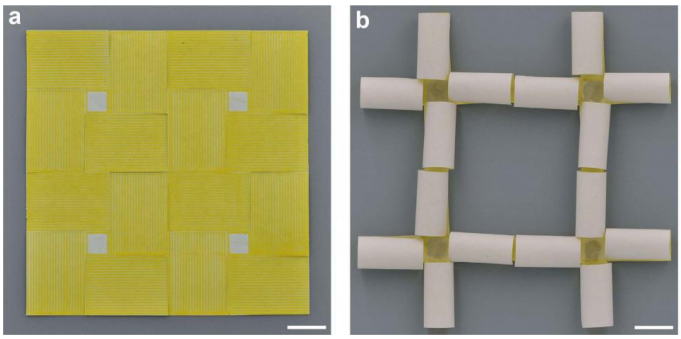

Figure A-19. A 3D periodic structure created from a 2D sheet by self-bending (Zhang et al., 2016).

Jamal et al. (2013) illustrated a shape alteration for tissue engineering purposes in which a 2D bio-origami planar pattern changed to a 3D pattern based on the self-bending operation (Figure A-20). This shape-shifting is enabled by the different swelling ratios of hydrogels and passive materials under water.

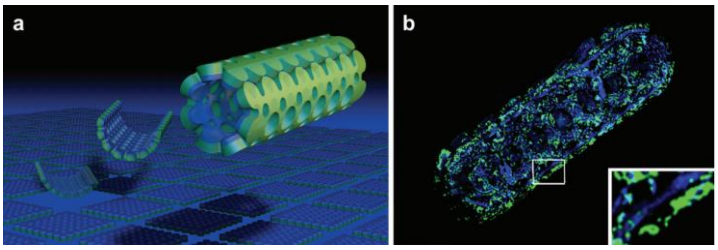

Figure A-20. A bio-origami 2D pattern transforms into a 3D pattern by self-bending: (a) Schematic illustration of the self-bending of PEG bilayer. (b) A fluorescent micrograph of a self-bended bilayer (Jamal et al., 2013).

Villar et al. (2013) illustrated 2D-to-3D self-bending behavior in which a flower-shaped network of droplets transforms into a hollow sphere. This is shown in Figure A-21. This shape-shifting is enabled by the osmolarity gradient of the droplets described earlier.

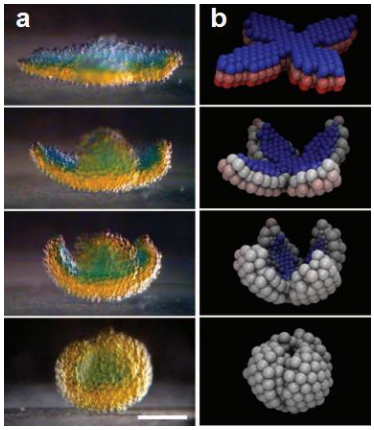

Figure A-21. (a) The experiment related to 2D-to-3D self-bending in which a flower-shaped network transforms into a hollow sphere. Scale bar, 200 µm (b) Simulation of (a) (Villar et al., 2013).

- **2D-to-3D Folding:**

As shown in Figure A-22, Tibbits (2014) printed a 2D flat plane that could be folded into a closed-surface cube, which presented 2D-to-3D shape-shifting behavior based on self-folding. This shape-shifting behavior is enabled by a stress mismatch between passive and active materials due to their different swelling behaviors under water.

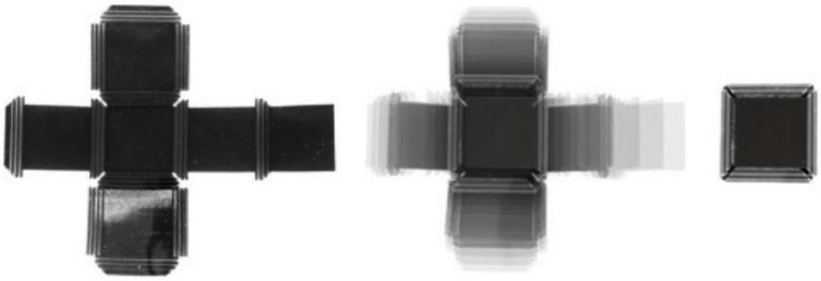

Figure A-22. An illustration of 2D to 3D shape-shifting by self-folding to make a cube (Tibbits, 2014).

The same shape-shifting behavior from a 2D pattern to 3D cube based on self-folding was also illustrated by Naficy et al. (2017), where both water and heat were required as stimulus. They printed bilayer hinges made of active and non-active gels. The active layer is a temperature-sensitive hydrogel. In a dry condition at room temperature, the cube is flat. When submerged in water at room temperature, the active hydrogel swells and the flat structure is folded. However, if the temperature of the water is increased above the lower critical solution temperature (LCST) of

the active hydrogel, the folded structure unfolds. This occurs because the active hydrogel collapses above its LCST (which is mainly due to the breaking of the hydrogen bondings).

As shown in Figure A-23, a truncated octahedron was created by Tibbits et al. (2014) and shows 2D to 3D shape-shifting behavior based on self-folding mechanism. This shape-shifting is enabled by the stress mismatch between passive and active materials due to their different swelling ratios.

Figure A-23. 2D-to-3D self-folding to make a truncated octahedron (Tibbits et al., 2014).

Ge et al. (2013) showed self-folding transformations from 2D flat sheets to 3D shapes, examples of which included an active origami box, pyramid, and airplanes (Figure A-24). These shape-shifting behaviors are triggered by heat in the usual shape memory cycles with the regular programming and recovery steps.

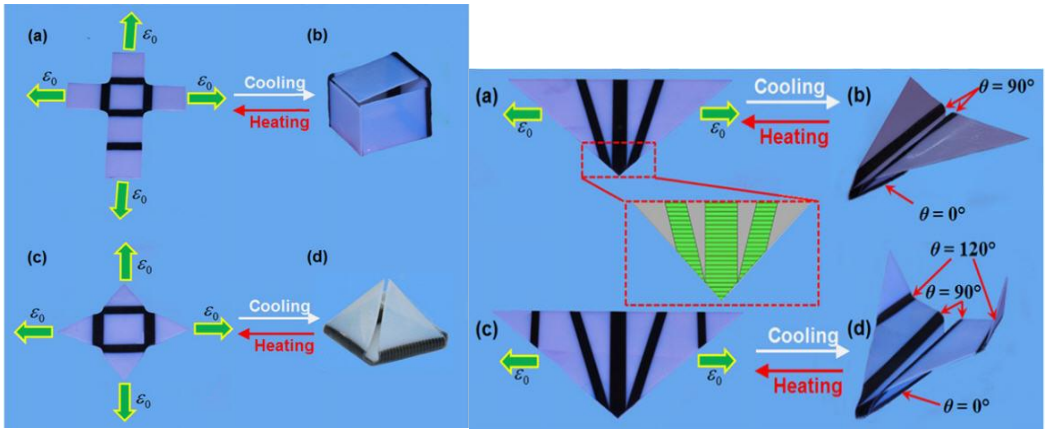

Figure A-24. An illustration of a 2D-to-3D alteration in which some origami shapes, such as an origami box, pyramid, and airplane can be generated by self-folding (Ge et al., 2014).

Mao et al. (2015) demonstrated a sequence of self-folding operations for transforming a 2D strip into 3D shape, as shown in Figure A-25. This shape-shifting behavior is also triggered by heat in the regular shape memory cycles with programming and recovery steps.

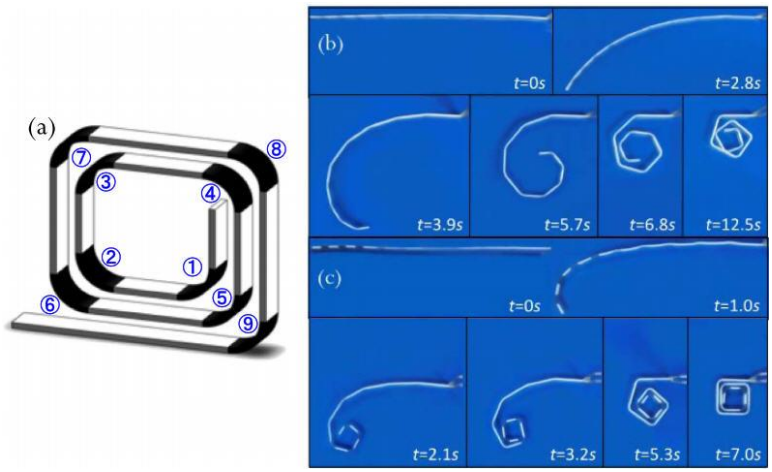

Figure A-25. Sequential self-folding from 2D to 3D (Mao et al., 2015).

- **2D-to-3D Twisting:**

Zhang et al. (2016) illustrated helical structures with different spiral degree patterns by twisting a 2D sheet and converting it to 3D shapes, as shown in **Error! Reference source not found.**. This shape-shifting behavior has a similar mechanism to that shown in Figure A-18 and Figure A-19. In addition, Zhang et al. (2018) printed the fibers with certain angles to induce twisting, and by adjusting the print angles of active fibers, the final twist angle would be changed.

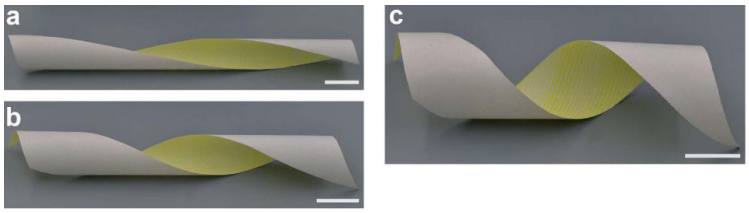

Figure A-26. Helical structures with different degrees of spiral by 2D-to-3D twisting (Zhang et al., 2016).

- **2D-to-3D Surface Curling:**

Tibbits et al. (2014) fabricated a surface grid structure with alternating upper and lower segments of expandable materials, which could yield a mathematical sinusoidal surface under water (Figure A-27). This was a demonstration of 2D to 3D shape-shifting behavior with a surface curling feature. This shape-shifting behavior is enabled by a stress mismatch between passive and active materials from their different swelling properties under water.

Figure A-27. 2D-to-3D sinusoidal shape-shifting by surface curling (Tibbits et al., 2014).

To further illustrate surface curling behavior, hair-like structures were generated from vertical linear strips by Tibbits et al. (2014) (Figure A-28). The mechanism is the same as above.

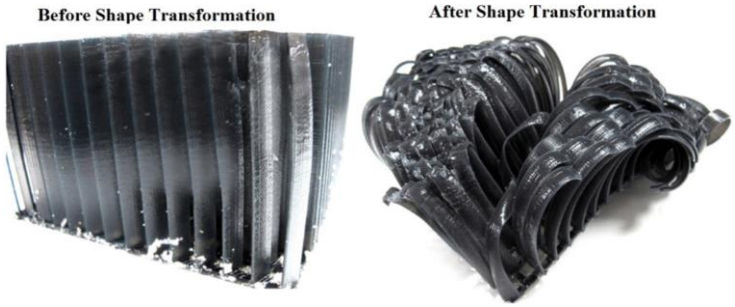

Figure A-28. An illustration of 2D-to-3D hair-like shape-shifting by surface curling (Tibbits et al., 2014).

Raviv et al. (2014) illustrated 2D-to-3D surface curling behavior with various configurations (Figure A-29). The mechanism is the same as that described above.

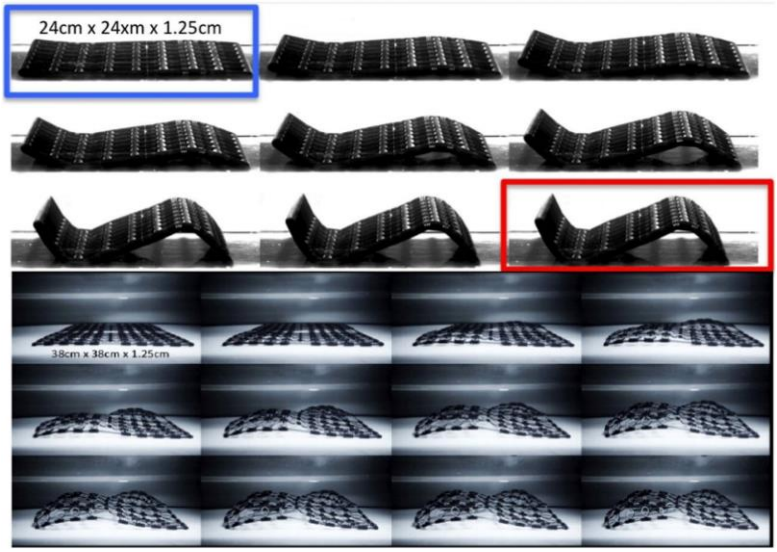

Figure A-29. 2D-to-3D surface curling (Raviv et al., 2014).

Ge et al. (2013) demonstrated 2D-to-3D shape-shifting behavior in which a flat sheet was transformed into a complex and non-uniform curvature shape as a sculpture (Figure A-30). This shape-shifting behavior is triggered by heat in the usual shape memory cycles.

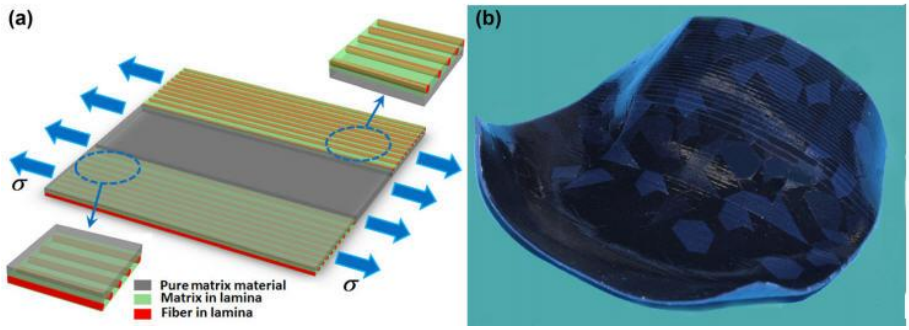

Figure A-30. An illustration of 2D-to-3D alteration in which a complex, non-uniform curvature sculpture is achieved: (a) Schematic of the flat laminate. (b) The final desired shape after the thermo-mechanical experiment (Ge et al., 2013).

- **2D-to-3D surface topographical change:**

In one experiment from Tibbits et al. (2014), mountain and valley features could be generated from concentric circles in the presence of an appropriate stimulus (Figure A-31). This is an illustration of 2D-to-3D change in surface topography. This shape-shifting behavior is enabled by a stress mismatch between passive and active materials from their different underwater swelling properties.

Figure A-31. An illustration of 2D-to-3D surface topographical changes where mountains and valleys are created on a flat surface (Tibbits et al., 2014).

Tibbits et al. (2014) showed another 2D-to-3D surface topographical change in Figure A-32. In this test, three shapes evolved as a function of time (zero minutes, thirty minutes, and twenty-four hours in contact with stimulus). These sinusoidal topographies are generated based on the

different swelling ratios between the active and passive materials. The concentrations of these materials vary from the center to the perimeter of the disc.

Figure A-32. 2D-to-3D shape-shifting with surface topography (Tibbits et al., 2014).

- **2D-to-3D Bending and Twisting:**

Gladman et al. (2016) demonstrated a combination of 2D-to-3D bending and twisting behavior with complex flower morphologies. This is produced by the biomimetic 4D printing process shown in Figure A-33. This shape-shifting behavior is caused by the differences in the swelling ratios of active and passive materials under water.

Figure A-33. 2D-to-3D shape-shifting by the combination of bending and twisting with complex flower morphologies (Gladman et al., 2016).

Ge et al. (2013) also demonstrated 2D-to-3D bending, twisting, and a combination of the two, as shown in Figure A-34. This shape-shifting behavior is triggered by heat in the usual shape memory cycles with the well-known programming and recovery steps.

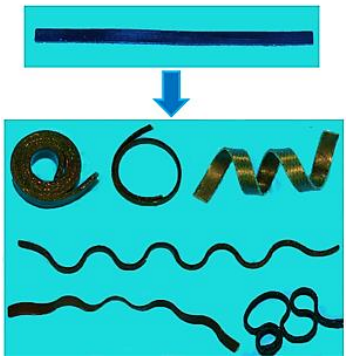

Figure A-34. Various 2D-to-3D shape-shifting behaviors (Ge et al., 2013).

- **3D-to-3D Bending:**

Kokkinis et al. (2015) showed 3D-to-3D self-bending in a bio-printed structure, as illustrated in Figure A-35. This shape-shifting behavior is triggered by the dissolution of an appropriate material into a suitable solvent, which will be further described in the section discussing shape-shifting mechanisms and stimuli.

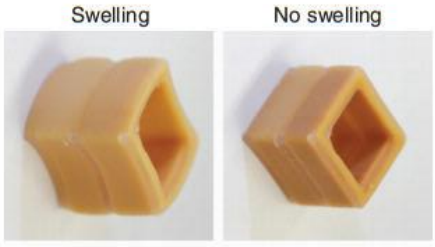

Figure A-35. An illustration of 3D-to-3D self-bending in a bio-printed structure (Kokkinis et al., 2015).

Mutlu et al. (2015) demonstrated the 3D-to-3D self-bending shape-shifting behavior in a prosthetic finger made from thermoplastic elastomer (TPE), as shown in Figure A-36.

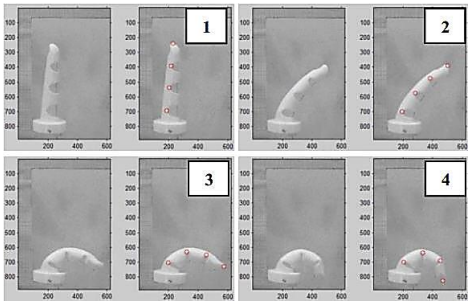

Figure A-36. 3D to 3D self-bending in a prosthetic finger (Mutlu et al., 2015).

- **3D-to-3D Linear Deformation**

Bakarich et al. (2015) demonstrated 3D-to-3D linear expansion and contraction behavior (Figure A-37). This shape-shifting behavior is enabled by linear free swelling or shrinkage of a thermo-responsive hydrogel in the cold or hot water.

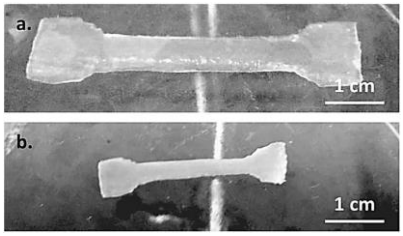

Figure A-37. 3D-to-3D shape-shifting by expansion and contraction (Bakarich et al., 2015).

- **3D-to-3D Non-Linear Deformation:**

Kuksenok et al. (2016) illustrated the concepts of global and local shrinkage and bending for 3D to 3D shape-shifting behavior. Two stimuli are needed for the global and local shape-shifting deformation (Figure A-38). The left side of Figure A-38 shows 3D-to-3D bending, while the right side indicates 3D-to-3D nonlinear shrinkage. The mechanism of this behavior will be described in further detail in the section discussing shape-shifting mechanisms and stimuli.

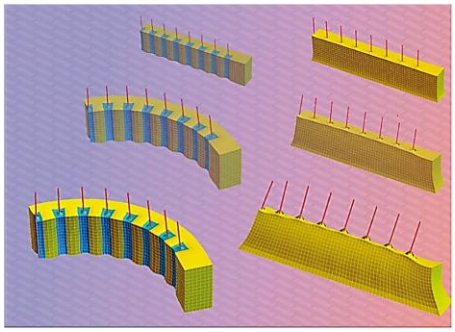

Figure A-38. Illustration of global and local shrinkage and bending for 3D-to-3D alterations by using two different stimuli (Kuksenok et al., 2016).

A.1.6 Discussions

In many applications, a 4D printing process can be used to avoid directly printing a complicated 3D shape. Instead, a lower-dimension shape can be printed first and then the other dimension(s) can be enabled in the target location with the required performance. Printing a lower-dimensional object is relatively easy, fast, and has lower manufacturing costs. Furthermore, the storage and transportation of lower-dimension objects are more convenient. In the study of 2D-to-3D shape-shifting behavior from Liu et al. (2016), the addition of the third dimension could add desired value or functions to the 2D substrates, which could be printed with various ordinary techniques such as inkjet, photolithography, and roll-to-roll printing.

Even though many shape-shifting types and dimensions have been demonstrated in the literature, hybrid shape-shifting behavior is largely unexplored. Future studies can focus on serial and parallel combinations of different shape-shifting types and dimensions. For example, a complex 3D structure can be generated by a designed series of bending and twisting from a 2D substrate. In some conditions, due to space restrictions, twisting shape-shifting is not directly accessible until the 2D pattern is first bent into a certain angle. Accordingly, self-bending can be designed as the first step of the shape-shifting sequence, which allows the structure to access the target location and then perform the desired twisting.

Sequential shape-shifting behavior can provide more complex actuations. However, all of the existing sequential shape-shifting studies are limited to folding deformation, whether it is fabricated from a 4D printing process (Mao et al., 2015; Lee et al., 2015; Baker et al., 2016) or other manufacturing processes (Laflin et al., 2012; Stoychev et al., 2013; Felton et al., 2013). Therefore, other sequential shape-shifting types and their combinations can be studied in future research in this area.

A.2 Applications

The droplets network illustrated by Villar et al. (2013) can be used as tissue engineering substrates or as support for the functionality of failing tissues (Figure 1-19).

Kokkinis et al. (2015) created smart key–lock connectors (Figure A-39) based on the experiments shown in Figure A-35. The walls are flat before swelling. After swelling, convex and concave deformations occur in the wall, which leads to a reduction in the internal size of the cuboid and finally the interlocking can be achieved. The key-lock connector can be used as a physical connection between biological parts in the body, such as tendons and muscle. In addition, it can

be used as the selective pick-and-place system in soft robots. Soft robotics is one main area, where 4D printing can provide benefits (Wallin et al., 2018).

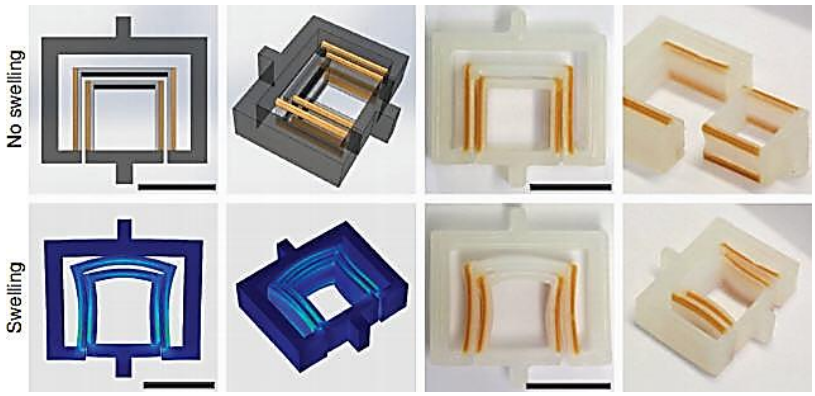

Figure A-39. Smart key–lock connectors that can be employed for various purposes (Kokkinis et al., 2015).

Bakarich et al. (2015) fabricated a skeletal muscle-like reversible actuator with high response speed based on the principle in Figure A-37. They incorporated it into a smart valve (Figure A-40) and controlled the water flow by self-opening of the valve in cold water and self-closing in hot water. This work shows one example of 4D printed soft mechanical actuators (Loh, 2016).

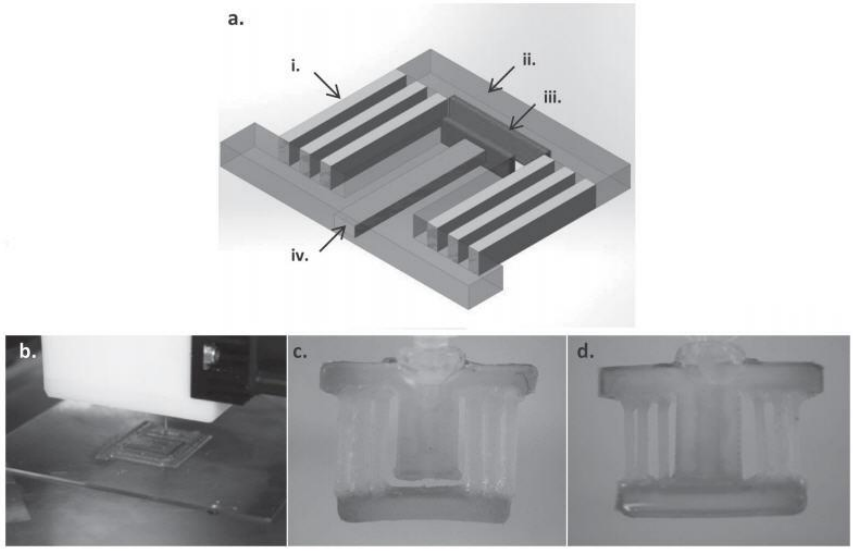

Figure A-40. (a) Computer-aided design of the smart valve, (b) Printing of the valve, (c) 4D printed valve in cold water, and (d) hot water (Bakarich et al., 2015).

Using a different stimulus, Nadgorny et al. (2016) printed a pH-responsive hydrogel valve that demonstrated dynamic and reversible swelling and shrinkage behavior that could regulate the

flow rate under various pH levels (Figure A-41). Additionally, this structure could serve as a useful platform for pH-responsive membranes (Orlov et al., 2007) and photonic gels (Kang et al., 2007).

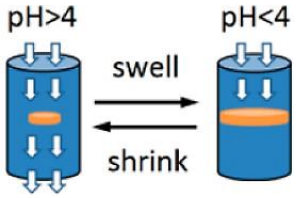

Figure A-41. pH-responsive flow regulating smart valve (Nadgorny et al., 2016).

Adaptive metamaterials with tunable bandgaps enabled by 4D printing were reported by Zhang et al. (2016) (Figure A-42) and later by Bodaghi et al. (2016) (Figure A-43). In both studies, the lattice structure could be reconfigured in a reversible manner, where heat was the external stimulus. The fabricated metamaterial shown in Figure A-43 could be applied as planar self-expanding/shrinking actuators (Bodaghi et al., 2016). The lattice structure demonstrated by Zhang et al. (2016) (Figure A-42) worked under the unconstrained-thermo-mechanics interaction mechanism, while the one reported by Bodaghi et al. (2016) (Figure A-43) worked under the constrained-thermo-mechanics interaction mechanism.

The mechanical properties of metamaterials depend on their geometrical architectures instead of their chemical compositions (Bodaghi et al., 2016). The adaptive metamaterials with tunable band gaps are useful for controlling the elastic waves (Zhang et al., 2016). Adaptive metamaterials can adjust their stiffness based on changes in geometry while keeping their mass constant. Therefore, they can be used as a switch between two different dynamic states (Bodaghi et al., 2016).

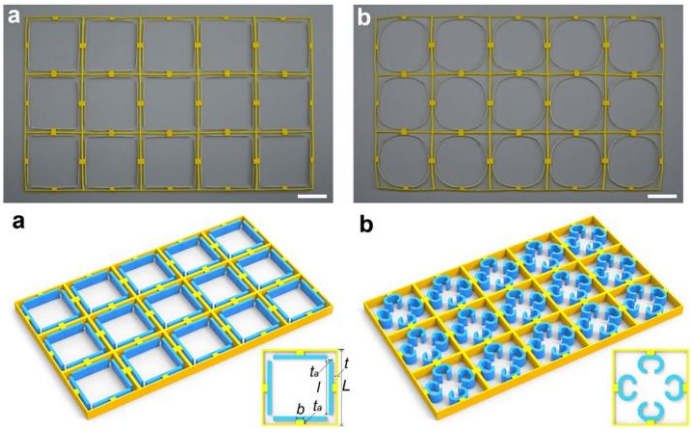

Figure A-42. Thermo-responsive adaptive metamaterials with tunable bandgaps (Zhang et al., 2016).

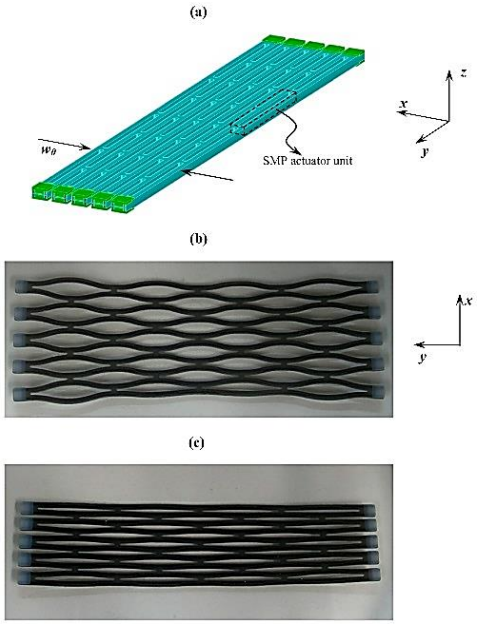

Figure A-43. Thermo-responsive adaptive metamaterials with tunable structures (Bodaghi et al., 2016).

Jiang and Wang (2016) fabricated and analyzed elastomer metamaterials (Figure A-44) that could be used as reversible shape-shifting connectors. The shape-shifting action is enabled by external mechanical loadings. These materials can be applied through the 4D printing process to bridge components for flexible twisting or bending (Jiang & Wang, 2016).

Figure A-44. Elastomer metamaterials (Jiang & Wang, 2016).

Kuksenok et al. (2016) (Figure A-38) developed a 4D-printed structure that could mimic the contraction of an accordion. They also developed a structure to mimic the lateral movement of a caterpillar. Their experiments were suitable to manufacture smart components for new adaptive devices, such as soft robots (Mao et al., 2016).

An active origami box, pyramid, and airplanes illustrated by Ge et al. (2014) show that the 4D printing process is capable of developing smart origami. Origami has attracted a significant amount of interest lately in an effort to solve engineering issues related to the packing of large

structures into small volumes, for the sake of storage and transportation (Ge et al. 2014). In this regard, Kowk et al. (2015) performed the design optimization of origami for freeform surfaces in 4D printing. In addition, Jamal et al. (2013) (Figure A-20) proposed and fabricated self-bending, bio-origami structures that could be used in the field of tissue engineering to analyze the behavior of cells and self-bending vascularized tissue structures. In addition, their findings can be applied to the field of microfluidic networks (Jamal et al., 2013).

The regeneration of Crambin protein structures through self-folding of a 1D strand in water was demonstrated by Tibbits et al. (2014) to serve as a potential solution for biomedical problems. A linear stretching joint, ring stretching joint, and folding joint had been demonstrated by Raviv et al. (2014). These joints could be used in other structures in practice. The development of a fully compliant prosthetic finger was another application that was demonstrated by Mutlu et al. (2015) (Figure A-36).

Wu et al. (2016) showed several smart structures including a smart hook, smart trestle, and a smart insect-like structure so that after the thermomechanical cycle, the structure could undergo shape-shifting between a planar shape and the desired hook, trestle, and insect-like shapes.

A 4D-printed, thermo-responsive, SMP-based, cardiovascular stent was fabricated by Ge et al. (2016) (Figure A-45). Stents are important devices to expand the human vessels and has been the focus of many studies from different perspectives (Anand et al., 2009; Yakacki et al., 2007; Yakacki et al., 2008). Traditional fabrication methods are difficult and time-consuming in providing complex geometries with high resolutions required by stents (Yakacki et al., 2007; Srivastava et al., 2010). Based on a high resolution PμSL additive manufacturing system, Ge et al. (2016) could manufacture the high-resolution stents with various diameters, heights, number of joints, ligament diameters, and inter-ligament angles. Similarly, a 4D-printed thermo-responsive stent (Figure A-46) was demonstrated by Bodaghi et al. (2016), in which the stent diameter could be changed reversibly while the height was kept constant. Both stents (Figure A-45 and Figure A-46) worked under the constrained-thermo-mechanics interaction mechanism. Wei et al. (2016) incorporated Fe_3O_4 in a thermo-responsive PLA-based ink and 4D printed a smart stent which could be guided magnetically and actuated remotely.

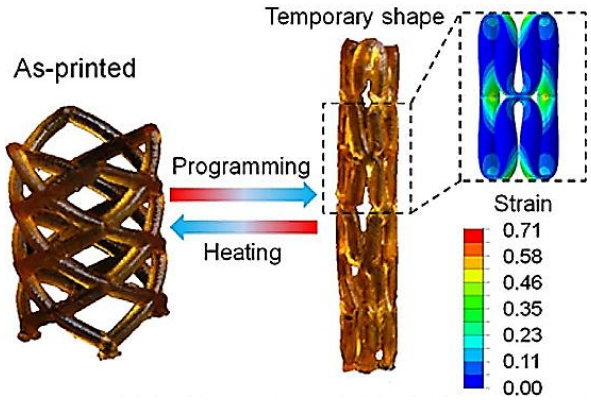

Figure A-45. A 4D-printed, thermo-responsive stent which is able to reversibly change its diameter and height (Ge et al., 2016).

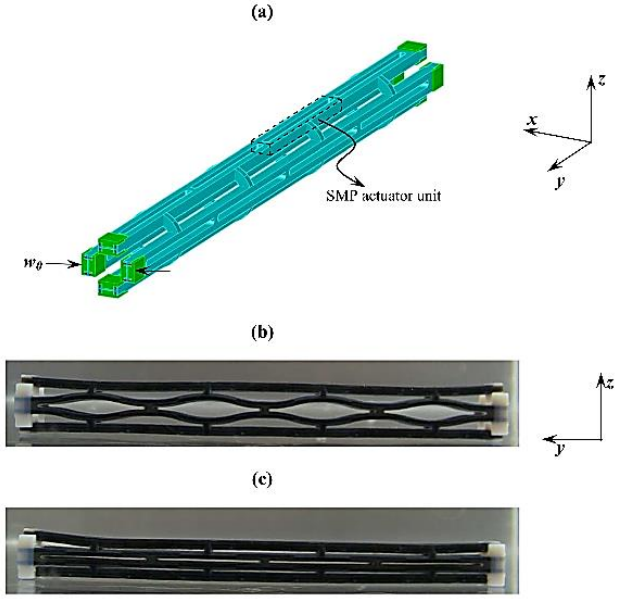

Figure A-46. A 4D-printed, thermo-responsive stent which is able to reversibly change its diameter (Bodaghi et al., 2016).

Zarek et al. (2016) 4D printed a thermo-responsive tracheal stent (Figure A-47), which solved two issues related with the current tracheal stents. First, it fits the arcade pattern and cartilaginous rings better and provides a stable state, which prevents migrations. Second, the shrunk form during insertion prevents the injurious insertion. After being inserted into the body, the tracheal stent can expand to the permanent shape with a local increment in temperature (Zarek et al., 2016).

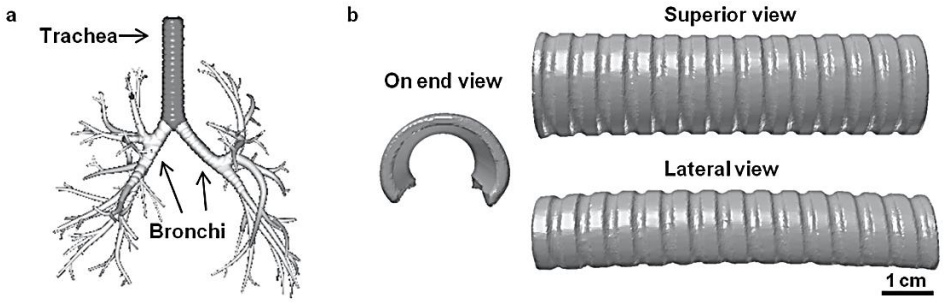

Figure A-47. 4D printed thermo-responsive tracheal stent (Zarek et al., 2016).

Ge et al. (2016) developed a SMP-based thermo-responsive multimaterial gripper, as shown in Figure A-48, which can be applied in drug delivery systems (DDS) (Malachowski et al., 2014).

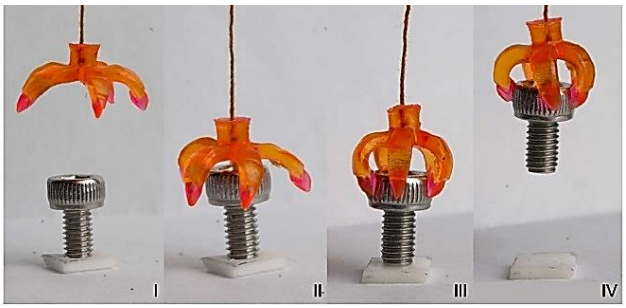

Figure A-48. 4D-printed shape memory gripper that can reversibly grab and release the objects by heat (Ge et al., 2016).

Self-adaptive and multi-functional textiles are some of the potential applications that can be improved by 4D printing (Truby & Lewis, 2016). Self-adaptive smart textile structure can be adapted to a new size without tensile loading, in contrast to the textiles made of elastic fibers (Figure A-49) (Hu et al., 2012). Multi-functional smart textiles are capable of managing the moisture or temperature of the body, monitoring wounds, providing skin care, protecting against harsh climates, or adaptively changing color of a dress (Hu et al., 2012).

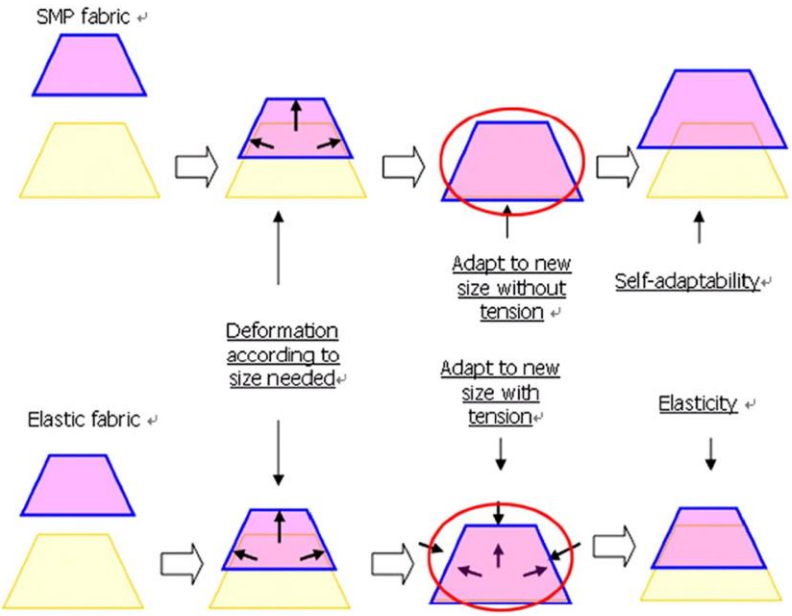

Figure A-49. Adaptability of textiles made of SMP vs. the textiles made of elastic fibers (Hu et al., 2012).

4D bio-printing (An et al., 2015; Gao et al., 2016) of stem cells directly into scaffolds is a significant advancement toward the creation of organs and tissues. The stimulation of stem cell differentiation can provide shape-shifting behavior in a 4D printed scaffold (Irvine & Venkatraman, 2016; Miao et al., 2016; Wei et al., 2016). Laser-based cell printing (Koch et al., 2016) can pave the way for 4D bio-printing of cells.

Recently, a 4D nano-printing process was demonstrated by Carbonell and Braunschweig (2016). The bottom-up 4D nano-printing process is expected to be an effective alternative to the conventional top-down techniques used for fabricating electronics, bioarrays, and functional substrates. Future developments in this area depend on further developments in surface chemistry and instrumentation (Carbonell & Braunschweig, 2016).

The additive construction of buildings can make a significant contribution to the construction industry (Labonnote et al., 2016). One of the primary technologies in this field is contour crafting (CC) (Khoshnevis, 2004). As Khoshnevis mentioned, the purpose of CC is the automated construction of one house or a colony of houses in a single run using layered manufacturing techniques (Figure A-50). CC is one of the few feasible methods for construction on planets in outer space, such as Mars (Khoshnevis, 2004). On the other hand, 4D printing can fabricate smart elements as building blocks that can be self-assembled after printing. Therefore, as Labonnote et

al. (2016) indicated, 4D printing and contour crafting can effectively complement each other to pave the way for the human colonization on Mars. One of the main challenges in 4D printed structures is that after a certain number of shape-shifting cycles, the 4D printed structure cannot effectively recover its original shape and degrades (Raviv et al., 2014). In addition to the degradation modeling and lifespan monitoring of 4D printed structures (Momeni et al., 2016), future studies should focus on the improvement of their lifespan.

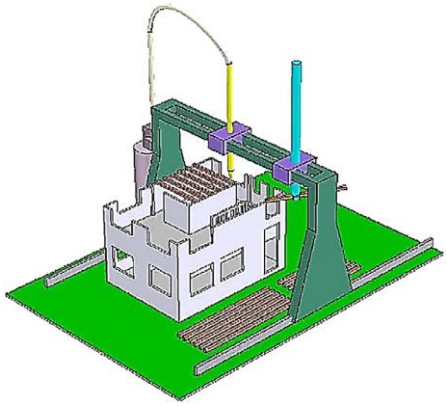

Figure A-50. Automated construction of a building in a single run using contour crafting technology (Khoshnevis, 2004).

In summary, 4D printing process applications are summarized in Figure A-51, along with the associated literature.

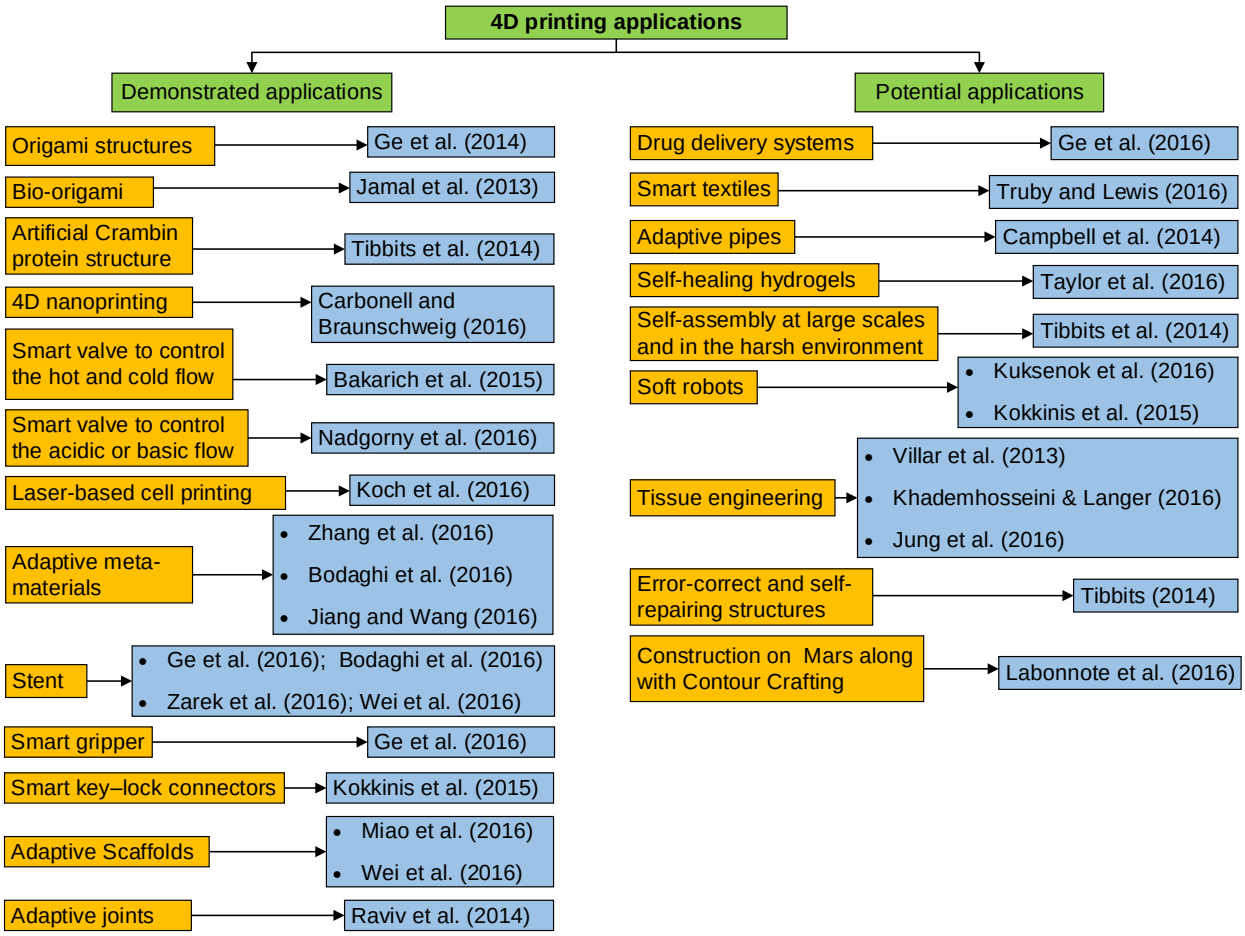

Figure A-51. Applications of the 4D printing process.

BIBLIOGRAPHY

Ali, I. M. S., O'Donovan, T. S., Reddy, K. S., & Mallick, T. K. (2013). An optical analysis of a static 3-D solar concentrator. *Solar Energy*, *88*, 57-70.

Alipour, N., Andersson, R. L., Olsson, R. T., Gedde, U. W., & Hedenqvist, M. S. (2016). VOC-Induced Flexing of Single and Multilayer Polyethylene Films As Gas Sensors. ACS applied materials & interfaces, 8(15), 9946-9953.

Al-Shohani, W. A., Al-Dadah, R., Mahmoud, S., & Algareu, A. (2016). Optimum design of V-trough concentrator for photovoltaic applications. *Solar Energy*, *140*, 241-254.

Amanlou, Y., Hashjin, T. T., Ghobadian, B., Najafi, G., & Mamat, R. (2016). A comprehensive review of uniform solar illumination at low concentration photovoltaic (lcpv) systems. *Renewable and Sustainable Energy Reviews*, *60*, 1430-1441.

Amano, R. S., & Sundén, B. (Eds.). (2014). *Aerodynamics of wind turbines: emerging topics*. WIT Press.

An, J., Teoh, J. E. M., Suntornnond, R., & Chua, C. K. (2015). Design and 3D printing of scaffolds and tissues. *Engineering*, *1*(2), 261-268.

Anand, L., Ames, N. M., Srivastava, V., & Chester, S. A. (2009). A thermo-mechanically coupled theory for large deformations of amorphous polymers. Part I: Formulation. *International Journal of Plasticity*, *25*(8), 1474-1494.

Apostoleris, H., Stefancich, M., & Chiesa, M. (2016). Tracking-integrated systems for concentrating photovoltaics. *Nature Energy*, 1, 16018.

Ashwill, T. D. (2010). Sweep-twist adaptive rotor blade: final project report (No. SAND2009-8037). Sandia National Laboratories.

Ashwill, T., Kanaby, G., Jackson, K., & Zuteck, M. (2010). Development of the sweep-twist adaptive rotor (STAR) blade. In 48th AIAA Aerospace Sciences Meeting Including the New Horizons Forum and Aerospace Exposition (p. 1582).

Athanasopoulos, N., & Siakavellas, N. (2018, July). Variable emissivity through multilayer patterned surfaces for passive thermal control: preliminary thermal design of a nano-

satellite. 48th International Conference on Environmental Systems. Albuquerque, New Mexico

Athanasopoulos, N., & Siakavellas, N. J. (2017). Smart patterned surfaces with programmable thermal emissivity and their design through combinatorial strategies. *Scientific reports*, *7*(1), 12908.

Avella, M., Buzarovska, A., Errico, M. E., Gentile, G., & Grozdanov, A. (2009). Eco-challenges of bio-based polymer composites. Materials, 2(3), 911-925.

Avid, A. Types of Flowers That Close at Night. Available at: http://homeguides.sfgate.com/types-flowers-close-night-56308.html (accessed July 2017).

Bakarich, S. E., Gorkin, R., & Spinks, G. M. (2015). 4D printing with mechanically robust, thermally actuating hydrogels. *Macromolecular rapid communications*, *36*(12), 1211-1217.

Baker, A. B., Wass, D. F., & Trask, R. S. (2016). 4D sequential actuation: combining ionoprinting and redox chemistry in hydrogels. *Smart Materials and Structures*, *25*(10), 10LT02.

Bandyopadhyay, A., & Heer, B. (2018). Additive manufacturing of multi-material structures. *Materials Science and Engineering: R: Reports*, *129*, 1-16.

Barthlott, W., Mail, M., Bhushan, B., & Koch, K. (2017). Plant surfaces: structures and functions for biomimetic innovations. Nano-Micro Letters, 9(2), 23.

Bazilevs, Y., Hsu, M. C., Kiendl, J., & Benson, D. J. (2012). A computational procedure for prebending of wind turbine blades. International Journal for Numerical Methods in Engineering, 89(3), 323-336.

Behl, M., & Lendlein, A. (2007). Shape-memory polymers. Materials today, 10(4), 20-28.

Bejan, A. (2016). *Advanced engineering thermodynamics*. John Wiley & Sons.

Bellos, E., & Tzivanidis, C. (2017). Parametric analysis and optimization of an Organic Rankine Cycle with nanofluid based solar parabolic trough collectors. *Renewable Energy*, *114*, 1376-1393.

Bensaude-Vincent, B. Self-Assembly, Self-Organization: A Philosophical Perspective on Converging Technologies Paper prepared for France/Stanford Meeting Avignon, December 2006.

Berens, A. R., & Hopfenberg, H. B. (1978). Diffusion and relaxation in glassy polymer powders: 2. Separation of diffusion and relaxation parameters. Polymer, 19(5), 489-496.

Bergström, L. M. (2011). Thermodynamics of self-assembly. In *Application of Thermodynamics to Biological and Materials Science*. InTech.

Best, J. P., Neubauer, M. P., Javed, S., Dam, H. H., Fery, A., & Caruso, F. (2013). Mechanics of pH-responsive hydrogel capsules. *Langmuir*, *29*(31), 9814-9823.

Bir, G., & Jonkman, J. (2007). Aeroelastic instabilities of large offshore and onshore wind turbines. In Journal of Physics: Conference Series (Vol. 75, No. 1, p. 012069). IOP Publishing.

Blees, M. K., Barnard, A. W., Rose, P. A., Roberts, S. P., McGill, K. L., Huang, P. Y., ... & McEuen, P. L. (2015). Graphene kirigami. *Nature*, *524*(7564), 204.

Bodaghi, M., Damanpack, A. R., & Liao, W. H. (2016). Self-expanding/shrinking structures by 4D printing. *Smart Materials and Structures*, *25*(10), 105034.

Bongers, P. M., & van Baars, G. E. (1991, December). Experimental validation of a flexible wind turbine model. In Decision and Control, 1991., Proceedings of the 30th IEEE Conference on (pp. 1660-1661). IEEE.

Bonner, M., de Oca, H. M., Brown, M., & Ward, I. M. (2010). A novel approach to predict the recovery time of shape memory polymers. *Polymer*, *51*(6), 1432-1436.

Bottasso, C. L., Campagnolo, F., Croce, A., & Tibaldi, C. (2013). Optimization-based study of bend–twist coupled rotor blades for passive and integrated passive/active load alleviation. *Wind Energy*, 16(8), 1149-1166.

Branham, M., Gutowski, T. G., Jones, A., & Sekulic, D. P. (2008, May). A thermodynamic framework for analyzing and improving manufacturing processes. In Electronics and the Environment, 2008. ISEE 2008. IEEE International Symposium on (pp. 1-6). IEEE.

Brøndsted, P., Lilholt, H., & Lystrup, A. (2005). Composite materials for wind power turbine blades. *Annu. Rev. Mater. Res.*, *35*, 505-538.

Bunse, K., Vodicka, M., Schönsleben, P., Brülhart, M., & Ernst, F. O. (2011). Integrating energy efficiency performance in production management–gap analysis between industrial needs and scientific literature. Journal of Cleaner Production, 19(6-7), 667-679.

Campbell, T. A., Tibbits, S., & Garrett, B. (2014). The programmable world. *Scientific American*, *311*(5), 60-65.

Carbonell, C., & Braunschweig, A. B. (2016). Toward 4D nanoprinting with tip-induced organic surface reactions. *Accounts of chemical research*, *50*(2), 190-198.

Carter, K. Plants That Open in Sunlight & Close in Dark. Available at: http://homeguides.sfgate.com/plants-open-sunlight-close-dark-28050.html (accessed July 2017).

Cengel, Y. A., & Boles, M. A. (2015). *Thermodynamics: An engineering approach*. New York: McGraw-Hill Education.

Chaves, J. (2015). *Introduction to nonimaging optics*. CRC press.

Chehouri, A., Younes, R., Ilinca, A., & Perron, J. (2015). Review of performance optimization techniques applied to wind turbines. *Applied Energy*, *142*, 361-388.

Chen, L., Harding, C., Sharma, A., & MacDonald, E. (2016). Modeling noise and lease soft costs improves wind farm design and cost-of-energy predictions. Renewable Energy, 97, 849-859.

Choi, J., Kwon, O. C., Jo, W., Lee, H. J., & Moon, M. W. (2015). 4D printing technology: A review. *3D Printing and Additive Manufacturing*, 2(4), 159-167.

Choong, Y. Y. C., Maleksaeedi, S., Eng, H., Wei, J., & Su, P. C. (2017). 4D printing of high performance shape memory polymer using stereolithography. Materials & Design, 126, 219-225.

Cock, F., Cuadri, A. A., García-Morales, M., & Partal, P. (2013). Thermal, rheological and microstructural characterisation of commercial biodegradable polyesters. *Polymer Testing*, *32*(4), 716-723.

Cock, F., Cuadri, A. A., García-Morales, M., & Partal, P. (2013). Thermal, rheological and microstructural characterisation of commercial biodegradable polyesters. *Polymer Testing*, 32(4), 716-723.

Cognet, V., du Pont, S. C., Dobrev, I., Massouh, F., & Thiria, B. (2017, February). Bioinspired turbine blades offer new perspectives for wind energy. In Proc. R. Soc. A (Vol. 473, No. 2198, p. 20160726). The Royal Society.

Čolić-Damjanovic, V. M., & Gadjanski, I. (2016, September). Potentials of fablabs for biomimetic architectural research. In *Multidisciplinary Engineering Design Optimization (MEDO), International Conference* (pp. 1-6). IEEE.

Corten, G. P., & Veldkamp, H. F. (2001). Aerodynamics: Insects can halve wind-turbine power. *Nature*, 412(6842), 41-42.

Costabile, G., Fera, M., Fruggiero, F., Lambiase, A., & Pham, D. (2017). Cost models of additive manufacturing: A literature review. International Journal of Industrial Engineering Computations, 8(2), 263-283.

Costello, H. (2018). 3D and 4D Printing Market: Latest Technology, Industry Demand, Future Growth Opportunities till 2022 by Key Players and Regional Analysis. Orbis Research. Available at: https://www.reuters.com/brandfeatures/venture-capital/article?id=29519.

Czugala, M., O'Connell, C., Blin, C., Fischer, P., Fraser, K. J., Benito-Lopez, F., & Diamond, D. (2014). Swelling and shrinking behaviour of photoresponsive phosphonium-based ionogel microstructures. Sensors and Actuators B: Chemical, 194, 105-113.

Dai, G., & Mishnaevsky, L. (2014). Fatigue of hybrid glass/carbon composites: 3D computational studies. *Composites Science and Technology*, *94*, 71-79.

Daneshazarian, R., Cuce, E., Cuce, P. M., & Sher, F. (2018). Concentrating photovoltaic thermal (CPVT) collectors and systems: Theory, performance assessment and applications. *Renewable and Sustainable Energy Reviews*, *81*, 473-492.

De Goeij, W. C., Van Tooren, M. J. L., & Beukers, A. (1999). Implementation of bending-torsion coupling in the design of a wind-turbine rotor-blade. *Applied Energy*, 63(3), 191-207.

De Volder, M. F., Tawfi ck, S. H., Baughman, R. H., & Hart, A. J. (2013). Carbon nanotubes: present and future commercial applications. *science*, *339*(6119), 535-539.

Dekker, H. Saxifraga. Available at: http://www.freenatureimages.eu/plants/Flora%20O-R/Ranunculus%20auricomus,%20Goldilocks%20Buttercup/index.html (accessed December 2017).

Demir, A. G., & Previtali, B. (2017). Multi-material selective laser melting of Fe/Al-12Si components. *Manufacturing letters*, *11*, 8-11.

Dicker, M. P., Duckworth, P. F., Baker, A. B., Francois, G., Hazzard, M. K., & Weaver, P. M. (2014). Green composites: A review of material attributes and complementary applications. *Composites part A: applied science and manufacturing*, *56*, 280-289.

Ding, Z., Yuan, C., Peng, X., Wang, T., Qi, H. J., & Dunn, M. L. (2017). Direct 4D printing via active composite materials. *Science advances*, *3*(4), e1602890.

Dodge, DM. (2006). The illustrated history of wind power development. Littleton, Colorado: U.S. Federal Wind Energy Program. Available at: http://www.telosnet.com/wind/early.html (accessed July 2017).

Dong, Y., Ghataura, A., Takagi, H., Haroosh, H. J., Nakagaito, A. N., & Lau, K. T. (2014). Polylactic acid (PLA) biocomposites reinforced with coir fibres: Evaluation of mechanical performance and multifunctional properties. Composites Part A: Applied Science and Manufacturing, 63, 76-84.

Drumheller, D. P., D'Antonio, G. C., Chapman, B. A., Allison, C. P., & Pierrakos, O. (2015, April). Design of a micro-wind turbine for implementation in low wind speed environments. In Systems and Information Engineering Design Symposium (SIEDS), 2015 (pp. 125-130). IEEE.

Drumright, R. E., Gruber, P. R., & Henton, D. E. (2000). Polylactic acid technology. *Advanced materials*, *12*(23), 1841-1846.

Duerr, F., Meuret, Y., & Thienpont, H. (2011). Tracking integration in concentrating photovoltaics using laterally moving optics. *Optics express*, 19(103), A207-A218.

Duffy, S. (2010). Linear Viscoelasticity: Mechanical (rheological) models. Lecture notes, Cleveland State University. Available at: http://academic.csuohio.edu/duffy_s/Linear_Visco.pdf (accessed December 2017).

Dwyer Instruments Inc. (2010). Product Categories. Retrieved May 29, 2017. Available at: https://www.dwyer-inst.com/PDF_files/400_IOM.pdf (accessed July 2017).

El Alaoui, R., Mounir, H., Boudi, E. M., El Marjani, A., Echab, H., & Mohsine, A. (2016, November). Performances comparison of wind turbine blades materials. In Renewable and Sustainable Energy Conference (IRSEC), 2016 International (pp. 375-380). IEEE.

Ellis, A. G., & Johnson, S. D. (2010). Floral mimicry enhances pollen export: the evolution of pollination by sexual deceit outside of the Orchidaceae. *The American Naturalist*, 176(5), E143-E151.

ElMaraghy, H. A., Youssef, A. M., Marzouk, A. M., & ElMaraghy, W. H. (2017). Energy use analysis and local benchmarking of manufacturing lines. Journal of Cleaner Production, 163, 36-48.

Eriksson, S., Bernhoff, H., & Leijon, M. (2008). Evaluation of different turbine concepts for wind power. *Renewable and Sustainable Energy Reviews*, 12(5), 1419-1434.

Esteban, M. D., Diez, J. J., López, J. S., & Negro, V. (2011). Why offshore wind energy?. *Renewable Energy*, 36(2), 444-450.

Fedorov, V., & Berggreen, C. (2014). Bend-twist coupling potential of wind turbine blades. In Journal of Physics: Conference Series (Vol. 524, No. 1, p. 012035). IOP Publishing.

Felton, S. M., Tolley, M. T., Shin, B., Onal, C. D., Demaine, E. D., Rus, D., & Wood, R. J. (2013). Self-folding with shape memory composites. *Soft Matter*, *9*(32), 7688-7694.

Foster, James J., Camilla R. Sharkey, Alicia VA Gaworska, Nicholas W. Roberts, Heather M. Whitney, and Julian C. Partridge. "Bumblebees learn polarization patterns." Current Biology 24, no. 12 (2014): 1415-1420.

Frewer, L. J., Norde, W., Fischer, A., & Kampers, F. (Eds.). (2011). *Nanotechnology in the agri-food sector: implications for the future*. John Wiley & Sons.

Fritz, B., Hünig, R., Schmager, R., Hetterich, M., Lemmer, U., & Gomard, G. (2017). Assessing the influence of structural disorder on the plant epidermal cells' optical properties: a numerical analysis. Bioinspiration & Biomimetics, 12(3), 036011.

Frohm, B., DeNizio, J. E., Lee, D. S. M., Gentile, L., Olsson, U., Malm, J., ... & Linse, S. (2015). A peptide from human semenogelin I self-assembles into a pH-responsive hydrogel. *Soft Matter*, *11*(2), 414-421.

Gao, B., Yang, Q., Zhao, X., Jin, G., Ma, Y., & Xu, F. (2016). 4D bioprinting for biomedical applications. *Trends in biotechnology*, *34*(9), 746-756.

Gardenia. Available at: https://www.gardenia.net/plant/crocus-vernus-flower-record-dutch-crocus (accessed July 2017).

Garlotta, D. (2001). A literature review of poly (lactic acid). Journal of Polymers and the Environment, 9(2), 63-84.

Ge, Q., Dunn, C. K., Qi, H. J., & Dunn, M. L. (2014). Active origami by 4D printing. *Smart Materials and Structures*, *23*(9), 094007.

Ge, Q., Qi, H. J., & Dunn, M. L. (2013). Active materials by four-dimension printing. *Applied Physics Letters*, *103*(13), 131901.

Ge, Q., Sakhaei, A. H., Lee, H., Dunn, C. K., Fang, N. X., & Dunn, M. L. (2016). Multimaterial 4D printing with tailorable shape memory polymers. *Scientific reports*, 6, 31110.

Ghasemi, S. E., & Ranjbar, A. A. (2017). Numerical thermal study on effect of porous rings on performance of solar parabolic trough collector. *Applied Thermal Engineering*, 118, 807-816.

Girard, R., Laquaine, K., & Kariniotakis, G. (2013). Assessment of wind power predictability as a decision factor in the investment phase of wind farms. *Applied Energy*, 101, 609-617.

Gladman, A. S., Matsumoto, E. A., Nuzzo, R. G., Mahadevan, L., & Lewis, J. A. (2016). Biomimetic 4D printing. *Nature materials*, *15*(4), 413-418.

Gong, X. L., Xiao, Y. Y., Pan, M., Kang, Y., Li, B. J., & Zhang, S. (2016). pH-and Thermal-Responsive Multishape Memory Hydrogel. *ACS applied materials & interfaces*, *8*(41), 27432-27437.

Gorjian, S., Ghobadian, B., Hashjin, T. T., & Banakar, A. (2014). Experimental performance evaluation of a stand-alone point-focus parabolic solar still. Desalination, 352, 1-17.

Grant, L. (1987). Diffuse and specular characteristics of leaf reflectance. Remote Sensing of Environment, 22(2), 309-322.

Gratson, G. M., & Lewis, J. A. (2005). Phase behavior and rheological properties of polyelectrolyte inks for direct-write assembly. *Langmuir*, *21*(1), 457-464.

Griffin, D. A. (2002). Evaluation of design concepts for adaptive wind turbine blades. Sandia National Laboratories, Report No. SAND2002-2424.

Guo, S. Z., Gosselin, F., Guerin, N., Lanouette, A. M., Heuzey, M. C., & Therriault, D. (2013). Solvent-Cast Three-Dimensional Printing of Multifunctional Microsystems. *Small*, *9*(24), 4118-4122.

Gutowski, T. G., Branham, M. S., Dahmus, J. B., Jones, A. J., Thiriez, A., & Sekulic, D. P. (2009). Thermodynamic analysis of resources used in manufacturing processes. *Environmental science & technology*, *43*(5), 1584-1590.

Gutowski, T., Dahmus, J., & Thiriez, A. (2006, May). Electrical energy requirements for manufacturing processes. In *13th CIRP international conference on life cycle engineering* (Vol. 31, pp. 623-638). CIRP International Leuven, Belgium.

Gutowski, T., Dahmus, J., Thiriez, A., Branham, M., & Jones, A. (2007, May). A thermodynamic characterization of manufacturing processes. In *Electronics & the Environment, Proceedings of the 2007 IEEE International Symposium on* (pp. 137-142). IEEE.

Gyftopoulos, E. P., & Beretta, G. P. (2005). *Thermodynamics: foundations and applications*. Courier Corporation.

Hager, M. D., Bode, S., Weber, C., & Schubert, U. S. (2015). Shape memory polymers: past, present and future developments. *Progress in Polymer Science*, *49*, 3-33.

Hansen, M. (2011, January). Aeroelastic properties of backward swept blades. In 49th AIAA Aerospace Sciences Meeting Including the New Horizons Forum and Aerospace Exposition (p. 260).

Hayat, K., & Ha, S. K. (2015). Load mitigation of wind turbine blade by aeroelastic tailoring via unbalanced laminates composites. Composite Structures, 128, 122-133.

Hayat, K., de Lecea, A. G. M., Moriones, C. D., & Ha, S. K. (2016). Flutter performance of bend–twist coupled large-scale wind turbine blades. *Journal of Sound and Vibration*, 370, 149-162.

He, S., Chen, P., Sun, X., & Peng, H. (2016). Stimuli-Responsive Materials From Carbon Nanotubes. *Industrial Applications of Carbon Nanotubes*, 151.

Heald, M. A. (1992). Uncertainty of the slope for highly correlated data. American Journal of Physics, 60(1), 11-11. of the slope for highly correlated data. American Journal of Physics, 60(1), 11-11.

Hedenstrom, A., & Liechti, F. E. L. I. X. (2001). Field estimates of body drag coefficient on the basis of dives in passerine birds. Journal of Experimental Biology, 204(6), 1167-1175.

Hiller, J., & Lipson, H. (2009). Design and analysis of digital materials for physical 3D voxel printing. *Rapid Prototyping Journal*, *15*(2), 137-149.

Hiller, J., & Lipson, H. (2010). Tunable digital material properties for 3D voxel printers. *Rapid Prototyping Journal*, *16*(4), 241-247.

Hirano, A., Hashimoto, T., Kitagawa, D., Kono, K., & Kobatake, S. (2017). Dependence of Photoinduced Bending Behavior of Diarylethene Crystals on Ultraviolet Irradiation Power. *Crystal Growth & Design*, *17*(9), 4819-4825.

Hohmann-Marriott, M. F. (Ed.). (2014). The structural basis of biological energy generation (Vol. 39). Springer Science & Business.

Holmes, J. W., Brøndsted, P., Sørensen, B. F., Jiang, Z., Sun, Z., & Chen, X. (2009). Development of a bamboo-based composite as a sustainable green material for wind turbine blades. *Wind Engineering*, *33*(2), 197-210.

Hoogedoorn, E., Jacobs, G. B., & Beyene, A. (2010). Aero-elastic behavior of a flexible blade for wind turbine application: A 2D computational study. *Energy*, 35(2), 778-785.

Howell, R., Qin, N., Edwards, J., & Durrani, N. (2010). Wind tunnel and numerical study of a small vertical axis wind turbine. *Renewable energy*, 35(2), 412-422.

Hu, J., Meng, H., Li, G., & Ibekwe, S. I. (2012). A review of stimuli-responsive polymers for smart textile applications. *Smart Materials and Structures*, *21*(5), 053001.

Huang, L., Jiang, R., Wu, J., Song, J., Bai, H., Li, B., ... & Xie, T. (2017). Ultrafast digital printing toward 4D shape changing materials. *Advanced Materials*, *29*(7).

Ichter, B., Steele, A., Loth, E., Moriarty, P., & Selig, M. (2016). A morphing downwind-aligned rotor concept based on a 13-MW wind turbine. *Wind Energy*, *19*(4), 625-637.

IEA, 2007a. Tracking Industrial, Energy Efficiency and CO2 Emissions. Available at: https://www.iea.org/publications/freepublications/publication/tracking_emissions.pdf (Accessed May 2018).

Irvine, S. A., & Venkatraman, S. S. (2016). Bioprinting and differentiation of stem cells. *Molecules*, *21*(9), 1188.

Jacobsen, M. (2016). Clearing the Way for Pivotal 21st-Century Innovation. In *Giftedness and Talent in the 21st Century* (pp. 163-179). SensePublishers.

Jacobson, M. Z., & Archer, C. L. (2012). Saturation wind power potential and its implications for wind energy. *Proceedings of the National Academy of Sciences*, 109(39), 15679-15684.

Jamal, M., Kadam, S. S., Xiao, R., Jivan, F., Onn, T. M., Fernandes, R., ... & Gracias, D. H. (2013). Bio-Origami Hydrogel Scaffolds Composed of Photocrosslinked PEG Bilayers. *Advanced healthcare materials*, *2*(8), 1142-1150.

Jespersen, K. M., & Mikkelsen, L. P. (2017). Three dimensional fatigue damage evolution in non-crimp glass fibre fabric based composites used for wind turbine blades. *Composites Science and Technology*, *153*, 261-272.

Ji, S., & Chen, B. (2016). Carbon footprint accounting of a typical wind farm in China. Applied *Energy*, 180, 416-423.

Jiang, Y., & Wang, Q. (2016). Highly-stretchable 3D-architected mechanical metamaterials. *Scientific reports*, *6*, 34147.

Jin, Y., Qin, S. J., & Huang, Q. (2016, August). Prescriptive analytics for understanding of out-of-plane deformation in additive manufacturing. In Automation Science and Engineering (CASE), 2016 IEEE International Conference on(pp. 786-791). IEEE.

Jung, J. P., Bhuiyan, D. B., & Ogle, B. M. (2016). Solid organ fabrication: comparison of decellularization to 3D bioprinting. *Biomaterials research*, *20*(1), 27.

Kaldellis, J. K., & Zafirakis, D. (2011). The wind energy (r) evolution: A short review of a long history. *Renewable Energy*, 36(7), 1887-1901.

Kang, Y., Walish, J. J., Gorishnyy, T., & Thomas, E. L. (2007). Broad-wavelength-range chemically tunable block-copolymer photonic gels. *Nature Materials*, *6*(12), 957.

Karathanassis, I. K., Papanicolaou, E., Belessiotis, V., & Bergeles, G. C. (2017). Design and experimental evaluation of a parabolic-trough concentrating photovoltaic/thermal (CPVT) system with high-efficiency cooling. *Renewable Energy*, 101, 467-483.

Kasaeian, A., Nouri, G., Ranjbaran, P., & Wen, D. (2018). Solar collectors and photovoltaics as combined heat and power systems: A critical review. *Energy Conversion and Management*, *156*, 688-705.

Kaviany, M. (2011). *Essentials of heat transfer: principles, materials, and applications*. Cambridge University Press.

Khademhosseini, A., & Langer, R. (2016). A decade of progress in tissue engineering. *Nature protocols*, *11*(10), 1775-1781.

Khakrah, H., Shamloo, A., & Hannani, S. K. (2017). Determination of Parabolic Trough Solar Collector Efficiency Using Nanofluid: A Comprehensive Numerical Study. *Journal of Solar Energy Engineering*, *139*(5), 051006.

Khamooshi, M., Salati, H., Egelioglu, F., Hooshyar Faghiri, A., Tarabishi, J., & Babadi, S. (2014). A review of solar photovoltaic concentrators. *International Journal of Photoenergy*, 2014, Article 958521.

Khoo, Z. X., Teoh, J. E. M., Liu, Y., Chua, C. K., Yang, S., An, J., ... & Yeong, W. Y. (2015). 3D printing of smart materials: A review on recent progresses in 4D printing. *Virtual and Physical Prototyping*, *10*(3), 103-122.

Khoshnevis, B. (2004). Automated construction by contour crafting—related robotics and information technologies. *Automation in construction*, *13*(1), 5-19.

Kim, B., La Flamme, K., & Peppas, N. A. (2003). Dynamic swelling behavior of pH-sensitive anionic hydrogels used for protein delivery. *Journal of Applied Polymer Science, 89*(6), 1606-1613.

Kim, J. M., & Dutta, P. S. (2012). Optical efficiency–concentration ratio trade-off for a flat panel photovoltaic system with diffuser type concentrator. *Solar Energy Materials and Solar Cells, 103*, 35-40.

Kishore, R. A., Coudron, T., & Priya, S. (2013). Small-scale wind energy portable turbine (SWEPT). *Journal of Wind Engineering and Industrial Aerodynamics*, 116, 21-31.

Koch, L., Deiwick, A., & Chichkov, B. (2016). Laser-Based Cell Printing. *3D Printing and Biofabrication*, 1-27.

Kokkinis, D., Schaffner, M., & Studart, A. R. (2015). Multimaterial magnetically assisted 3D printing of composite materials. *Nature communications, 6*, 8643.

Kooi, C. J., Wilts, B. D., Leertouwer, H. L., Staal, M., Elzenga, J. T. M., & Stavenga, D. G. (2014). Iridescent flowers? Contribution of surface structures to optical signaling. *New Phytologist, 203*(2), 667-673.

Krawczyk, P., Beyene, A., & MacPhee, D. (2013). Fluid structure interaction of a morphed wind turbine blade. International Journal of Energy Research, 37(14), 1784-1793.

Krogsgaard, M., Behrens, M. A., Pedersen, J. S., & Birkedal, H. (2013). Self-healing mussel-inspired multi-pH-responsive hydrogels. *Biomacromolecules, 14*(2), 297-301.

Kruth, J. P., Leu, M. C., & Nakagawa, T. (1998). Progress in additive manufacturing and rapid prototyping. CIRP Annals-Manufacturing Technology, 47(2), 525-540.

Kuethe, A. M., & Chow, C. Y. (1976). *Fondations of aerodynamics*. John Wiley & Sons.

Kuksenok, O., & Balazs, A. C. (2016). Stimuli-responsive behavior of composites integrating thermo-responsive gels with photo-responsive fibers. *Materials Horizons, 3*(1), 53-62.

Kwok, T. H., & Chen, Y. (2017). GDFE: Geometry-Driven Finite Element for Four-Dimensional Printing. Journal of Manufacturing Science and Engineering, 139(11), 111006.

Kwok, T. H., Wang, C. C., Deng, D., Zhang, Y., & Chen, Y. (2015). Four-dimensional printing for freeform surfaces: design optimization of origami and kirigami structures. *Journal of Mechanical Design, 137*(11), 111413.

Labonnote, N., Rønnquist, A., Manum, B., & Rüther, P. (2016). Additive construction: State-of-the-art, challenges and opportunities. *Automation in Construction, 72*, 347-366.

Laflin, K. E., Morris, C. J., Muqeem, T., & Gracias, D. H. (2012). Laser triggered sequential folding of microstructures. *Applied Physics Letters, 101*(13), 131901.

Lamoureux, A., Lee, K., Shlian, M., Forrest, S. R., & Shtein, M. (2015). Dynamic kirigami structures for integrated solar tracking. *Nature communications*, 6.

Larwood, S. M., & Zutek, M. (2006). Swept wind turbine blade aeroelastic modeling for loads and dynamic behavior.

Larwood, S., Van Dam, C. P., & Schow, D. (2014). Design studies of swept wind turbine blades. *Renewable Energy*, 71, 563-571.

Lauff, C., Simpson, T. W., Frecker, M., Ounaies, Z., Ahmed, S., von Lockette, P., ... & Lien, J. M. (2014, August). Differentiating bending from folding in origami engineering using active materials. In *Proceedings of the ASME 2014 International Design Engineering Technical Conferences & Computers and Information Engineering Conference* (p. V05BT08A040).

Le Duigou, A., Castro, M., Bevan, R., & Martin, N. (2016). 3D printing of wood fibre biocomposites: From mechanical to actuation functionality. *Materials & Design*, *96*, 106-114.

Lebel, L. L., Aissa, B., Khakani, M. A. E., & Therriault, D. (2010). Ultraviolet-Assisted Direct-Write Fabrication of Carbon Nanotube/Polymer Nanocomposite Microcoils. *Advanced Materials*, *22*(5), 592-596.

Lee, Y., Lee, H., Hwang, T., Lee, J. G., & Cho, M. (2015). Sequential folding using light-activated polystyrene sheet. *Scientific reports*, *5*.

Levenberg, K. (1944). A method for the solution of certain non-linear problems in least squares. *Quarterly of applied mathematics*, *2*(2), 164-168.

Lewis, J. A. (2006). Direct ink writing of 3D functional materials. *Advanced Functional Materials*, *16*(17), 2193-2204.

Lewis, J. A. (2015). 3D Printing: Making the Future, Science Research Public Lectures.

Li, B., Hong, J., Yan, S., & Liu, Z. (2013). Multidiscipline topology optimization of stiffened plate/shell structures inspired by growth mechanisms of leaf veins in nature. Mathematical Problems in Engineering, 2013.

Li, G., Yan, Q., Xia, H., & Zhao, Y. (2015). Therapeutic-ultrasound-triggered shape memory of a melamine-enhanced poly (vinyl alcohol) physical hydrogel. ACS applied materials & interfaces, 7(22), 12067-12073.

Li, H., Gao, X., & Luo, Y. (2016). Multi-shape memory polymers achieved by the spatio-assembly of 3D printable thermoplastic building blocks. *Soft matter*, *12*(13), 3226-3233.

Liebst, B. S. (1986). Wind turbine gust load alleviation utilizing curved blades. Journal of Propulsion and Power, 2(4), 371-377.

Ligon, S. C., Liska, R., Stampfl, J., Gurr, M., & Mülhaupt, R. (2017). Polymers for 3D printing and customized additive manufacturing. *Chemical reviews*, *117*(15), 10212-10290.

Lind, J. U., Busbee, T. A., Valentine, A. D., Pasqualini, F. S., Yuan, H., Yadid, M., ... & Vlassak, J. J. (2017). Instrumented cardiac microphysiological devices via multimaterial three-dimensional printing. *Nature materials*, 16(3), 303.

Liu, W., & Gong, J. (2011). Adaptive bend-torsional coupling wind turbine blade design imitating the topology structure of natural plant leaves. INTECH Open Access Publisher.

Liu, W., Gong, J., Liu, X., & Zhang, X. (2009, May). A kind of innovative design methodology of wind turbine blade based on natural structure. In Information and Computing Science, 2009. ICIC'09. Second International Conference on (Vol. 4, pp. 350-354). IEEE.

Liu, W., Hou, W., Nan, S., & Ou, Y. (2006, November). Manufacturing-oriented bionic design method for wind turbine blade. In Technology and Innovation Conference, 2006. ITIC 2006. International (pp. 470-476). IET.

Liu, Y., Dong, H., Lohse, N., Petrovic, S., & Gindy, N. (2014). An investigation into minimising total energy consumption and total weighted tardiness in job shops. *Journal of Cleaner Production*, *65*, 87-96.

Liu, Y., Genzer, J., & Dickey, M. D. (2016). "2D or not 2D": Shape-programming polymer sheets. *Progress in Polymer Science*, *52*, 79-106.

Lobitz, D. W., Veers, P. S., & Migliore, P. G. (1996). Enhanced performance of HAWTs using adaptive blades (No. CONF-960154--). Sandia National Laboratory.

Lobitz, D. W., Veers, P. S., Eisler, G. R., Laino, D. J., Migliore, P. G., & Bir, G. (2001). The use of twist-coupled blades to enhance the performance of horizontal axis wind turbines. SAND2001-1003, Sandia National Laboratories, Albuquerque, NM.

Loh, X. J. (2016). Four-dimensional (4D) printing in consumer applications. *Polymers for Personal Care Products and Cosmetics*, *20*, 108-116.

Lopes, L. R., Silva, A. F., & Carneiro, O. S. (2018). Multi-material 3D printing: The relevance of materials affinity on the boundary interface performance. *Additive Manufacturing*, *23*, 45-52.

Loth, E., Steele, A., Qin, C., Ichter, B., Selig, M. S., & Moriarty, P. (2017). Downwind pre-aligned rotors for extreme-scale wind turbines. *Wind Energy*, 20(7).

Maatallah, T., Houcine, A., El Alimi, S., & Nasrallah, S. B. (2018). A novel solar concentrating system based on a fixed cylindrical reflector and tracking receiver. *Renewable Energy*, *117*, 85-107.

MacDonald, A. E., Clack, C. T., Alexander, A., Dunbar, A., Wilczak, J., & Xie, Y. (2016). Future cost-competitive electricity systems and their impact on US CO2 emissions. *Nature Climate Change*, 6(5).

MacDonald, E., & Wicker, R. (2016). Multiprocess 3D printing for increasing component functionality. *Science*, 353(6307), aaf2093.

MacPhee, D. W., & Beyene, A. (2016). Fluid–structure interaction analysis of a morphing vertical axis wind turbine. Journal of Fluids and Structures, 60, 143-159.

MacPhee, D., & Beyene, A. (2011, September). A flexible turbine blade for passive blade pitch control in wind turbines. In Power Engineering and Automation Conference (PEAM), 2011 IEEE (Vol. 1, pp. 196-199). IEEE.

MacPhee, David W., and Asfaw Beyene. "Experimental and Fluid Structure Interaction analysis of a morphing wind turbine rotor." *Energy* 90 (2015): 1055-1065.

Madala, S., & Boehm, R. F. (2016). Effect of reflection losses on stationary dielectric-filled nonimaging concentrators. *Journal of Photonics for Energy*, 6(4), 047002-047002.

Madala, S., & Boehm, R. F. (2017). A review of nonimaging solar concentrators for stationary and passive tracking applications. Renewable and Sustainable Energy Reviews, 71, 309-322.

Mahajan, R. L., Mueller, R., Williams, C. B., Reed, J., Campbell, T. A., & Ramakrishnan, N. (2012, November). Cultivating emerging and black swan technologies. In ASME 2012 International Mechanical Engineering Congress and Exposition (pp. 549-557). American Society of Mechanical Engineers.

Major, M. (2018). Engineers Create 4D Printer that Combines Four 3D Printing Techniques. Interesting Engineering. Available at: https://interestingengineering.com/engineers-create-4d-printer-that-combines-four-3d-printing-techniques (accessed June 2018).

Malachowski, K., Breger, J., Kwag, H. R., Wang, M. O., Fisher, J. P., Selaru, F. M., & Gracias, D. H. (2014). Stimuli-Responsive Theragrippers for Chemomechanical Controlled Release. *Angewandte Chemie*, *126*(31), 8183-8187.

Mallegni, N., Phuong, T. V., Coltelli, M. B., Cinelli, P., & Lazzeri, A. (2018). Poly (lactic acid)(PLA) Based Tear Resistant and Biodegradable Flexible Films by Blown Film Extrusion. Materials, 11(1), 148.

Malthus TR (1798), An essay on the principle of population.

Manwell, J. F., McGowan, J. G., & Rogers, A. L. (2010). *Wind energy explained: theory, design and application*. John Wiley & Sons.

Mao, S., Dong, E., Jin, H., Xu, M., & Low, K. H. (2016, October). Locomotion and gait analysis of multi-limb soft robots driven by smart actuators. In *Intelligent Robots and Systems (IROS), 2016 IEEE/RSJ International Conference on* (pp. 2438-2443). IEEE.

Mao, Y., Ding, Z., Yuan, C., Ai, S., Isakov, M., Wu, J., ... & Qi, H. J. (2016). 3D printed reversible shape changing components with stimuli responsive materials. *Scientific reports*, *6*, 24761.

Mao, Y., Yu, K., Isakov, M. S., Wu, J., Dunn, M. L., & Qi, H. J. (2015). Sequential self-folding structures by 3D printed digital shape memory polymers. *Scientific reports*, *5*, 13616.

Marefati, M., Mehrpooya, M., & Shafii, M. B. (2018). Optical and thermal analysis of a parabolic trough solar collector for production of thermal energy in different climates in Iran with comparison between the conventional nanofluids. *Journal of Cleaner Production*, *175*, 294-313.

Marlec Eng. Co. Ltd. Rutland 914i Windcharger, Owners Manual: Installation and Operation.

Marquardt, D. W. (1963). An algorithm for least-squares estimation of nonlinear parameters. *Journal of the society for Industrial and Applied Mathematics*, *11*(2), 431-441.

Marvel, K., Kravitz, B., & Caldeira, K. (2013). Geophysical limits to global wind power. Nature Climate Change, 3(2), 118-121.

Matsumoto, E. (2016). Phytomimetic 4D Printing. KITP Sheets 16. Available at: http://online.kitp.ucsb.edu/online/sheets16/matsumoto/ (accessed December 2017).

McClendon, J. H. (1984). The micro-optics of leaves. I. Patterns of reflection from the epidermis. American Journal of Botany, 1391-1397.

Meng, H., & Li, G. (2013). A review of stimuli-responsive shape memory polymer composites. *Polymer*, *54*(9), 2199-2221.

Miao, S., Zhu, W., Castro, N. J., Nowicki, M., Zhou, X., Cui, H., ... & Zhang, L. G. (2016). 4D printing smart biomedical scaffolds with novel soybean oil epoxidized acrylate. *Scientific reports*, *6*, 27226.

Miller, L. M., & Kleidon, A. (2016). Wind speed reductions by large-scale wind turbine deployments lower turbine efficiencies and set low generation limits. *Proceedings of the National Academy of Sciences*, 113(48), 13570-13575.

Miller, L. M., Brunsell, N. A., Mechem, D. B., Gans, F., Monaghan, A. J., Vautard, R., ... & Kleidon, A. (2015). Two methods for estimating limits to large-scale wind power generation. *Proceedings of the National Academy of Sciences*, 112(36), 11169-11174.

Mishnaevsky, L., Branner, K., Petersen, H. N., Beauson, J., McGugan, M., & Sørensen, B. F. (2017). Materials for Wind Turbine Blades: An Overview. *Materials*, *10*(11), 1285.

Mittal, V., Akhtar, T., & Matsko, N. (2015). Mechanical, thermal, rheological and morphological properties of binary and ternary blends of PLA, TPS and PCL. Macromolecular Materials and Engineering, 300(4), 423-435.

Mohsenzadeh, M., & Shafii, M. B. (2017). A novel concentrating photovoltaic/thermal solar system combined with thermoelectric module in an integrated design. *Renewable Energy*, 113, 822-834.

Momeni, F., & Ni, J. (2018). Nature-inspired smart solar concentrators by 4D printing. *Renewable Energy*, 122, 35-44.

Momeni, F., Jin, X., & Ni, J. (2016). A Microscopic Approach for Generic Degradation Modeling. *International journal of prognostics and health management*, *7*.

Momeni, F., Liu, X., & Ni, J. (2017). A review of 4D printing. Materials & Design, 122, 42-79.

Momeni, F., Sabzpoushan, S., Valizadeh, R., Morad, M. R., Liu, X., & Ni, J. Plant leaf-mimetic smart wind turbine blades by 4D printing. *Renewable Energy 130C* (2019) pp. 329-351.

Monzón, M. D., Paz, R., Pei, E., Ortega, F., Suárez, L. A., Ortega, Z., ... & Clow, N. (2017). 4D printing: processability and measurement of recovery force in shape memory polymers. *The International Journal of Advanced Manufacturing Technology*, *89*(5-8), 1827-1836.

Moyroud, E., Wenzel, T., Middleton, R., Rudall, P. J., Banks, H., Reed, A., ... & Vignolini, S. (2017). Disorder in convergent floral nanostructures enhances signalling to bees. Nature, 550(7677), 469.

Murdani, A., Hadi, S., & Amrullah, U. S. (2017). Flexural Properties and Vibration Behavior of Jute/Glass/Carbon Fiber Reinforced Unsaturated Polyester Hybrid Composites for Wind Turbine Blade. In *Key Engineering Materials* (Vol. 748, pp. 62-68). Trans Tech Publications.

Musgrove, P. (2010). Wind power (p. 323). Cambridge: Cambridge University Press.

Mutlu, R., Alici, G., in het Panhuis, M., & Spinks, G. (2015, July). Effect of flexure hinge type on a 3D printed fully compliant prosthetic finger. In *Advanced Intelligent Mechatronics (AIM), 2015 IEEE International Conference on* (pp. 790-795). IEEE.

Myers, C. R., Arwade, S. R., Iesulauro, E., Wawrzynek, P. A., Grigoriu, M., Ingraffea, A. R., ... & Sethna, J. P. (1998). Digital material: a framework for multiscale modeling of defects in solids. *MRS Online Proceedings Library Archive*, *538*.

Nadgorny, M., Xiao, Z., Chen, C., & Connal, L. A. (2016). Three-Dimensional Printing of pH-Responsive and Functional Polymers on an Affordable Desktop Printer. *ACS applied materials & interfaces*, *8*(42), 28946-28954.

Naficy, S., Gately, R., Gorkin, R., Xin, H., & Spinks, G. M. (2017). 4D printing of reversible shape morphing hydrogel structures. *Macromolecular Materials and Engineering*, *302*(1).

NASA Glen research center page. Available at: https://www.grc.nasa.gov/www/k-12/airplane/drageq.html (accessed January 2018).

Nath, N. K., Pejov, L., Nichols, S. M., Hu, C., Saleh, N. I., Kahr, B., & Naumov, P. (2014). Model for photoinduced bending of slender molecular crystals. Journal of the American Chemical Society, 136(7), 2757-2766.

Naumov, P., Chizhik, S., Panda, M. K., Nath, N. K., & Boldyreva, E. (2015). Mechanically responsive molecular crystals. *Chemical reviews*, *115*(22), 12440-12490.

News Staff / Source, (2018). Pioneering 4D Printer Developed. Sci-News.com. Available at: http://www.sci-news.com/technologies/4d-printer-05837.html (accessed June 2018).

Nicholls-Lee, R. F., Turnock, S. R., & Boyd, S. W. (2013). Application of bend-twist coupled blades for horizontal axis tidal turbines. *Renewable Energy*, 50, 541-550.

Nilakantan, J. M., Huang, G. Q., & Ponnambalam, S. G. (2015). An investigation on minimizing cycle time and total energy consumption in robotic assembly line systems. Journal of Cleaner Production, 90, 311-325.

Noyes, C., Qin, C., & Loth, E. (2018). Pre-aligned downwind rotor for a 13.2 MW wind turbine. *Renewable Energy*, *116*, 749-754.

Oliver, K., Seddon, A., & Trask, R. S. (2016). Morphing in nature and beyond: a review of natural and synthetic shape-changing materials and mechanisms. *Journal of Materials Science*, *51*(24), 10663-10689.

Orlov, M., Tokarev, I., Scholl, A., Doran, A., & Minko, S. (2007). pH-responsive thin film membranes from poly (2-vinylpyridine): water vapor-induced formation of a microporous structure. *Macromolecules*, *40*(6), 2086-2091.

Ota, Y., Araki, K., Lee, K. H., Yamaguchi, M., & Nishioka, K. (2017, September). Estimation of conversion efficiency for partially static concentrator with III-V on Si solar cell. In *AIP Conference Proceedings* (Vol. 1881, No. 1, p. 020010). AIP Publishing.

Palermo, E. (2013). Why Do Flowers Close Up at Night?. Live Science. Available at: https://www.livescience.com/34569-why-flowers-close-at-night-nyctinasty.html (accessed July 2017).

Parida, B., Iniyan, S., & Goic, R. (2011). A review of solar photovoltaic technologies. *Renewable and sustainable energy reviews*, 15(3), 1625-1636.

Parkin, J. (1928). The glossy petal of Ranunculus. *Annals of Botany*, *42*(167), 739-755.

Pavese, C., Kim, T., & Murcia, J. P. (2017). Design of a wind turbine swept blade through extensive load analysis. *Renewable Energy*, 102, 21-34.

Pei, E. (2014). 4D Printing: dawn of an emerging technology cycle. *Assembly Automation*, *34*(4), 310-314.

Pei, E., & Loh, G. H. (2018). Technological considerations for 4D printing: an overview. Progress in Additive Manufacturing, 1-13.

Peraza-Hernandez, E. A., Hartl, D. J., Malak Jr, R. J., & Lagoudas, D. C. (2014). Origami-inspired active structures: a synthesis and review. *Smart Materials and Structures*, *23*(9), 094001.

Picot, N., Verelst, D. R., & Larsen, T. J. (2011). Free yawing stall-controlled downwind wind turbine with swept blades and coned rotor. EWEA Annual Event 2011.

Politakis, G., Haans, W., & van Bussel, G. (2008). Suppression of classical flutter using a'smart blade'. In 46th AIAA Aerospace Sciences Meeting and Exhibit (p. 1301).

Popescu, G. A., Mahale, T., & Gershenfeld, N. (2006, January). Digital materials for digital printing. In *NIP & Digital Fabrication Conference* (Vol. 2006, No. 3, pp. 58-61). Society for Imaging Science and Technology.

Pozo Morales, A., Güemes, A., Fernandez-Lopez, A., Carcelen Valero, V., & De La Rosa Llano, S. (2017). Bamboo–Polylactic Acid (PLA) Composite Material for Structural Applications. *Materials*, *10*(11), 1286.

ProFlowers. (2011). How Do Flowers Open and Close?. Available at: http://www.proflowers.com/blog/how-do-flowers-open-and-close (accessed July 2017).

Puranik, A. S., Pao, L. P., White, V. M., & Peppas, N. A. (2016). Synthesis and characterization of pH-responsive nanoscale hydrogels for oral delivery of hydrophobic therapeutics. *European Journal of Pharmaceutics and Biopharmaceutics*, *108*, 196-213.

Pytel, A. & Kiusalaas, J. (2012). Mechanics of materials. (2nd ed), Cengage Learning, Stamford, USA.

Qi, H. J., & Dunn, M. L. (2010). Thermomechanical behavior and modeling approaches. *Shape-Memory Polymers and Multifunctional Composites*, 65.

Rabl, A. (1976). Comparison of solar concentrators. *Solar energy*, 18(2), 93-111.

Rafsanjani, A., & Bertoldi, K. (2017). Buckling-Induced Kirigami. *Physical Review Letters*, *118*(8), 084301.

Rahimifard, S., Seow, Y., & Childs, T. (2010). Minimising Embodied Product Energy to support energy efficient manufacturing. CIRP annals, 59(1), 25-28.

Raviv, D., Zhao, W., McKnelly, C., Papadopoulou, A., Kadambi, A., Shi, B., ... & Raskar, R. (2014). Active printed materials for complex self-evolving deformations. *Scientific reports*, *4*, 7422.

Reddy, K. S., Mallick, T. K., Vikram, T. S., & Sharon, H. (2014). Design and optimisation of elliptical hyperboloid concentrator with helical receiver. *Solar energy*, *108*, 515-524.

Reis, M. O., Olivato, J. B., Bilck, A. P., Zanela, J., Grossmann, M. V. E., & Yamashita, F. (2018). Biodegradable trays of thermoplastic starch/poly (lactic acid) coated with beeswax. Industrial Crops and Products, 112, 481-487.

Riveros-Rosas, D., Sánchez-González, M., Arancibia-Bulnes, C. A., & Estrada, C. A. (2011). Influence of the size of facets on point focus solar concentrators. *Renewable energy*, 36(3), 966-970.

Riziotis, V. A., Voutsinas, S. G., Manolas, D. I., Politis, E. S., & Chaviaropoulos, P. K. (2010). Aeroelastic analysis of pre-curved rotor blades. In Proceedings of the European Wind Energy Conference and Exhibition (EWEC'10).

Robinson, S., Kaboodrangi, A. H., Dunham, S., & Shepherd, R. (2018). Materials for 3D Printing Cardiovascular Devices. In *3D Printing Applications in Cardiovascular Medicine* (pp. 33-59). Academic Press.

Roy, D., Cambre, J. N., & Sumerlin, B. S. (2010). Future perspectives and recent advances in stimuli-responsive materials. *Progress in Polymer Science*, *35*(1), 278-301.

Ruiz-Morales, J. C., Tarancón, A., Canales-Vázquez, J., Méndez-Ramos, J., Hernández-Afonso, L., Acosta-Mora, P., ... & Fernández-González, R. (2017). Three dimensional printing of components and functional devices for energy and environmental applications. *Energy & Environmental Science*, 10(4), 846-859.

Ryu, J., D'Amato, M., Cui, X., Long, K. N., Jerry Qi, H., & Dunn, M. L. (2012). Photo-origami—Bending and folding polymers with light. *Applied Physics Letters*, *100*(16), 161908.

Sandia lab presentations. (2012). Available at: https://www.quora.com/What-is-the-most-efficient-design-for-a-wind-turbine (accessed July 2017).

Sartori, L., Bortolotti, P., Croce, A., & Bottasso, C. L. (2016, September). Integration of prebend optimization in a holistic wind turbine design tool. In Journal of Physics: Conference Series (Vol. 753, No. 6, p. 062006). IOP Publishing.

Saunders, S. (2018). Powerful New 4D Printer Speeds Next-Generation, Next-Dimension 3D Printing. 3dprint.com. Available at: https://3dprint.com/207493/4d-printer-at-acs-meeting/ (accessed June 2018).

Saygin, D., Patel, M.K., & Gielen, D.J. (2010). Global industrial energy efficiency benchmarking: an energy policy tool R. Wright (Ed.), UNIDO Working Paper, Vienna, Austria.

Schledjewski, R., Lloret Pertegas, S., Blößl, Y., Anusic, A., Resch-Fauster, K., Mahendran, A. R., & Wuzella, G. (2017). High Performance Green Composites for Green Technologies. In *Key Engineering Materials* (Vol. 742, pp. 271-277). Trans Tech Publications.

Schubel, P. J., & Crossley, R. J. (2012). Wind turbine blade design. Energies, 5(9), 3425-3449.

Schweiger, J., Beuer, F., Stimmelmayr, M., Edelhoff, D., Magne, P., & Güth, J. F. (2016). Histo-anatomic 3D printing of dental structures. *British dental journal*, *221*(9), 555-560.

Sears, F. W., Salinger, G. (1975). *Thermodynamics, kinetic theory, and statistical thermodynamics*., 3rd edn. Addison-Wesley

Sedaghat, A., Liu, X., Whitty, J., & Tang, X. (2012). Wind power of small wind turbines in turbulent open jets. *Scientia Iranica*, 19(2), 272-281.

Sellami, N., Mallick, T. K., & McNeil, D. A. (2012). Optical characterisation of 3-D static solar concentrator. *Energy Conversion and Management*, *64*, 579-586.

Seow, Y., & Rahimifard, S. (2011). A framework for modelling energy consumption within manufacturing systems. CIRP Journal of Manufacturing Science and Technology, 4(3), 258-264.

Shamoon, T. Flowers That Close During the Day. Available at: http://homeguides.sfgate.com/flowers-close-during-day-37643.html (accessed July 2017).

Shultz, D. (2017). Wind turbines inspired by insect wings are 35% more efficient. Available at: http://www.sciencemag.org/news/2017/02/wind-turbines-inspired-insect-wings-are-35-more-efficient (accessed July 2017).

Sombatdee, S., Amornsakchai, T., & Saikrasun, S. (2018). Effects of polylactic acid and rPET minor components on phase evolution, tensile and thermal properties of polyethylene-based composite fibers. Polymers for Advanced Technologies, 29(3), 1123-1137.

Somerville, C., Bauer, S., Brininstool, G., Facette, M., Hamann, T., Milne, J., ... & Vorwerk, S. (2004). Toward a systems approach to understanding plant cell walls. *Science*, 306(5705), 2206-2211.

Song, A. Y., Oh, Y. A., Roh, S. H., Kim, J. H., & Min, S. C. (2016). Cold oxygen plasma treatments for the improvement of the physicochemical and biodegradable properties of polylactic acid films for food packaging. Journal of food science, 81(1).

Speck, O., Speck, D., Horn, R., Gantner, J., & Sedlbauer, K. P. (2017). Biomimetic bio-inspired biomorph sustainable? An attempt to classify and clarify biology-derived technical developments. *Bioinspiration & biomimetics*, *12*(1), 011004.

Srivastava, V., Chester, S. A., & Anand, L. (2010). Thermally actuated shape-memory polymers: experiments, theory, and numerical simulations. *Journal of the Mechanics and Physics of Solids*, *58*(8), 1100-1124.

Stäblein, A. R., Hansen, M. H., & Pirrung, G. (2017). Fundamental aeroelastic properties of a bend–twist coupled blade section. *Journal of Fluids and Structures*, 68, 72-89.

Steed, J. W., Turner, D. R., & Wallace, K. (2007). *Core concepts in supramolecular chemistry and nanochemistry*. John Wiley & Sons.

Steele, C. R. (2000). Shell stability related to pattern formation in plants. *Journal of Applied Mechanics*, 67(2), 237-247.

Stoychev, G., Turcaud, S., Dunlop, J. W., & Ionov, L. (2013). Hierarchical multi-step folding of polymer bilayers. *Advanced Functional Materials*, *23*(18), 2295-2300.

Stuart, M. A. C., Huck, W. T., Genzer, J., Müller, M., Ober, C., Stamm, M., ... & Winnik, F. (2010). Emerging applications of stimuli-responsive polymer materials. *Nature materials*, *9*(2), 101.

Su, W., & Song, W. (2015). Nonlinear Aeroelastic Modeling and Analysis of Flexible Wind Turbine Blades. In 56th AIAA/ASCE/AHS/ASC Structures, Structural Dynamics, and Materials Conference (p. 0178).

Sun, L., & Huang, W. M. (2010). Mechanisms of the multi-shape memory effect and temperature memory effect in shape memory polymers. *Soft Matter*, *6*(18), 4403-4406.

Sun, L., Huang, W. M., Ding, Z., Zhao, Y., Wang, C. C., Purnawali, H., & Tang, C. (2012). Stimulus-responsive shape memory materials: a review. *Materials & Design*, *33*, 577-640.

Sutherland, H. J. (1999). *A summary of the fatigue properties of wind turbine materials* (No. SAND99-2613J). Sandia National Labs., Albuquerque, NM (US); Sandia National Labs., Livermore, CA (US).

Swolfs, Y. (2017). Perspective for Fibre-Hybrid Composites in Wind Energy Applications. *Materials*, *10*(11), 1281.

Tang, R., & Wang, J. (2013). A note on multiple reflections of radiation within CPCs and its effect on calculations of energy collection. *Renewable energy*, *57*, 490-496.

Taylor, D. L. (2016). Self-Healing Hydrogels. *Advanced Materials*.

Taylor, L. (2017). 9 Fragrant Flowers That Bloom in the Evening. Countryliving. Available at: http://www.countryliving.com/gardening/garden-ideas/g806/choosing-fragrant-flowers-0609/?slide=9 (accessed July 2017).

Taylor, L. (2017). 9 Fragrant Flowers That Bloom in the Evening. Countryliving. Available at: http://www.countryliving.com/gardening/garden-ideas/g806/choosing-fragrant-flowers-0609/?slide=7 (accessed July 2017).

Thérien-Aubin, H., Wu, Z. L., Nie, Z., & Kumacheva, E. (2013). Multiple shape transformations of composite hydrogel sheets. *Journal of the American Chemical Society*, *135*(12), 4834-4839.

Tian, Y., & Zhao, C. Y. (2013). A review of solar collectors and thermal energy storage in solar thermal applications. *Applied energy*, 104, 538-553.

Tibbits, S. (2014). 4D printing: multi-material shape change. *Architectural Design*, *84*(1), 116-121.

Tibbits, S. The emergence of "4D printing", TED conference, (2013).

Tibbits, S., McKnelly, C., Olguin, C., Dikovsky, D., & Hirsch, S. (2014). 4D Printing and universal transformation.

Timoshenko, S. & Gere, J. M. Mechanics of Materials (Van Nostrand Reinhold Co., New York, 1973).

Timoshenko, S. (1925). Analysis of bi-metal thermostats. *JOSA*, *11*(3), 233-255.

Tina, G. M., & Scandura, P. F. (2012). Case study of a grid connected with a battery photovoltaic system: V-trough concentration vs. single-axis tracking. *Energy conversion and management*, *64*, 569-578.

Tobushi, H., Hashimoto, T., Hayashi, S., & Yamada, E. (1997). Thermomechanical constitutive modeling in shape memory polymer of polyurethane series. *Journal of intelligent material systems and structures*, *8*(8), 711-718.

TracePro User's Manual. Release 7.8, Lambda Research Corporation, 25 Porter Road, Littleton, MA 01460, USA, 2017. https://www.lambdares.com/wp-content/uploads/TraceProDownload/TracePro_User_Manual.pdf

Truby, R. L., & Lewis, J. A. (2016). Printing soft matter in three dimensions. *Nature*, *540*(7633), 371-378.

Tummala, A., Velamati, R. K., Sinha, D. K., Indraja, V., & Krishna, V. H. (2016). A review on small scale wind turbines. *Renewable and Sustainable Energy Reviews*, 56, 1351-1371.

UCSB ScienceLine. Why do some flowers close at night and some stay open at night?. Available at: http://scienceline.ucsb.edu/getkey.php?key=3098 (accessed July 2017).

Vaezi, M., Chianrabutra, S., Mellor, B., & Yang, S. (2013). Multiple material additive manufacturing–Part 1: a review: this review paper covers a decade of research on

multiple material additive manufacturing technologies which can produce complex geometry parts with different materials. *Virtual and Physical Prototyping*, *8*(1), 19-50.

van der Kooi, C. J., Elzenga, J. T. M., Dijksterhuis, J., & Stavenga, D. G. (2017). Functional optics of glossy buttercup flowers. *Journal of The Royal Society Interface*, *14*(127), 20160933.

van Doorn, W. G., & van Meeteren, U. (2003). Flower opening and closure: a review. *Journal of experimental botany*, 54(389), 1801-1812.

van Manen, T., Janbaz, S., & Zadpoor, A. A. (2017). Programming 2D/3D shape-shifting with hobbyist 3D printers. *Materials Horizons*, *4*(6), 1064-1069.

Veers, P. S., & Lobitz, D. W. (2003). U.S. Patent No. H2,057. Washington, DC: U.S. Patent and Trademark Office.

Veers, P., Bir, G., & Lobitz, D. (1998, January). Aeroelastic tailoring in wind-turbine blade applications. In Proceedings, *Windpower* (Vol. 98, pp. 291-304).

Verelst, D. R., & Larsen, T. J. (2010). Load consequences when sweeping blades-A case study of a 5 MW pitch controlled wind turbine. Danmarks Tekniske Universitet, Risø Nationallaboratoriet for Bæredygtig Energi.

Verhulst PF (1838), Notice sur la loi que la population suit dans son accroissement. Correspondence Mathematique et Physique, 10:113–121.

Vignolini, S., Davey, M. P., Bateman, R. M., Rudall, P. J., Moyroud, E., Tratt, J., ... & Glover, B. J. (2012). The mirror crack'd: both pigment and structure contribute to the glossy blue appearance of the mirror orchid, Ophrys speculum. *New Phytologist*, *196*(4), 1038-1047.

Vignolini, S., Thomas, M. M., Kolle, M., Wenzel, T., Rowland, A., Rudall, P. J., ... & Steiner, U. (2011). Directional scattering from the glossy flower of Ranunculus: how the buttercup lights up your chin. *Journal of The Royal Society Interface*, rsif20110759.

Villar, G., Graham, A. D., & Bayley, H. (2013). A tissue-like printed material. *Science*, *340*(6128), 48-52.

Villazon, L. (2009). Why do poppy flowers open in the morning and close at night?. Sciencefocus. Available at: http://www.sciencefocus.com/qa/why-do-poppy-flowers-open-morning-and-close-night (accessed July 2017).

Vincent, J. F. (2006). The materials revolution. *Journal of Bionic Engineering*, *3*(4), 217-234.

Vogelmann, T. C. (1993). Plant tissue optics. Annual review of plant biology, 44(1), 231-251.

Von Bertalanffy, L. (1938). A quantitative theory of organic growth (inquiries on growth laws. II). *Human biology*, *10*(2), 181-213.

Wallin, T. J., Pikul, J., & Shepherd, R. F. (2018). 3D printing of soft robotic systems. *Nature Reviews Materials*, 1.

Waluyo, J. (2015). 14 Beautiful Flowers which Blooming at Night. INVORMA. Available at: http://invorma.com/10-beautiful-flowers-which-blooming-at-night/ (accessed July 2017).

Wan, S., Cheng, L., & Sheng, X. (2015). Effects of yaw error on wind turbine running characteristics based on the equivalent wind speed model. Energies, 8(7), 6286-6301.

Wang, B., Hina, K., Zou, H., Zuo, D., & Yi, C. (2018). Thermal, crystallization, mechanical and decomposition properties of poly (lactic acid) plasticized with poly (ethylene glycol). Journal of Vinyl and Additive Technology, 24, E154-E163.

Wang, J., Bai, G., & Kong, X. (2017). Single-Loop Foldable 8R Mechanisms with Multiple Modes. In *New Trends in Mechanism and Machine Science* (pp. 503-510). Springer International Publishing.

Wang, J., Yang, S., Jiang, C., Yan, Q., & Lund, P. D. (2017). A novel 2-stage dish concentrator with improved optical performance for concentrating solar power plants. *Renewable Energy*, 108, 92-97.

Wang, Q., & Zhao, X. (2014). Phase diagrams of instabilities in compressed film-substrate systems. *Journal of applied mechanics*, *81*(5), 051004.

Wang-Iverson, P., Lang, R. J., & Mark, Y. I. M. (Eds.). (2016). *Origami 5: Fifth International Meeting of Origami Science, Mathematics, and Education*. CRC Press.

Wang-yu, L. I. U., & ZHANG, Y. (2010). Network study of plant leaf topological pattern and mechanical property and its application. Advances in Natural Science, 3(2), 82-92.

Wehner, R., & Bernard, G. D. (1993). Photoreceptor twist: a solution to the false-color problem. Proceedings of the National Academy of Sciences, 90(9), 4132-4135.

Wei, H., Zhang, Q., Yao, Y., Liu, L., Liu, Y., & Leng, J. (2016). Direct-Write Fabrication of 4D Active Shape-Changing Structures Based on a Shape Memory Polymer and Its Nanocomposite. *ACS applied materials & interfaces*, *9*(1), 876-883.

Whitesides, G. M., & Boncheva, M. (2002). Beyond molecules: Self-assembly of mesoscopic and macroscopic components. *Proceedings of the National Academy of Sciences*, *99*(8), 4769-4774.

Whitesides, G. M., & Grzybowski, B. (2002). Self-assembly at all scales. *Science*, *295*(5564), 2418-2421.

Wikipedia. Mirabilis jalapa. Available at: https://en.wikipedia.org/wiki/Mirabilis_jalapa (accessed July 2017).

Wikipedia. Nicotiana tabacum. Available at: https://en.wikipedia.org/wiki/Nicotiana_tabacum (accessed July 2017).

Wooden Shoe Tulip Farm. Available at: http://www.woodenshoe.com/shop/tulips/jan-reus/ (accessed July 2017).

Woodruff, M. A., & Hutmacher, D. W. (2010). The return of a forgotten polymer—polycaprolactone in the 21st century. *Progress in polymer science*, *35*(10), 1217-1256.

Wu, J., Yuan, C., Ding, Z., Isakov, M., Mao, Y., Wang, T., ... & Qi, H. J. (2016). Multi-shape active composites by 3D printing of digital shape memory polymers. *Scientific reports*, *6*, 24224.

Xie, D., Qin, W., Wang, P., Shuai, Y., Zhou, Y., & Zhu, Q. (2017). Influences of Leaf-Specular Reflection on Canopy BRF Characteristics: A Case Study of Real Maize Canopies With a 3-D Scene BRDF Model. IEEE Transactions on Geoscience and Remote Sensing, 55(2), 619-631.

Xie, T. (2010). Tunable polymer multi-shape memory effect. *Nature*, *464*(7286), 267.

Yakacki, C. M., Shandas, R., Lanning, C., Rech, B., Eckstein, A., & Gall, K. (2007). Unconstrained recovery characterization of shape-memory polymer networks for cardiovascular applications. *Biomaterials*, *28*(14), 2255-2263.

Yakacki, C. M., Shandas, R., Safranski, D., Ortega, A. M., Sassaman, K., & Gall, K. (2008). Strong, Tailored, Biocompatible Shape-Memory Polymer Networks. *Advanced functional materials*, *18*(16), 2428-2435.

Young, H. J. (2002). Diurnal and nocturnal pollination of Silene alba (Caryophyllaceae). *American Journal of Botany*, 89(3), 433-440.

Young, M. ALL3DP Company, (2016), Available from, https://all3dp.com/4d-printing/, accessed August 2016.

Yu, K., Dunn, M. L., & Qi, H. J. (2015). Digital manufacture of shape changing components. *Extreme Mechanics Letters*, *4*, 9-17.

Yu, K., Xie, T., Leng, J., Ding, Y., & Qi, H. J. (2012). Mechanisms of multi-shape memory effects and associated energy release in shape memory polymers. *Soft Matter*, *8*(20), 5687-5695.

Zarek, M., Mansour, N., Shapira, S., & Cohn, D. (2017). 4D Printing of Shape Memory-Based Personalized Endoluminal Medical Devices. *Macromolecular rapid communications*, *38*(2).

Zhang, H., Chen, H., Han, Y., Liu, H., & Li, M. (2017). Experimental and simulation studies on a novel compound parabolic concentrator. *Renewable Energy*, 113, 784-794.

Zhang, Q., Yan, D., Zhang, K., & Hu, G. (2015). Pattern transformation of heat-shrinkable polymer by three-dimensional (3D) printing technique. *Scientific reports*, 5, 8936.

Zhang, Q., Zhang, K., & Hu, G. (2016). Smart three-dimensional lightweight structure triggered from a thin composite sheet via 3D printing technique. *Scientific reports, 6*, 22431.

Zhang, X., Ma, C., Song, X., Zhou, Y., & Chen, W. (2016). The impacts of wind technology advancement on future global energy. *Applied Energy*, 184, 1033-1037.

Zhang, X., Yu, Z., Wang, C., Zarrouk, D., Seo, J. W. T., Cheng, J. C., ... & Zhang, J. (2014). Photoactuators and motors based on carbon nanotubes with selective chirality distributions. *Nature communications, 5*.

Zhou, C., Chen, Y., Yang, Z., & Khoshnevis, B. (2013). Digital material fabrication using mask-image-projection-based stereolithography. *Rapid Prototyping Journal*, *19*(3), 153-165.

Zhou, J., & Sheiko, S. S. (2016). Reversible shape-shifting in polymeric materials. *Journal of Polymer Science Part B: Polymer Physics*, *54*(14), 1365-1380.

Zhou, X., An, L., Wang, Z., & Zhao, H. (2015). Bend-Twist Coupling Characteristics Calculations of 5MW Wind Turbine Blades based on 3D Shell Model.

Zhou, Y., Hauser, A. W., Bende, N. P., Kuzyk, M. G., & Hayward, R. C. (2016). Waveguiding Microactuators Based on a Photothermally Responsive Nanocomposite Hydrogel. Advanced Functional Materials, 26(30), 5447-5452.

Zhou, Y., Huang, W. M., Kang, S. F., Wu, X. L., Lu, H. B., Fu, J., & Cui, H. (2015). From 3D to 4D printing: approaches and typical applications. *Journal of Mechanical Science and Technology*, *29*(10), 4281-4288.

Zumdahl SS, DeCoste JD (2016) *Chemical principles*, 8th edn. Cengage Learning

Zuteck, M. D. (2002). Adaptive blade concept assessment: curved planform induced twist investigation. Sandia National Laboratories.